THE APE ATLAS

David L. Williamson[1], Michael Blackburn[2], Brian J. Hoskins[3], Kensuke Nakajima[4], Wataru Ohfuchi[5], Yoshiyuki O. Takahashi[6], Yoshi-Yuki Hayashi[6], Hisashi Nakamura[7], Masaki Ishiwatari[8], John L. McGregor[9], Hartmut Borth[10], Volkmar Wirth[11], Helmut Frank[12], Peter Bechtold[13], Nils P. Wedi[13], Hirofumi Tomita[14], Masaki Satoh[15], Ming Zhao[16], Isaac M. Held[16], Max J. Suarez[17], Myong-In Lee[18], Masahiro Watanabe[19], Masahide Kimoto[19], Yimin Liu[20], Zaizhi Wang[21], Andrea Molod[22], Kavirajan Rajendran[23], Akio Kitoh[24] and Rachel Stratton[25]

[1](NCAR) National Center for Atmospheric Research, Boulder, CO, USA
[2](CGAM) National Centre for Atmospheric Science, The University of Reading, Berkshire, UK
[3](CGAM) The University of Reading, Reading, Berkshire, UK
[4](AGU) Kyushu University, Kyushu, Japan
[5](AGU) Japan Agency for Marine-Earth Science and Technology, Japan
[6](AGU) Kobe University, Kobe, Japan
[7](AGU) The University of Tokyo, Tokyo, Japan
[8](AGU) Hokkaido University, Hokkaido, Japan
[9](CSIRO) CMAR, Aspendale, Australia
[10](DWD) Theoretical Meteorologie, University of Hamburg, Hamburg, Germany
[11](DWD) Institute for Atmospheric Physics, University of Mainz, Mainz, Germany
[12](DWD) Research and Development, Deutscher Wetterdienst, Offenbach, Germany
[13](ECMWF) European Centre for Medium Range Weather Forecasts, Reading, Berkshire, UK
[14](FRCGC) Advanced Institute for Computational Science, RIKEN, Japan
[15](FRCGC) Atmosphere and Ocean Research Institute, University of Tokyo, Kashiwa, Japan
[16](GFDL) Geophysical Fluid Dynamics Laboratory, Princeton University, Princeton, NJ, USA
[17](GSFC) GMAO, NASA Goddard Space Flight Center, Greenbelt, MD, USA
[18](GSFC) Ulsan National Institute of Science and Technology, Korea
[19](K1JAPAN) Atmosphere and Ocean Research Institute, The University of Tokyo, Japan
[20](LASG) LASG, Institute of Atmospheric Physics, CAS, Beijing, China
[21](LASG) National Climate Center, China Meteorological Administration, China
[22](MIT) GMAO, NASA Goddard Space Flight Center, Greenbelt, MD, USA
[23](MRI) C-MMACS, National Aerospace Laboratories, Bangalore, India
[24](MRI) Meteorological Research Institute, Tsukuba, Japan
[25](UKMO) Met Office, Exeter, Devon, UK

NCAR TECHNICAL NOTES

The Technical Notes series provides an outlet for a variety of NCAR Manuscripts that contribute in specialized ways to the body of scientific knowledge but that are not suitable for journal, monograph, or book publication. Reports in this series are issued by the NCAR scientific divisions. Designation symbols for the series include:

EDD–*Engineering, Design, or Development Reports*
Equipment descriptions, test results, instrumentation, and operating and maintenance manuals.

IA–*Instructional Aids*
Instruction manuals, bibliographies, film supplements, and other research or instructional aids.

PPR–*Program Progress Reports*
Field program reports, interim and working reports, survey reports, and plans for experiments.

PROC–*Proceedings*
Documentation or symposia, colloquia, conferences, workshops, and lectures. (Distribution may be limited to attendees).

STR–*Scientific and Technical Reports*
Data compilations, theoretical and numerical investigations, and experimental results.

THE APE ATLAS

David L. Williamson[1], Michael Blackburn[2], Brian J. Hoskins[3], Kensuke Nakajima[4], Wataru Ohfuchi[5], Yoshiyuki O. Takahashi[6], Yoshi-Yuki Hayashi[6], Hisashi Nakamura[7], Masaki Ishiwatari[8], John L. McGregor[9], Hartmut Borth[10], Volkmar Wirth[11], Helmut Frank[12], Peter Bechtold[13], Nils P. Wedi[13], Hirofumi Tomita[14], Masaki Satoh[15], Ming Zhao[16], Isaac M. Held[16], Max J. Suarez[17], Myong-In Lee[18], Masahiro Watanabe[19], Masahide Kimoto[19], Yimin Liu[20], Zaizhi Wang[21], Andrea Molod[22], Kavirajan Rajendran[23], Akio Kitoh[24] and Rachel Stratton[25]

[1](NCAR) National Center for Atmospheric Research, Boulder, CO, USA
[2](CGAM) National Centre for Atmospheric Science, The University of Reading, Berkshire, UK
[3](CGAM) The University of Reading, Reading, Berkshire, UK
[4](AGU) Kyushu University, Kyushu, Japan
[5](AGU) Japan Agency for Marine-Earth Science and Technology, Japan
[6](AGU) Kobe University, Kobe, Japan
[7](AGU) The University of Tokyo, Tokyo, Japan
[8](AGU) Hokkaido University, Hokkaido, Japan
[9](CSIRO) CMAR, Aspendale, Australia
[10](DWD) Theoretical Meteorologie, University of Hamburg, Hamburg, Germany
[11](DWD) Institute for Atmospheric Physics, University of Mainz, Mainz, Germany
[12](DWD) Research and Development, Deutscher Wetterdienst, Offenbach, Germany
[13](ECMWF) European Centre for Medium Range Weather Forecasts, Reading, Berkshire, UK
[14](FRCGC) Research Institute for Global Change, JAMSTEC, Yokohama, Japan
[15](FRCGC) Atmosphere and Ocean Research Institute, University of Tokyo, Kashiwa, Japan
[16](GFDL) Geophysical Fluid Dynamics Laboratory, Princeton University, Princeton, NJ, USA
[17](GSFC) GMAO, NASA Goddard Space Flight Center, Greenbelt, MD, USA
[18](GSFC) Ulsan National Institute of Science and Technology, Korea
[19](K1JAPAN) Atmosphere and Ocean Research Institute, The University of Tokyo, Japan
[20](LASG) LASG, Institute of Atmospheric Physics, CAS, Beijing, China
[21](LASG) National Climate Center, China Meteorological Administration, China
[22](MIT) GMAO, NASA Goddard Space Flight Center, Greenbelt, MD, USA
[23](MRI) C-MMACS, National Aerospace Laboratories, Bangalore, India
[24](MRI) Meteorological Research Institute, Tsukuba, Japan
[25](UKMO) Met Office, Exeter, Devon, UK

The parenthetical abbreviation preceding each institutional affiliation identifies the model described in Chapter 3 with which each author is affiliated.

Contents

A NOTE ON THE LIST OF FIGURES WHICH FOLLOWS

The figures for each chapter appear at the end of their respective chapter. This prevents the text from being broken into many small pieces scattered among the figures. However, it can make it more difficult to locate desired figures. Therefore, to make it easier to navigate the following List of Figures, Chapter and Section numbers and titles have been inserted into the list in **UPPER CASE, BOLD FACE** type. The page numbers in the List of Figures assigned to these divisions are the pages where the associated figures begin and not the page numbers where the text can be found. The text page numbers are given in the Table of Contents. The Figure numbers and figure identification are in normal type. This should help to quickly find desired figures associated with each section. Variables are indicated by their APE names defined in Section 2.6.1.

List of Figures

4.2 MAINTENANCE OF ZONAL MEAN STATE 72

    4.2.1 DYNAMICAL BUDGETS: (CO-)VARIANCES 72

        MULTI-MODEL MEAN AND STANDARD DEVIATION

        INDIVIDUAL MODELS

List of Tables

Acknowledgments

Chapter 1

Introduction

This Atlas presents statistical analyses of the simulations submitted to the Aqua-Planet Experiment (APE) data archive. The simulations are from global Atmospheric General Circulation Models (AGCM) applied to a water-covered earth. The AGCMs include ones actively used or being developed for numerical weather prediction or climate research. Some are mature, application models and others are more novel and thus less well tested in Earth-like applications.

The experiment applies AGCMs with their complete parameterization package to an idealization of the planet Earth which has a greatly simplified lower boundary that consists of an ocean only. It has no land and its associated orography, and no sea ice. The ocean is represented by Sea Surface Temperatures (SST) which are specified everywhere with simple, idealized distributions. Thus in the hierarchy of tests available for AGCMs, APE falls between tests with simplified forcings such as those proposed by Held and Suarez (1994) and Boer and Denis (1997) and Earth-like simulations of the Atmospheric Modeling Intercomparison Project (AMIP, Gates et al., 1999). Blackburn and Hoskins (2013) summarize the APE and its aims. They discuss where the APE fits within a modeling hierarchy which has evolved to evaluate complete models and which provides a link between realistic simulation and conceptual models of atmospheric phenomena. The APE bridges a gap in the existing hierarchy.

The goals of APE are to provide a benchmark of current model behaviors and to stimulate research to understand the cause of inter-model differences. APE is sponsored by the World Meteorological Organization (WMO) joint Commission on Atmospheric Science (CAS), World Climate Research Program (WCRP) Working Group on Numerical Experimentation (WGNE).

Chapter 2 of this Atlas provides an overview of the specification of the eight APE experiments and of the data collected. Chapter 3 lists the participating models and includes brief descriptions of each. Chapters 4 through 7 present a wide variety of statistics from the 14 participating models for the eight different experiments. Additional intercomparison figures created by Dr. Yukiko Yamada in AGU group are available at http://www.gfd-dennou.org/library/ape/comparison/.

This Atlas is intended to present and compare the statistics of the APE simulations but does not contain a discussion of interpretive analyses. Such analyses are left for journal papers such as those included in the Special Issue of the *Journal of the Meteorological Society of Japan* (2013, Vol. 91A) devoted to the APE. Two papers in that collection provide an overview of the simulations. One (Blackburn et al., 2013) concentrates on the CONTROL simulation and the other (Williamson et al., 2013) on the response to changes in the meridional SST profile. Additional papers provide more detailed analysis of the basic simulations, while others describe various sensitivities and applications.

The APE experiment data base holds a wealth of data that is now publicly available from the APE web site: http://climate.ncas.ac.uk/ape/. We hope that this Atlas will stimulate future analyses and investigations to understand the large variation seen in the model behaviors.

Chapter 2

Experimental Design

The APE design follows Neale and Hoskins (2000a). Some modifications and additions were made to their specifications to complete the design. Complete details are specified on the APE web site: http://climate.ncas.ac.uk/ape/ under *Experimental Design* and *Requested Diagnostics*. The experimental specifications were grouped into Requirements and Recommendations and are summarized in the following.

2.1 Radiative Forcing and Orbital Parameters

2.1.1 Insolation

Required:

Fixed equinoctial insolation, symmetric about the equator, but including the diurnal cycle, in all experiments. Solar constant is 1365 W m^{-2}.

To obtain perpetual symmetric forcing with the prescribed solar irradiance, the Earth orbit parameters should be modified, setting eccentricity and obliquity to zero, to give a circular equinoctial orbit. The distribution of solar irradiance will then be independent of the calendar.

The use of Earth's elliptical orbit at vernal equinox is strongly discouraged. The Earth-Sun distance at vernal equinox is less than the annual average, increasing solar irradiance relative to the prescribed "solar constant". It is also difficult to identify the precise point in the calendar at which insolation is symmetric about the equator.

2.1.2 GHGs and Ozone

Required:

CO_2: 348 ppmv, as in AMIP II.

Specified zonally symmetric latitude-height distribution of ozone, symmetrized about the equator, corresponding to the annual mean climatology used in AMIP II (Wang et al., 1995; Liang and Wang, 1996). The data are available from the APE home page by following the links under *Experimental Design*.

2.1.3 Well-mixed Radiatively Active Gases

Recommended:

Follow AMIP II recommendations: [CH_4]: 1650 ppbv; [N_2O]: 306 ppbv. Halocarbon concentrations should yield 0.24 W m^{-2} radiative forcing. Use of an "equivalent" [CO_2] is not recommended.

2.1.4 Aerosols

Recommended:

No radiatively active aerosol. Any aerosol specification for cloud condensation should use an oceanic distribution which is fixed in time, zonally symmetric and symmetric about the equator.

2.1.5 Calendar

Recommended:

A 365 or 360 day year, with variable- or fixed-length months respectively. The 3.5 year integration length means that a realistic calendar can be used if integrations are started in March of a leap year. Insolation does not follow the calendar.

2.2 Atmospheric Mass

Recommended:

Specify the initial dry mass of the atmosphere to be equivalent to a global mean surface pressure of 101080 Pa. This is 101325 Pa minus 245 Pa, which corresponds to a global moisture content of 25.006 kg m^{-2} using the recommended value for surface gravity. Dry mass should be conserved throughout the integration, although that depends in the individual models. There is no topography.

2.3 Surface Boundary Conditions

Required:

The prescribed SST distributions for the control and sensitivity experiments follow Neale and Hoskins (2000a). There is no sea ice, the minimum SST is 0°C. The zonal average distributions are shown in Figure 2.1 and the deviations from the zonal average are shown in Figure 2.2. The SST distributions as functions of latitude (φ) and longitude (λ) are given by:

PEAKED

$$T_s(\lambda, \varphi) = \begin{cases} 27\left[\left(\frac{60-|\varphi|}{60}\right)\right] & \text{if } |\varphi| < 60 \\ 0 & \text{if } |\varphi| \geq 60 \end{cases} \tag{2.1}$$

CONTROL

$$T_s(\lambda, \varphi) = \begin{cases} 27\left[1 - \sin^2\left(\frac{90}{60}\varphi\right)\right] & \text{if } |\varphi| < 60 \\ 0 & \text{if } |\varphi| \geq 60 \end{cases} \tag{2.2}$$

QOBS

$$T_s(\lambda, \varphi) = \begin{cases} 27\left(\frac{1}{2}\right)\left\{\left[1 - \sin^2\left(\frac{90}{60}\varphi\right)\right] + \left[1 - \sin^4\left(\frac{90}{60}\varphi\right)\right]\right\} & \text{if } |\varphi| < 60 \\ 0 & \text{if } |\varphi| \geq 60 \end{cases} \tag{2.3}$$

FLAT

$$T_s(\lambda, \varphi) = \begin{cases} 27\left[1 - \sin^4\left(\frac{90}{60}\varphi\right)\right] & \text{if } |\varphi| < 60 \\ 0 & \text{if } |\varphi| \geq 60 \end{cases} \tag{2.4}$$

CONTROL_5N

$$T_s(\lambda, \varphi) = \begin{cases} 27\left[1 - \sin^2\left(\frac{90}{55}(\varphi - 5)\right)\right] & \text{if } 5 \leq |\varphi| < 60 \\ 27\left[1 - \sin^2\left(\frac{90}{65}(\varphi - 5)\right)\right] & \text{if } -60 < |\varphi| \leq 5 \\ 0 & \text{if } |\varphi| \geq 60 \end{cases} \tag{2.5}$$

For the following experiments the anomalies T_{anom} are added to the **CONTROL** SST given above.

1KEQ

$$T_{anom}(\lambda, \varphi) = \begin{cases} \cos^2\left(|\varphi|\frac{90}{15}\right)\cos^2\left(|\lambda - 90|\frac{90}{30}\right) & \text{if } |\varphi| < 15 \text{ and } |\lambda - 90| < 30 \\ 0 & \text{otherwise} \end{cases} \tag{2.6}$$

3KEQ

$$T_{anom}(\lambda, \varphi) = \begin{cases} 3\cos^2\left(|\varphi|\frac{90}{15}\right)\cos^2\left(|\lambda - 90|\frac{90}{30}\right) & \text{if } |\varphi| < 15 \text{ and } |\lambda - 90| < 30 \\ 0 & \text{otherwise} \end{cases} \tag{2.7}$$

3KW1

$$T_{anom}(\lambda, \varphi) = \begin{cases} 3\cos^2\left(|\varphi|\frac{90}{30}\right)\sin\lambda & \text{if } |\varphi| < 30 \\ 0 & \text{if } |\varphi| \geq 30 \end{cases} \tag{2.8}$$
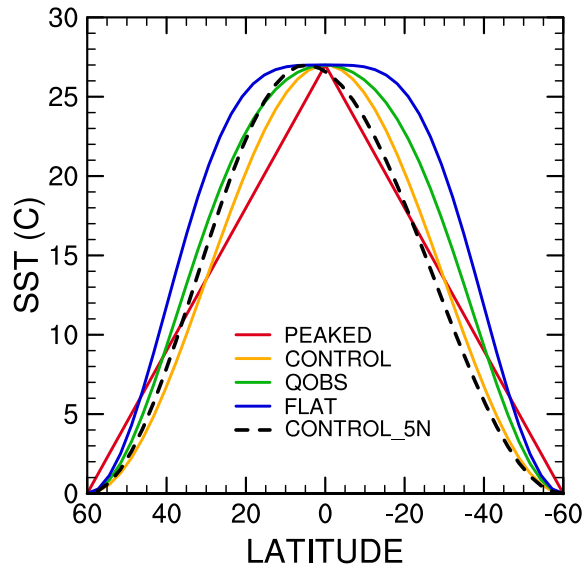
Figure 2.1: Zonal average SST for PEAKED, CONTROL, QOBS, FLAT and CONTROL_5N experiments, °C
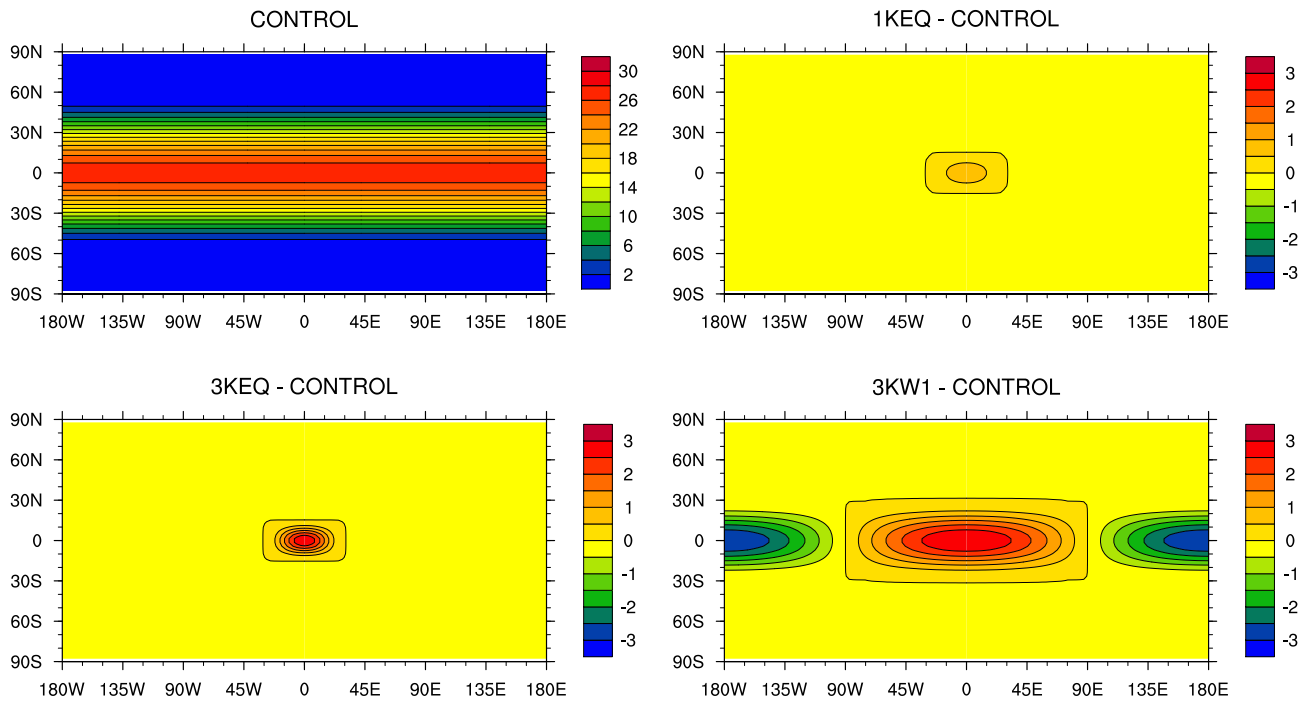
Figure 2.2: SST for CONTROL, 1KEQ-CONTROL, 3KEQ-CONTROL and 3KW1-CONTROL experiments, °C.

6

Table 2.1: Recommended Geophysical Constants and Parameters.

Earth rotation rate	$\omega = 7.292115 \times 10^{-5}$ s^{-1}	[1]
Mean Earth radius	a = 6371.0 km	[2]
Mean surface gravity	g = 9.79764 m s^{-2}	[2]
Gas constant for dry air	$R_d = 287.04$ J kg^{-1}K^{-1}	[3]
Specific heat capacity for dry air	$C_{pd} = 1004.64$ J kg^{-1}K$^{-1} = 7R_d/2$	
(consistent)	$\kappa = R_d/C_{pd}$	
Water vapour gas constant	$R_v = 461.50$ J kg^{-1}K^{-1}	[3]
Water vapour specific heat capacity	$C_{pv} = 1846.0$ J kg^{-1}K$^{-1} = 4R_v$	
Latent heat of vaporization at 0°C	$L_v = 2.501 \times 10^6$ J kg^{-1}	[3]
Latent heat of fusion at 0°C	$L_i = 3.337 \times 10^5$ J kg^{-1}	[3]
Latent heat of sublimation at 0°C	$L_v + L_i = 2.834 \times 10^6$ J kg^{-1}	[3]

[1] Dickey (1995)
[2] Rounding of surface gravity averaged over the Earth ellipsoid 9.797644656 m s^{-2}, in Moritz (1992)
[3] Emanuel (1994) which references List (1951) and Iribarne and Godson (1973).

Quoted values for the temperature dependent specific heat capacities and their ratios with the gas constants vary in the literature, and List (1951) quoted them only to limited accuracy. Hence the theoretical recommendations quoted above.

2.4 Geophysical constants and parameters

Recommended geophysical constants and parameters are provided in Table 2.1.

2.5 Experimental Strategy

Required:

The simulation period is 3.5 years for each experiment, omitting the first 0.5 years as spin-up. Each experiment is started from a model-simulated state, obtained from either an earth-like simulation or a previous aqua-planet integration. The 6-month spin-up should be checked to establish that equilibration was achieved during this period. Preliminary studies suggested that the 3-year sample was adequate for many statistics. However, this should be verified for some of the more complex statistics in the future.

Table 2.2: Requested Data and Diagnostics, Time Sampling and Domains.

Data	Names	Time averaging	Domain
REQUESTED DATA AND DIAGNOSTICS			
GT	Single-Level Global Average Time Series	Daily	Global Average
SH	Single-Level Time Averages (λ, φ)	3-yearly	0-360°, 90°S-90°N
ML	Multi-Level Time Averages (λ, φ, p)	3-yearly	0-360°, 90°S-90°N, P17
TR	Single-Level Transients (λ, φ)	6-hourly	0-360°, 90°S-90°N
MF	Multi-Level Zonal Mean (Co-)variances (φ, p)	3-yearly	90°S-90°N, P17
PF	Parametrization Forcing (λ, φ, η)	3-yearly	0-360°, 90°S-90°N, model levels
DERIVED DIAGNOSTICS			
GA	Single-Level Global-Time Averages	3-yearly	Global Average
SZ	Single-Level Zonal-Time Averages (φ)	3-yearly	90°S-90°N
MZ	Multi-Level Zonal-Time Averages (φ, p)	3-yearly	90°S-90°N, P17
ME	Multi-Level Meridional-Time Averages (λ, p)	3-yearly	10°S-10°N, P17

2.6 Data Collected

2.6.1 Standard Data and Diagnostics

The APE proposal requested the submission of a variety of data sets to the archive, and suggested a number of standard diagnostics that can be computed from them (see under *requested diagnostics*, http://climate.ncas.ac.uk/ape/). The standard diagnostics were considered necessary for the adequate analysis and intercomparison of the experiments. The list is an amalgamation of requested diagnostics taken from the AMIP II standard model output, the WGNE standard diagnostics of mean climate and selected diagnostics which have proved useful in analyzing previous aqua-planet and dynamical core experiments. Many, but not all, of the standard diagnostics are included in this ATLAS along with a few additional diagnostics which have proven informative.

Table 2.2 summarizes the data sets requested for submission to the APE archive and categories of derived diagnostics. The first column contains a two letter designation that is included in the dataset names. It indicates a category or class of standard diagnostics to be described below and is prepended to variable names in the definitions of the standard diagnostics in the following tables. The data are taken from the final 3 years of each 6-month + 3-year integration after ensuring that the simulation reached a statistical equilibrium after the first 6 months.

Except for the parameterized forcing terms, the multi-level data sets are requested on 17 standard pressure levels (1000, 925, 850, 700, 600, 500, 400, 300, 250, 200, 150, 100, 70, 50, 30, 20, 10 hPa). Because the parameterization forcing terms often depend strongly on the actual

model level, they are requested on model levels which for the models in APE are σ (Phillips, 1957), hybrid (Simmons and Strüfing, 1981) or height. The η in the table simply stands for general model levels, not for a particular vertical coordinate.

For 6-hourly, daily, and 3-yearly time-averages, the data are accumulated at every time-step. Exceptions to this in the following standard diagnostics are marked with a †. Those data should be sampled from instantaneous values four times a day at 00, 06, 12 and 18z. Because of their size, the transient data (TR) are requested for year 3 of the experiments only.

In the tables of standard diagnostics which follow, the first column contains a diagnostic index, prepended by the two letter class designation. The second column indicates the necessary data source, again with a variable index prepended by the two letter class designation. A blank in the Data column means the diagnostic can be calculated from diagnostics elsewhere in the same table. The diagnostic name is in the last column. These names are also prepended by the two letter class designation.

We first describe the requested data sets, top component of Table 2.2, followed by a description of diagnostics that can be derived from these collected data, bottom component of Table 2.2. Table 2.3 lists the data collected for single-level global average daily average time series (GT) and associated diagnostics. Along with other uses, these diagnostic provide an assessment of model stability throughout the experiment period. They can also be used to calculate global-time averages. Table 2.4 lists the data collected for single-level (λ, φ) time averages (SH) and associated diagnostics to be plotted as contour maps. The SH list is a super-set of the GT list with variables 01 though 25 being the same and SH30 matching GT25. There is a further set of single-level (λ, φ) time average diagnostics which are extracted from the multi-level data set (ML) to be described next. We include them here for continuity in the SH sequence. The single-level fields are listed in Table 2.5 and numbered SH31 through SH53. The multi-level time average data set (ML) is listed in Table 2.6. This is the only requested data category that does not have an analysis (first column) associated with it. Rather it is the basis for several other derived diagnostics categories (SH, MZ and ME).

Table 2.7 lists high frequency (6-hourly) single-level fields (TR) collected to examine the transient activity of the models. Types of analyses envisioned include tropical wave activity via Wheeler and Kiladis (1999) analysis, storm-track activity and frequency distributions. The data collected to allow examination of the time averaged atmospheric flux of quantities by mid-latitude wave activity (MF) will be described at the end of this section (Table 2.11).

In order to gain insight into the balance and interactions within each model and how models compare, optional diagnostics of the parameterization tendencies were requested (PF). These are zonal-time averages for the zonally symmetric experiments and time averages for the zonally asymmetric experiments. They are listed in Table 2.10.

We now describe the diagnostics that can be derived from the collected data. The first category is global average, time average diagnostics (GA). The variables are identical to those in global-average time series (GT) in Table 2.3. Thus a separate table is not provided. Simply replace GT with GA and gt_ with ga_ to create such a table. These global average time averages (GA) can be calculated from either the GT or SH data sets. The next category is zonal average, time averages of single level fields (SZ). These variables are identical to those in single-level time average series (SH01 through SH30) in Table 2.4. Thus, again, a separate table is not provided. Simply replace SH with SZ and sh_ with sz_ to create such a table. Zonal average, time averages of multi-level fields (MZ) are requested in Table 2.8. These are calculated from

Table 2.3: Single-Level Global Average Time Series (GT).

Analysis	Data	Name	Units	Diagnostic
GT01	GT01	TOA incident shortwave radiation (+ve downward) (SW_{TOAi})	Wm^{-2}	gt_sw_toai
GT02	GT02	TOA reflected shortwave radiation (+ve downward) (SW_{TOAr})	Wm^{-2}	gt_sw_toar
GT03		TOA net shortwave radiation (+ve downward) (SW_{TOA})	Wm^{-2}	gt_sw_toa
GT04	GT04	TOA net longwave radiation (+ve upward) (LW_{TOA})	Wm^{-2}	gt_lw_toa
GT05		TOA radiation residual (+ve upward) ($LW_{TOA} - SW_{TOA}$)	Wm^{-2}	gt_rflux_toa
GT06		TOA albedo (α) (SW_{TOAr}/SW_{TOAi})	fraction	gt_albedo
GT07	GT07	Cloud fraction (CLD_F)	fraction	gt_cld_frac
GT08	GT08	Vertically integrated cloud water (CLD_W)	kg m^{-2}	gt_cldw
GT09	GT09	Vertically integrated cloud ice (CLD_I)	kg m^{-2}	gt_cldi
GT10		Total precipitation rate (PPN_T)	kg m^{-2}s^{-1}	gt_tppn
GT11	GT11	Convective precipitation rate (PPN_C)	kg m^{-2}s^{-1}	gt_cppn
GT12	GT12	Dynamic/Large-scale precipitation rate (PPN_D)	kg m^{-2}s^{-1}	gt_dppn
GT13	GT13	Evaporation rate ($EVAP$)	kg m^{-2}s^{-1}	gt_evap
GT14		Evaporation rate minus total precipitation rate ($EVAP - PPN_T$)	kg m^{-2}s^{-1}	gt_emp
GT15	GT15	Surface incident shortwave radiation (+ve downward) (SW_{Si})	Wm^{-2}	gt_sswi
GT16	GT16	Surface reflected shortwave radiation (+ve downward) (SW_{Sr})	Wm^{-2}	gt_sswr
GT17		Surface net shortwave radiation (+ve downward) (SW_S)	Wm^{-2}	gt_ssw
GT18	GT18	Surface downwelling longwave radiation (+ve upward) (LW_{Sd})	Wm^{-2}	gt_slwd
GT19	GT19	Surface upwelling longwave radiation(+ve upward) (LW_{Su})	Wm^{-2}	gt_slwu
GT20		Surface net longwave radiation (+ve upward) (LW_S)	Wm^{-2}	gt_slw
GT21	GT21	Surface latent heat flux (+ve upward) (LH)	Wm^{-2}	gt_slh
GT22	GT22	Surface sensible heat flux (+ve upward) (SH)	Wm^{-2}	gt_ssh
GT23		Surface residual ($SW_S - LW_S - LH - SH$) (+ve downward)	Wm^{-2}	gt_rflux_sfce
GT24	†GT24	Surface air temperature (at 2 m) (TS_{air})	K	gt_t2m
GT25	†GT25	Surface pressure (Ps)	Pa	gt_ps

the multi-level data set (ML). Finally multi-level equatorial slices, averaged in latitude (ME), are listed in Table 2.9. These are also calculated from the multi-level data set (ML).

Table 2.4: Single-Level (2-D) Latitude-Longitude fields (SH).

Analysis	Data	Name	Units	Diagnostic
SH01	SH01	TOA incident shortwave radiation (+ve downward) (SW_{TOAi})	Wm^{-2}	sh_sw_toai
SH02	SH02	TOA reflected shortwave radiation (+ve downward) (SW_{TOAr})	Wm^{-2}	sh_sw_toar
SH03		TOA net shortwave radiation (+ve downward) (SW_{TOA})	Wm^{-2}	sh_sw_toa
SH04	SH04	TOA net longwave radiation (+ve upward) (LW_{TOA})	Wm^{-2}	sh_lw_toa
SH05		TOA radiation residual (+ve upward) ($LW_{TOA} - SW_{TOA}$)	Wm^{-2}	sh_rflux_toa
SH06		TOA albedo (α) (SW_{TOAr}/SW_{TOAi})	fraction	sh_albedo
SH07	SH07	Cloud fraction (CLD_F)	fraction	sh_cld_frac
SH08	SH08	Vertically integrated cloud water (CLD_W)	kg m^{-2}	sh_cldw
SH09	SH09	Vertically integrated cloud ice (CLD_I)	kg m^{-2}	sh_cldi
SH10		Total precipitation rate (PPN_T)	kg m^{-2}s^{-1}	sh_tppn
SH11	SH11	Convective precipitation rate (PPN_C)	kg m^{-2}s^{-1}	sh_cppn
SH12	SH12	Dynamic/Large-scale precipitation rate (PPN_D)	kg m^{-2}s^{-1}	sh_dppn
SH13	SH13	Evaporation rate ($EVAP$)	kg m^{-2}s^{-1}	sh_evap
SH14		Evaporation rate minus total precipitation rate ($EVAP - PPN_T$)	kg m^{-2}s^{-1}	sh_emp
SH15	SH15	Surface incident shortwave radiation (+ve downward) (SW_{Si})	Wm^{-2}	sh_sswi
SH16	SH16	Surface reflected shortwave radiation (+ve downward) (SW_{Sr})	Wm^{-2}	sh_sswr
SH17		Surface net shortwave radiation (+ve downward) (SW_S)	Wm^{-2}	sh_ssw
SH18	SH18	Surface downwelling longwave radiation (+ve upward) (LW_{Sd})	Wm^{-2}	sh_slwd
SH19	SH19	Surface upwelling longwave radiation(+ve upward) (LW_{Su})	Wm^{-2}	sh_slwu
SH20		Surface net longwave radiation (+ve upward) (LW_S)	Wm^{-2}	sh_slw
SH21	SH21	Surface latent heat flux (+ve upward) (LH)	Wm^{-2}	sh_slh
SH22	SH22	Surface sensible heat flux (+ve upward) (SH)	Wm^{-2}	sh_ssh
SH23		Surface residual ($SW_S - LW_S - LH - SH$) (+ve downward)	Wm^{-2}	sh_rflux_sfce
SH24	†SH24	Surface air temperature (at 2 m) (TS_{air})	K	sh_t2m
SH25	†SH25	Surface specific humidity (at 2 m) (q_S)	kg kg^{-1}	sh_q2m
SH26	SH26	Zonal surface stress (+ve for eastward wind) (τ_{su})	N m^{-2}	sh_tauu
SH27	SH27	Meridional surface stress (+ve for northward wind) (τ_{sv})	N m^{-2}	sh_tauv
SH28	†SH28	Surface zonal wind (at 10 m)	ms^{-1}	sh_u10m
SH29	†SH29	Surface meridional wind (at 10 m)	ms^{-1}	sh_v10m
SH30	†SH30	Surface pressure (Ps)	Pa	sh_ps

Table 2.5: Single-Level (2-D) Latitude-Longitude Slice from 3-D fields (SH).

Analysis	Data	Name	Units	Diagnostic
SH31	†ML01	Zonal wind at 200 hPa (u_{200})	ms^{-1}	sh_u200
SH32	†ML01	Zonal wind at 850 hPa (u_{850})	ms^{-1}	sh_u850
SH33	†ML02	Meridional wind at 200 hPa (v_{200})	ms^{-1}	sh_v200
SH34	†ML02	Meridional wind at 850 hPa (v_{850})	ms^{-1}	sh_v850
SH35	†ML04	Omega at 500 hPa (ω_{500})	Pa s^{-1}	sh_om500
SH36	†ML05	Geopotential height at 500 hPa (Z_{500})	m	sh_z500
SH37	†ML03	Temperature at 700 hPa (T_{700})	K	sh_t700
SH38	†ML01,02	Divergence at 200 hPa (D_{200})	s^{-1}	sh_div200
SH39	†ML01,02	Divergence at 850 hPa (D_{850})	s^{-1}	sh_div850
SH40	†ML01,02	Relative Vorticity at 200 hPa (ζ_{200})	s^{-1}	sh_vort200
SH41	†ML01,02	Relative Vorticity at 850 hPa (ζ_{850})	s^{-1}	sh_vort850
SH42	†ML01,02	Streamfunction at 200 hPa (ψ_{200})	m^{2}s^{-1}	sh_psi200
SH43	†ML01,02	Streamfunction at 850 hPa (ψ_{850})	m^{2}s^{-1}	sh_psi850
SH44	†ML01,02	Velocity potential at 200 hPa (χ_{200})	m^{2}s^{-1}	sh_chi200
SH45	†ML01,02	Velocity potential at 850 hPa (χ_{850})	m^{2}s^{-1}	sh_chi850
SH46	†ML01,02	Zonal rotational velocity at 200 hPa ($u_{\psi 200}$)	ms^{-1}	sh_upsi200
SH47	†ML01,02	Zonal rotational velocity at 850 hPa ($u_{\psi 850}$)	ms^{-1}	sh_upsi850
SH48	†ML01,02	Meridional rotational velocity at 200 hPa ($v_{\psi 200}$)	ms^{-1}	sh_vpsi200
SH49	†ML01,02	Meridional rotational velocity at 850 hPa ($v_{\psi 850}$)	ms^{-1}	sh_vpsi850
SH50	†ML01,02	Zonal divergent velocity at 200 hPa ($u_{\chi 200}$)	ms^{-1}	sh_uchi200
SH51	†ML01,02	Zonal divergent velocity at 850 hPa ($u_{\chi 850}$)	ms^{-1}	sh_uchi850
SH52	†ML01,02	Meridional divergent velocity at 200 hPa ($v_{\chi 200}$)	ms^{-1}	sh_vchi200
SH53	†ML01,02	Meridional divergent velocity at 850 hPa ($v_{\chi 850}$)	ms^{-1}	sh_vchi850

Table 2.6: Multiple-Level 3-D Time Averages (ML).

Analysis	Data	Name	Units	Diagnostic
	†ML01	Zonal wind (u)	ms^{-1}	ml_u
	†ML02	Meridional wind (v)	ms^{-1}	ml_v
	†ML03	Temperature (T)	K	ml_t
	†ML04	Vertical velocity (ω)	Pa s^{-1}	ml_om
	†ML05	Geopotential height (Z)	m	ml_z
	†ML06	Specific humidity (q)	kg kg^{-1}	ml_q
	†ML07	Relative humidity (RH)	%	ml_rh

Table 2.7: Single-Level 2-D Transients (TR).

Analysis	Data	Name	Units	Diagnostic
TR01	TR01	Total precipitation rate (PPN_T)	kg m^{-2}s^{-1}	tr_tppn
TR02	TR02	TOA net longwave radiation (+ve upward) (LW_{TOA})	Wm^{-2}	tr_lw_toa
TR03	†TR03	Vertical velocity at 500 hPa (ω_{500})	Pa s^{-1}	tr_om500
TR04	†TR04	Zonal wind at 250 hPa (u_{250})	ms^{-1}	tr_u250
TR05	†TR05	Meridional wind at 250 hPa (v_{250})	ms^{-1}	tr_v250
TR06	†TR06	Surface pressure (P_s)	Pa	tr_mslp

Table 2.8: Multiple-Level Zonal Means (MZ).

Analysis	Data	Name	Units	Diagnostic
MZ01	†ML01	Zonal wind (u)	ms^{-1}	mz_u
MZ02	†ML02	Meridional wind (v)	ms^{-1}	mz_v
MZ03	†ML03	Temperature (T)	K	mz_t
MZ04	†ML04	Vertical velocity (ω)	Pa s^{-1}	mz_om
MZ05	†ML05	Geopotential height (Z)	m	mz_z
MZ06	†ML06	Specific humidity (q)	kg kg^{-1}	mz_q
MZ07	†ML07	Relative humidity (RH)	%	mz_rh
MZ08	†ML02 or †ML04	Mean meridional circulation (ψ_{MMC})	kg s^{-1}	mz_mmc
MZ09	†ML03	Potential temperature (θ)	K	mz_th
MZ10	†ML03,06	Equivalent potential temperature (θ_e)	K	mz_the
MZ11	†ML03,06	Saturated equivalent potential temperature (θ_e^*)	K	mz_thes

Table 2.9: Multiple-Level Equatorial Slices (ME).

Analysis	Data	Name	Units	Diagnostic
ME01	†ML01	Zonal wind (u)	ms^{-1}	me_u
ME02	†ML04	Vertical velocity (ω)	Pa s^{-1}	me_om
ME03	†ML06	Specific humidity (q)	kg kg^{-1}	me_q
ME04	†ML07	Relative humidity (RH)	%	me_rh
ME05	†ML03	Potential temperature (θ)	K	me_th
ME06	†ML03,06	Equivalent potential temperature (θ_e)	K	me_the
ME07	†ML03,06	Saturated equivalent potential temperature (θ_e^*)	K	me_thes

Table 2.10: Parameterization Tendencies (PF).

Analysis	Data	Name	Units	Diagnostic
PF01	PF01	Temperature tendency – Total $(\partial T/\partial t)$	Ks^{-1}	pf_t
PF02	PF02	Temperature tendency – Short wave $(\partial T/\partial t)_{SW}$	Ks^{-1}	pf_t_sw
PF03	PF03	Temperature tendency – Long wave $(\partial T/\partial t)_{LW}$	Ks^{-1}	pf_t_lw
PF04	PF04	Temperature tendency – Turbulence $(\partial T/\partial t)_{TURB}$	Ks^{-1}	pf_t_turb
PF05	PF05	Temperature tendency – Convection $(\partial T/\partial t)_{CONV}$	Ks^{-1}	pf_t_conv
PF06	PF06	Temperature tendency – Cloud $(\partial T/\partial t)_{LSCLD}$	Ks^{-1}	pf_t_cld
PF07	PF07	Temperature tendency – Dissipation $(\partial T/\partial t)_{DISP}$	Ks^{-1}	pf_t_disp
PF08	PF08	Specific humidity tendency – Total $(\partial q/\partial t)$	$kg\ kg^{-1}s^{-1}$	pf_q
PF09	PF09	Specific humidity tendency – Turbulence $(\partial q/\partial t)_{TURB}$	$kg\ kg^{-1}s^{-1}$	pf_q_turb
PF10	PF10	Specific humidity tendency – Convection $(\partial q/\partial t)_{CONV}$	$kg\ kg^{-1}s^{-1}$	pf_q_conv
PF11	PF11	Specific humidity tendency – Cloud $(\partial q/\partial t)_{LSCLD}$	$kg\ kg^{-1}s^{-1}$	pf_q_cld
PF12	PF12	Specific humidity tendency – Negative q fix $(\partial q/\partial t)_{NEGQ}$	$kg\ kg^{-1}s^{-1}$	pf_q_negq
PF13	PF13	Zonal velocity tendency – Total $(\partial u/\partial t)$	ms^{-2}	pf_u
PF14	PF14	Zonal velocity tendency – Turbulence $(\partial u/\partial t)_{TURB}$	ms^{-2}	pf_u_turb
PF15	PF15	Zonal velocity tendency – Convection $(\partial u/\partial t)_{CONV}$	ms^{-2}	pf_u_conv
PF16	PF16	Zonal velocity tendency – Gravity-wave drag $(\partial u/\partial t)_{GWD}$	ms^{-2}	pf_u_gwd
PF17	PF17	Meridional velocity tendency – Total $(\partial v/\partial t)$	ms^{-2}	pf_v
PF18	PF18	Meridional velocity tendency – Turbulence $(\partial v/\partial t)_{TURB}$	ms^{-2}	pf_v_turb
PF19	PF19	Meridional velocity tendency – Convection $(\partial v/\partial t)_{CONV}$	ms^{-2}	pf_v_conv
PF20	PF20	Meridional velocity tendency – Gravity-wave drag $(\partial v/\partial t)_{GWD}$	ms^{-2}	pf_v_gwd

Co-variance statistics describe the contribution to the averaged flux of quantities by mid-latitude wave activity. Define an overbar $\overline{(\ )}$ to be the time average, prime ($'$) to be the deviation from the time average, square brackets [ ] to be the zonal average and star (*) to be the deviation from the zonal average. The zonally averaged co-variance of two quantities α and β may be partitioned into components

$$\left[\overline{\alpha\beta}\right] = [\overline{\alpha}]\left[\overline{\beta}\right] + \left[\overline{\alpha}^*\overline{\beta}^*\right] + \overline{[\alpha]'[\beta]'} + \overline{[\alpha'^*\beta'^*]} \tag{2.9}$$

where $\left[\overline{\alpha\beta}\right]$ is the total, $[\overline{\alpha}]\left[\overline{\beta}\right]$ is the contribution from the stationary mean meridional circulation, $\left[\overline{\alpha}^*\overline{\beta}^*\right]$ is the contribution from the stationary eddies, $\overline{[\alpha]'[\beta]'}$ .is the contribution from the transient mean meridional circulation and $\overline{[\alpha'^*\beta'^*]}$ is the contribution from the transient eddies. In the Diagnostics column of Table 2.11 the generic _xx_ is replaced by _sm_ for the stationary mean, _se_ for the stationary eddies, _tm_ for the transient mean meridional circulation, and _te_ for the transient eddy fluxes. The total fluxes have _xx_ replaced with just a single underscore _ . To be more explicit, in terms of variable names, Eqn. 2.9 for the zonal wind variance (first row of Table 2.11) can be written symbolically as

$$\text{mf\_uu} = \text{mf\_sm\_uu} + \text{mf\_se\_uu} + \text{mf\_tm\_uu} + \text{mf\_te\_uu} \tag{2.10}$$

The stationary mean is calculated from the multi-level zonal mean (ML) data. The other quadratic terms must be saved. The transient terms can be calculated as residuals from the mean at each time period.

$$\overline{[\alpha]'[\beta]'} = \overline{[\alpha][\beta]} - [\overline{\alpha}]\left[\overline{\beta}\right] \tag{2.11}$$

$$\overline{[\alpha'^*\beta'^*]} = \overline{[\alpha^*\beta^*]} - \left[\overline{\alpha}^*\overline{\beta}^*\right] \tag{2.12}$$

Diagnostic consistency and numerical accuracy must be considered for the component and residual calculations, particularly for models with staggered grids.

Table 2.11: Co-variance statistics (MF).

Name	Variables (α, β)	Units	Diagnostic
Zonal wind variance	(u, u)	$\mathrm{m}^2\mathrm{s}^{-2}$	mf_*xx*_uu
Meridional wind variance	(v, v)	$\mathrm{m}^2\mathrm{s}^{-2}$	mf_*xx*_vv
Temperature variance	(T, T)	K^2	mf_*xx*_tt
Vertical velocity variance	(ω, ω)	$\mathrm{Pa}^2\mathrm{s}^{-2}$	mf_*xx*_omom
Geopotential variance	(Φ, Φ)	$(\mathrm{m}^2\mathrm{s}^{-2})^2$	mf_*xx*_phiphi
Specific humidity variance	(q, q)	$(\mathrm{kg\ kg}^{-1})^2$	mf_*xx*_qq
Poleward zonal momentum flux	(u, v)	$\mathrm{m}^2\mathrm{s}^{-2}$	mf_*xx*_uv
Vertical zonal momentum flux	(u, ω)	$\mathrm{mPa\ s}^{-2}$	mf_*xx*_uom
Vertical meridional momentum flux	(v, ω)	$\mathrm{mPa\ s}^{-2}$	mf_*xx*_vom
Poleward temperature flux	(v, T)	$\mathrm{ms}^{-1}\mathrm{K}$	mf_*xx*_vt
Vertical temperature flux	(ω, T)	$\mathrm{Pa\ s}^{-1}\mathrm{K}$	mf_*xx*_omt
Poleward moisture flux	(v, q)	$\mathrm{ms}^{-1}\mathrm{kg\ kg}^{-1}$	mf_*xx*_vq
Vertical moisture flux	(ω, q)	$\mathrm{Pa\ s}^{-1}\mathrm{kg\ kg}^{-1}$	mf_*xx*_omq
Poleward geopotential flux	(v, Φ)	$\mathrm{m}^3\mathrm{s}^{-3}$	mf_*xx*_vphi

2.6.2   Additional Recommended Diagnostics

Two additional sets of diagnostics were proposed in the APE specification. They can be calculated from the collected data described above. They involve the Transformed Eulerian Mean and Vertically Integrated Budgets. These diagnostics have not yet been calculated from the APE data and are not included in this ATLAS. We recommend that some group take on these analyses in the future as they both should add to our knowledge of the models' behaviors.

Transformed Eulerian Mean (TE)

The Transformed Eulerian Mean (TEM) momentum balance is the clearest way to analyze forcing of the zonally averaged flow by the zonally asymmetric (transient plus stationary) eddies. The recommended diagnostics are summarised in Table 2.12 and are defined in the equations below. The calculations are performed on pressure levels.

Meridional wind

$$[v]^* = [\overline{v}] - \frac{\partial}{\partial p}\left(\left[\overline{v^*\theta^*}\right] \Big/ \frac{\partial\left[\overline{\theta}\right]}{\partial p}\right) \tag{2.13}$$

Omega

$$[\omega]^* = [\overline{\omega}] + \frac{1}{R_e\cos\phi}\frac{\partial}{\partial\phi}\left(\cos\phi\left[\overline{v^*\theta^*}\right] \Big/ \frac{\partial\left[\overline{\theta}\right]}{\partial p}\right) \tag{2.14}$$

Mean-meridional circulation

$$[\Psi]^* = \frac{2\pi R_e\cos\phi}{g}\int_0^p [v]^*\,dp \tag{2.15}$$

Eliassen-Palm Fluxes

$$\mathbf{F} = (F_\phi, F_p) \tag{2.16}$$

Northward

$$F_\phi = R_e\cos\phi\left\{\left(\left[\overline{v^*\theta^*}\right] \Big/ \frac{\partial\left[\overline{\theta}\right]}{\partial p}\right)\left[\frac{\partial\overline{u}}{\partial p}\right] - \overline{u^*v^*}\right\} \tag{2.17}$$

Downward

$$F_p = R_e\cos\phi\left\{\left(\left[\overline{v^*\theta^*}\right] \Big/ \frac{\partial\left[\overline{\theta}\right]}{\partial p}\right)\left(f - \frac{1}{R_e\cos\phi}\frac{\partial}{\partial\phi}\left([\overline{u}]\cos\phi\right)\right) - \overline{u^*\omega^*}\right\} \tag{2.18}$$

Zonal mean Div **F**

$$[\nabla\cdot\mathbf{F}] = \left(\frac{1}{R_e\cos\phi}\frac{\partial}{\partial\phi}\left(\cos\phi F_\phi\right), \frac{\partial F_P}{\partial p}\right) \tag{2.19}$$

Table 2.12: Transformed Eulerian Mean (TE).

Analysis	Data	Name	Units	Diagnostic
TE01	†ML02,03, †MF38,66	TEM Meridional wind ($[v]^*$)	m s^{-1}	te_v
TE02	†ML03,04, †MF38,66	TEM Omega ($[\omega]^*$)	Pa s^{-1}	te_om
TE03		TEM Mean meridional circulation ($[\Psi]^*$)	kg s^{-1}	te_mmc
TE04	†ML01,03, MF35,38,63,66	Northward Eliassen-Palm Flux (F_ψ)	m^{3}s^{-2}	te_fphi
TE05	†ML01,03, MF36,38,64,66	Downward Eliassen-Palm Flux (F_p)	pa m^{2}s^{-2}	te_fp
TE06		TEM Zonal maen Div F ($[\nabla \cdot \mathbf{F}]$)	m^{2}s^{-2}	te_civf

Vertically Integrated Budgets (VB)

These diagnostics closely follow the AMIP II subproject 33, *Atmospheric Transports and Energetics*, proposed by G. J. Boer and S. J. Lambert. More details are presented in their proposal which is available from http://www-pcmdi.llnl.gov/projects/amip/DIAGSUBS/diagsp.php. To a good approximation, the time and zonally averaged, vertically integrated transport equation for a quantity χ takes the following form when some minor source/sink terms are ignored.

$$\frac{1}{R_e \cos\phi}\frac{\partial}{\partial\phi}\left(\cos\phi F_\phi\right) = \left[\overline{S}_{TOA}\right] + \left[\overline{S}_{SFC}\right] = \mathbf{S} \tag{2.20}$$

where

$$
\begin{aligned}
F_\phi &= F_{sz} + F_{se} + F_{tz} + F_{te} \\
&= \int_0^{P_0} [\overline{\chi v}]\frac{dp}{g} \\
&= \int_0^{P_0} [\overline{\chi}]\,[\overline{v}]\frac{dp}{g} + \int_0^{P_0} \overline{[\chi^*]\,[v^*]}\frac{dp}{g} + \int_0^{P_0} \overline{[\chi']\,[v']}\frac{dp}{g} + \int_0^{P_0} \left[\overline{\chi'^* v'^*}\right]\frac{dp}{g}
\end{aligned} \tag{2.21}
$$

The recommended diagnostics are summarised in Table 2.13 for the standard budgets specified below.

Angular Momentum

Absolute angular momentum is $M = R_e \cos\phi\,(\Omega R_e \cos\phi + u)$ and, to a good approximation, the equation for the relative angular momentum budget is given by

$$F_{AM} = R_e \cos\phi \int_0^{P_0} [\overline{uv}] \tag{2.22}$$

$$S_{AM} = R_e \cos\phi\,[\overline{\tau}_{su}] \tag{2.23}$$

Hydrology

The moisture q budget is given by

$$F_q = R_e \cos\phi \int_0^{P_0} [\overline{qv}] \tag{2.24}$$

$$S_q = \left[\overline{EVAP}\right] - \left[\overline{PPN_T}\right] \tag{2.25}$$

18

Energy

Dry static energy ($H_d = C_p T + \Phi$) and moist latent energy ($H_m = Lq$) budgets are given by

$$F_{H_d} = \int_0^{P_0} \left[\overline{H_d v} \right] \tag{2.26}$$

$$S_{H_d} = \left[\overline{SW}_{TOA} \right] - \left[\overline{LW}_{TOA} \right] - \left[\overline{SW}_{SFC} \right] - \left[\overline{LW}_{SFC} \right] + \left[\overline{SH} \right] \tag{2.27}$$

$$F_{H_m} = \int_0^{P_0} \left[\overline{H_m v} \right] \tag{2.28}$$

$$S_{H_m} = \left[\overline{LH} \right] \tag{2.29}$$

Mass Budget Check

As a check in the above calculations due to net mass fluxes, the vertically integrated mass flux, given by equation 2.30, is also calculated

$$F_v = \int_0^{P_0} \left[\overline{v} \right] \tag{2.30}$$

Note that some diagnostics involve repeated calculations from previous diagnostics and the moist energy fluxes simply require multiplication of the moisture fluxes by a constant latent heat of vaporisation (L) value. However, the diagnostics are included for completeness. The flux quantities are requested as diagnostics in order that associated total transports ($T = 2\pi R_e F_\phi \cos\phi$) may also be obtained.

Table 2.13: Vertically Integrated Budgets (VB).

Analysis	Data	Name	Units	Diagnostic
VB01	†MF21	F_{AM} – Stationary Zonal Fluxes $\left(R_e \cos\phi \int_0^{P_0} [\overline{u}]\,[\overline{v}]\,\frac{dp}{g}\right)$	kg ms^{-2}	vb_am_sz
VB02	†MF35	F_{AM} – Stationary Eddy Fluxes $\left(R_e \cos\phi \int_0^{P_0} [\overline{u}^*\overline{v}^*]\,\frac{dp}{g}\right)$	kg ms^{-2}	vb_am_se
VB03	†MF49	F_{AM} – Transient Zonal Fluxes $\left(R_e \cos\phi \int_0^{P_0} \overline{[u]'\,[v]'}\,\frac{dp}{g}\right)$	kg ms^{-2}	vb_am_tz
VB04	†MF63	F_{AM} – Transient Eddy Fluxes $\left(R_e \cos\phi \int_0^{P_0} \left[\overline{u'^*v'^*}\right]\,\frac{dp}{g}\right)$	kg ms^{-2}	vb_am_te
VB05	SH26	F_{AM} – Surface Turbulent Stress $\left([\overline{\tau}_{su}]\,R_e \cos\phi\right)$	kg ms^{-2}	vb_am_tau
VB06	†MF26	F_q – Stationary Zonal Fluxes $\left(\int_0^{P_0} [\overline{v}]\,[\overline{q}]\,\frac{dp}{g}\right)$	kg m^{-1}s^{-1}	vb_q_sz
VB07	†MF40	F_q – Stationary Eddy Fluxes $\left(\int_0^{P_0} [\overline{v}^*\overline{q}^*]\,\frac{dp}{g}\right)$	kg m^{-1}s^{-1}	vb_q_se
VB08	†MF54	F_q – Transient Zonal Fluxes $\left(\int_0^{P_0} \overline{[v]'\,[q]'}\,\frac{dp}{g}\right)$	kg m^{-1}s^{-1}	vb_q_tz
VB09	†MF68	F_q – Transient Eddy Fluxes $\left(\int_0^{P_0} \left[\overline{v'^*q'^*}\right]\,\frac{dp}{g}\right)$	kg m^{-1}s^{-1}	vb_q_te
VB10	SH13	F_q – Evaporation $\left(\left[\overline{EVAP}\right]\right)$	kg m^{-1}s^{-1}	vb_q_evap
VB11	SH11,12	F_q – Total Precipitation $\left(\left[\overline{PPN_T}\right]\right)$	kg m^{-1}s^{-1}	vb_q_tppn
VB12	†MF24,28	F_{H_d} – Dry Stationary Zonal Fluxes $\left(\int_0^{P_0} [\overline{v}]\,[\overline{h_d}]\,\frac{dp}{g}\right)$	Jm^{-1}s^{-1}	vb_hd_sz
VB13	†MF38,42	F_{H_d} – Dry Stationary Eddy Fluxes $\left(\int_0^{P_0} \left[\overline{v}^*\overline{h_d}^*\right]\,\frac{dp}{g}\right)$	Jm^{-1}s^{-1}	vb_hd_se
VB14	†MF52,56	F_{H_d} – Dry Transient Zonal Fluxes $\left(\int_0^{P_0} \overline{[v]'\,[h_d]'}\,\frac{dp}{g}\right)$	Jm^{-1}s^{-1}	vb_hd_tz
VB15	†MF66,70	F_{H_d} – Dry Transient Eddy Fluxes $\left(\int_0^{P_0} \left[\overline{v'^*h_d'^*}\right]\,\frac{dp}{g}\right)$	Jm^{-1}s^{-1}	vb_hd_te
VB16	SH01,02,04	F_{H_d} – Dry $[S]$, TOA $\left(\left[\overline{SW}_{TOA}\right] + \left[\overline{LW}_{TOA}\right]\right)$	Jm^{-1}s^{-1}	vb_hd_toa
VB17	SH15,16,18,19,22	F_{H_d} – Dry $[S]$, Surface $\left(\left[\overline{SW}_{SFC}\right] + \left[\overline{LW}_{SFC}\right] + \left[\overline{SH}\right]\right)$	Jm^{-1}s^{-1}	vb_hd_surf
VB18	†MF26	F_{H_m} – Moist Stationary Zonal Fluxes $\left(\int_0^{P_0} [\overline{v}]\,[\overline{h_m}]\,\frac{dp}{g}\right)$	Jm^{-1}s^{-1}	vb_hm_sz
VB19	†MF40	F_{H_m} – Moist Stationary Eddy Fluxes $\left(\int_0^{P_0} \left[\overline{v}^*\overline{h_m}^*\right]\,\frac{dp}{g}\right)$	Jm^{-1}s^{-1}	vb_hm_se
VB20	†MF54	F_{H_m} – Moist Transient Zonal Fluxes $\left(\int_0^{P_0} \overline{[v]'\,[h_m]'}\,\frac{dp}{g}\right)$	Jm^{-1}s^{-1}	vb_hm_tz
VB21	†MF68	F_{H_m} – Moist Transient Eddy Fluxes $\left(\int_0^{P_0} \left[\overline{v'^*h_m'^*}\right]\,\frac{dp}{g}\right)$	Jm^{-1}s^{-1}	vb_hm_te
VB22	SH21	F_{H_m} – Moist $[S]$, Surface $\left(S_M = \left[\overline{LH}\right]\right)$	Jm^{-1}s^{-1}	vb_hm_surf
VB23	†ML02	F_v – Mass Budget $\left(\int_0^{P_0} [\overline{v}]\,\frac{dp}{g}\right)$	kg m^{-1}s^{-1}	vb_m

2.6.3 Additional Transient Data Collected (TRnn)

During the analysis of the data originally collected for APE it became evident that the single-level transient data highlighted a large variety of simulated tropical transient activity in the APE models as will be seen below in Sections 4.3, 5.3, 6.3 and 7.3. However the data were insufficient to diagnose the vertical structure of dominant propagating features, necessary to catalogue and understand differences between the models and to compare with observed tropical structures, including the Madden-Julian Oscillation. For this reason, additional 6-hourly time series of selected three-dimensional tropical fields were requested to complement the original collection. These were to be obtained from a 1-year rerun of the APE control experiment using the same model version as submitted to the main APE database, even if an exact (bit-level) reproduction of the original experiment was not possible. Global data were requested, so that transient statistics could also be produced for the extratropical storm-tracks.

A subset of the APE modeling groups, namely AGU, CSIRO, ECM-CY29, ECM-CY32, GSFC, LASG, and NCAR, were able to rerun their simulations to collect these data. The data archive is maintained by the AGU consortium in Japan. Since files were too large to be made available over the internet, please contact the AGU group if you wish to use the data (ape-ml@gfd-dennou.org). Additional details are available under *Requested Diagnostics* on the APE web site (http://climate.ncas.ac.uk/ape/).

The requested transient data are summarized in Table 2.14. Several single-level variables (TR01 through TR08) were requested, to be combined into a single file TR00, similar to the original TR data request. Because of size, each multi-level variable was requested as a separate file, TR11 through TR27. Multi-level dynamical variables (TR11 through TR17) were to be supplied on the 17 standard pressure levels, with dimension metadata from the original ML file. Multi-level parameterization tendencies or forcing variables (TR18 through TR27) were to be supplied on model levels, using dimension metadata from the original PF file. Note that the first variable in Table 2.14 (precipitation rate) replicates the first variable in Table 2.7 to allow comparison with the original data.

Analyses of these additional transient data are not included in this Atlas. They are presented in Nakajima et al. (2013) in the special issue of the *Journal of the Meteorological Society of Japan* (2013, Vol. 91A) devoted to the APE.

Table 2.14: Additional Transient Data for Tropical Transient Analysis (TRnn).

File	Data	Name	Units	Diagnostic
TR00	TR01	Total precipitation rate (PPN_T)	kg m^{-2}s^{-1}	tr_tppn
TR00	TR02	TOA net longwave radiation (+ve upward) (LW_{TOA})	Wm^{-2}	tr_lw_toa
TR00	†TR06	Surface pressure (P_s)	Pa	tr_mslp
TR00	TR07	Surface latent heat flux (+ve upward) (LH)	Wm^{-2}	tr_slh
TR00	TR08	Surface sensible heat flux (+ve upward) (SH)	Wm^{-2}	tr_ssh
TR11	†TR11	Zonal wind (u)	ms^{-1}	tr_u
TR12	†TR12	Meridional wind (v)	ms^{-1}	tr_v
TR13	†TR13	Temperature (T)	K	tr_t
TR14	†TR14	Vertical velocity (ω)	Pa s^{-1}	tr_om
TR15	†TR15	Geopotential height (Z)	m	tr_z
TR16	†TR16	Specific humidity (q)	kg kg^{-1}	tr_q
TR17	†TR17	Relative humidity (RH)	%	tr_rh
TR18	TR18*	Temperature tendency – Total ($\partial T/\partial t$)	Ks^{-1}	tr_t
TR19	TR19	Temperature tendency – Short wave ($\partial T/\partial t$)$_{SW}$	Ks^{-1}	tr_t_sw
TR20	TR20	Temperature tendency – Long wave ($\partial T/\partial t$)$_{LW}$	Ks^{-1}	tr_t_lw
TR21	TR21	Temperature tendency – Turbulence ($\partial T/\partial t$)$_{TURB}$	Ks^{-1}	tr_t_turb
TR22	TR22	Temperature tendency – Convection ($\partial T/\partial t$)$_{CONV}$	Ks^{-1}	tr_t_conv
TR23	TR23	Temperature tendency – Cloud ($\partial T/\partial t$)$_{LSCLD}$	Ks^{-1}	tr_t_cld
TR24	TR24*	Specific humidity tendency – Total ($\partial q/\partial t$)	kg kg^{-1}s^{-1}	tr_q
TR25	TR25	Specific humidity tendency – Turbulence ($\partial q/\partial t$)$_{TURB}$	kg kg^{-1}s^{-1}	tr_q_turb
TR26	TR26	Specific humidity tendency – Convection ($\partial q/\partial t$)$_{CONV}$	kg kg^{-1}s^{-1}	tr_q_conv
TR27	TR27	Specific humidity tendency – Cloud ($\partial q/\partial t$)$_{LSCLD}$	kg kg^{-1}s^{-1}	tr_q_cld

* Total tendency refers to total parameterized tendency, excluding the dynamical tendency.

Chapter 3

Participating Modeling Groups

This section describes the models used in APE. The section titles correspond to the abbreviations used to identify the models throughout this Atlas.

3.1 AGU

AGU for APE used AFES (Agcm For the Earth Simulator) version 1.22 (Ohfuchi et al., 2004). While the original code of AFES was adopted from the version5.4.02 of an AGCM developed jointly by the Center for Climate System Research (CCSR) of the University of Tokyo and the Japanese National Institute for Environmental Sciences (NIES) (Numaguti et al., 1997a), it was completely rewritten from scratch in order to exploit vector-parallel computing on the Earth Simulator. AFES won Gordon Bell Award for Peak Performance at Supercomputing 2002 for its computational efficiency (Shingu et al., 2002). The CCSR/NIES AGCM has been used for several international modeling efforts, including future projections for the Intergovernmental Panel for Climate Change and Atmospheric Model Intercomparison Project. AFES has been used for various weather and climate simulations. AFES's dynamical core is primitive equation semi-implicit Eulerian spectral transform, and tracer transport is Eulerian spectral with negative value fixer. Vertical diffusion scheme is Mellor and Yamada (1974, 1982) level 2. Cumulus convection parameterization is Emanuel scheme (Emanuel, 1991; Emanuel and Živković-Rothman, 1999). AFES uses cloud scheme of Le Treut and Li (1991).

3.2 CGAM

CGAM ran a version of the UK Met Office global atmospheric model, HadAM3, in APE. HadAM3 forms part of the coupled model HadCM3 and has been used in many studies of climate variability and climate change. It was the final operational version of the Met Office Eulerian grid-point atmospheric model, before the introduction of a semi-Lagrangian dynamical core, HadGAM. The UK Met Office ran a pre-release version of HadGAM1 in APE (see Section 3.14). Pope et al. (2000) summarizes the formulation of HadAM3 and includes references to the model's main components. The dynamical core (Cullen and Davies, 1991; Cullen, 1993) is hydrostatic and uses an Eulerian advection scheme for both dynamics and water vapor transport on an Arakawa B grid. The boundary layer parameterization is that developed by Smith (1990, 1993). Moist and dry convection are parameterized using the mass flux formulation of Gregory

and Rowntree (1990), with the addition of convective downdrafts (Gregory and Allen, 1991) and convective momentum transport (Gregory et al., 1997). The precipitation scheme is described by Senior and Mitchell (1993), with the evaporation of precipitation described by Gregory (1995). The model uses the prognostic cloud scheme of Smith (1990), modified by Gregory and Rowntree (1996), which diagnoses cloud ice, cloud water and cloud amount from the primary model variables total moisture and liquid water potential temperature. The radiation scheme is that of Edwards and Slingo (1996), with modifications by Cusack et al. (1998, 1999a).

Pope et al. (2000) describes HadAM3's representation of present-day climate using statistics from AMIP experiments, comparing it with the previous version HadAM2b. Both versions used the model's standard resolution, 2.5° in latitude and 3.75° in longitude with 19 levels. Climate simulations on an aqua-planet by HadAM3 at this standard resolution were first described by Neale and Hoskins (2000b). For APE, HadAM3 uses 30 levels, approximately doubling the tropospheric resolution of the standard version. This follows studies which found positive impacts of increased vertical resolution, on the simulation of tropical convection and tropical variability (Inness et al., 2001), and on the transport and distribution of water vapor (Pope et al., 2001).

3.3   CSIRO

CSIRO ran a version of the Conformal-Cubic Atmospheric Model (CCAM). CCAM is formulated on the quasi-uniform conformal-cubic grid. CCAM is hydrostatic, with two-time-level semi-implicit time differencing. It employs semi-Lagrangian horizontal advection with bi-cubic horizontal interpolation (McGregor, 1996), in conjunction with total-variation-diminishing vertical advection. The grid is unstaggered, but the winds are transformed reversibly to/from C-staggered locations before/after the gravity wave calculations, providing good dispersion characteristics (McGregor, 2005a). Three-dimensional Cartesian representation is used during the calculation of departure points, and also for the advection or diffusion of vector quantities. Further details of the model dynamical formulation is provided by McGregor (2005b) and McGregor and Dix (2001, 2008). GFDL parameterizations are used for longwave and shortwave radiation (Schwarzkopf and Fels, 1991; Lacis and Hansen, 1974), with interactive cloud distributions determined by the liquid and ice-water scheme of Rotstayn (1997). The model employs a stability-dependent boundary layer scheme based on Monin-Obukhov similarity theory (McGregor et al., 1993), together with non-local vertical mixing (Holtslag and Boville, 1993) and also enhanced mixing of cloudy boundary layer air (Smith, 1990). CCAM includes a simple parameterization to enhance sea surface temperatures under conditions of low wind speed and large downward solar radiation, affecting the calculation of surface fluxes. For these simulations a shallow convection parameterization was not used. The cumulus convection scheme uses the mass-flux closure described by McGregor (2003), and includes both downdrafts and detrainment.

3.4   DWD

GME (Majewski et al., 2002) is the operational global numerical weather prediction model of Deutscher Wetterdienst (DWD). It is a hydrostatic model which operates on an icosahedral-hexagonal grid following Baumgardner (1983). This grid is almost uniform across the whole

globe without convergence of grid lines near the poles. Time integration is done with a leap-frog time scheme with semi-implicit correction following Simmons and Burridge (1981), Eulerian advection of temperature and momentum, and semi-Lagrangian advection of moisture variables.

For radiation GME employs the scheme of Ritter and Geleyn (1992). Grid scale precipitation is calculated following Doms et al. (2005) with modifications by Seifert (2003). Deep and shallow convection are based on the mass flux approach of Tiedtke (1989). Turbulent fluxes are based on Louis (1979) in the Prandtl layer, and on a diagnostic level-two scheme of Mellor and Yamada (1974) above. Cloudiness is derived from specific cloud liquid water content, relative humidity, convective activity, and stability. For the APE experiments the model was run without a mass and energy fixer. The global energy balance of the GME was tuned to a setup with continents.

3.5 ECMWF (ECM-CY29 and ECM-CY32)

The integrated forecasting system (IFS) model is ECMWF's global atmospheric model component used for all operational data assimilation and forecast applications. The dynamical core is two-time-level, semi-implicit, semi-Lagrangian and applies spectral transforms between grid-point space (where the physical parametrizations and advection are computed) and spectral space (where the linear semi-implicit system is solved, and where derivatives and horizontal diffusion are computed). The IFS hydrostatic dynamical core is described in more detail in Simmons and Burridge (1981); Ritchie et al. (1995); Temperton et al. (2001) and references therein. The APE simulations of IFS used a $T_L 159$ horizontal resolution with an associated linear, reduced Gaussian grid with 160 latitudes and 320 gridpoints along the near equatorial latitudes. In the vertical, the model was discretised using a finite-element scheme over 60 hybrid vertical levels (Untch and Hortal, 2004) and the model top at 0.1hPa. The time-step used was $dt = 1800s$. The coupling between the physics and the dynamics and a summary of the individual parametrization schemes can be found in Beljaars et al. (2004). The impact of the radiation scheme is described in Morcrette et al. (2008) and details of the boundary layer scheme can be found in Beljaars (1995a). The convection parametrization is based on a mass flux scheme described in Tiedtke (1989) and the prognostic cloud scheme is described in Tiedtke (1993). The latest documentation of IFS can be found at ECMWF (2010). ECMWF participated in APE with two versions of physical parametrization packages in the IFS, cycle 29r2 (denoted ECM-CY29) and cycle 32r3 (denoted ECM-CY32). Cycle 29r2 was the operational forecast model at ECMWF between 28/06/2005 - 1/02/2006 and cycle 32r3 was operational between 06/11/07 - 03/06/08. The convection parametrization in cycle 29r2 is evaluated in Bechtold et al. (2004). The differences between the two model versions, mainly due to the changes in the convection and the vertical diffusion schemes, and the improvements in the representation of atmospheric variability and signatures of equatorially-trapped waves in cycle 32r3 are documented in Bechtold et al. (2008).

3.6 FRCGC (now RIGC/JAMSTEC)

NICAM (Nonhydrostatic ICosahedral Atmospheric Model) is a new type of Atmospheric General Circulation Model (AGCM). This model has been developed for the future high resolution AGCM, directed to simulate each cloud explicitly over the globe, as a Global Cloud Resolving

Model (GCRM). Now, 3.5km-mesh / 7km-mesh global simulation with explicit cloud process is already performed using the Earth Simulator, T2K-Tsukuba system, and the Athena Cray XT4 system in NICS/ORNL (USA). Historically, NICAM was first developed by cooperation of FRCGC (now, RIGC/ JAMSTEC) and CCSR (now, AORI in the University of Tokyo) so as that it can be run with high computational efficiency. Several new numerical techniques for horizontal grid configuration such as the spring dynamics grid (Tomita et al., 2001, 2002) and for the nonhydrostatic scheme with total energy conservation (Satoh, 2002, 2003) are developed for this purpose. Assembling these techniques, NICAM dynamical core was established in 2004 (Tomita and Satoh, 2004). For tracer advection, a simple but accurate scheme was developed and implemented (Miura, 2007). Most recent introduction to NICAM including the physical scheme appears in Satoh et al. (2008).

3.7 GFDL

The AM2.1 model is the atmospheric component of the GFDL Coupled Model 2.1 (CM2.1, Delworth et al., 2006) that was one of the two models used for GFDL's participation in the IPCC AR4. This version of the atmospheric model was developed based on AM2.0 model (GAMDT, 2004) and contains essentially identical atmospheric physics package except AM2.0 B-grid finite difference dynamical core was replaced by a finite volume (FV) dynamical core (Lin, 2004). It turns out that the insertion of the FV dynamical core necessitates some retuning of the cloud scheme to achieve global top of atmospheric (TOA) radiative balance. The details of the AM2.0/AM2.1 model physics was documented in GAMDT (2004).

To give a brief summary, AM2.1 has a horizontal resolution of $2°$ latitude x $2.5°$ longitude and 24 vertical levels with the lowest model level about 30 m above the surface. There 9 full levels in the lowest 1.5 km above the surface with relatively coarse resolution (roughly 2 km) in the upper troposphere. The prognostic variables are the zonal and meridional wind components, surface pressure, temperature, and tracers. The tracers include the specific humidity of water vapor, cloud liquid, cloud ice and cloud fraction. The cumulus convection scheme used in AM2.1 is the relaxed Arakawa-Schubert (RAS) formulation (Moorthi and Suarez, 1992) with local modifications documented in GAMDT (2004). Cumulus momentum transport is represented by vertical diffusion proportional to the cumulus mass flux. The large-scale/stratiform clouds are treated as 3 separate prognostic variables following Tiedtke (1993). Cloud microphysics are parameterized based on Rotstayn (1997) and Rotstayn et al. (2000). Fluxes of large-scale rain and snow are diagnosed and the amount of precipitation flux inside and outside of clouds is tracked separately (Jakob and Klein, 2000). Clouds are assumed to randomly overlap for radiative flux calculation. The parameterization of the turbulence in convective planetary boundary layer (PBL) and stratocumulus layer follows Lock et al. (2000). For layers of the atmosphere that are not part of either a convective PBL or a stratocumulus layer, a local mixing parameterization is used. For unstable layers, the mixing coefficient of Louis (1979) is used. For stable turbulent layers, conventional stability functions for which mixing ceases when the Richardson number exceeds 0.2 are used except near the surface. Surface fluxes are computed using Monin-Obukhov similarity theory with a gustiness enhancement to wind speed used in the surface flux calculations (Beljaars, 1995b). For all the above parameterizations, the details in the implementations are often not identical to the original schemes, but all local modifications are documented in GAMDT (2004) and are identical to those used in CM2.1 coupled model simulation in the CMIP3 archive.

3.8 GSFC

The GSFC model is the atmospheric component of version 1 of the NASA Seasonal to Interannual Prediction Project coupled prediction system (NSIPP 1), which has been used for seasonal prediction at NASA Goddard. It is a finite-difference dynamical core based on a C-grid in the horizontal, with 34 vertical levels in a standard (Suarez and Takacs, 1995; Takacs and Suarez, 1996). The parameterizations of solar and infrared radiative heating rates are described in Chou and Suarez (1999) and Chou and Suarez (1994). Penetrative convection is parameterized using the Relaxed Arakawa-Schubert (RAS) scheme (Moorthi and Suarez, 1992), which have been updated by including a more detailed condensate budget in the updraft (Bacmeister et al., 2000). Clouds are obtained from an empirically-based, diagnostic relative humidity scheme in which the cloud cover at each grid point depends directly on the results of the large-scale and convective cloudiness. The boundary layer and turbulence is parameterized based on the local diffusion scheme by Louis et al. (1982). The land surface model (LSM) is the Mosaic LSM of Koster and Suarez (1994). The model uses the gravity-wave drag parameterization described by Zhou et al. (1996). A more detailed description of the model components are found in Bacmeister et al. (2000), where the simulated model climatology forced by observed sea surface temperature is also presented. The model was also tested in the idealized configuration as in the control case of APE, but coupled with a slab mixed-layer ocean in Lee et al. (2008).

3.9 K1JAPAN

The AGCM used in this group is the atmospheric component of a global climate model called Model for Interdisciplinary Research On Climate version 3 (MIROC3 K-1 Model Developers, 2004), which is one of the Japanese community models collaboratively developed at the Center for Climate System Research (CCSR) [1], the University of Tokyo, the National Institute for Environmental Studies (NIES), and the Frontier Research Center for Global Change (FRCGC) [2]. The MIROC3 has been contributing to the IPCC fourth assessment report and widely used to study past, present and future climate changes (Emori et al., 2005; Kimoto, 2005; Nozawa et al., 2005, among others). The atmospheric component model, referred to as the CCSR/NIES/FRCGC AGCM, is based on a global spectral dynamical core (Numaguti et al., 1997b), with the flux-form semi-Lagrangian treatment for conservative quantities such as water vapor (Lin and Rood, 1996).

A standard physics package is included in the CCSR/NIES/FRCGC AGCM. The radiative transfer is calculated by the k-distribution scheme proposed by Nakajima et al. (2000). The number of absorption bands and channels is 18 and 37, respectively. The cumulus scheme employed in the CCSR/NIES/FRCGC AGCM is a prognostic closure based on Pan and Randall (1998). In order to represent the effect of the free-tropospheric relative humidity on the generation of cumulus clouds, an empirical triggering function by Emori et al. (2001) has been adopted. The formation and dissipation of clouds were represented by a diagnostic large-scale condensation scheme proposed by Le Treut and Li (1991) and a simple microphysics scheme. The cloud fraction is the diagnostic variable in this scheme and cloud liquid and ice have been

---

[1] Currently Atmosphere and Ocean Research Institute (AORI)
[2] Currently Research Institute for Global Change (RIGC)

separated with a given function of temperature. Ogura et al. (2008) found that the climate sensitivity in MIROC3 is primarily controlled by the crude representation of clouds, and hence, is replaced by prognostic schemes in the newer version (Watanabe et al., 2010). The vertical diffusion scheme is based on Mellor and Yamada (1974, 1982), with a closure level of 2.5, including a cloud effect (Smith 1991). The other parameterization schemes such as the surface heat fluxes and the gravity wave drag are also included (see K-1 Model Developers, 2004, for the details).

3.10 LASG

The model used in the APE experiments (Wang et al., 2008; Liu et al., 2010) is a spectral AGCM (named SAMIL) which is the atmospheric component of the flexible global ocean-atmosphere-land system (FGOALS) developed by the State Key Laboratory of Atmospheric Sciences and Geophysical Fluid Dynamics/Institute of Atmospheric Physics (LASG/IAP) (Wu and Coauthors, 1997). Its dynamic framework uses a "standard atmosphere reduction" scheme (Zeng, 1963; Phillips, 1973) in which a time independent standard atmosphere is introduced and subtracted to reduce the calculation errors of the pressure gradient force. Semi-implicit time integration is used. The resolution of SAMIL model is flexible, and two optional dynamical frameworks in η-coordinate and in σ-coordinate systems are designed, while multiple schemes with corresponding physical processes are provided and can be conveniently selected for comparison studies. In the present study, the dynamical framework adopted is the σ-coordinate system with 9 vertical layers, and rhomboidally truncated at wave-number 42 in the horizontal (R42) roughly $2.8°$ longitude $\times$ $1.66°$ latitude Gaussian grid (Wang et al., 2004). Also included are a K-distribution radiation scheme that was originally developed by Shi (1981) and Slingo's cloud diagnosis scheme (Slingo, 1987) that depends on relative humidity and vertical velocity. The convection process is handled with the Manabe moist adjustment scheme (Manabe et al., 1965). Two other cumulus convection parameterizations are also transplanted into SAMIL: the Arakawa-type cumulus parameterization scheme developed by Zhang and McFarlane (1995) and cumulus convection parameterization developed by Tiedtke (1989). Turbulent fluxes are given by the vertical diffusion scheme of Louis (1979) based on Monin-Obukov similarity theory. A detailed description of the model can be found in Zhang et al. (2000) and Wang et al. (2004).

3.11 MIT

The MIT general circulation model (MITgcm) dynamical core is an Eulerian grid point model that can be configured to simulate either atmospheric or oceanic flow (Marshall et al., 2004; Adcroft et al., 2004). The dynamical core used for the APE experiments runs on an NCEP eta-type coordinate in the vertical (Adcroft and Campin, 2004) and a cubed-sphere projection of the globe in the horizontal. The coupling between the dynamical core and the physics is such that the physics runs on its own grid in the vertical to assure that the vertical resolution is retained near the surface over the land (and topography). The treatment of the alternative vertical grid is called GridAlt (Molod, 2009). The physics package for the MITgcm APE experiments includes parameterization schemes for atmospheric convection, large scale precipitation and cloud cover, longwave and shortwave radiation, turbulence, and gravity wave drag. Convection

is parameterized using the Relaxed Arakawa-Schubert scheme (RAS, Moorthi and Suarez, 1992) and includes a scheme for the re-evaporation of falling rain (Sud and Molod, 1988). RAS is a mass flux scheme with an updraft only detraining plume cloud model and a quasi-equilibrium closure. The longwave radiative processes are described by Chou and Suarez (1994), and include absorption due to cloud water, water vapor, carbon dioxide, ozone, N_2O and methane. The shortwave is from Chou (1990) and Chou (1992) and includes absorption by water vapor, ozone, carbon dioxide, oxygen, cloud water, and aerosols and includes scattering by clouds water and aerosols. The turbulence parameterization is based on the Level 2.5 second order closure scheme of Helfand and Labraga (1988) and includes a moist turbulence scheme to handle the buoyancy effects of the vapor to liquid phase transition (Helfand et al., 1991). The Monin-Obukhov surface layer parameterization is described in Helfand and Schubert (1995). The gravity wave drag parameterization is based on Zhou et al. (1996).

3.12   MRI

The atmospheric GCM (MRI/JMA98) is used for APE. This AGCM has been developed based on a version of the operational weather forecasting model of the Japan Meteorological Agency (JMA). Some physical process schemes are replaced with those of the original JMA version. Details of the AGCM are described in Shibata et al. (1999). The dynamic framework is based on a spectral transform method. A multi-parameter random model based on Shibata and Aoki (1989) is used for terrestrial radiation. Absorption due to CH4 and N2O is treated in addition to H2O, CO2 and O3. The model calculates solar radiation formulated by Shibata and Uchiyama (1992) with delta-two-stream approximation. An explicit treatment of the direct effect of sulfate aerosols is included. The optical properties (diffusivity, single scattering albedo and asymmetry parameters) of sulfate aerosol are substituted by those for the LOWTRAN rural aerosol, which is composed of a mixture of 70% water soluble substance (ammonium and calcium sulfate and organic compounds) and 30% dust-like particles. Since complex refractive indices for water soluble and dust-like aerosols are very similar, particularly in the solar wavelength region, and can be regarded as identical in a first-order approximation, those parameters are applicable for sulfate aerosols as a whole. The effects of relative humidity on solution concentration and radius distribution of aerosol are incorporated. For deep moist convection, the Arakawa-Schubert scheme with prognostic closure similar to Randall and Pan (1993) is used. For other physical parameterizations, mid-level convection that is moist convection rooted in a free atmosphere, large-scale condensation, vertical diffusion with a level-2 turbulence closure scheme based on Mellor and Yamada (1974) are used. Cloud diagnostic follows Sugi et al. (1990).

3.13   NCAR

The Community Atmosphere Model Version 3 (CAM3) was developed as the atmospheric component of the Community Climate System Model (CCSM3, Collins et al., 2006a). An overview of the CAM3 is provided by Collins et al. (2006b) and a complete technical description by Collins et al. (2004). The dynamical core is semi-implicit Eulerian spectral transform. Tracer transport is by shape preserving semi-Lagrangian grid point scheme. Various aspects of the CAM3 are presented in a series of papers in a special issue of the Journal of Climate (2006, Vol. 19,

2121–2632). The CAM3 is closely related to its predecessor CAM2 (Collins et al., 2003; Kiehl and Gent, 2004) with a few of its component parameterizations essentially unchanged. CAM3 includes the PBL parameterization of Holtslag and Boville (1993), the Zhang and McFarlane (1995) deep convection parameterization, the Hack (1994) shallow convection parameterization, and a prognostic cloud water parameterization (Rasch and Kristjansson, 1998). Modifications were introduced into the cloud and precipitation processes by Boville et al. (2006), Zhang et al. (2003) and Collins et al. (2006b). As part of the development and evaluation of CAM3, adjustable coefficients in the parameterization of clouds and precipitation were modified (Hack et al., 2006b). Many of the improvements in the climate statistics from simulations with CAM3 over CAM2 are described in Collins et al. (2006a), Collins et al. (2006b), Boville et al. (2006), Hack et al. (2006a) and Rasch et al. (2006). Hurrell et al. (2006) describe the overall dynamical simulation of the CAM3.

3.14   UKMO (N48 and N96)

The UK Met Office used a pre-release version of HadGEM1. HadGEM1 is described in detail in Martin et al. (2006). The dynamical core is non-hydrostatic, semi-Lagrangian, with conservative monotone treatment of moisture variables and a semi-implicit time integration (Davies et al., 2005). The radiation scheme is Edwards and Slingo (1996) with additions by Cusack et al. (1999a). The boundary layer scheme uses non-local mixing for unstable boundary layers (Lock et al., 2000) and a Richardson number scheme for stable layers (Smith, 1993). The micro-physics is a mixed phase scheme including prognostic ice (Wilson and Ballard, 1999). The cloud scheme is due to Smith (1990). The convection scheme is a revised version of the Gregory and Rowntree (1990) mass flux scheme diagnosing shallow and deep convection. Deep and shallow convection use different entrainment and detrainment rates. Deep convection uses a CAPE closure and shallow convection a closure due to Grant (2001). The convective momentum parametrization is based on flux-gradient relationships (Grant and Brown, 1999).

The differences between the pre-release version and HadGEM1 are;

- HadGEM1 uses a parametrized RH-crit (Cusack et al., 1999b), in its cloud scheme whereas the pre-release version was still using the prescribed critical relative humidity as HadCM3 (Pope et al., 2000)

- No interactive aerosols included.

- Small differences to the treatment of ice crystals by radiation.

Due to limitations in computer resource at the time only some of the APE simulations were run at the higher N96 (1.875° x 1.25°) resolution, most of the rest being at N48 (3.75° x 2.5°). The only differences between the N48 and N96 simulations were in certain resolution dependent dynamics parameters used by the Helmholtz solver. Both resolutions used a basic 30 minutes time step with 3 hourly calls to radiation and three sweeps of convection per model time step. Unlike previous resolution work (Pope and Stratton, 2002), the prescribed critical relative humidity profile used by the cloud scheme was not altered with resolution.

3.15 Summary Tables

Tables 3.1 through 3.4 summarize the characteristics of the models. They can only provide labels for the different model characteristics that are indicative of their definitions and serve as a reminder. In some cases they may be useful only to cognoscenti. The actual schemes can only be determined by the details presented in the references.

Table 3.1: Dynamical properties of participating models

GROUP SYMBOL	MODEL	DYNAMICAL CORE	WATER VAPOR TRANSPORT	MASS FIXER	ENERGY FIXER
AGU	AFES	Eulerian spec	Eulerian spec	Yes	No
CGAM	HadAM3	lat-lon grid point	Eulerian grid	Yes	Yes
CSIRO	CCAM	conf cubic semi-Lag	semi-Lag	Yes	No
DWD	GME	icosahedral grid	semi-Lag grid	No	No
ECM-CY29	IFS	semi-Lag spec	semi-Lag grid	Yes	No
ECM-CY32	IFS	semi-Lag spec	semi-Lag grid	No	No
FRCGC	NICAM	icosahedral Eulerian	Eulerian	No[1]	No[1]
GFDL	AM2.1	lat-lon finite volume	finite volume	Yes	Yes
GSFC	NSIPP-1	lat-lon grid point	Eulerian centered	Yes	No
K1JAPAN	AGCM v.5.7	Eulerian spec	semi-Lag grid	Yes	No
LASG	SAMIL	Eulerian spec	Eulerian grid	Yes	No
MIT	MIT-GCM	cubed sphere	Eulerian grid	No	No
MRI	MRI/JMA98	Eulerian spec	Eulerian spec	Yes	No
NCAR	CAM3	Eulerian spec	semi-Lag grid	Yes	Yes
UKMO(N48)	pre-HadGAM1	semi-Lag lat-lon grid	semi-Lag	Yes[2]	Yes
UKMO(N96)	pre-HadGAM1	semi-Lag lat-lon grid	semi-Lag	Yes[2]	Yes

spec = spectral transform, grid = grid point, semi-Lag = semi-Lagrangian, conf cubic = conformal cubic

[1] Both conserved by numerical scheme
[2] for water vapor, dry mass conserved by dynamics

Table 3.2: Resolution and tuning of participating models

MODEL NUMBER	GROUP SYMBOL	HORIZONTAL RESOLUTION	VERTICAL RESOLUTION	TOA[1] TUNED FOR EARTH CLIMATE
1	AGU	T39	L48	No
2	CGAM	3.75° x 2.5°	L30	Yes
3	CSIRO	~210 km (C48)	L18	No
4	DWD	~ 1°	L31	Yes
5	ECM-CY29	T159	L60	No
6	ECM-CY32	T159	L60	No
7	FRCGC	~7 km	L54	No
8	GFDL	2.5° x 2°	L24	Yes
9	GSFC	3.75° x 3°	L34	No
10	K1JAPAN	T42	L20	Yes
11	LASG	R42	L9	No
12	MIT	~280 km	L40	No
13	MRI	T42	L30	No
14	NCAR	T42	L26	Yes
15	UKMO(N48)	3.75° x 2.5°	L38	Weakly[2]
16	UKMO(N96)	1.875° x 1.25°	L38	Weakly[2]

[1] Top of atmosphere radiative fluxes
[2] During the development phase of HadGEM1 the TOA fluxes of AMIP runs were monitored to check that they did not widely diverge from balance but were not actively tuned.

Table 3.3: Parameterizations of participating models: I (see text for details)

GROUP SYMBOL	PBL	SHALLOW CONVECTION	DEEP CONVECTION
AGU	Mellor-Yamada	None	Emanuel
CGAM	Smith	Gregory-Rowntree	Gregory-Rowntree
CSIRO	Holtslag-Boville	None	McGregor
DWD	Louis	Tiedtke	Tiedtke
ECM-CY29	Louis-Beljaars	Tiedtke	Bechtold et al. 2004
ECM-CY32	Louis-Beljaars	Bechtold et al. 2008	Bechtold et al. 2008
FRCGC	Mellor-Yamada	None	None
GFDL	Lock	RAS	RAS
GSFC	Louis	RAS	RAS
K1JAPAN	Mellor-Yamada	None	Pan-Randall
LASG	Local vert diffusion	None	Manabe
MIT	Mellor-Yamada	RAS	RAS
MRI	Mellor-Yamada	Randall-Pan	Randall-Pan
NCAR	Holtslag-Boville	Hack	Zhang-McFarlane
UKMO(N48)	Lock/Richardson	Gregory 1990 /Grant	Gregory 1999
UKMO(N96)	Lock/Richardson	Gregory 1990 /Grant	Gregory 1999

RAS = Relaxed Arakawa-Schubert

Table 3.4: Parameterizations of participating models: II (see text for details)

GROUP SYMBOL	CLOUD	CLOUD FRACTION	CLOUD OVERLAP
AGU	LeTreut-Li	Diagnostic	max/random
CGAM	Smith (prognostic)	Diagnostic	max/random
CSIRO	Rostayn (prognostic)	Diagnostic	random
DWD	Doms & Foerster, Seifert	Diagnostic	max/random
ECM-CY29	Tiedtke	Prognostic	max/random
ECM-CY32	Tiedtke	Prognostic	max/random
FRCGC	Grabowski Microphysics	Diagnostic	0/1
GFDL	Tiedtke	Prognostic	random
GSFC	Diagnostic	Diagnostic	max/random
K1JAPAN	LeTreut-Li	Diagnostic	max/random
LASG	Slingo (diagnostic)	Slingo diag	random
MIT	Slingo-Ritter	Diagnostic	max/random
MRI	Sugi et al.	Diagnostic	max/random
NCAR	Rasch-Kristjansson	Diagnostic	max/random
UKMO(N48)	Smith (prognostic)	Diagnostic	max/random
UKMO(N96)	Smith (prognostic)	Diagnostic	max/random

Chapter 4

CONTROL Experiment

We summarize the collective APE model behavior for many statistics with a multi-model mean. For the CONTROL experiment the multi-model mean is the average of all models except FRCGC which was only run for a short time and is not necessarily in a climate balance. The statistics are calculated on each model's submitted data grid, then linearly interpolated to a 1° latitude-longitude grid to calculate the multi-model mean. For each model, values poleward of the last model latitude were obtained by constant extrapolation. The average is computed and plotted on the 1° grid. Differences of individual models with the multi-model mean atmosphere are also calculated on the 1° grid. We emphasize that all statistics are calculated for each model first on the model's submitted data grid, then interpolated to the common grid. Statistics are not calculated from multi-model averaged variables. The models are weighted equally for the mean even though with some statistics there are model outliers. The sample size is large enough that the impact of outliers is generally small, although there are a few exceptions. Some impact of dropping models from the average can be determined by comparing statistics from the CONTROL experiment in this chapter with the same statistics for the CONTROL in later chapters which compare several experiments. In those comparisons the multi-model mean from the CONTROL is comprised of fewer models since not all models submitted all experiments, and for the cross-experiment comparisons, the set of models in the multi-mean must be uniform. For many models the submitted data grid is the model grid itself. For a few the model data were interpolated to a latitude-longitude grid for submission. DWD and FRCGC data were interpolated from icosahedral grids and CSIRO and MIT from cubed sphere grids. ECMWF data were interpolated from the T159 Gaussian latitude-longitude grid to a uniform 2° latitude-longitude grid before submission. In this report references to calculations on the model grid mean that the calculations are done on the model submitted data grid, as distinct from the 1° interpolated grid.

The multi-model mean should not be thought of as a best estimate of the aqua-planet climate. It is simply a convenient way to summarize the properties of the current set of atmospheric general circulation models. No one model is a good match for the multi-model mean. In general the individual models all differ from the multi-model mean.

To indicate concisely the variability of the APE models we calculate the inter-model standard deviation. The standard deviation of the statistics is also calculated after the statistics are interpolated to the 1° grid. We provide plots of the statistics for all the individual models as well. Individual model plots are made on each model's submitted grid, i.e. they show the statistics before interpolation to the 1° grid.

As will be seen when the individual model plots are presented in the following, a few models have missing values for some variables, e.g. where the lowest specified analysis pressure surface falls below the lowest model surface and extrapolation was not performed, or just some bad data. The multi-model mean and standard deviation at each point of the 1° grid was computed over all models that did not have missing values, point-by-point. The majority of models had complete fields obtained by extrapolation below the lowest model surface. Thus the multi-model mean generally does not show a discontinuity associated with the missing data of a few models.

For all experiments except CONTROL_5N, the APE forcing is symmetric about the equator. As a result the climate is also symmetric about the equator. Therefore we symmetrize plots in latitude about the equator and plot from pole to equator. Asymmetric fields such as the meridional velocity, v, are shown in the Northern Hemisphere sense. We chose the abscissa to be the sine of latitude to provide more visibility to the structures in the equatorial region.

The multi-model mean and standard deviation are most useful for illustrating zonal averages of 3-dimensional fields. For zonal averages of 2-dimensional fields the collective model behavior is illustrated by combing the graphs many models on one plot. However, with 14, models as is the case here, combining all on one plot makes it difficult to identify individual models. Therefore we generally divide the models across two side-by-side plots to present single-level fields.

4.1   Mean State

4.1.1   Zonal-Time Average Poleward Energy Transport

Figure 4.1 shows the zonal-time average poleward energy transport for the multi-model mean and for Earth estimates. The figure shows the total transport and the atmosphere and ocean components. Figure 4.2 shows the three transports for the individual models. We include the poleward transports to allow comparison of the forcing of the atmospheric circulation in APE with that for Earth. The annual average earth values are described and plotted in Fasullo and Trenberth (2008). Their data were accessed on May 24, 2010 from http://www.cgd.ucar.edu/cas/catalog/ocean/obs_vq_am_estimates.txt. Gleckler et al. (1995) show the transports from 15 AMIP Earth-like simulations.

The transport for the APE models is calculated following Gleckler et al. (1995). The total transport is that required to balance the top of atmosphere net radiative flux, the ocean transport is that implied to balance the surface net flux and atmospheric transport is the difference between the two. The net fluxes from the SH data sets at the top of the atmosphere and at the surface are integrated from pole to pole after the global average is removed. Where possible, the integration weights are obtained from the model meta-data. For spectral models on a Gaussian quadrature grid these are the Gaussian weights. For models without integration weights, if latitude bounds (grid cell edges) are provided, the weights are the difference of the sine of the bounds. If latitude bounds are not provided, they are set to the average of the adjacent cell centers. The northern and southern hemispheres are averaged together for the plots.

4.1.2   Global-Time Averages and Budgets

Figures 4.3 through 4.7 show global-time average variables as bar plots for each model, calculated from the global time-series (GT) data sets. The whiskers with each bar range from plus one to

minus one standard deviation of the time series of the daily-global averages. The fields shown are tppn, cppn, dppn, evap, emp, ps, ts2m, cld_frac, albedo, cldw, cldi, sw_toa, lw_toa, rflux_toa, ssw, slw, slh, ssh, rflux_sfce and rflux.

The net total flux out of atmosphere (rflux) shown in Figure 4.7 is calculated from the residual TOA radiative flux (rflux_toa) and residual surface flux (rflux_sfce). A non-zero value of that total flux does not necessarily reflect a lack of total energy conservation in a model. For example the NCAR model includes an energy fixer which ensures total energy is conserved yet the net flux indicated in the figure is -2.24 W m^{-2}. This seeming contradiction arises because APE requested the radiation fields at the *top of the atmosphere* (TOA), but model conservation involves fields at the *top of the model* (TOM) and the two are not necessarily the same. In earth-like simulations TOA fluxes are useful to compare with satellite observations. TOM fluxes are useful to monitor model energy conservation. In the NCAR model the net downward solar fluxes at TOA and TOM differ by $\sim$2.5 W m^{-2} due to ozone absorption above the model top.

In many fields DWD has very little temporal variation compared to all other models, as indicated by the standard deviation of the daily averages. This is probably due to a loss of precision in the output variables. They accumulate the quantities over the length of the run and calculate the higher frequency sampling by differencing the accumulated values.

ECM-CY32 has relatively large variation in the global average surface pressure (Figure 4.4) which is not consistent with the variation in evaporation minus precipitation (emp, Figure 4.3), i.e. it cannot be explained by a change in the mass of the atmospheric water vapor. It is in fact due to a monotonic positive trend. Over the 1095 daily average samples, the values increase monotonically from 1012.37 mb at the beginning to 1023.34 mb at the end, with an average increase of 0.010 mb per day. It appears that the mass fixer in the model was not applied in this version.

GFDL has a low global average surface pressure of 100174.7 Pa. They probably did not add mass to compensate for removing the mountains. APE recommended that the initial dry mass be equivalent to a global mean surface pressure of $101325 - 245 = 101080$ Pa. The 245 Pa corresponds to a global moisture content of 25.006 kg m^{-2} using the recommended value for surface gravity.

4.1.3 Zonal-Time Averages, 2-D Fields

Figures 4.8 through 4.14 show zonal-time averages for single level fields from the SH data sets: tppn, cppn, dppn, evap, emp, cld_frac, albedo, ps, sw_toa, lw_toa, rflux_toa, ssw, slw, rflux_sfce, slh, ssh, rflux, tauu and tauv.

4.1.4 Zonal-Time Averages, 3-D Fields

Figure 4.15 shows the multi-model mean and standard deviation of the zonal-time average for the basic state variables from the ML data sets: u, t, v, om, q and rh.

Figure 4.16 shows the same fields from Earth-like AMIP simulations. We include the multi-model mean and standard deviation for the AMIP simulations in the CMIP3 data base for comparison with the APE multi-model mean and standard deviation. The AMIP data were obtained from the the World Climate Research Programme's (WCRP's) Coupled Model Intercomparison Project phase 3 (CMIP3) multi-model dataset, http://www-pcmdi.llnl.gov/ipcc/about_ipcc.php.

The multi-model mean and standard deviation were calculated for the nine models that submitted AMIP data on all requested pressure levels.

Figures 4.17 through 4.28 show the same fields from the individual APE models and their differences with the APE multi-model mean.

4.2   Maintenance of Zonal Mean State

4.2.1   Dynamical Budgets (variances and co-variances)

This section presents the MF data set co-variance statistics (Eqn. 2.9) which describe, among other things, the contribution to the averaged flux of quantities by mid-latitude wave activity. Since the CONTROL experiment has no variation in longitude in the forcing (except for the diurnal cycle) the stationary eddies are small compared to the other terms in Eqn.(2.9). Therefore, in this section we consider the stationary mean meridional circulation (sm_), the transient eddy fluxes (te_) and the transient mean (tm_). The relative size of a few stationary eddy variances and co-variances can be seen later in Section 4.4.2 which includes them to indicate the contribution of low frequency wavenumber 5 structures to the meridional transport. The relevant figures are 4.101 through 4.104.

Figures 4.29 through 4.33 show the multi-model mean and standard deviation of the stationary mean (sm_), transient eddy (te_) and transient mean (tm_) components of the variances uu, tt, vv, omom and qq and of the co-variances vt, uv, uom, vq and omp. The models not included in the multi-model mean and standard deviation are CGAM, FRCGC, MRI, UKMO(N48) and UKMO(N96) which did not submit MF data.

Figures 4.34 through 4.69 show the same fields for the individual models.

4.2.2   Parameterization Forcing

The parameterization forcing terms (PF data sets) were considered optional so that not all modeling groups contributed a PF file to the APE archive. AGU, DWD, ECMWF, GSFC, K1JAPAN, LASG, NCAR and UKMO submitted PF files, although not all of them included all parameterization terms. We plot whatever was available and the layout of the figures is thus different for each variable.

One issue that becomes apparent in processing the parameterization terms is that it is not clear that all groups mean the same thing for some of the terms. In addition the APE definitions or specifications were not as clear as could be. The difficulties are compounded by the fact that different models do not split up the components in the same way in their fundamental definitions and derivations. However, the available fields are plotted in this section and provide some indication of what the parameterization terms look like along with the variability between models. Probably the most unambiguous terms are the longwave and shortwave radiation tendencies, the total parameterization tendencies and the convection parameterization tendency, although the latter is less certain because shallow convection may or may not be included. Three models (K1JAPAN, NCAR and UKMO) apparently submitted the total tendency rather than the total parameterization tendency, the APE specification was ambiguous. Of course, the time average of the total tendency is basically zero since the models are in a climate equilibrium. Since these

groups seemed to include all the parameterization terms, the total tendency for those models in Figures 4.70 and 4.77 is derived as the sum of the individual terms.

Figures 4.70 through 4.76 show the parameterization temperature tendencies: t, t_conv, t_cld, t_turb, t_sw, t_lw and t_disp. The variable t_turb was not clearly defined in the APE specifications, thus groups appear not to have submitted exactly the same term. For example, GSFC does not include the surface flux. In their model the surface fluxes explicitly change the first level data, then the turbulent fluxes mix it vertically as a second step. The NCAR model, on the other hand, uses the surface fluxes as a boundary condition for the vertical mixing by the PBL so the surface fluxes are included in the turbulence. These differences are reflected in the plots in that the GSFC would show a strong reversal of sign between the first level above the ground and the second. To avoid this distraction we mask out the first level in the GSFC plots. The NCAR model along with most of the others, shows no sign reversal. The surface flux component itself is compared in Figure 4.13 of Section 4.1.3. In this section, for any models that do not include the surface flux, the plots of turbulence can be compared above the first layer. The surface flux was also not included in the total parameterization tendency from the GSFC model. Again we mask the first level in the plot. The UKMO model appears to combine the large-scale cloud and boundary layer, their parameterizations do not allow them to be split apart. We plot this combination as t_turb. The UKMO model also has a tendency from large-scale precipitation. We plot this as t_cld.

NCAR and the UKMO include an energy fixer to ensure energy conservation. These terms are very small and independent of location. They are not included in any of the parameterization terms and can be thought of as part of the dynamical approximations.

Figures 4.77 through 4.81 show the parameterization specific humidity tendencies: q, q_conv, q_cld, q_turb and q_negq. Concerning q_negq, the NCAR model numerical transport approximations are positive definite for q and the model does not require a negative fixer. However the model does include a water vapor mass fixer to compensate for the semi-Lagrangian approximations which do not conserve water vapor. The NCAR group put the fixer tendency in the q_negq variable to provide it for comparison to computational terms in other models. The UKMO used a targeted q diffusion to control grid-point storms. This term is given in q_negq for their model.

Figures 4.82 through 4.85 show the parameterization zonal wind tendencies (u, u_conv, u_turb and u_gwd) and Figures 4.86 through 4.89 show the parameterization meridional wind tendencies (v, v_conv, v_turb and v_gwd). Only K1JAPAN and GSFC reported non-zero values of u_gwd and v_gwd. The GSFC are plotted but the K1JAPAN are not since their values ranged from -1.0×10^{-18} to 1.0×10^{-18} m sec^{-1} day^{-1}.

4.3 Tropical Variability

4.3.1 Hovmöller Diagrams

Figure 4.90 shows Hovmöller Diagrams for each model of equatorial precipitation (tppn) averaged from $-5°$ to $+5°$ latitude (mm day^{-1}). The period analyzed is the first 30 days of the submitted TR data.

4.3.2 Wavenumber-Frequency Spectra

The equatorial wave propagation characteristics of the model simulations are illustrated via wavenumber-frequency diagrams calculated from the 6-hourly TR data sets following the spectral analysis methodology of Wheeler and Kiladis (1999). Figure 4.91 shows the log of the power of the symmetric component of the unnormalized spectra of the precipitation (tppn) averaged from 10°S to 10°N. Figure 4.92 shows the anti-symmetric component. Figures 4.93 and 4.94 show the symmetric and anti-symmetric components of the outgoing longwave radiation (lw_toa), respectively. In these figures the upper left panel is a template which labels what have become the conventional dispersion curves for these diagrams for equatorial waves with equivalent depths of 12, 25 and 50 m; symmetric modes have odd meridional mode-numbers, and anti-symmetric modes have even meridional mode-numbers (see Wheeler and Kiladis, 1999). The symmetric template indicates Kelvin waves (KELVIN), n=1 equatorial Rossby waves (ER), n=1 eastward inertio-gravity waves (EIG) and n=1 westward inertio-gravity waves (WIG). The anti-symmetric template indicates n=0 mixed Rossby-gravity wave (MRG), n=0 and 2 eastward inertio-gravity waves (EIG) and n=0 westward inertio-gravity waves (WIG).

The full power is plotted in the wavenumber-frequency figures without removing a background spectrum in order to allow a comparison of the overall power of the waves. Normalization by a smooth background field such as done by Wheeler and Kiladis for Earth observations isolates spectral peaks that are often associated with specific normal modes or waves, but since the normalization is done individually for each model, the overall signal associated with the power is contained in the background spectrum. In the aqua-planet, the wave-like signals are apparent in the full field, and normalization by a smooth background is not as necessary as in Earth-like simulations. For reference, the figures include the conventional dispersion curves, but unlabeled.

4.3.3 Precipitation Frequency Distributions

Figure 4.95 shows the precipitation (tppn) frequency distributions for each model. The frequency distribution provides information about the extremes simulated by the models. In this section we graph the frequency distribution of 6-hour averaged precipitation in the tropical region calculated from all grid points between 10°S to 10°N from the TR data sets. Each column in Figure 4.95 shows a triplet of plots. The first row gives the fraction of the time the precipitation is in each 0.1 mm day^{-1} bin ranging from 0 to 12 mm day^{-1}. The center row gives the fraction of the time the precipitation is in each 1 mm day^{-1} bin ranging from 0 to 120 mm day^{-1}. The bottom row gives the fraction of the time the precipitation is in each 10 mm day^{-1} bin ranging from 0 to 1200 mm day^{-1}. In each plot the left-most bin is the fraction of the time the precipitation is exactly 0, and the right-most bin the fraction of time the precipitation exceeds 12, 120 or 1200 mm day^{-1}.

The smallest rates are difficult to discern in Fig. 4.95. Therefore Fig. 4.96 is included provide details of zero and light precipitation. For each model the figure plots the fraction of the time the 6-hour averaged precipitation at grid points between 10°S to 10°N is zero and the fraction of time it is positive and less than 0.01, less than 0.1 and less than 1.0 mm day^{-1}. Note, the smallest category, $0 < p \leq 0.01$, is one tenth of the smallest bin represented in the first row of Fig. 4.95.

Some of the variation among models seen in Fig. 4.95 is likely to be due to different grid sizes. To eliminate variation due to the grid size, Fig. 4.97 shows the fraction calculated after the model grid data have been conservatively mapped to a 5° latitude-longitude grid. There is still a very large variation between models. There is also a large variation in the extremes when the model data are mapped to a 10° latitude-longitude grid as seen in Fig. 4.98. This indicates that even at very large scales the models do not agree.

4.4   Extratropics

4.4.1   Low Frequency Variability

A very noticeable wavenumber-five pattern often appears in mid-latitudes in long time averages of APE simulations. It is most noticeable in maps of the meridional velocity where wavenumber five can often be seen as the dominant pattern. Figure 4.99 illustrates this for the APE models for the CONTROL case. It shows the time average 250 mb meridional velocity (v250) with the zonal average removed. Watanabe (2005), Cash et al. (2007) and Watanabe (2007) have discussed this mode and its relationship to the annular mode. Watanabe (2005) describes it as a slowly propagating, wavenumber-five disturbance forced by high-frequency eddies. More recently Zappa et al. (2011) have studied this phenomenon and conclude that it arises from marginally stable baroclinic waves. Unfortunately the design of the APE experiment and the data collected do not allow a thorough examination of the phenomenon. As will be seen below, the three-year averages of the three-dimensional fields in the ML data show large, seemingly random variations between models in amplitude and phase of the wave. Of course the APE boundary conditions have no longitudinal variation and cannot influence the phase in long time averages. The only phase determinant in the APE is the diurnal cycle which has no influence this phenomenon. The one year of 6-hourly TR data of a few two-dimensional fields is too short and does not allow examination of vertical aspects.

Nevertheless, as seen in Figure 4.99 many APE models indicate a significant mid-latitude wavenumber-five structure in the 3-year average. The characteristics of wavenumber five are indicated in Fig. 4.100. The top row shows the amplitude of wavenumber-five of 3-year average meridional velocity at 30°N and 30°S at 250 mb. The left panel shows all the APE models except FRCGC which was not integrated for three years. The models are identified by their number in Table 3.2. Clearly, there is no consistency in amplitudes. The right panel shows the amplitude for 24 successive 3-year averages from a 72 year integration of the NCAR model. This provides an indication of the natural variability in the relationship. The APE models are consistent with this variability, with models 1, 8 and 12 having slightly lower amplitudes. The bottom row shows the percent variance explained by wavenumber five at 30°N in the APE models (left) and in the 24 NCAR samples (right).

The top panels of Fig. 4.100 show the amplitude of 3-year average wavenumber five at 30°N and 30°S as a function of its harmonic phase difference between the hemispheres. The difference indicates the degree to which phase locking of wavenumber five between northern and southern mid-latitudes night occur. For the NCAR model the phase differences are clustered around 180° (meridional velocity out of phase, geopotential in-phase), suggesting significant phase interaction between the hemispheres. There is little evidence of phase interaction across

all the APE models, but NCAR does show higher apparent amplitude of wavenumber five than many of other models. These aspects are discussed in Blackburn et al. (2013).

4.4.2 Stationary Eddy Co-variances: Total and Wavenumber 5

Figures 4.101 through 4.104 show the stationary eddy (se_) variances (uu, vv) and co-variances (uv, vt) for the individual models for the total fields and for the fields spectrally filtered to contain longitudinal wavenumber 5 only. These figures are calculated from the time averaged three dimensional ML files rather than from the MF (co-)variance files themselves. This permits Fourier filtering before the stationary eddies are computed. The stationary eddies for the wavenumber 5 are presented to provide an estimate of the contribution of the low frequency wavenumber 5 component to the total stationary eddies.

4.4.3 Wavenumber-Frequency Spectra

Figure 4.105 shows wavenumber-frequency diagrams of the log of the power of symmetric modes of the meridional velocity at 250 mb (v250) at 30° latitude where the wavenumber 5 structures tend to maximize in the CONTROL experiment. Figure 4.106 shows the anti-symmetric modes. The diagrams are calculated from the 1-year sample of 6-hourly TR data from each model. The diagrams are for each model and for the multi-model mean.

The low frequency wavenumber-5 behavior is seen. Most models show power in eastward and westward propagating wavenumber 5 increasing with increasing period from above 30 days to the resolved limit. The eastward propagating waves tend to have more power than the westward. Power in both directions could indicate propagation in different directions at different times, or a standing oscillation, the former being more likely. The one year sample is relatively short for these longer periods, resulting in large noise in the lower frequencies and preventing any significant comparison between models of this low frequency variability.

Most models also show cells which might be associated with particular propagating Rossby modes with a preferred meridional mode number. For example the symmetric modes show
- westward propagating wavenumber 3 with period of around 5 days,
- westward propagating wavenumber 4 with period of around 10 days,
- eastward propagating wavenumber 6 with period of around 7 to 10 days and
- eastward propagating wavenumber 7 with period of around 4 to 5 days,

and the anti-symmetric show
- westward propagating wavenumber 4 with period of around 10 days,
- eastward propagating wavenumber 6 with period of around 7 to 10 days and
- eastward propagating wavenumber 7 with period of around 4 to 5 days.

Of course, for each longitudinal wavenumber there are many meridional modes, each with a different frequency. Thus a range of frequencies has power for each wavenumber. Because the periods differ somewhat between models, the cells are washed out in the multi-model mean, but are still apparent. Without doing a modal analysis we cannot say which meridional and vertical modes are dominant. For an atmosphere at rest, the theoretical Rossby modes all propagate westward, however the westerly zonal jets can Doppler shift some modes to be eastward propagating. The CGAM model has a different behavior than the other models, with more power at

higher frequencies and fewer obvious cells of power indicating no particular propagating Rossby modes dominate.

4.5   Global 2-D Spectra

Kinetic energy spectra at 250 mb from the CONTROL experiment are shown by the solid lines in Figure 4.107. The divergent components are shown with dashed lines. The upper reference line has a -3 slope and the lower one has a $-5/3$ slope. The spectra are computed following Appendix B of Jakob et al. (1993). The atmospheric spectrum is observed to have a -3 slope over the scales contained in the models in Figure 4.107 (Nastrom and Gage, 1985). The kinetic energy spectra provide some indication of the damping from a dynamical core. The damping is due to explicit horizontal diffusion terms added to the dynamical equations, is inherent in the numerical approximations themselves, or is a combination of the two. The total kinetic energies of AGU, K1JAPAN, LASG, MRI and NCAR all follow the -3 slope to near the truncation limit. These are all Eulerian spectral transform models and control the accumulation of energy in the smallest scales with a diffusion term on vorticity and divergence, usually of a ∇^4 form. The diffusion coefficient can usually be chosen to yield a straight tail for the spectrum which usually follows a -3 slope at resolutions of these models. The divergent component from these models follows a $-5/3$ slope. The total kinetic energies of the other models tail off faster than -3 with that of MIT decreasing the fastest with increasing wavenumber. However, the MIT slope beyond about wavenumber 40 might be influenced by the interpolation from the model grid to the latitude-longitude grid used for the data submitted to the APE archive. The steeper slopes are seen in both the total and divergent components. This behavior in the total also implies that the rotational component has a steeper slope as well. The stronger damping implied by this structure is often due to inherent damping of the numerical approximations of the dynamical cores. At higher resolutions, the damping at a given wavenumber by these numerical processes decreases as seen by comparing UKMO(N48) and UKMO(N96). Among the various models, the damping of the higher wavenumbers varies by a factor of 2 to 4. The steeper slopes indicate more damping near the truncation limit. A slope steeper than -3 may be desirable to reduce spectral ringing and grid scale noise (MacVean, 1983).

Figure 4.108 shows the spectra of the 500 mb pressure vertical velocity (ω) variance from the CONTROL experiment. A wide range of behaviors is seen approaching the truncation limits. Some models such as AGU, ECM-CY29, KiJAPAN, LASG and MRI have a fairly straight approach to the limit, although not all with the same slope. Others have a concave structure with a faster decrease in variance approaching the limit. The spectrum of ω in the atmosphere has not been estimated from observations.
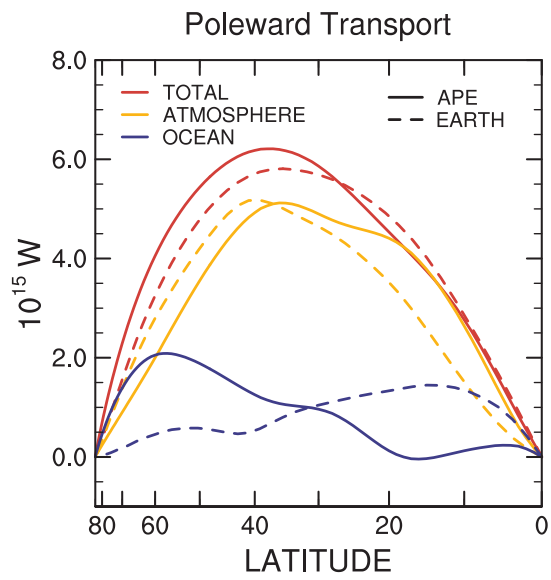
Figure 4.1: Multi-model mean zonal-time average poleward energy transports.
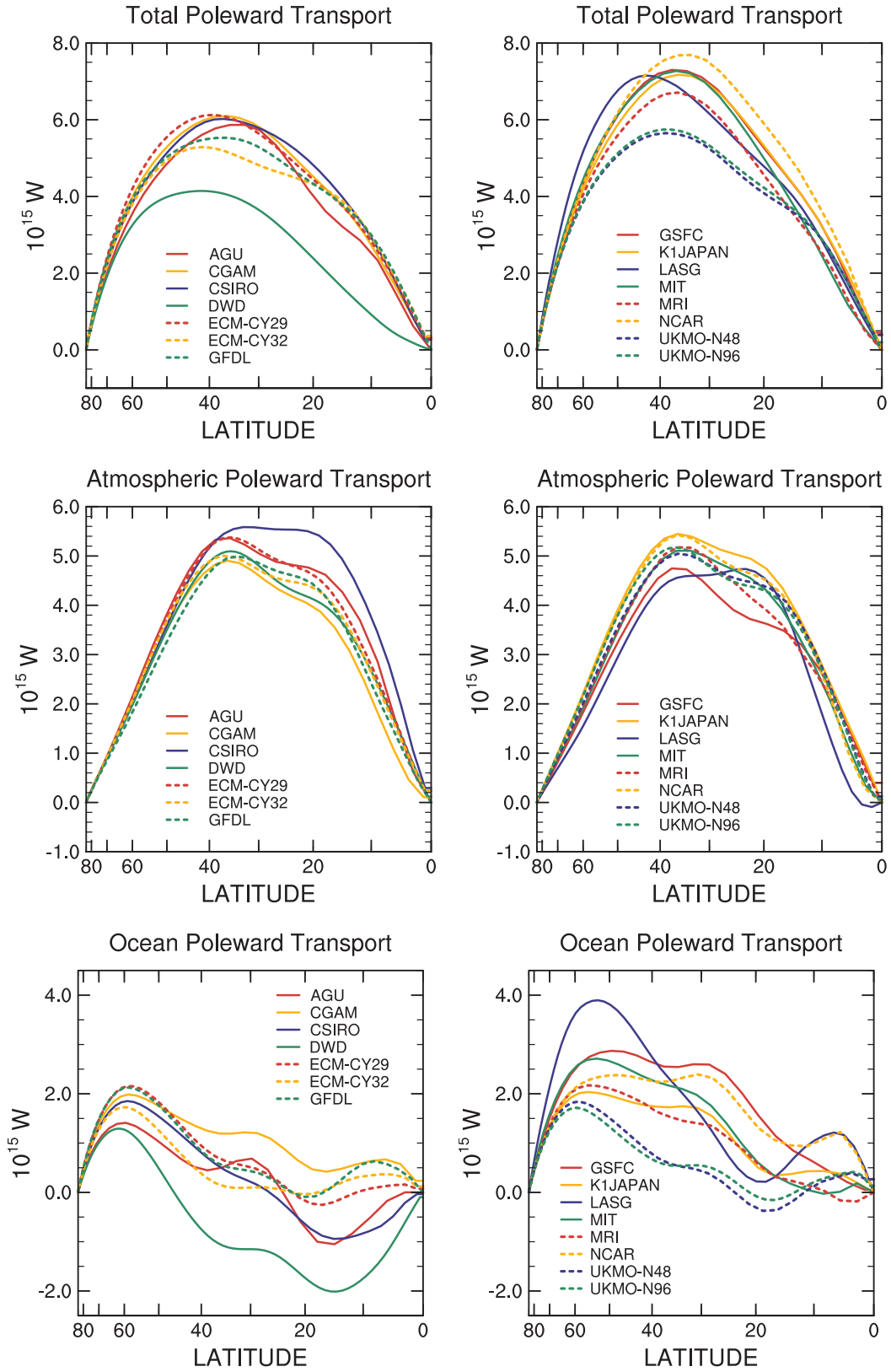
Figure 4.2: Individual model zonal-time average poleward energy transports.
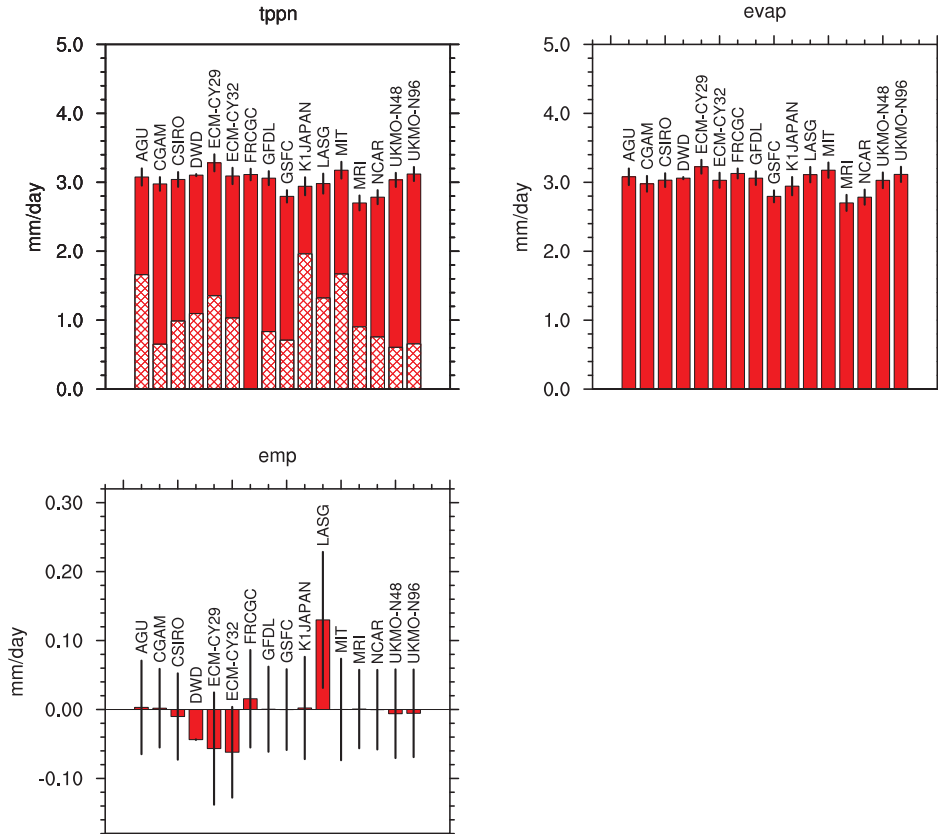
Figure 4.3: Global-time average total precipitation (tppn), evaporation (evap) and evaporation minus precipitation (emp) for individual models. The total precipitation is divided into convective precipitation (cppn, solid) and large-scale precipitation (dppn, cross-hatched), mm day^{-1}.
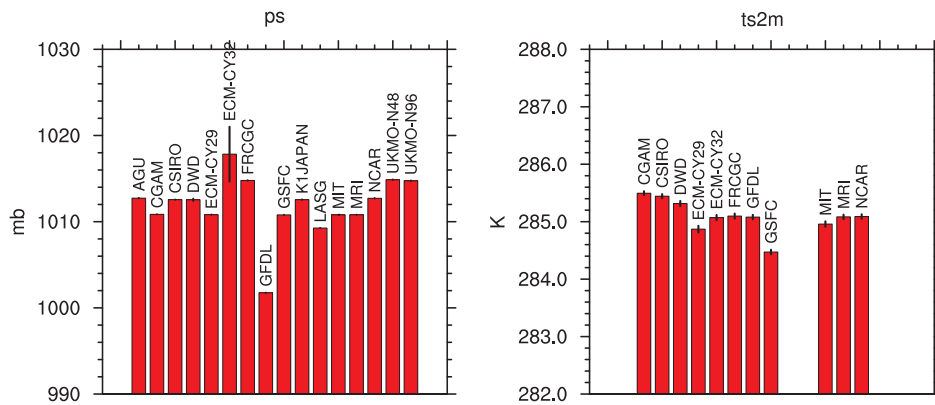
Figure 4.4: Global-time average surface pressure (ps), mb, and two meter temperature (ts2m) for individual models, K.
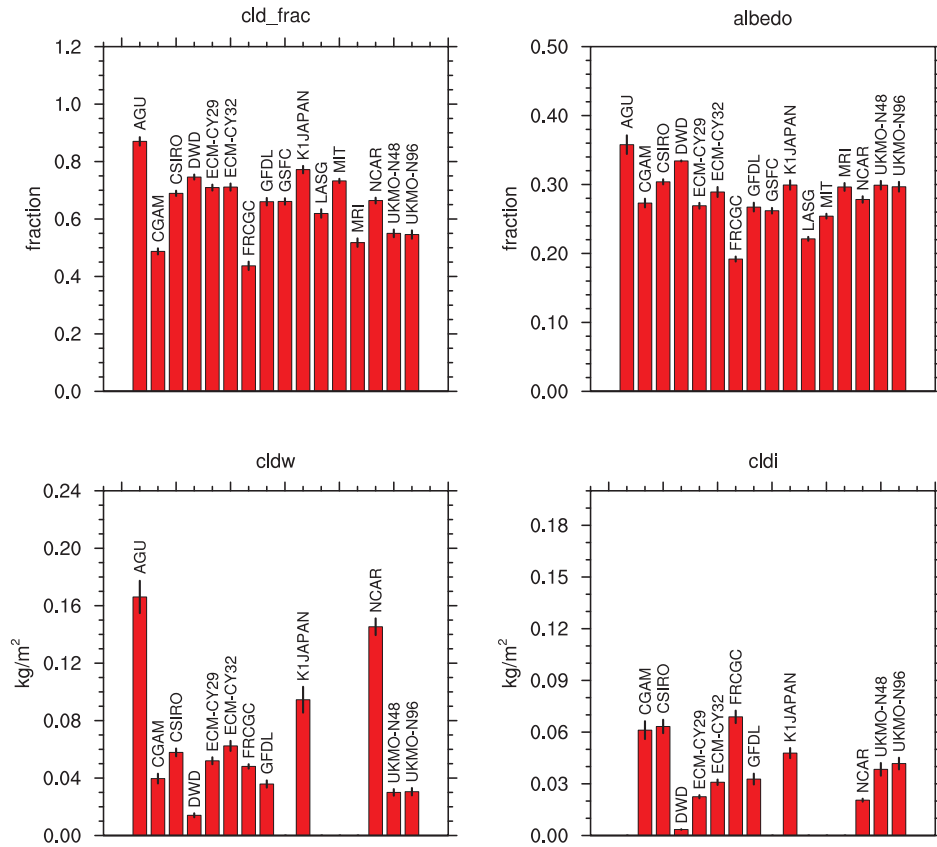
Figure 4.5: Global-time average cloud fraction (cld_frac), fraction; albedo (albedo), fraction; cloud water (cldw), kg m^{-2} and cloud ice (cldi) for individual models, kg m^{-2}.
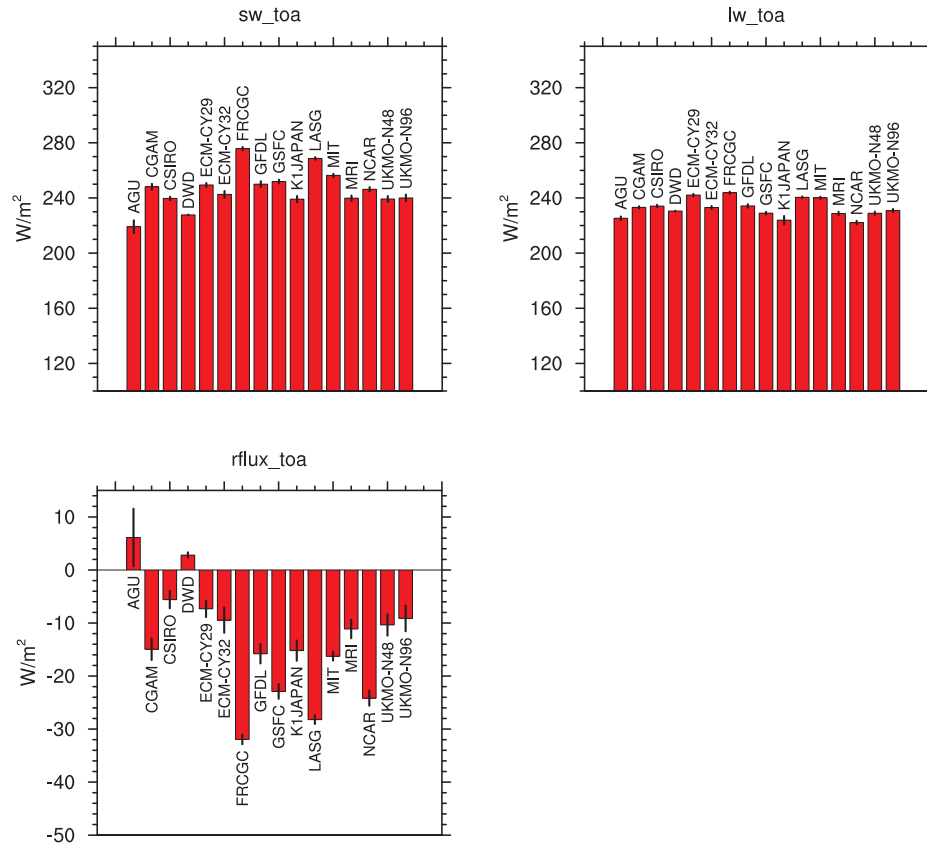
Figure 4.6: Global-time average net shortwave (sw_toa, +ve downward), net longwave (lw_toa, +ve upward), and residual (rflux_toa, +ve upward) TOA radiative fluxes for individual models, W m^{-2}.
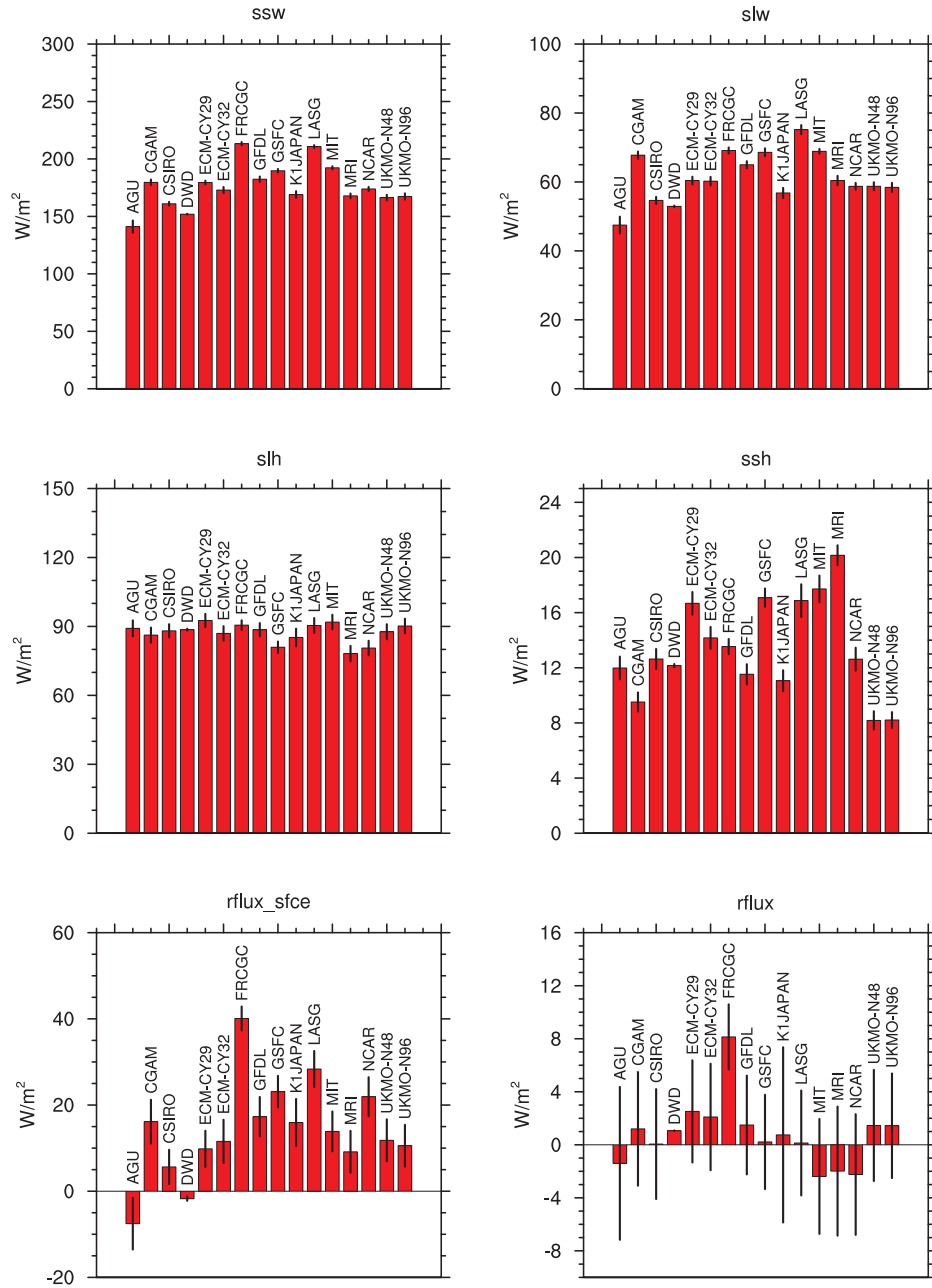
Figure 4.7: Global-time average net shortwave (ssw, +ve downward), net longwave (slw, +ve upward), latent heat (slh), sensible heat (ssh) and residual (rflux_sfce, +ve downward) surface fluxes, and net total flux (rflux, +ve out of atmosphere) for individual models, W m^{-2}.
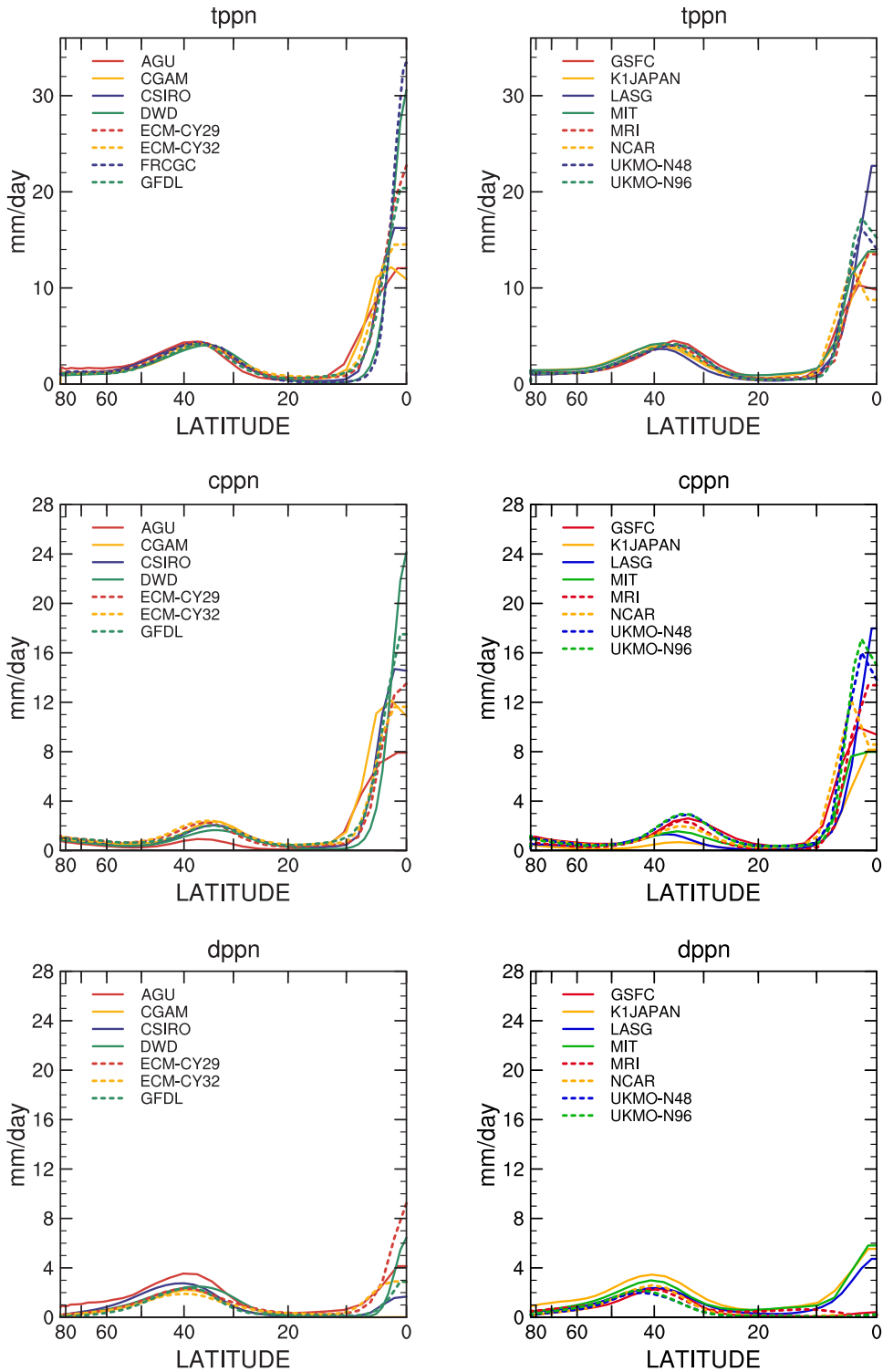
Figure 4.8: Zonal-time average total, convective and large scale precipitation (tppn, cppn, dppn), mm day^{-1}.
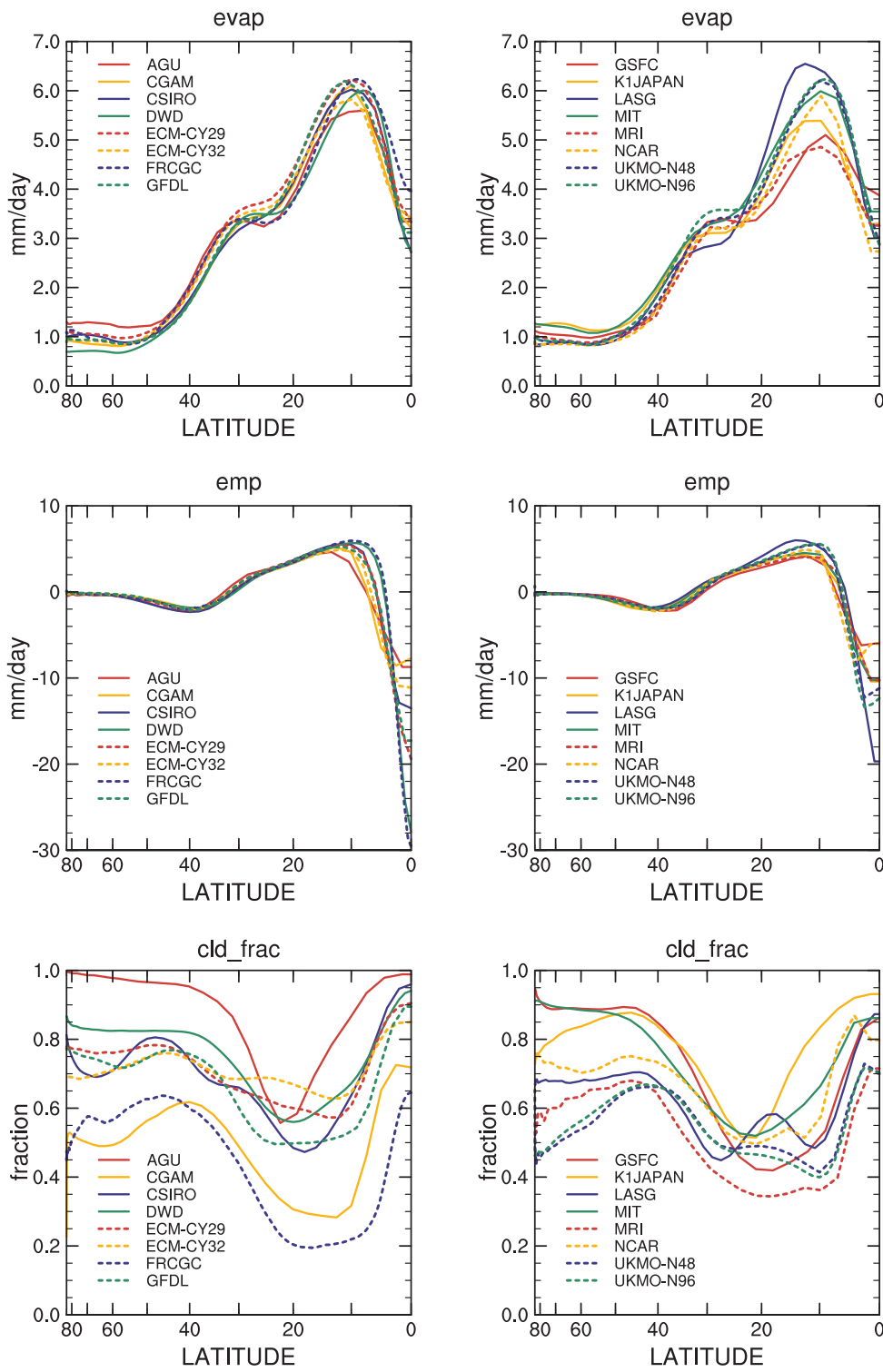
Figure 4.9: Zonal-time average evaporation (evap) and evaporation minus precipitation (emp), mm day^{-1}, and cld_frac, fraction.
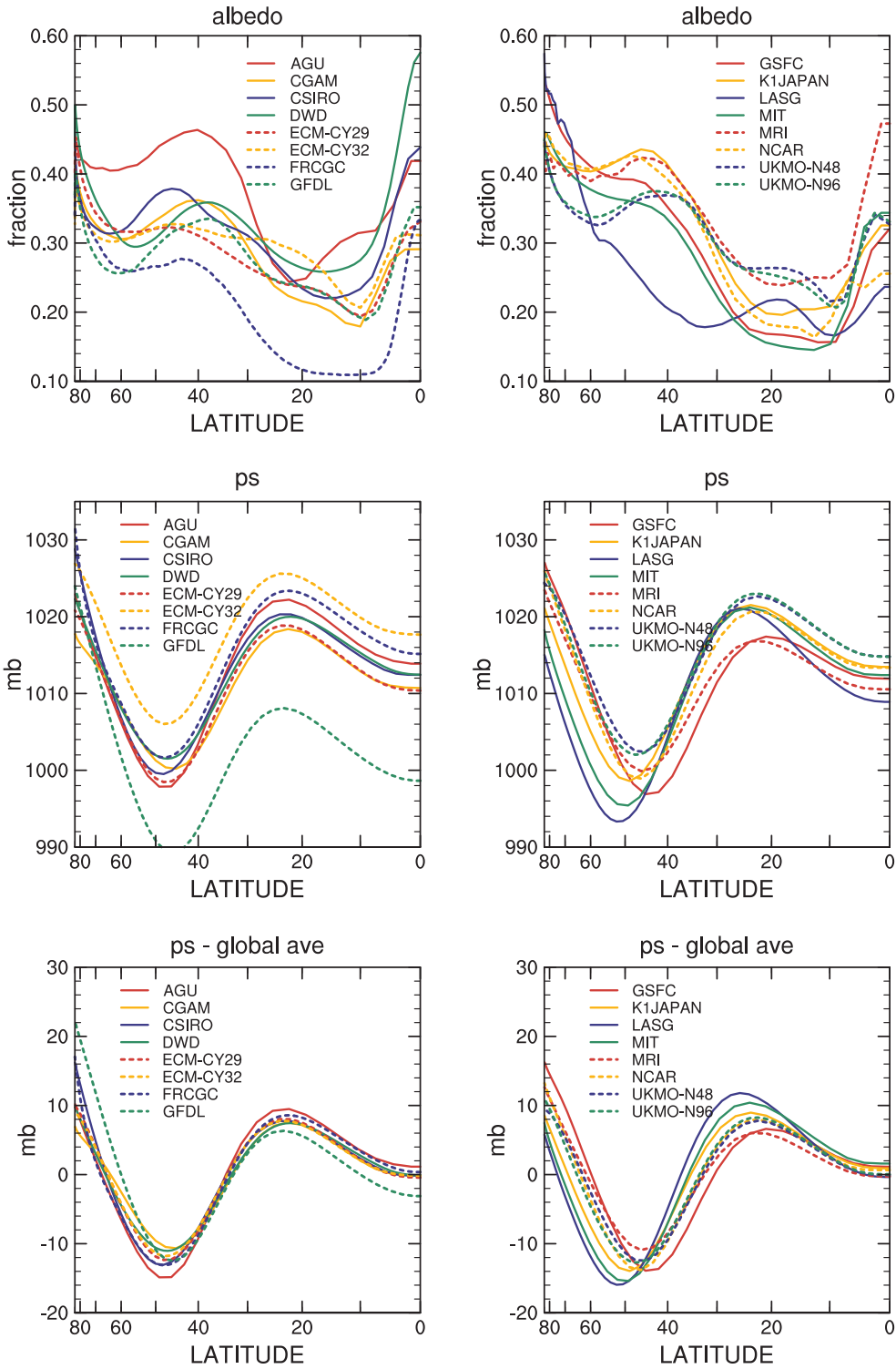
Figure 4.10: Zonal-time average albedo (fraction) and surface pressure (ps), mb.
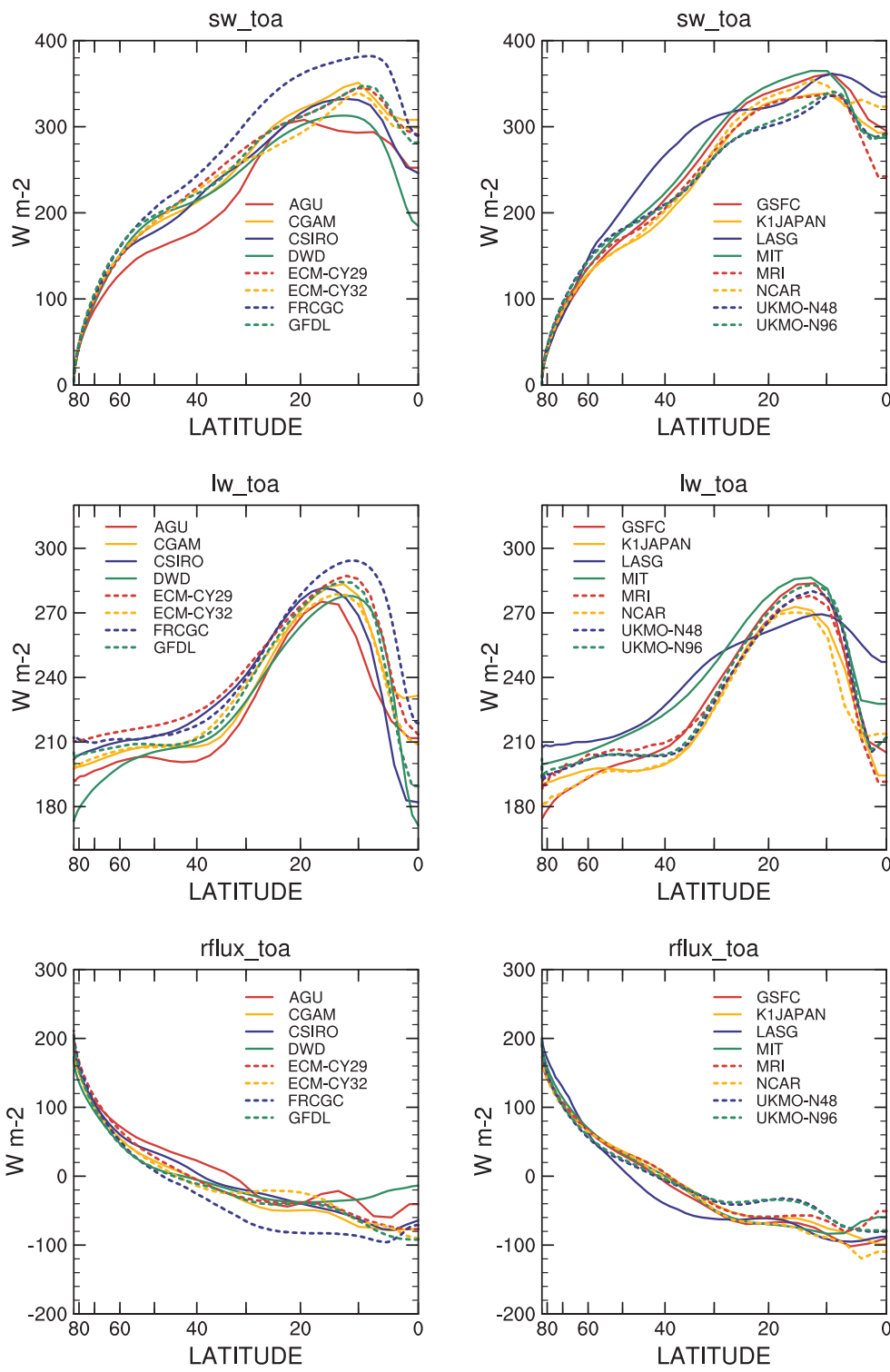
Figure 4.11: Zonal-time average net shortwave (sw_toa, +ve downward), net longwave (lw_toa, +ve upward), and residual (rflux_toa, +ve upward) TOA radiative fluxes, W m^{-2}.
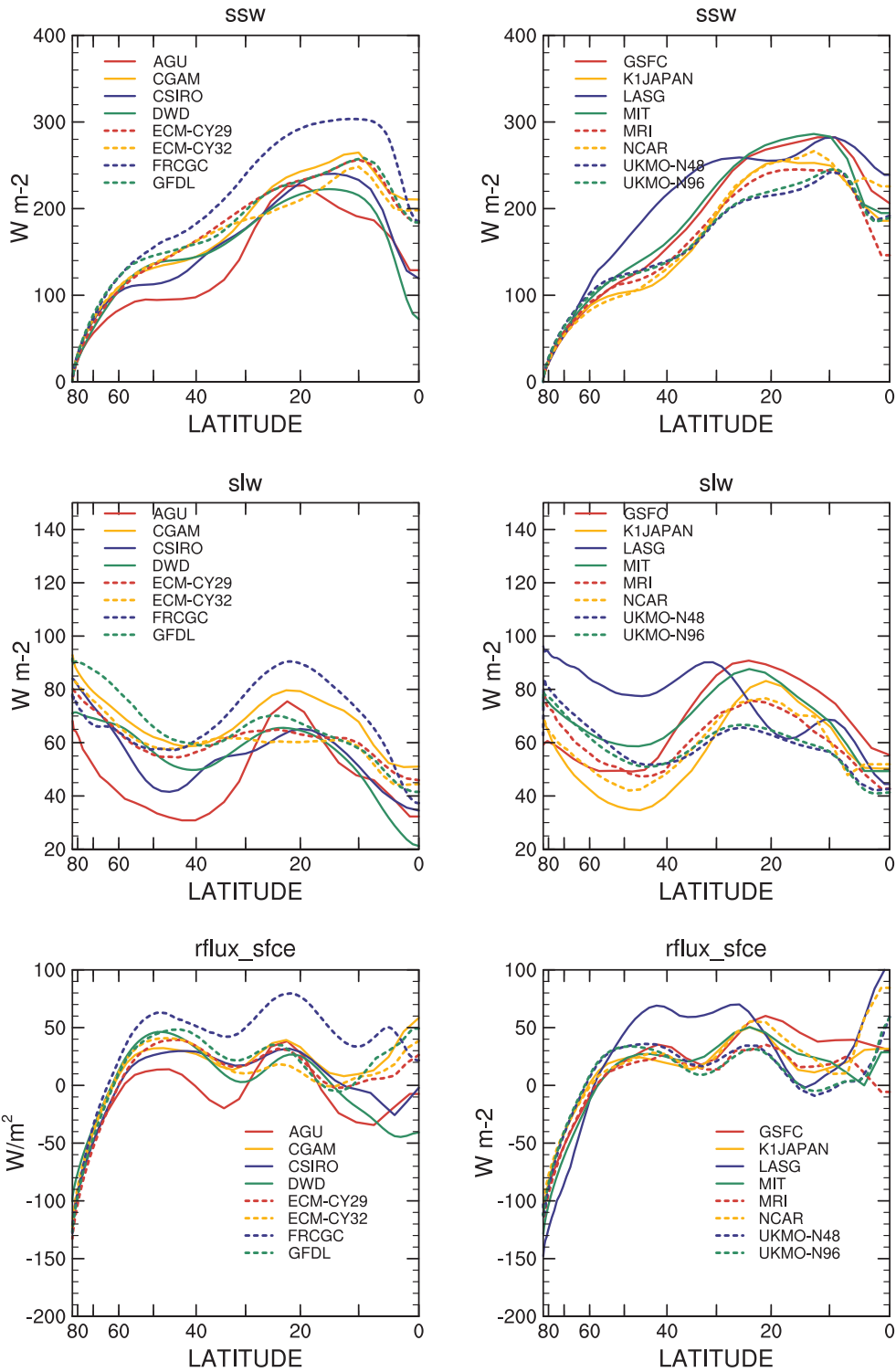
Figure 4.12: Zonal-time average net shortwave (ssw, +ve downward), net longwave (slw, +ve upward) and residual (rflux_sfce, +ve downward) surface fluxes, W m^{-2}.
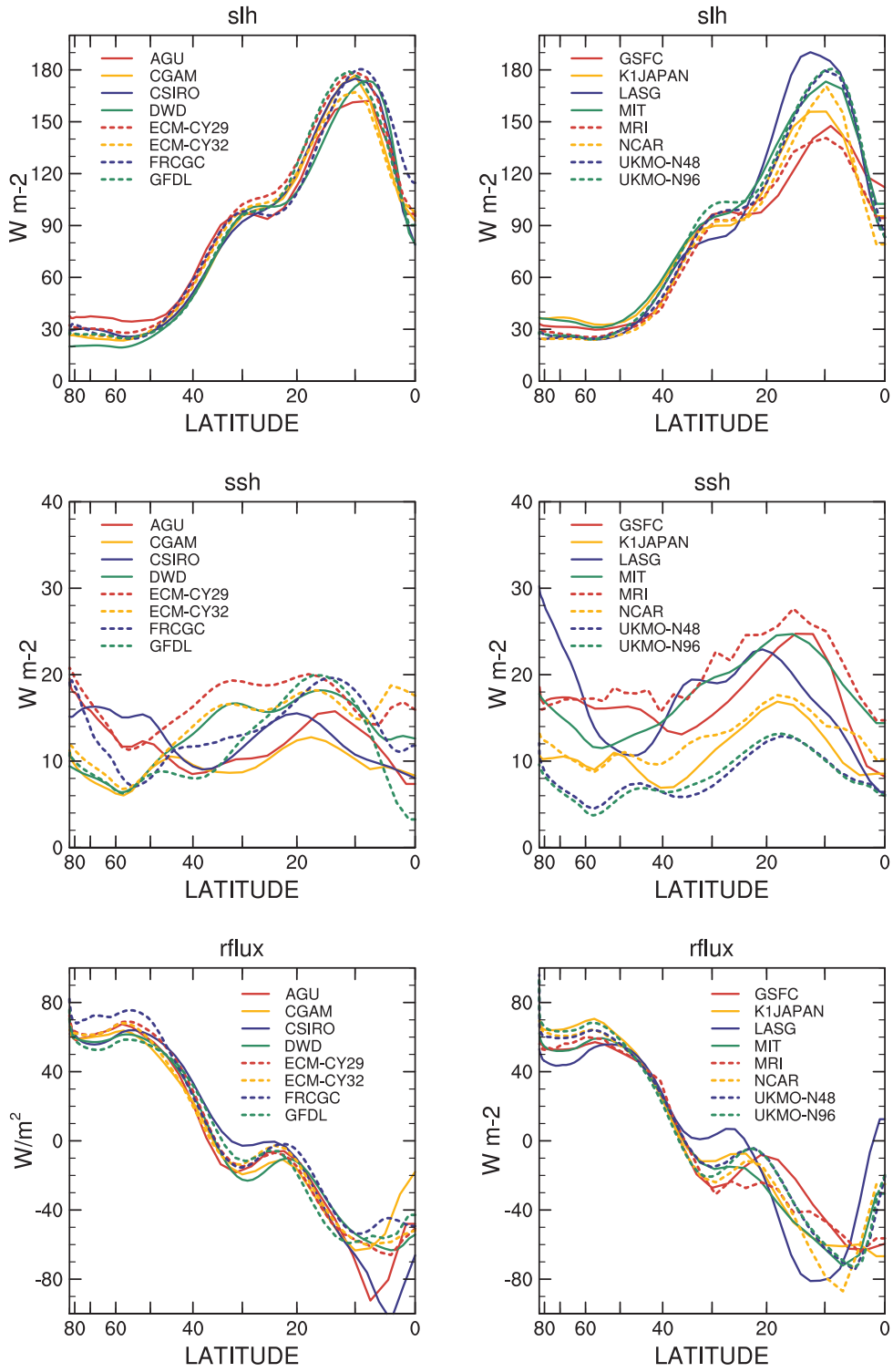
Figure 4.13: Zonal-time average latent (slh) and sensible heat fluxes (ssh), and net atmospheric energy flux (rflux, positive out of atmosphere), W m^{-2}.
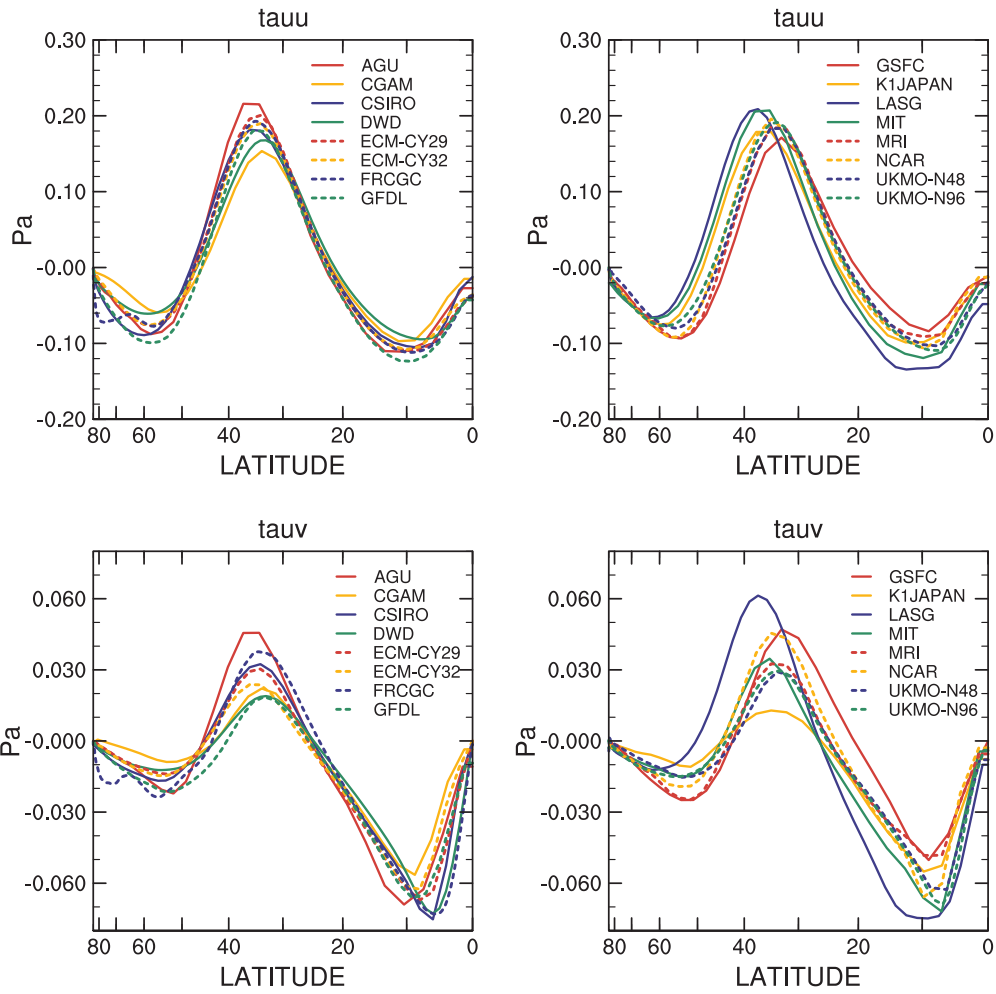
Figure 4.14: Zonal-time average zonal and meridional surface stresses (tauu and tauv), N m^{-2}.
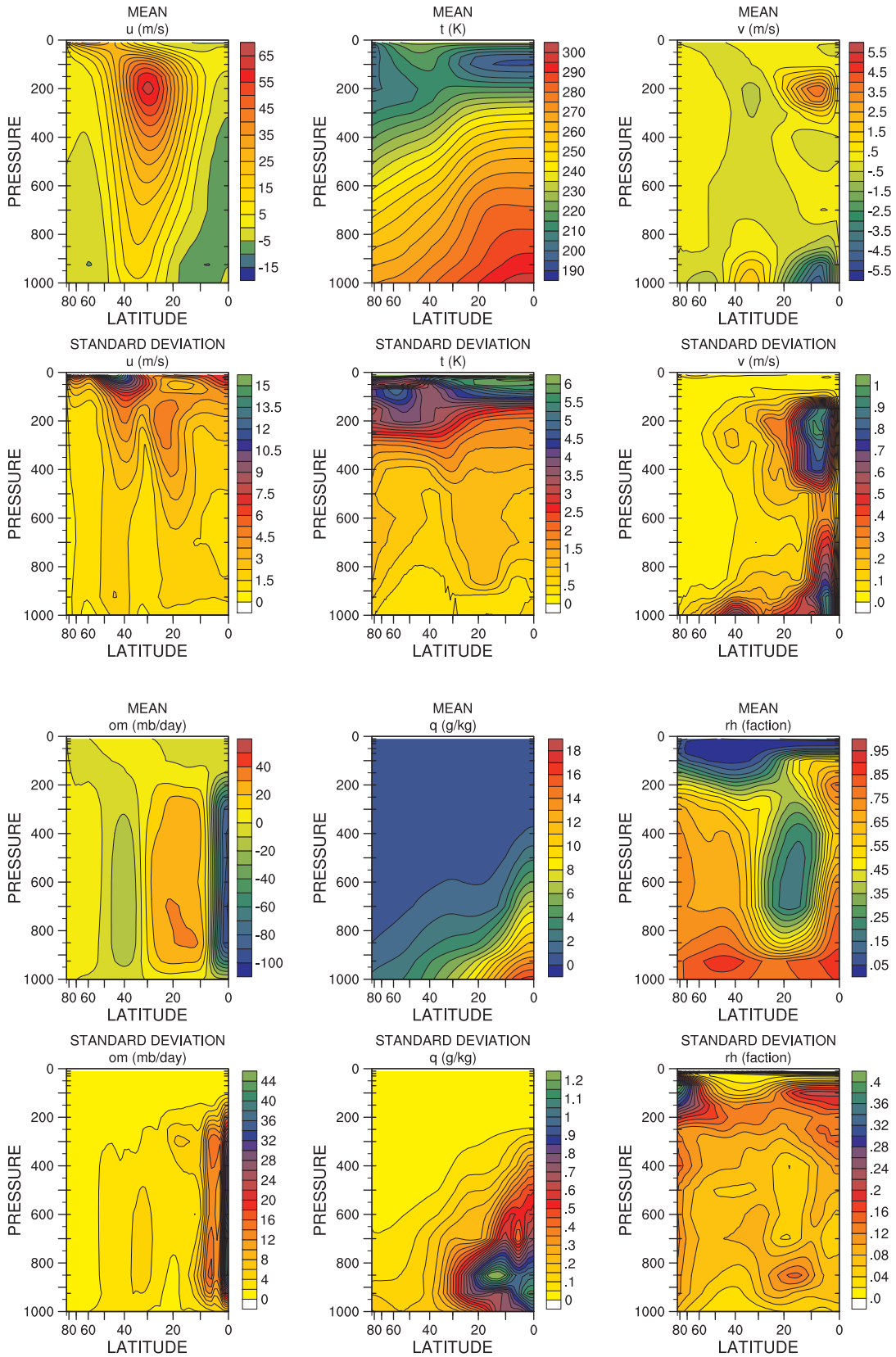
Figure 4.15: Zonal-time average APE multi-model mean and standard deviation zonal wind (u), temperature (t), meridional wind (v), vertival wind (om), specific humidity (q) and relative humidity (rh).
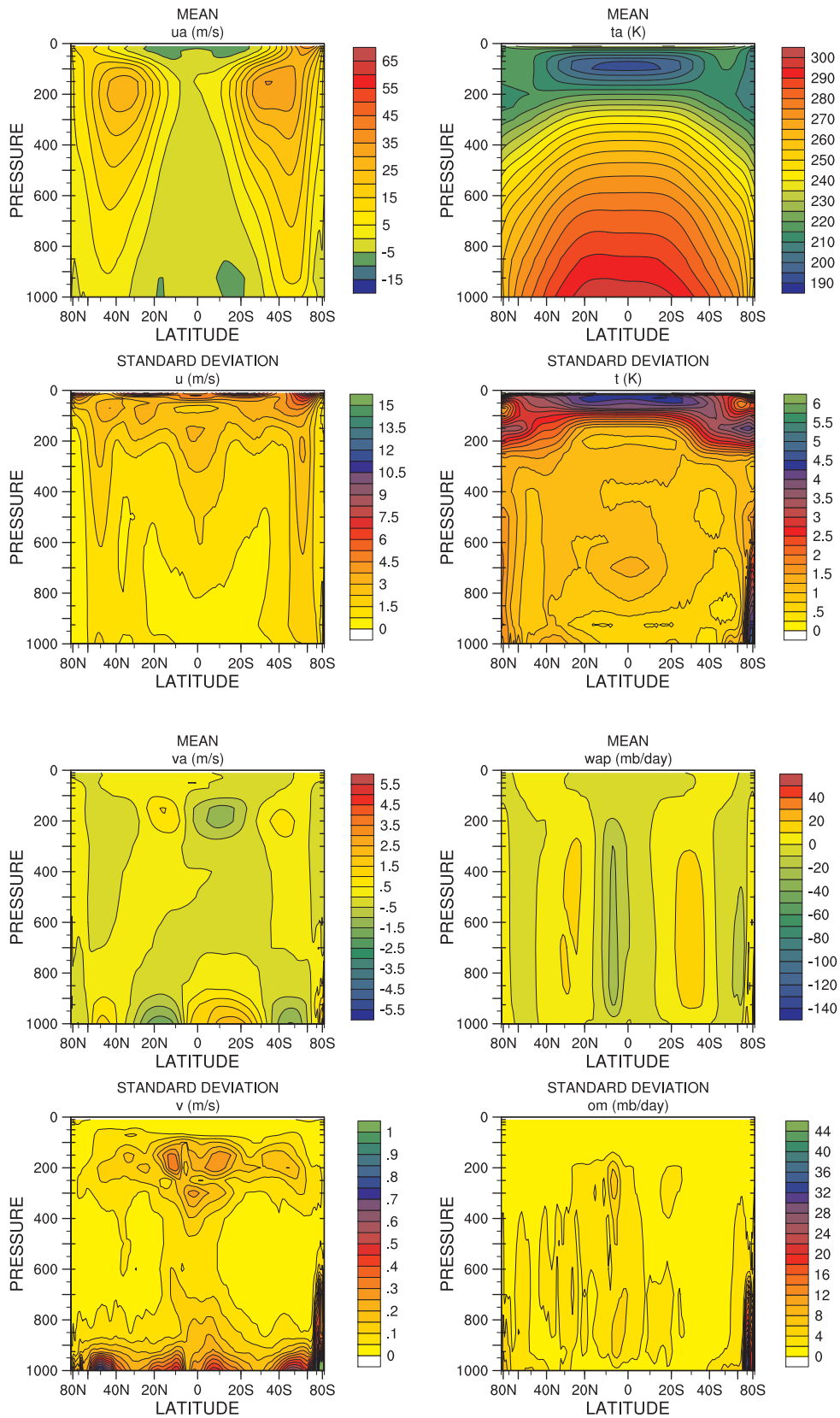
Figure 4.16: Zonal-time average AMIP multi-model mean and standard deviation zonal wind (ua, u), temperature (ta, t), meridional wind (va, v), vertival wind (wap, om), specific humidity (hus, q) and relative humidity (hur, rh).
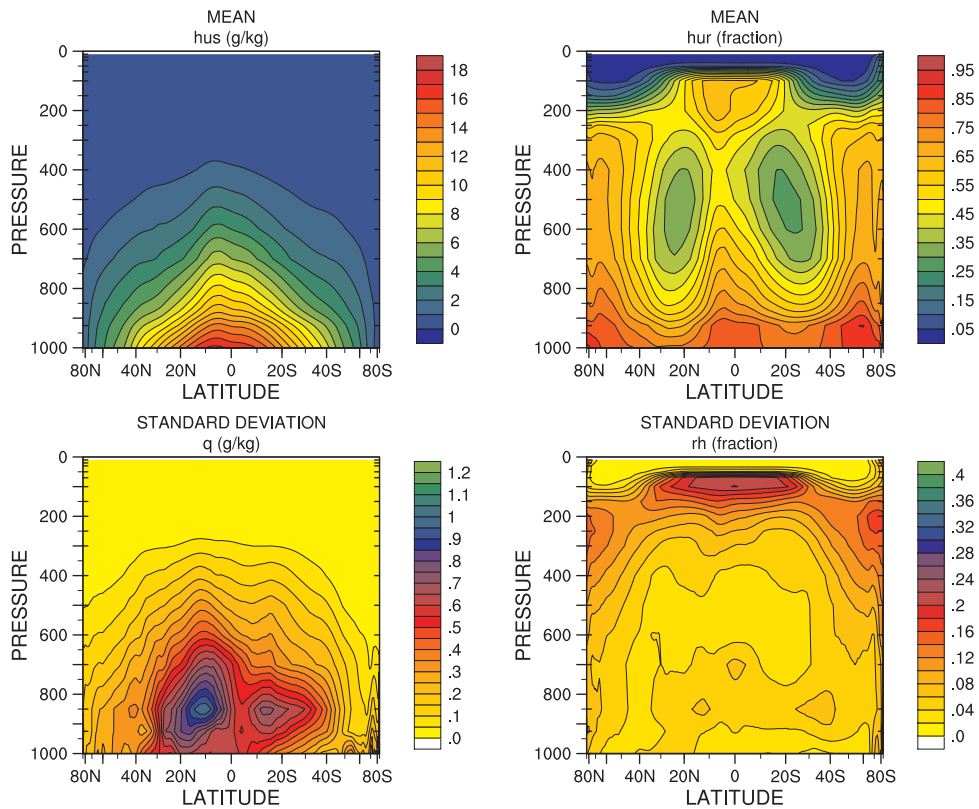
Figure 4.16 (continued): Zonal-time average AMIP multi-model mean and standard deviation zonal wind (ua, u), temperature (ta, t), meridional wind (va, v), vertival wind (wap, om), specific humidity (hus, q) and relative humidity (hur, rh).
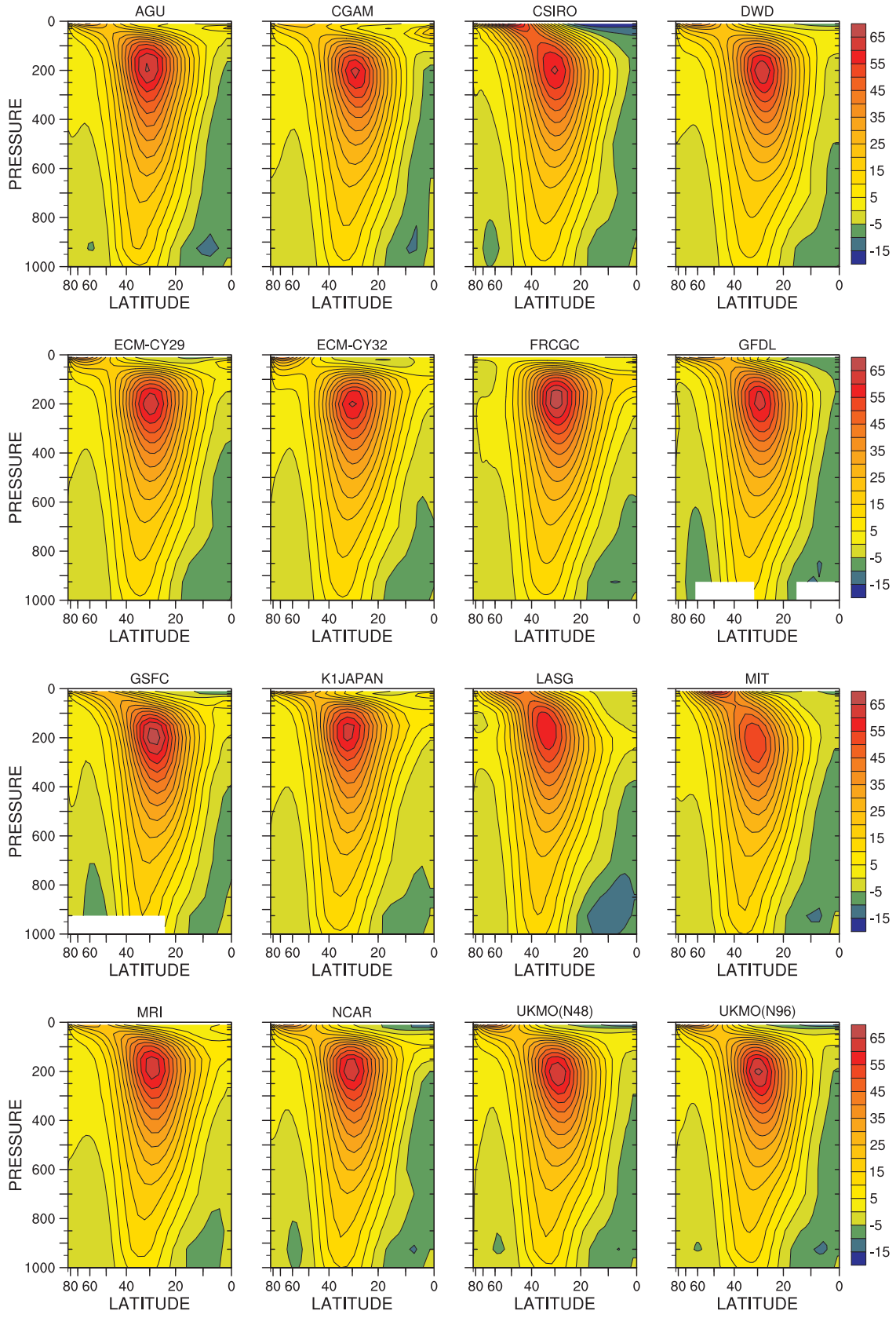
Figure 4.17: Zonal-time average zonal wind (u) for individual models, m s^{-1}.
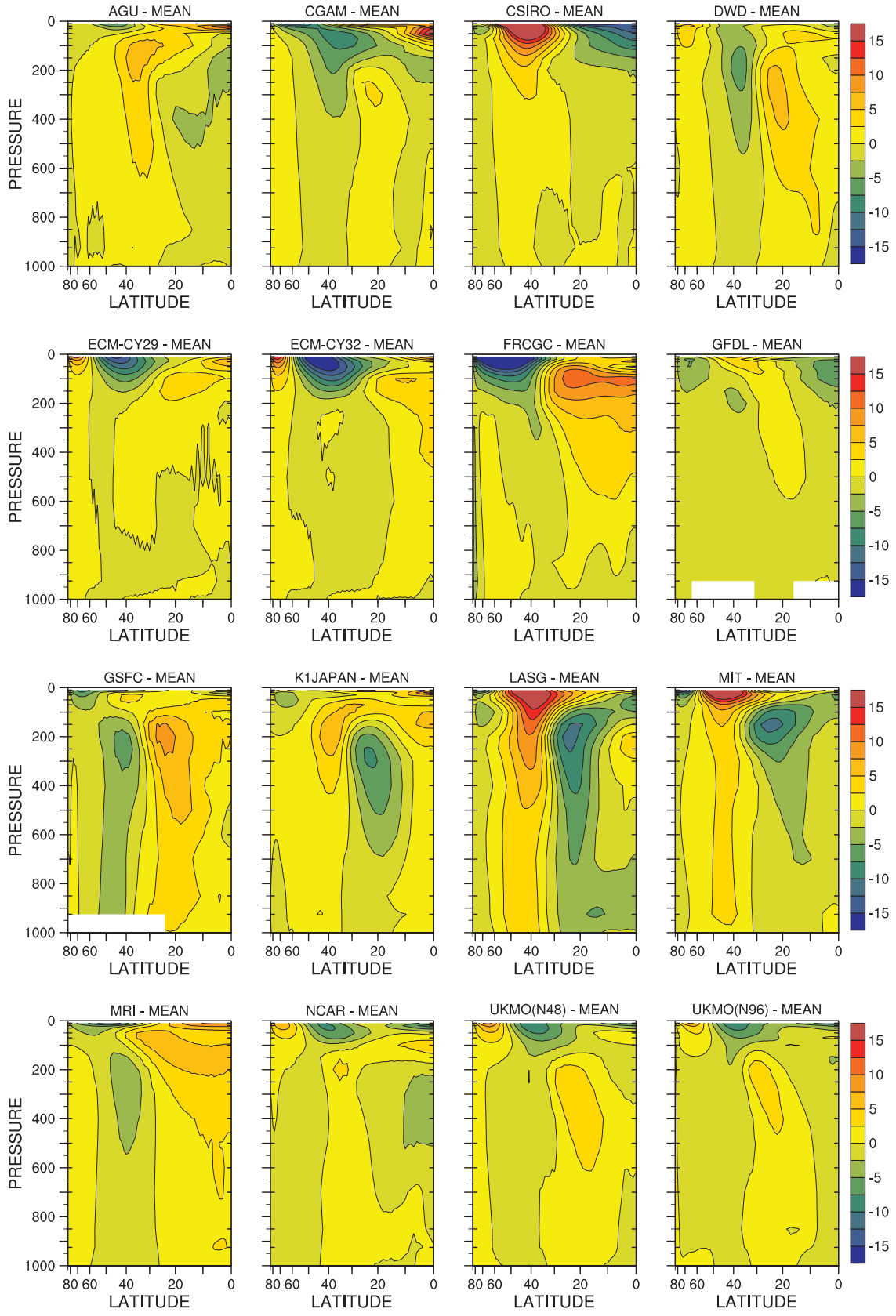
Figure 4.18: Zonal-time average zonal wind (u), individual models minus multi-model mean, m s^{-1}.
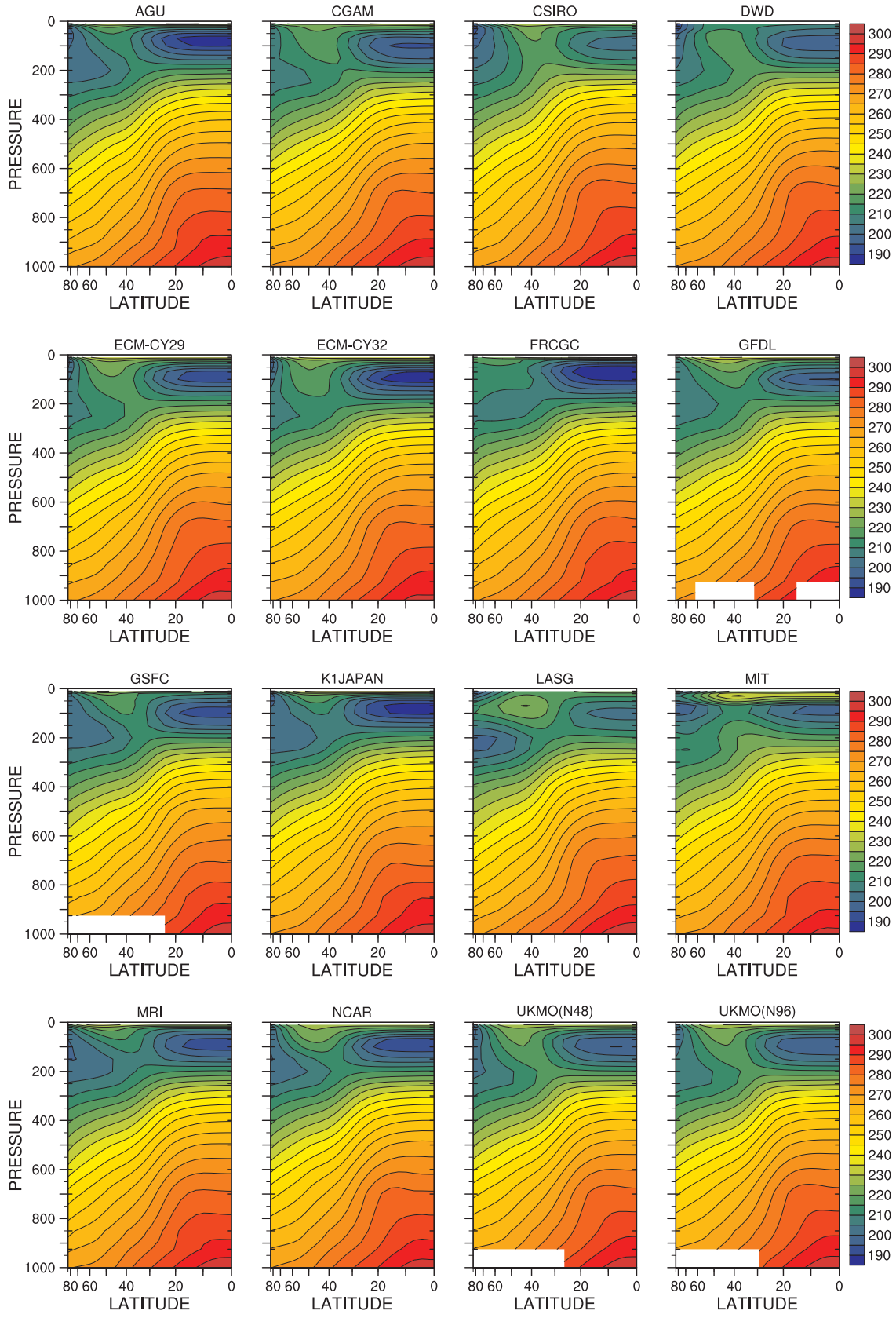
Figure 4.19: Zonal-time average temperature (t) for individual models, K.
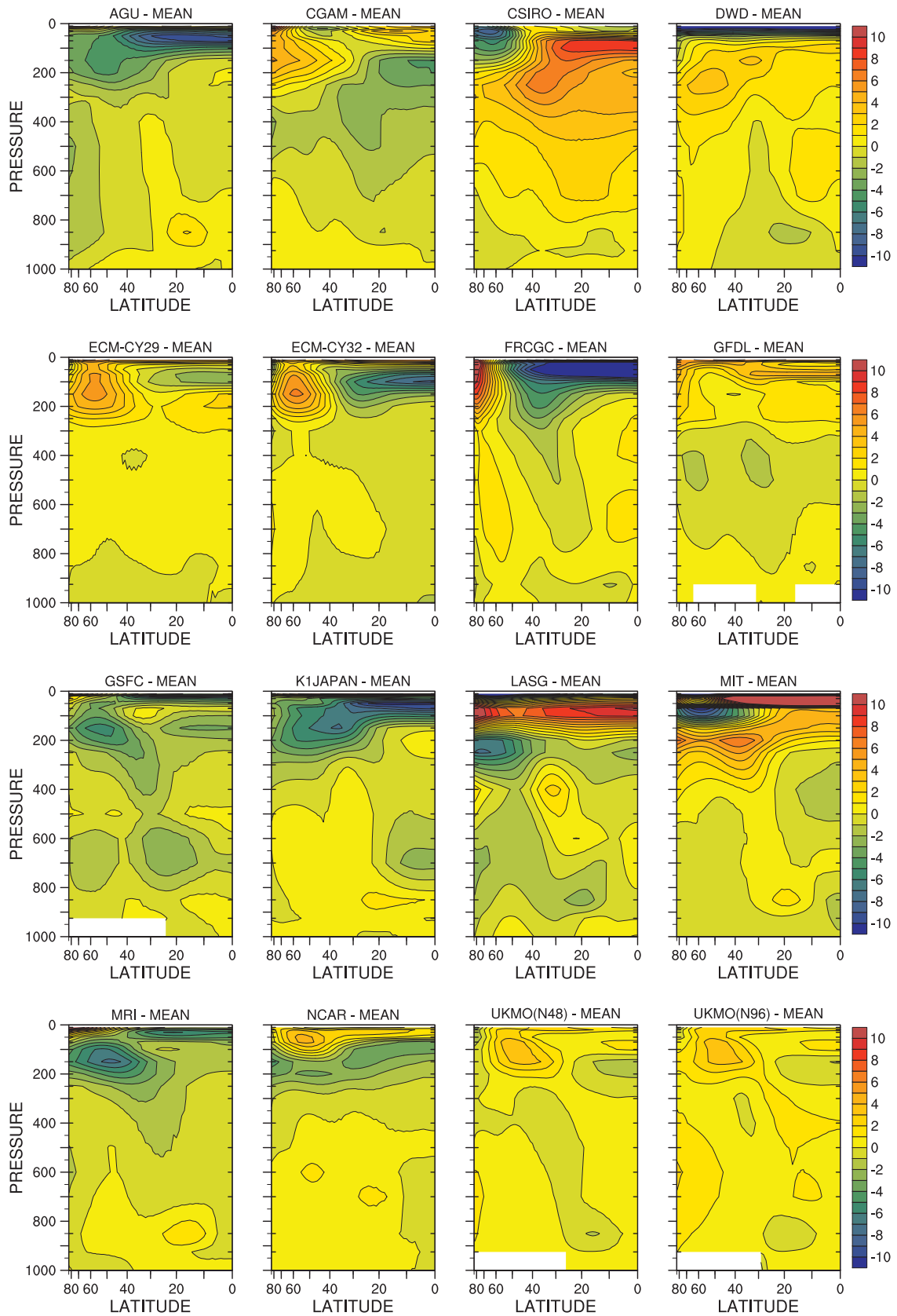
Figure 4.20: Zonal-time average temperature (t), individual models minus multi-model mean, K.
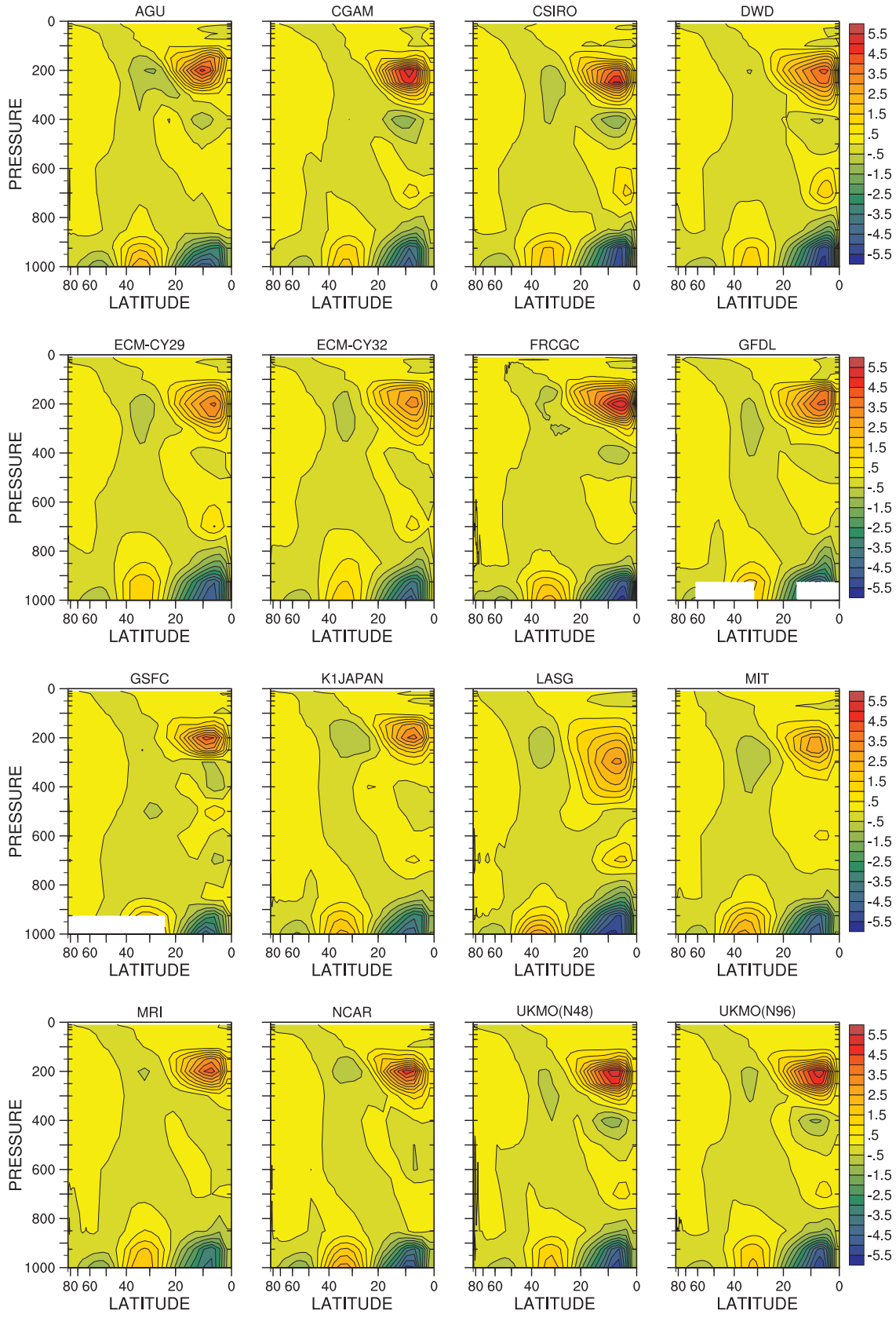
Figure 4.21: Zonal-time average meridional wind (v) for individual models, m s^{-1}.
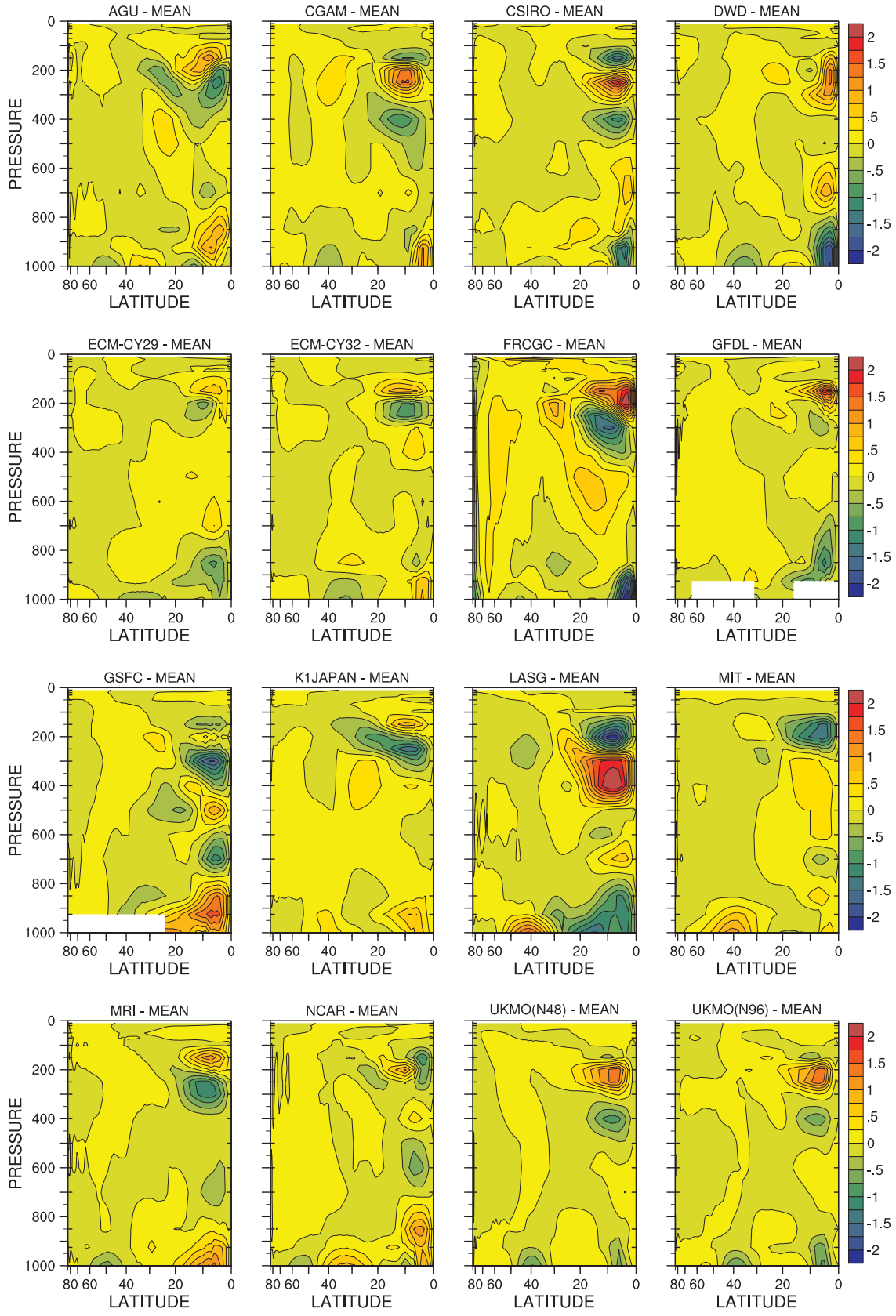
Figure 4.22: Zonal-time average meridional wind (v), individual models minus multi-model mean, m s^{-1}.
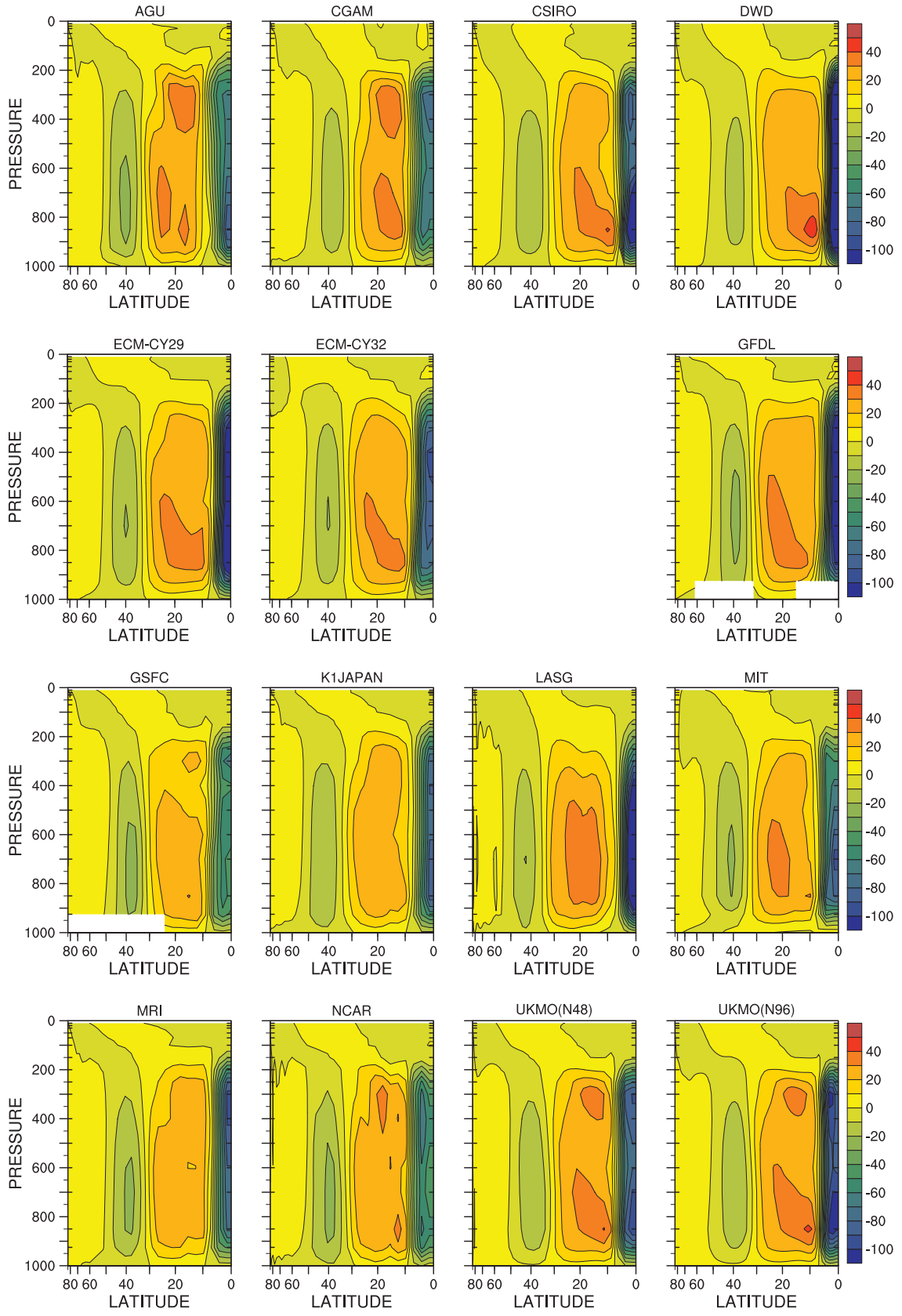
Figure 4.23: Zonal-time average vertical velocity (om) for individual models, mb day^{-1}.
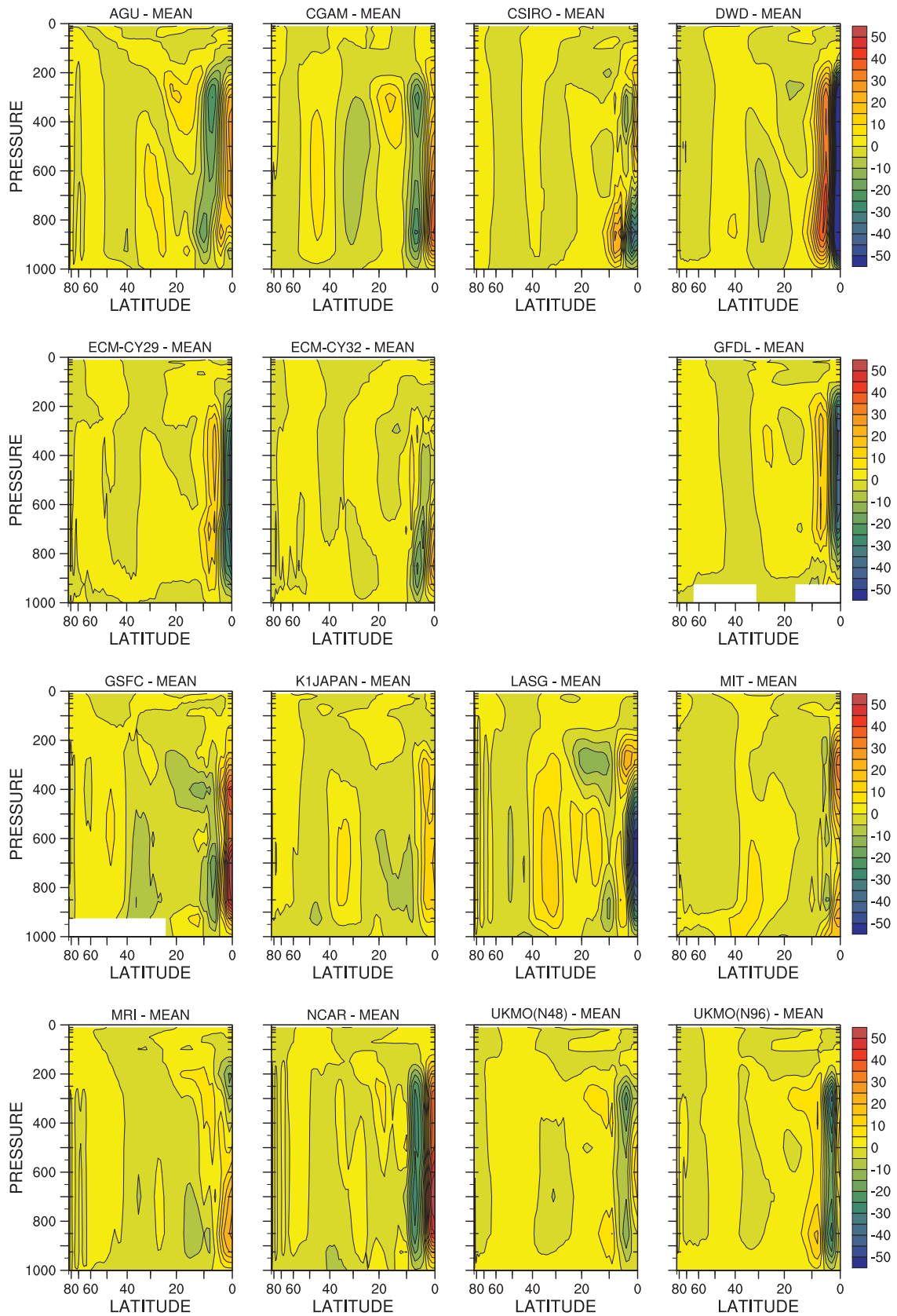
Figure 4.24: Zonal-time average vertical velocity (om), individual models minus multi-model mean, mb day^{-1}.
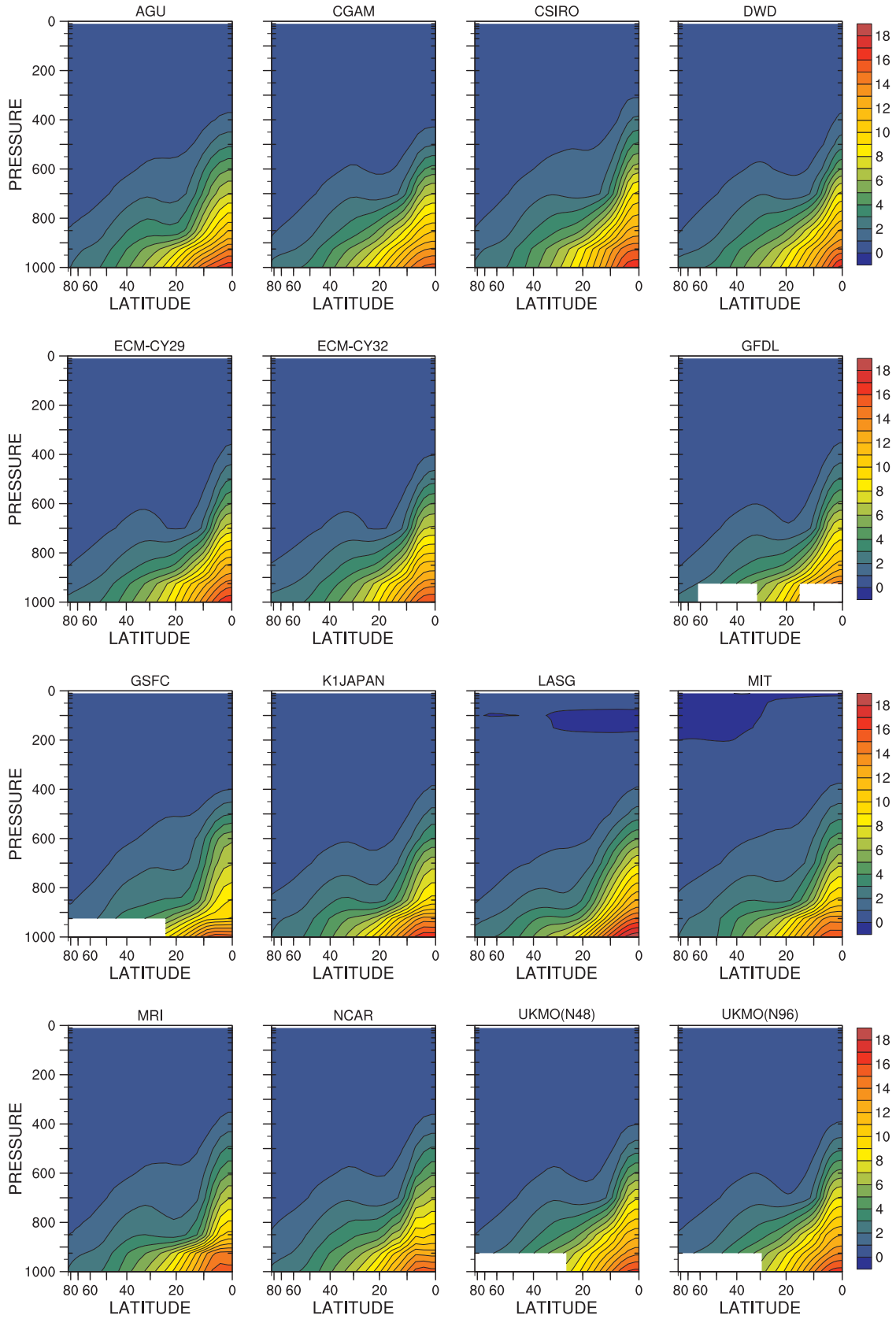
Figure 4.25: Zonal-time average specific humidity (q) for individual models, g kg^{-1}.
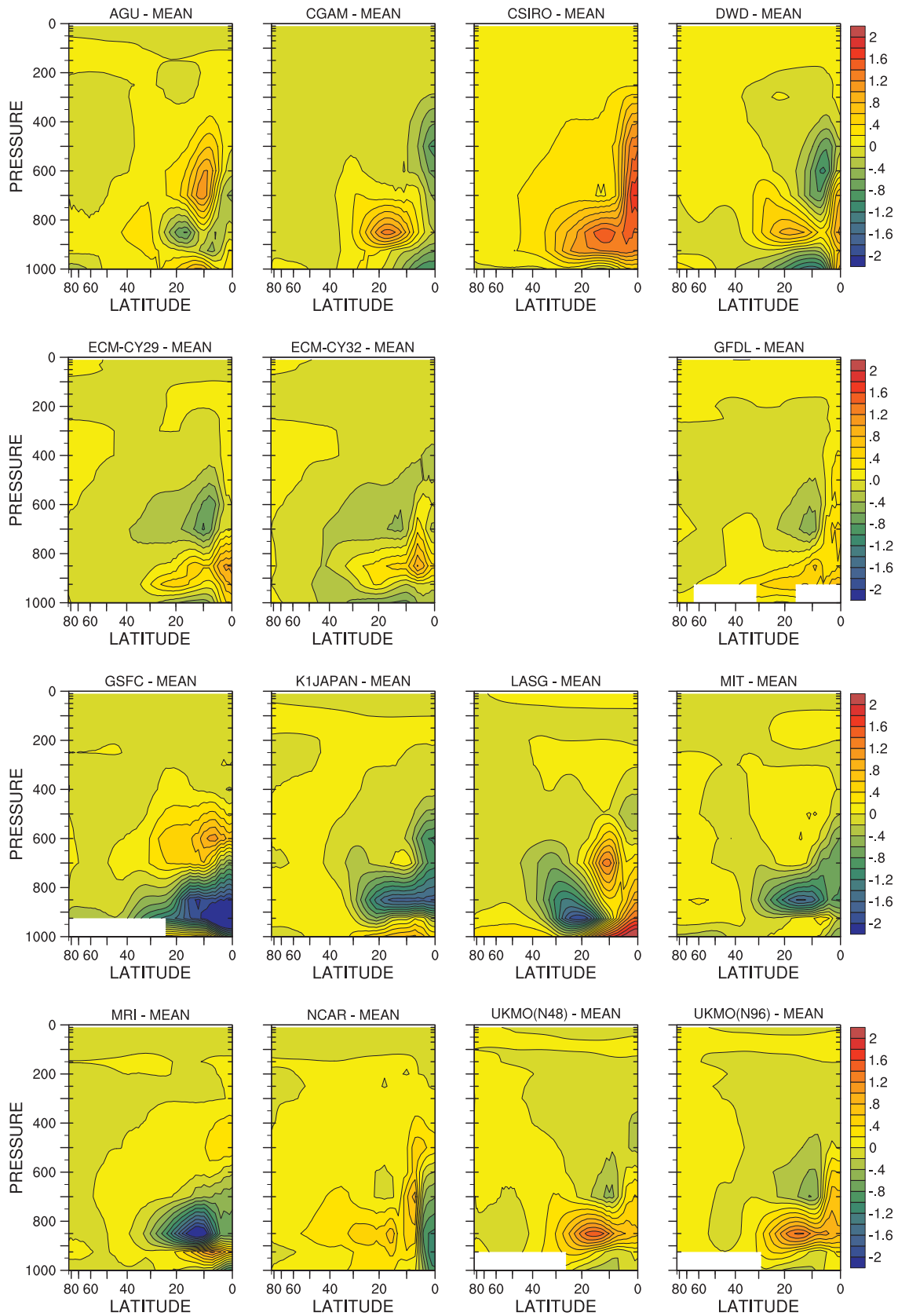
Figure 4.26: Zonal-time average specific humidity (q), individual models minus multi-model mean, g kg^{-1}.
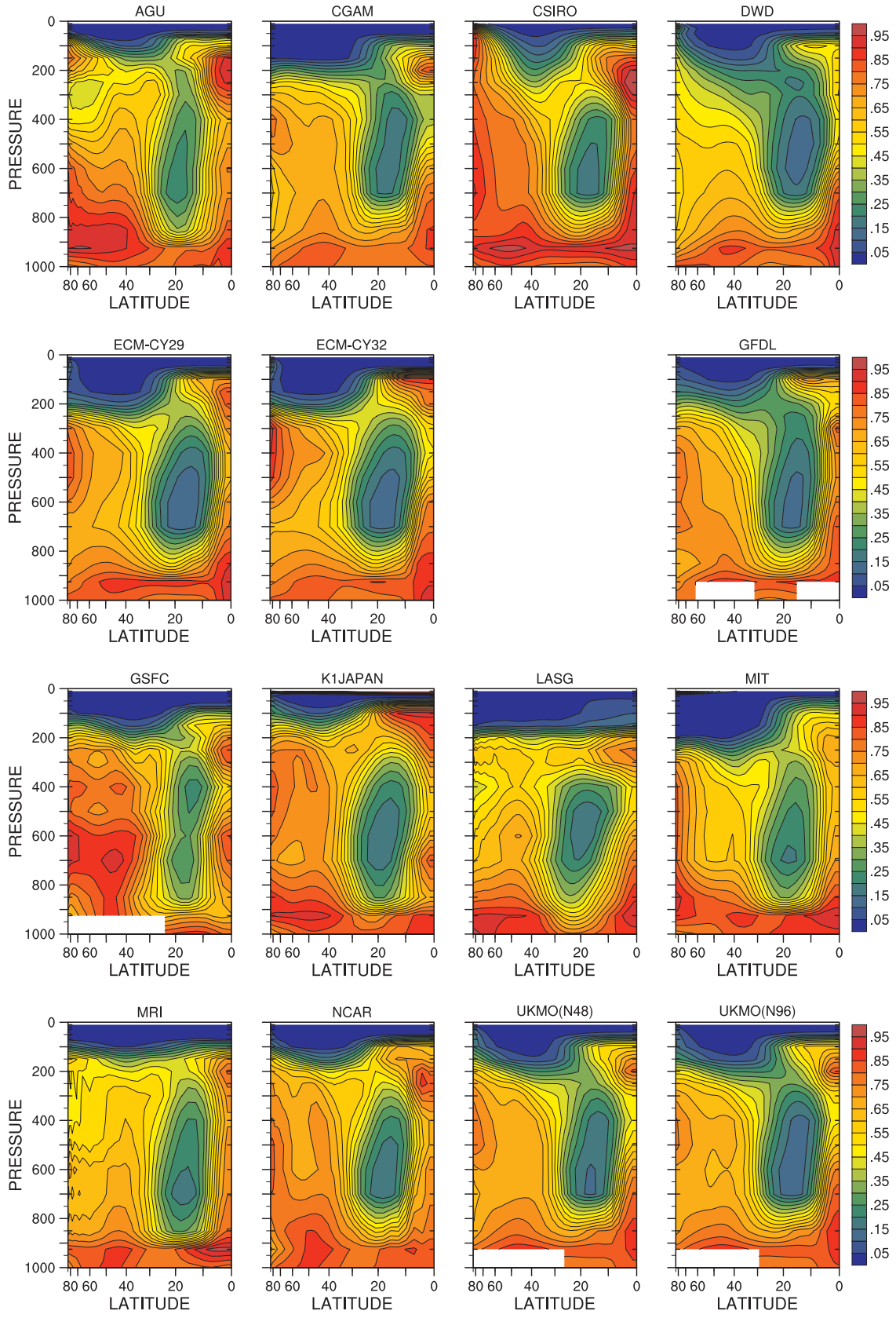
Figure 4.27: Zonal-time average relative humidity (rh) for individual models, fraction.
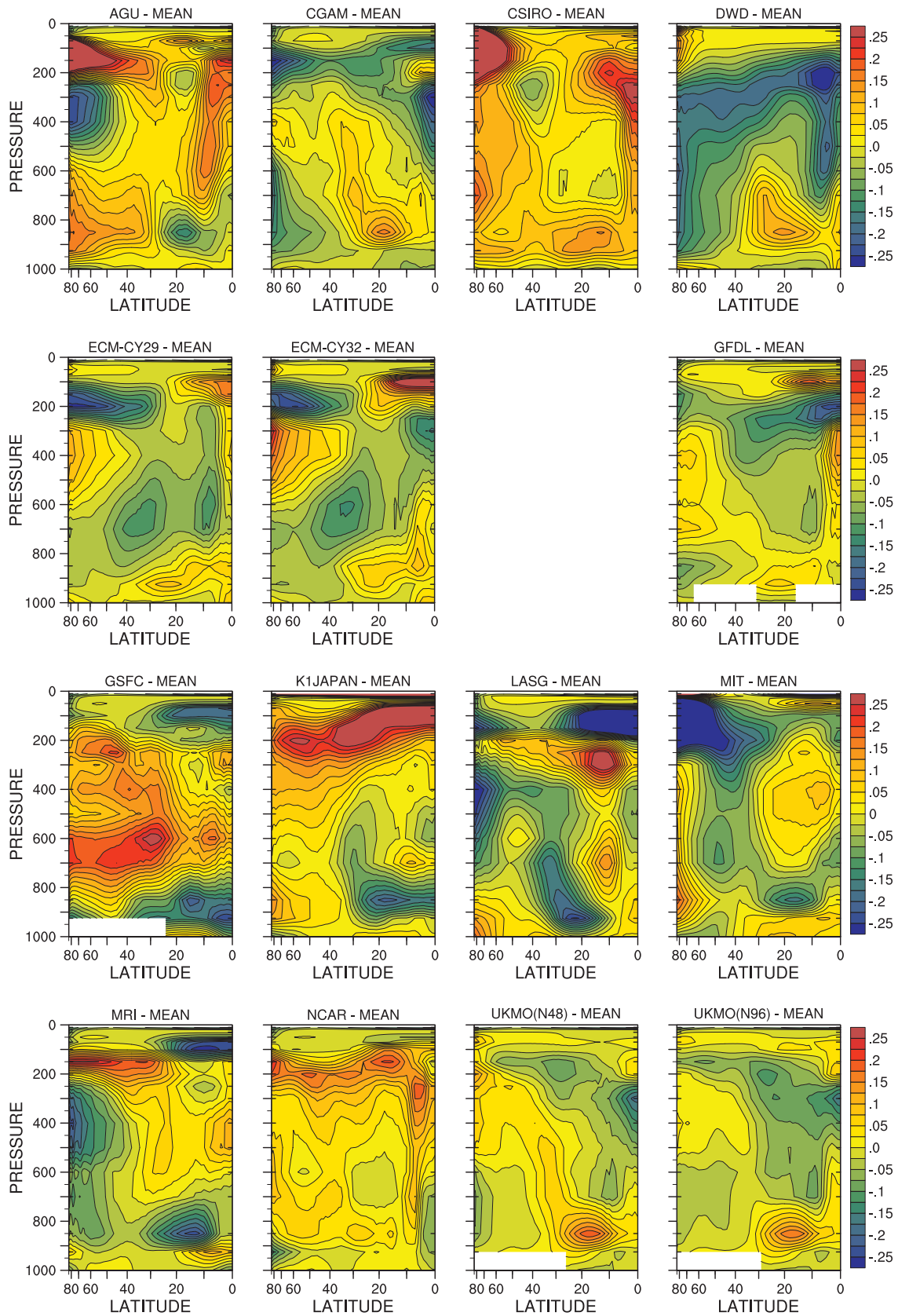
Figure 4.28: Zonal-time average relative humidity (rh), individual models minus multi-model mean, fraction.
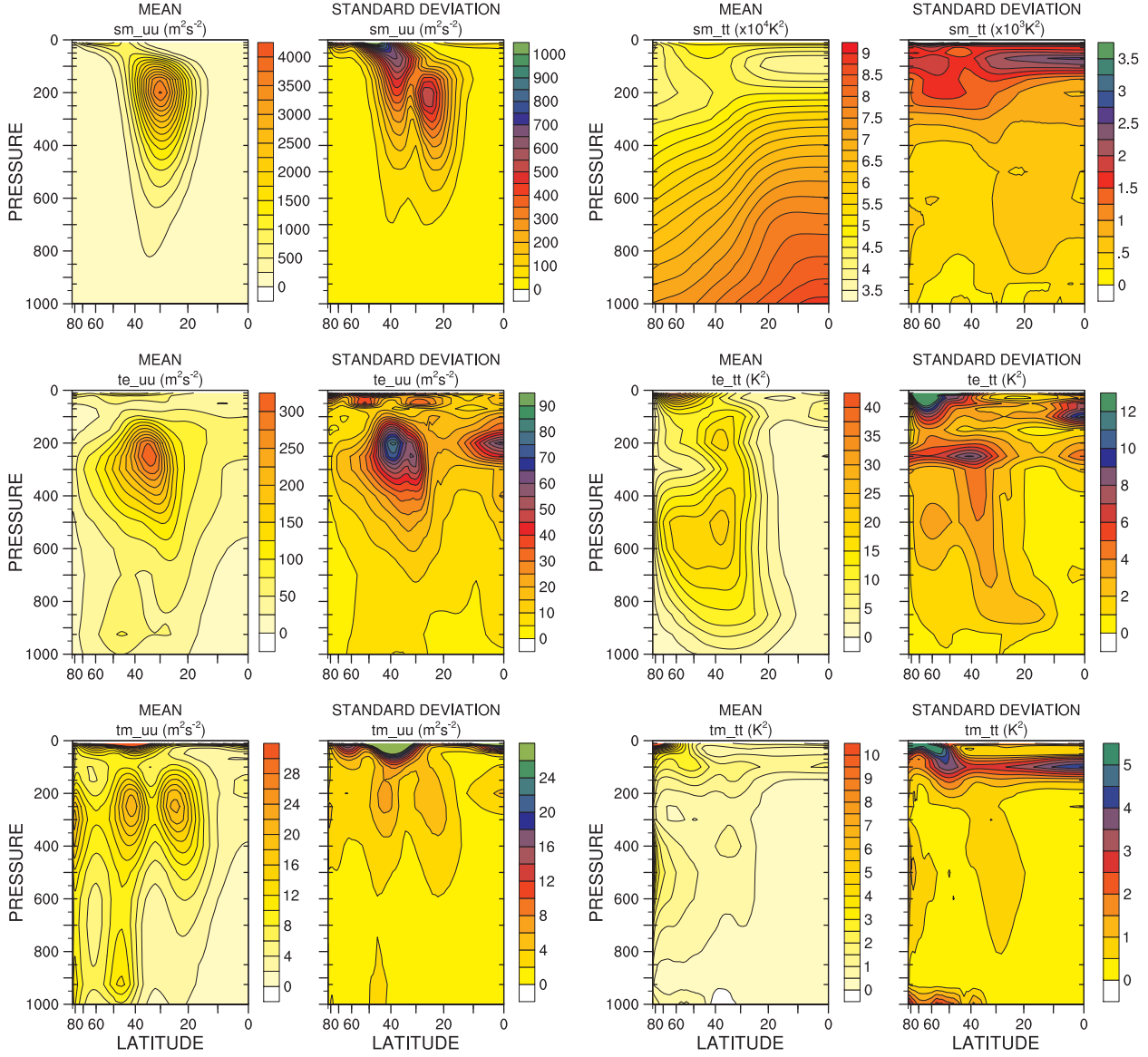
Figure 4.29: Multi-model mean and standard deviation of variances, stationary mean, sm_, transient eddy, te_, and transient mean, tm_, for uu, tt: $[\overline{u}]^2$, $\overline{\left[(u'^*)^2\right]}$ and $\overline{[u]'^2}$; $\left[\overline{T}\right]^2$, $\overline{\left[(T'^*)^2\right]}$ and $\overline{[T]'^2}$.

72
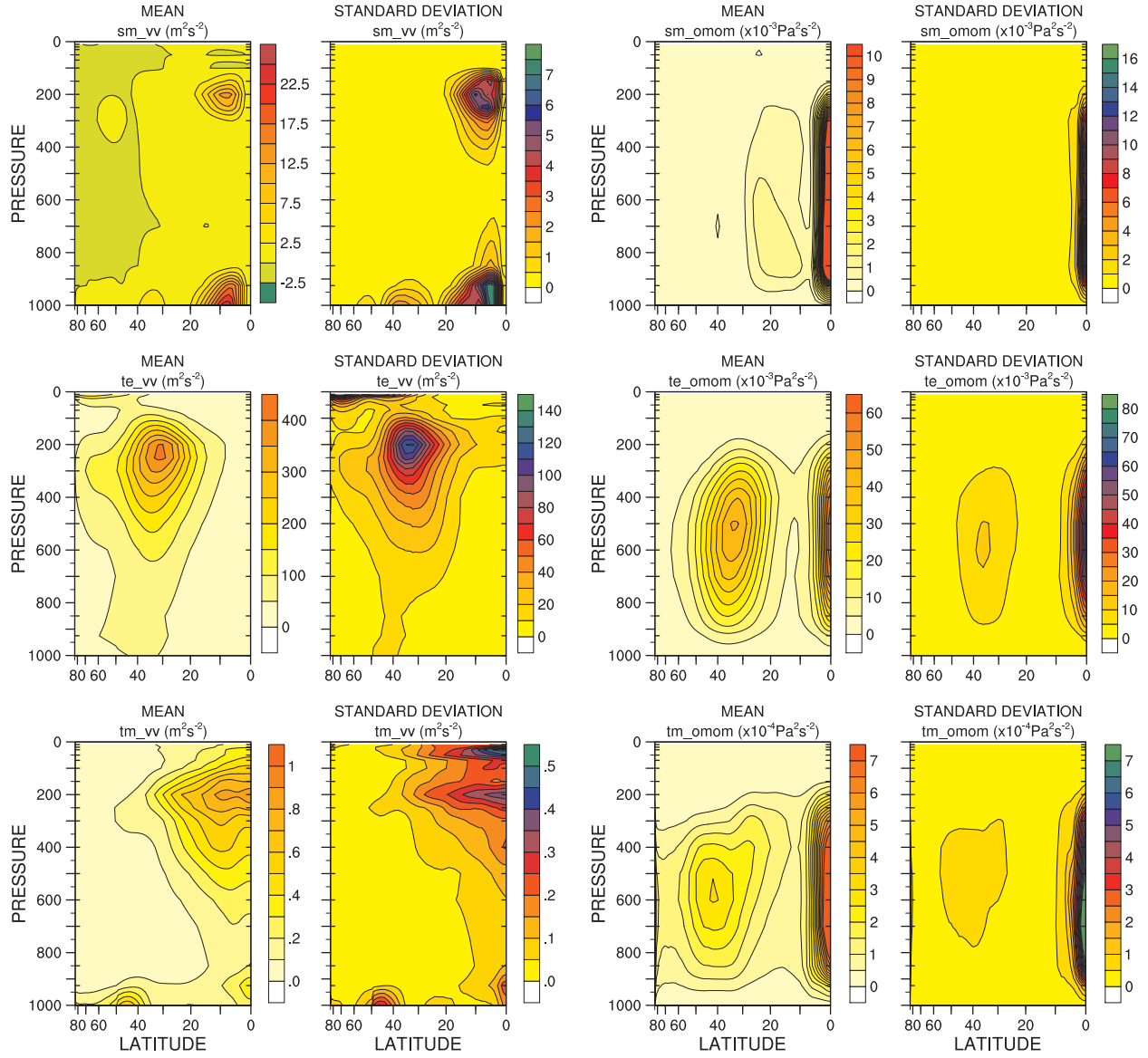
Figure 4.30: Multi-model mean and standard deviation of variances, stationary mean, sm_, transient eddy, te_, and transient mean, tm_, for vv, omom: $[\overline{v}]^2$, $\overline{[(v'^*)^2]}$ and $\overline{[v]'}^2$; $[\overline{\omega}]^2$, $\overline{[(\omega'^*)^2]}$ and $\overline{[\omega]'}^2$
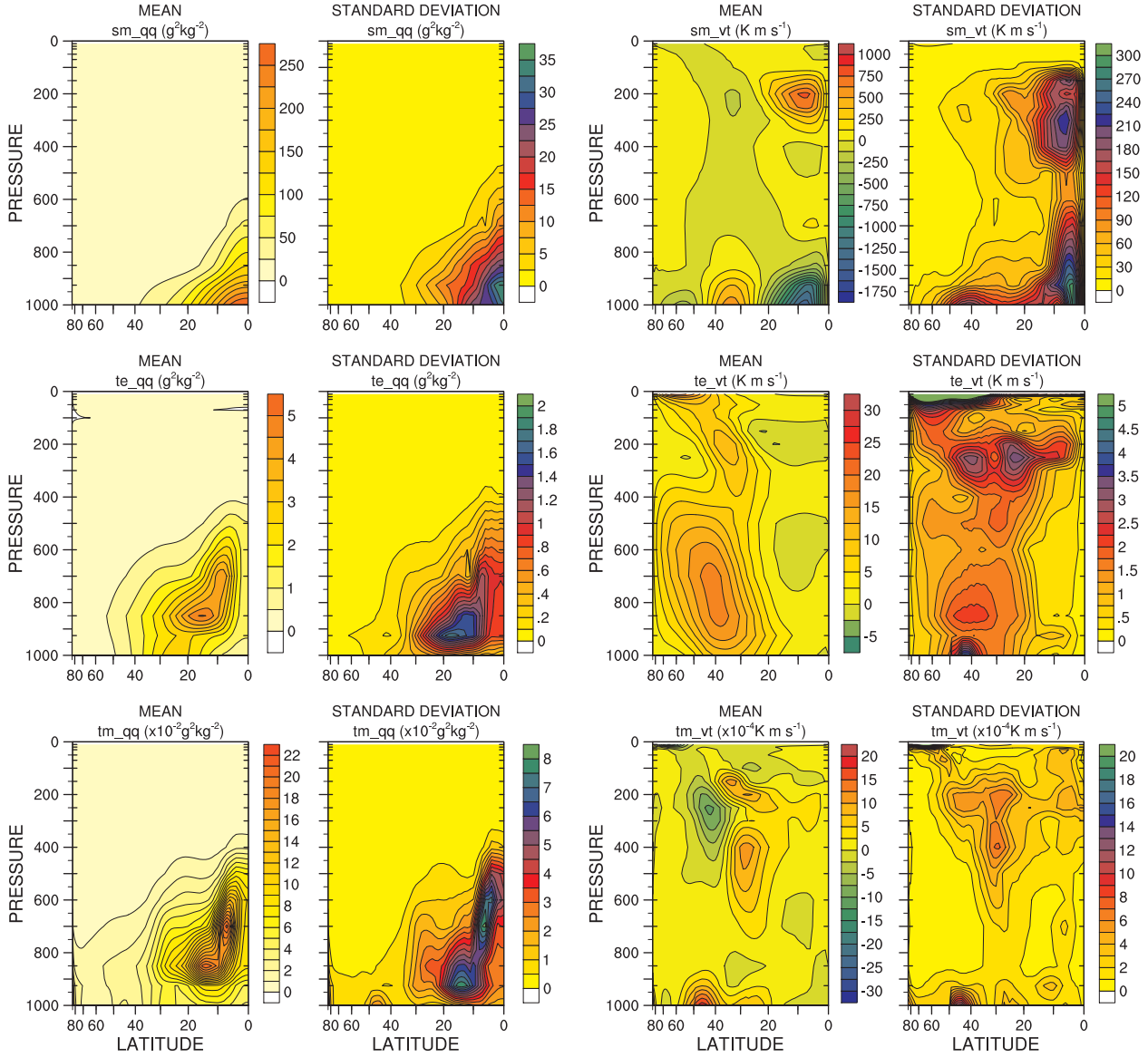
Figure 4.31: Multi-model mean and standard deviation of (co-)variances, stationary mean, sm_, transient eddy, te_, and transient mean, tm_, for qq, vt: $\left[\overline{q}\right]^2$, $\overline{\left[(q'^*)^2\right]}$ and $\overline{[q]'^2}$; $[\overline{v}]\left[\overline{T}\right]$, $\overline{[v'^*T'^*]}$, $\overline{[v]'[T]'}$.
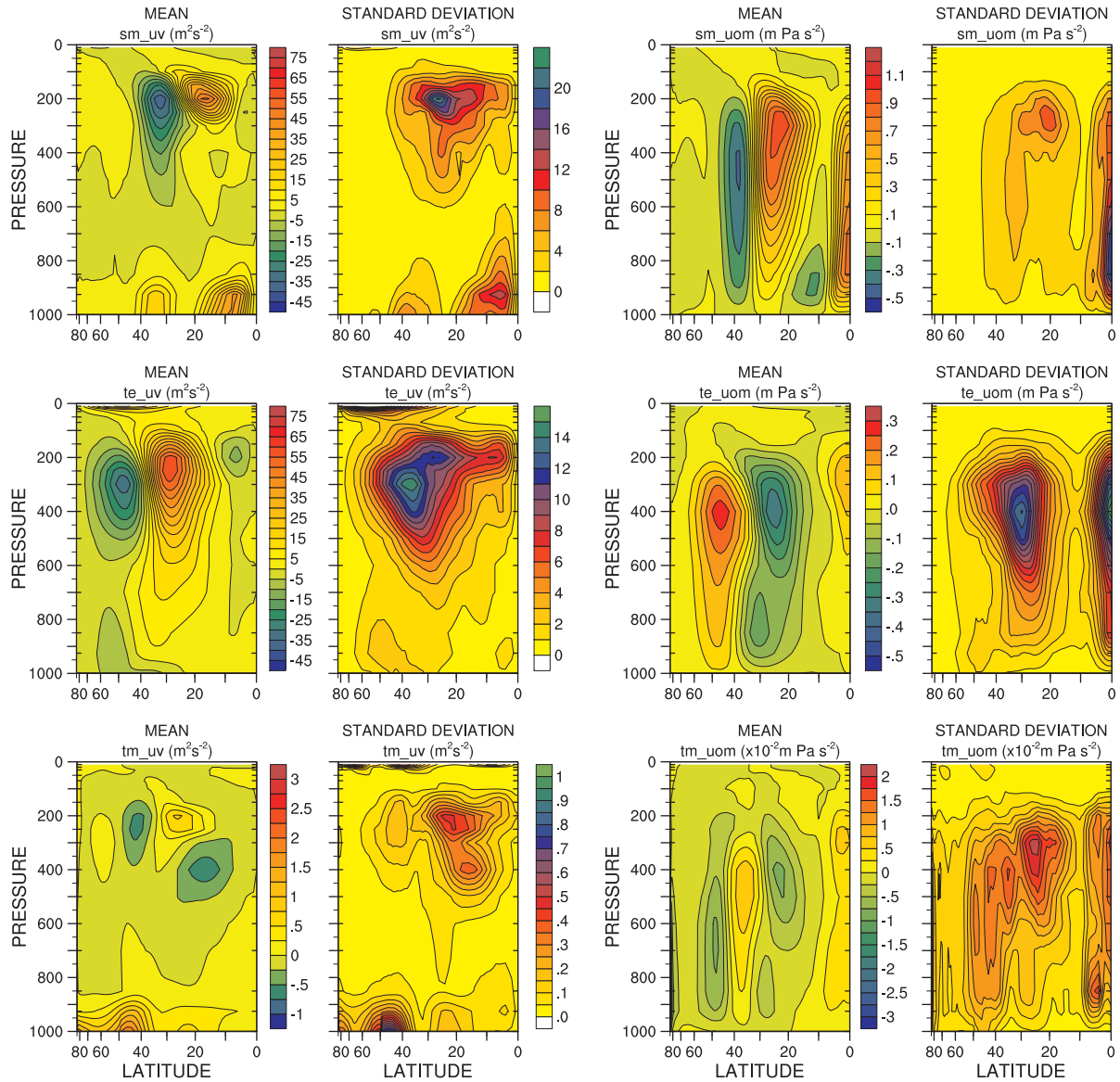
Figure 4.32: Multi-model mean and standard deviation of co-variances, stationary mean, sm_, transient eddy, te_, and transient mean, tm_, for uv, uom: $[\overline{u}]\,[\overline{v}]$, $\overline{[u'^* v'^*]}$ and $\overline{[u]'\,[v]'}$; $[\overline{u}]\,[\overline{\omega}]$, $\overline{[u'^* \omega'^*]}$ and $\overline{[u]'\,[\omega]'}$.
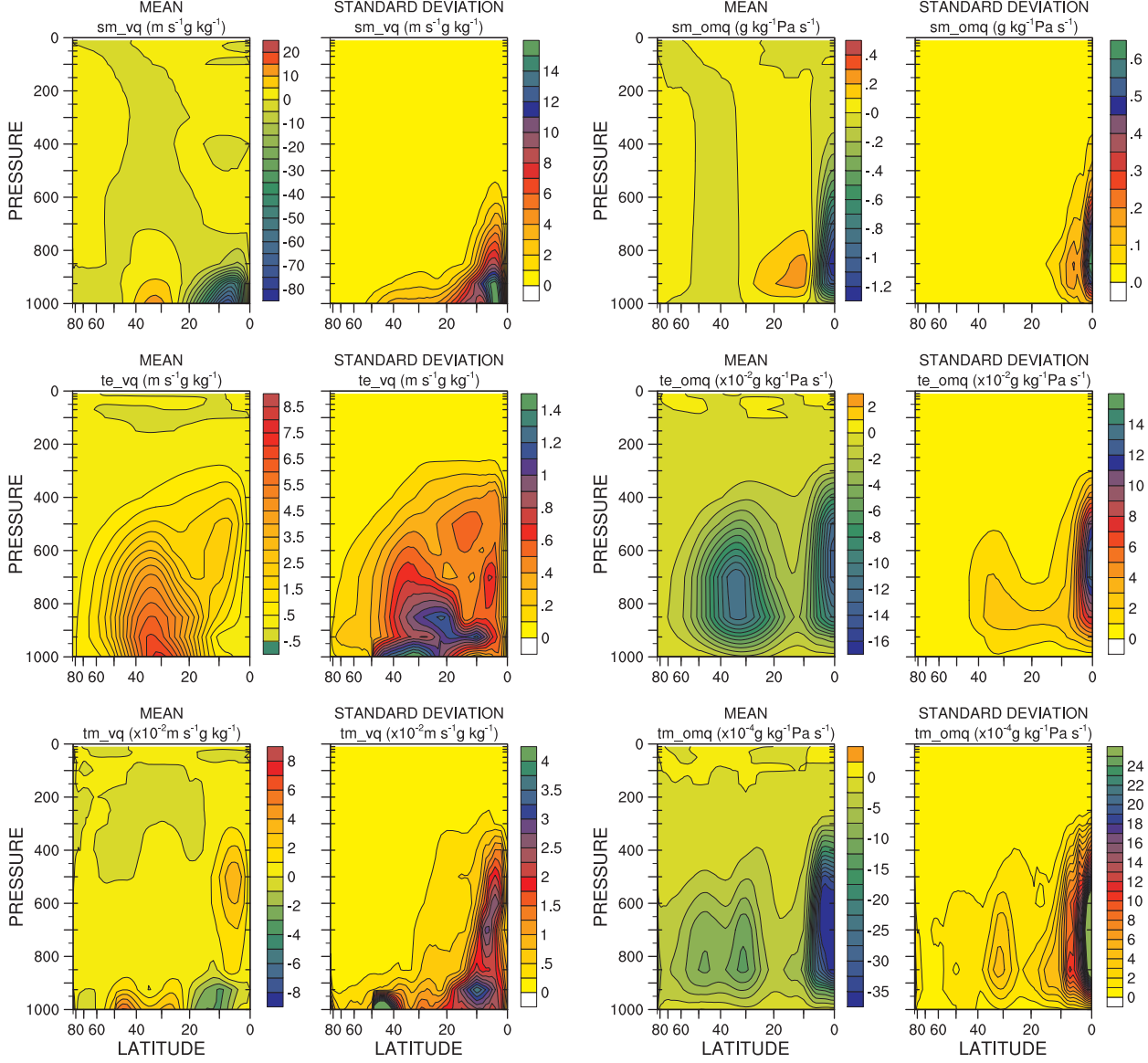
Figure 4.33: Multi-model mean and standard deviation of co-variances, stationary mean, sm_, transient eddy, te_, and transient mean, tm_, for vq, omq: $[\overline{v}]\,[\overline{q}]$, $\overline{[v'^{*}q'^{*}]}$ and $\overline{[v]'\,[q]'}$; $[\overline{\omega}]\,[\overline{q}]$, $\overline{[\omega'^{*}q'^{*}]}$ and $\overline{[\omega]'\,[q]'}$.

76
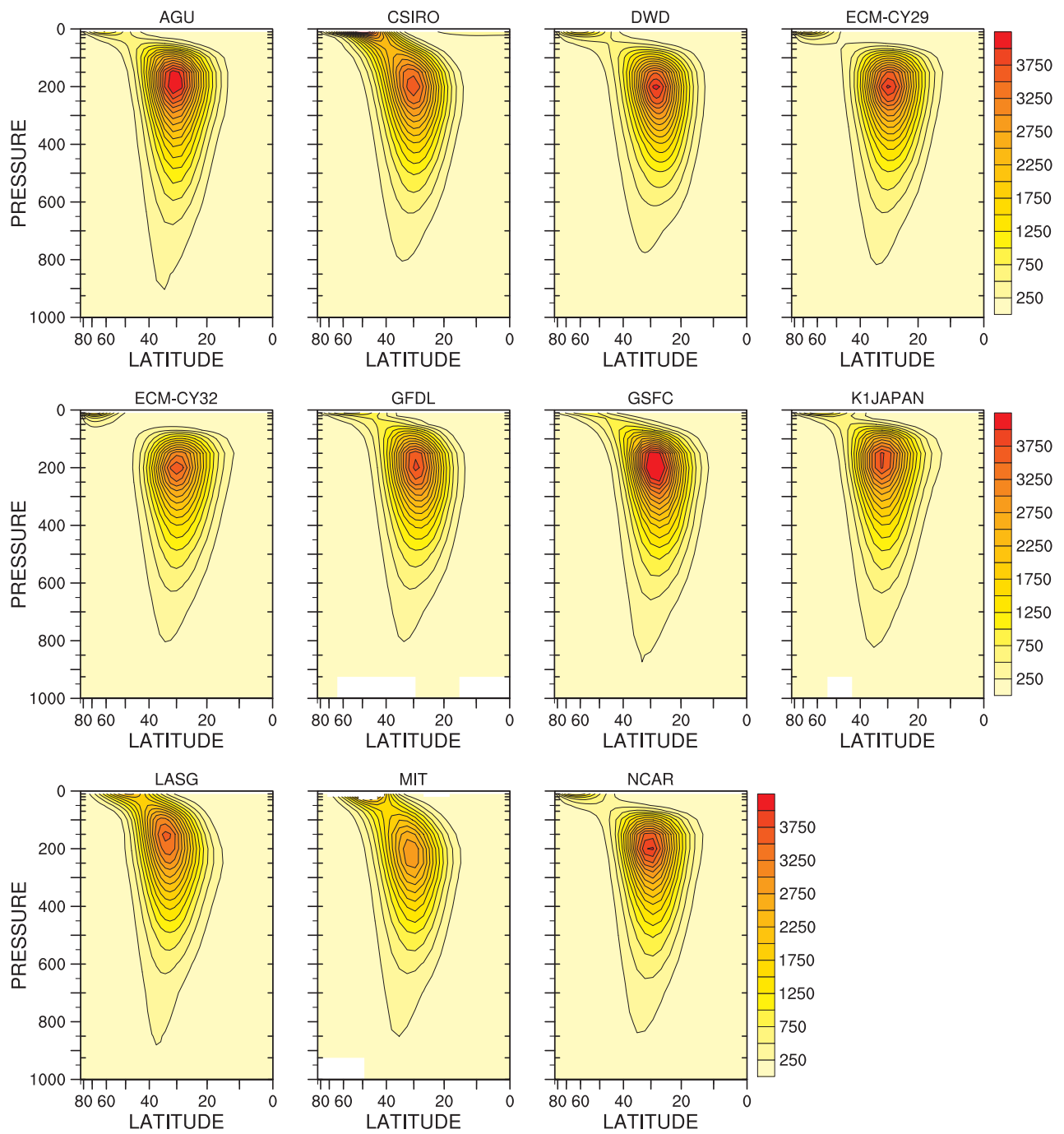
Figure 4.34: Individual model u variance, stationary mean, sm_uu, $[\overline{u}]^2$, m^2 s^{-2}.
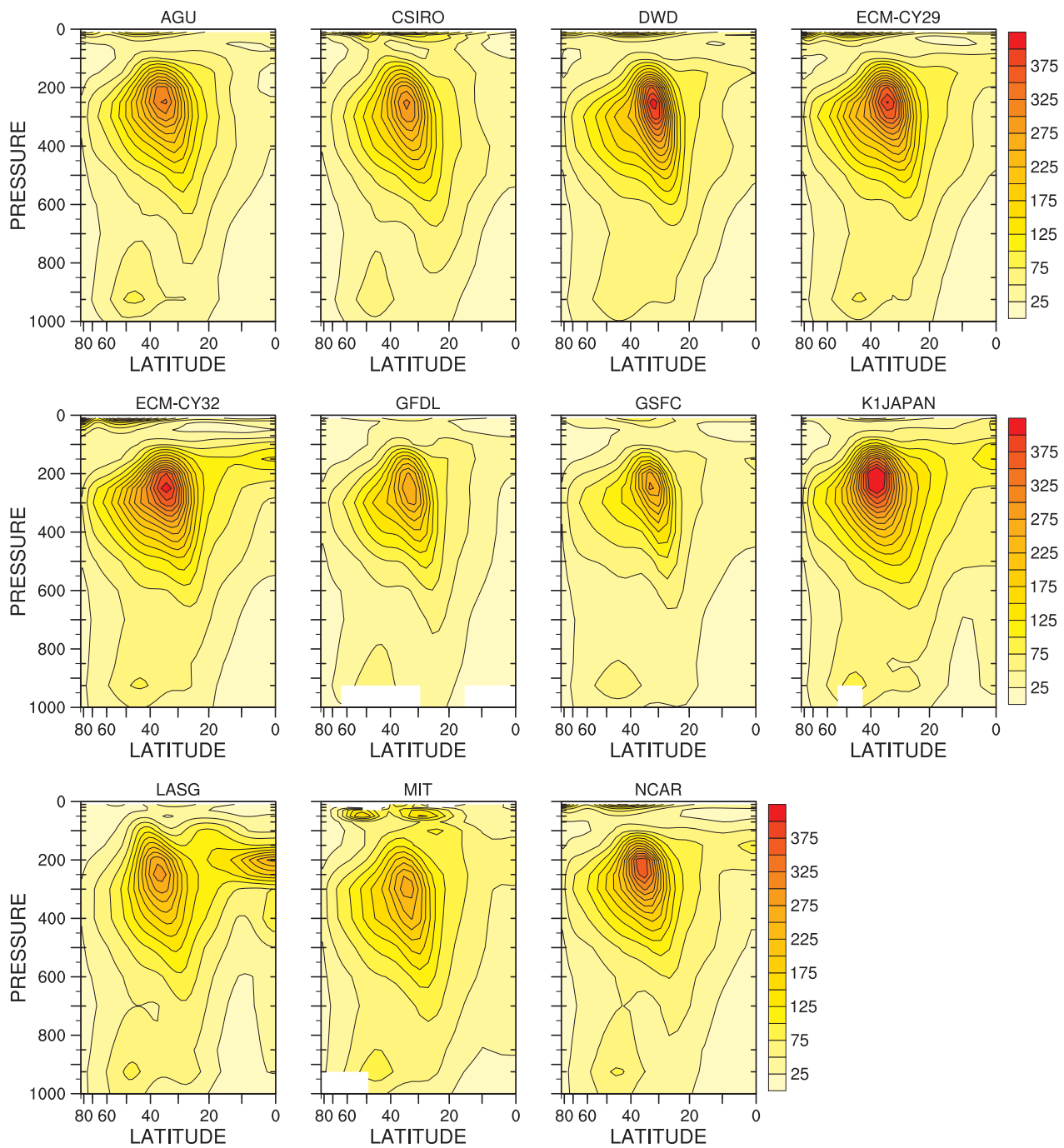
Figure 4.35: Individual model u variance, transient eddy, te_uu, $\overline{\left[(u'^*)^2\right]}$, m^2 s^{-2}.
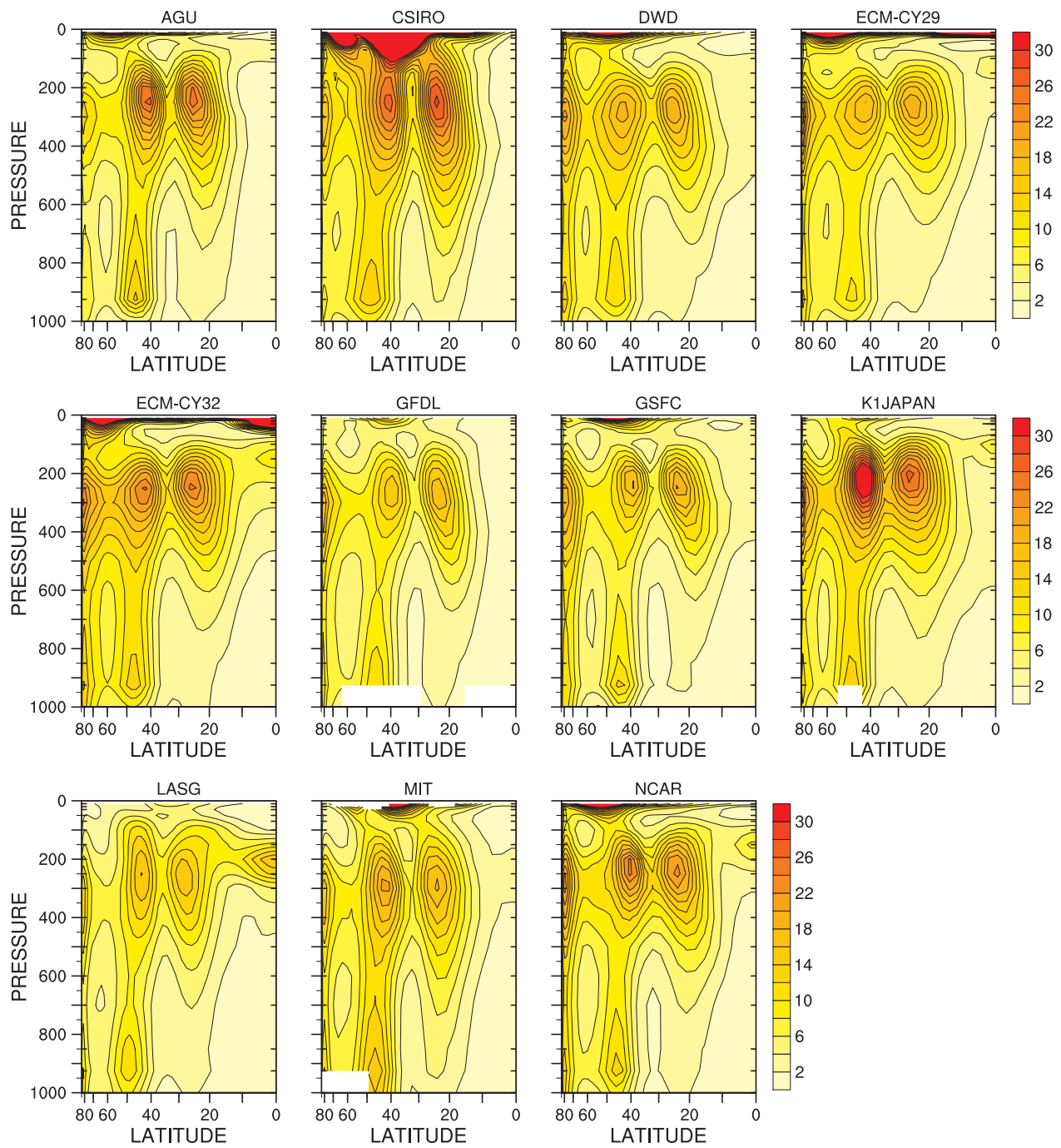
Figure 4.36: Individual model u variance, transient mean, tm_uu, $\overline{[u]'^2}$, m^2 s^{-2}.
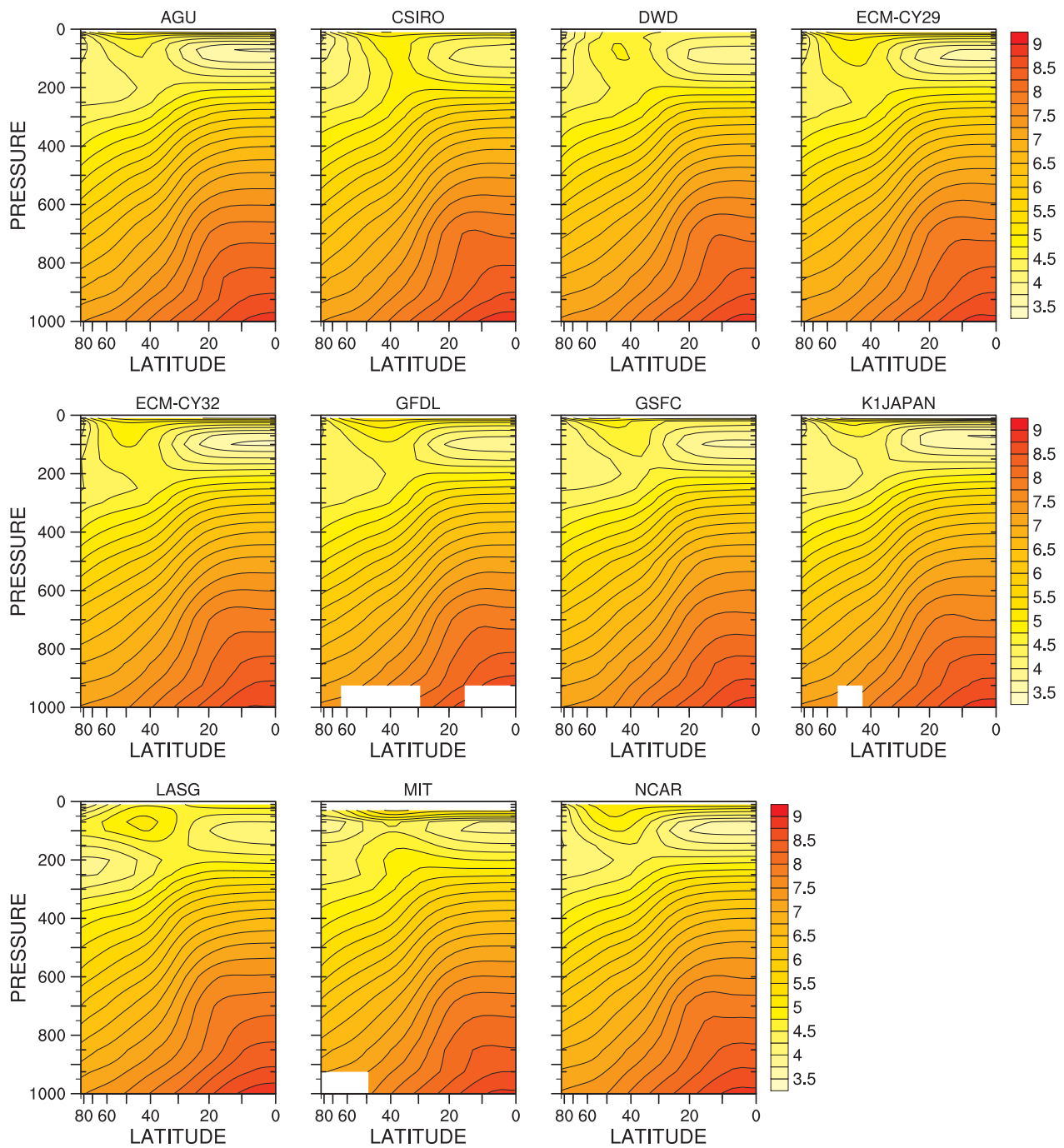
Figure 4.37: Individual model T variance, stationary mean, sm_tt, $\left[\overline{T}\right]^2$, $\times 10^4$ K^2.
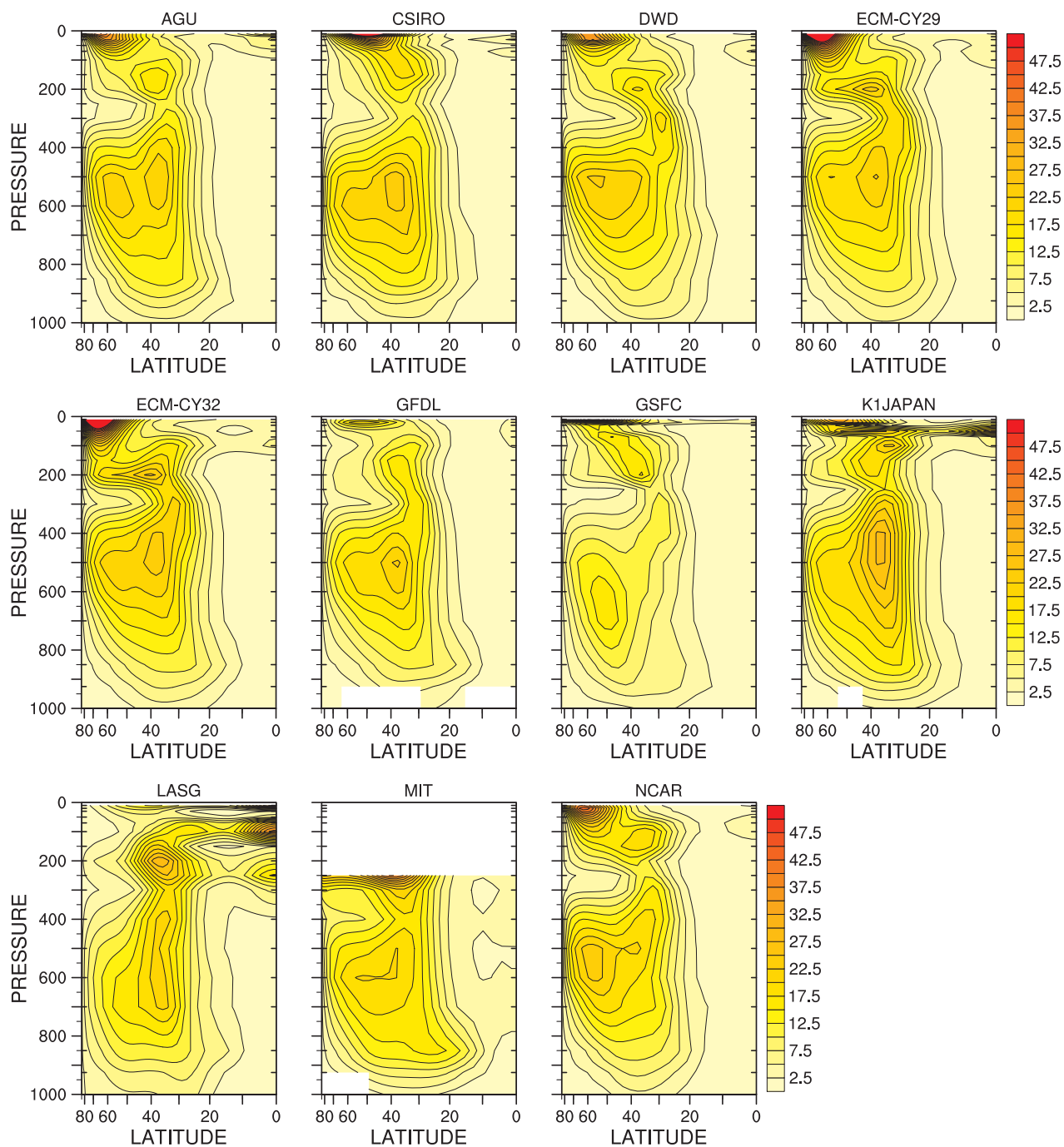
Figure 4.38: Individual model T variance, transient eddy, te_tt, $\overline{\left[(T'^*)^2\right]}$, K^2.
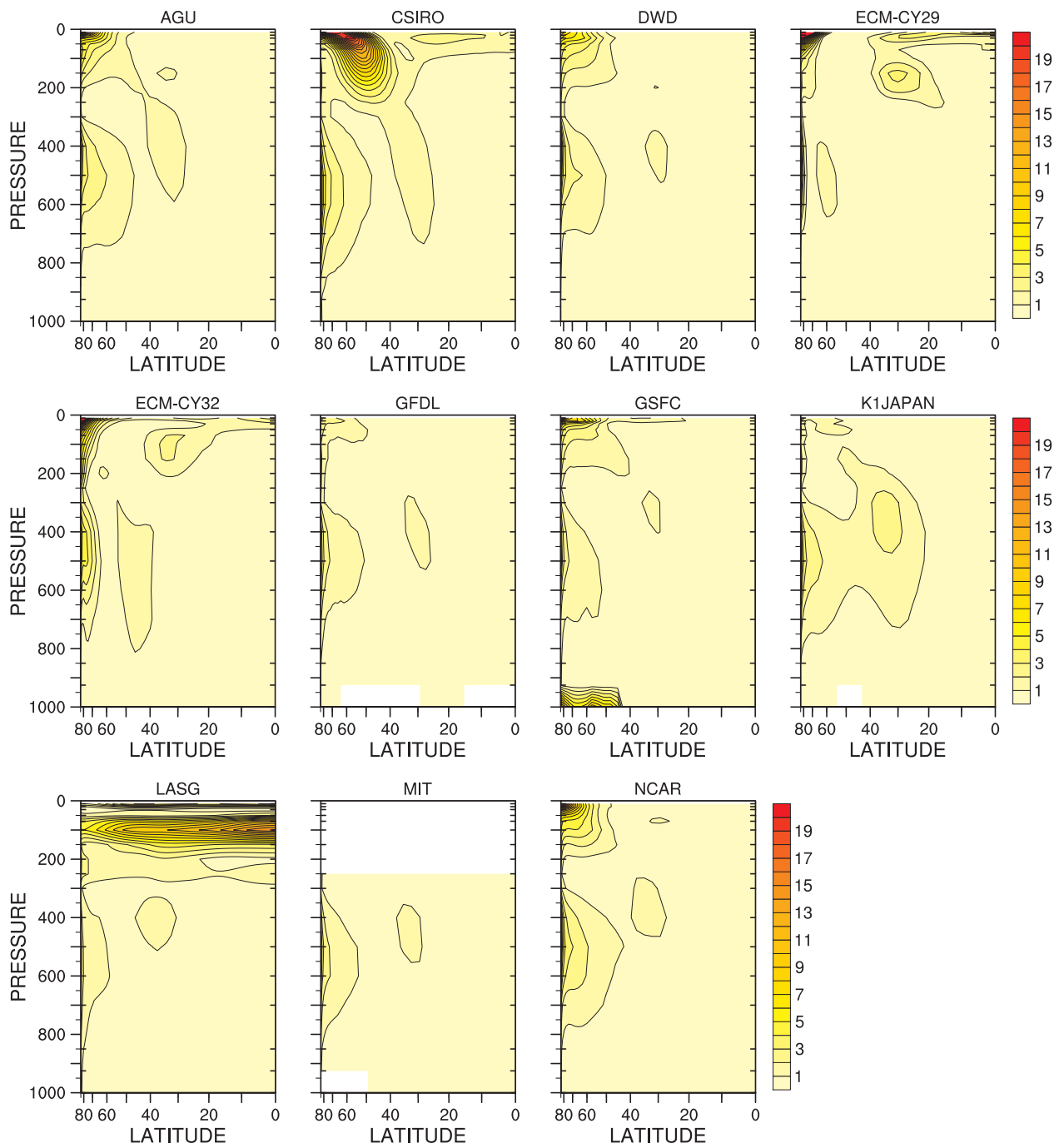
Figure 4.39: Individual model T variance, transient mean, tm_tt, $\overline{[T]'^2}$, K^2.
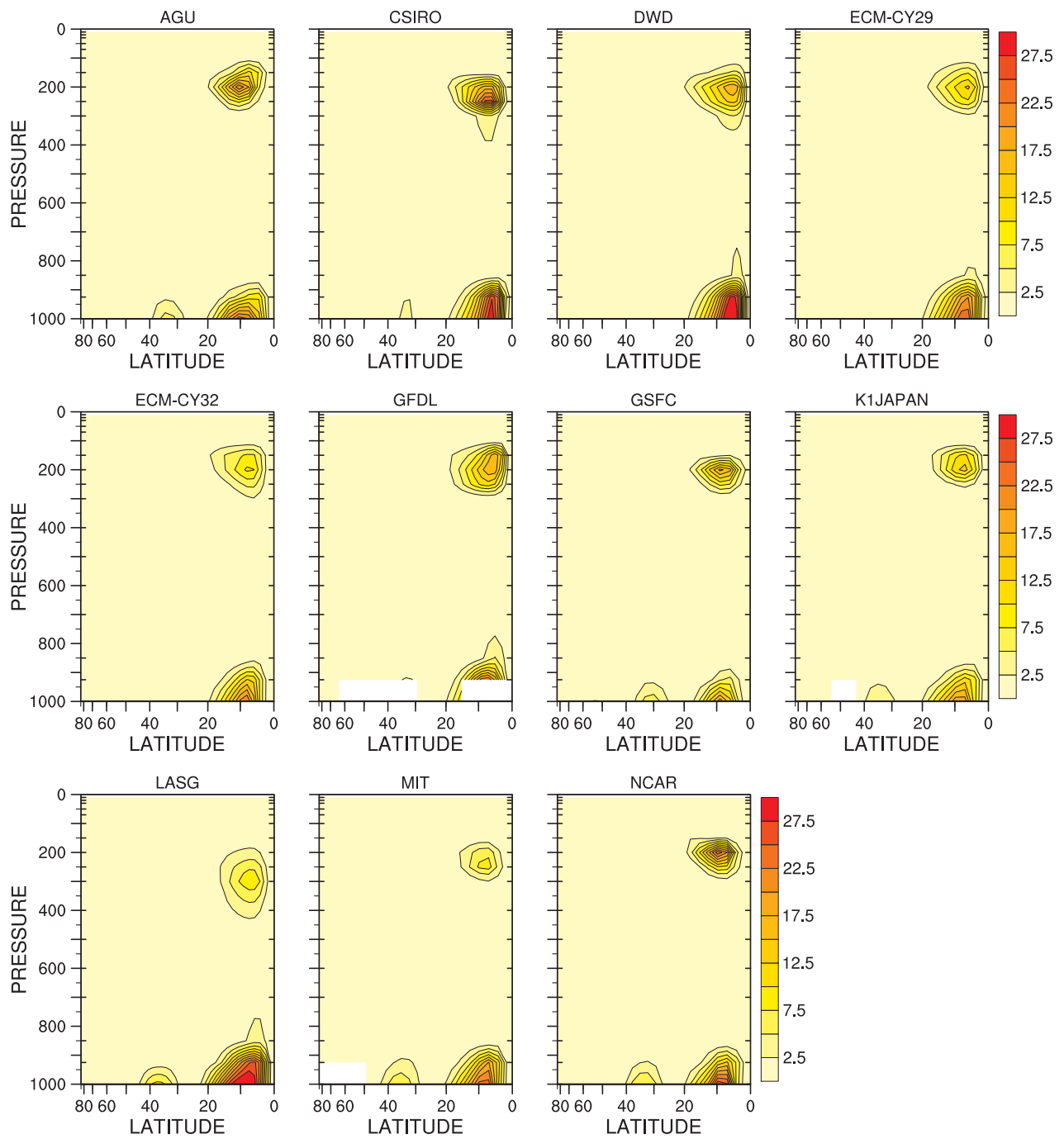
Figure 4.40: Individual model v variance, stationary mean, sm_vv, $[\overline{v}]^2$, m^2 s^{-2}.
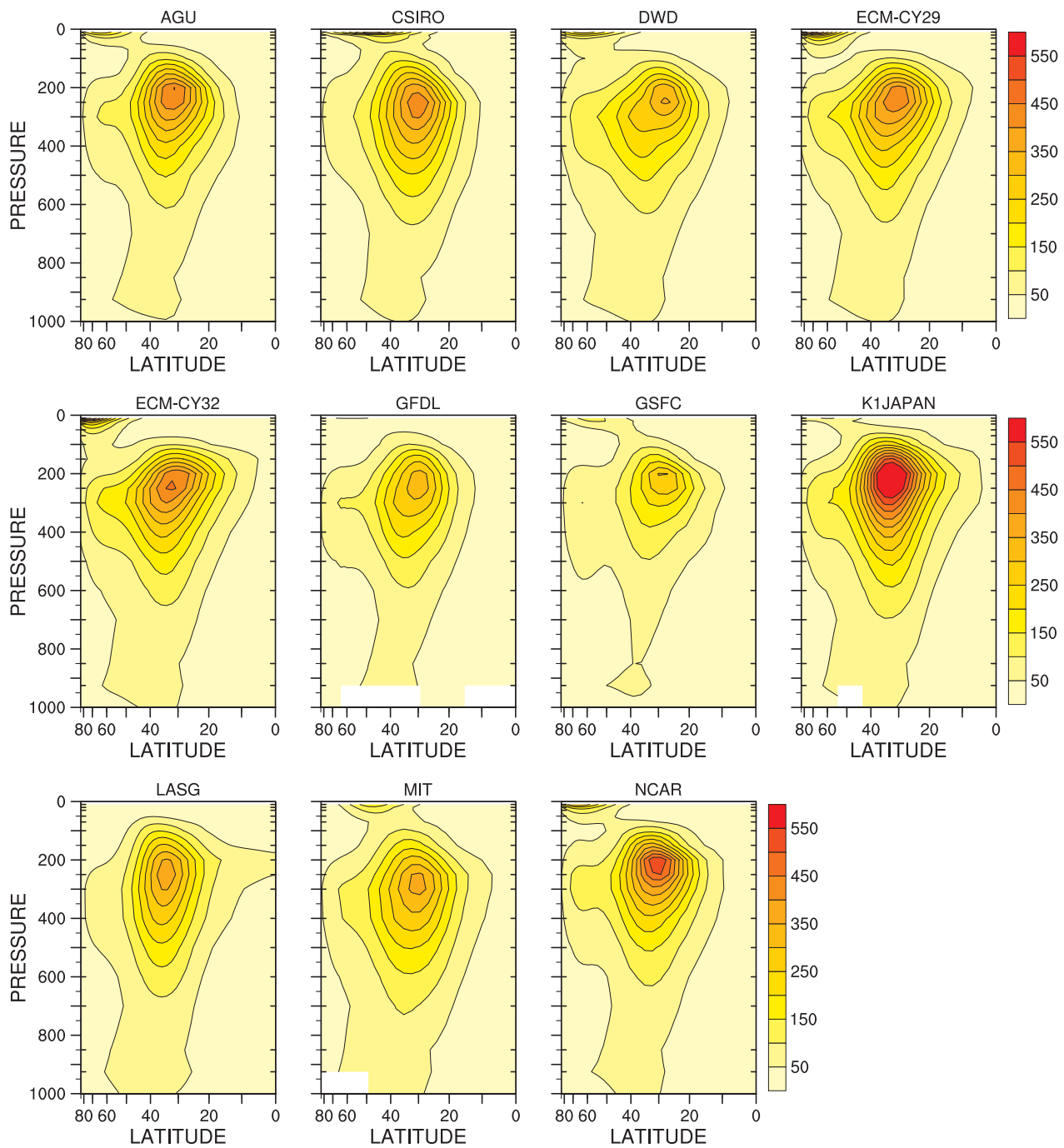
Figure 4.41: Individual model v variance, transient eddy, te_vv, $\overline{\left[(v'^{*})^{2}\right]}$, m^2 s^{-2}.
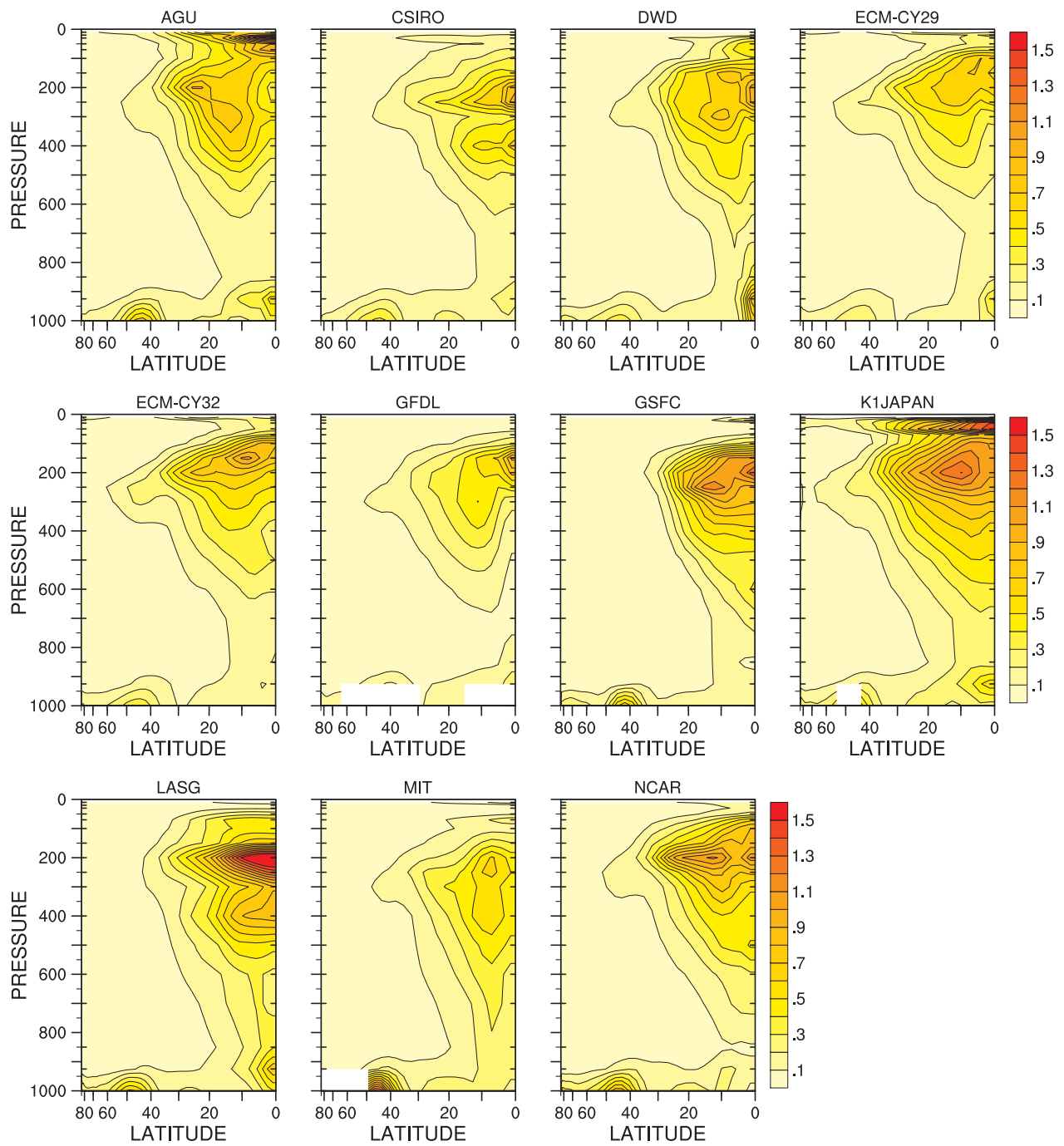
Figure 4.42: Individual model v variance, transient mean, tm_vv, $\overline{[v]'^2}$, m^2 s^{-2}.
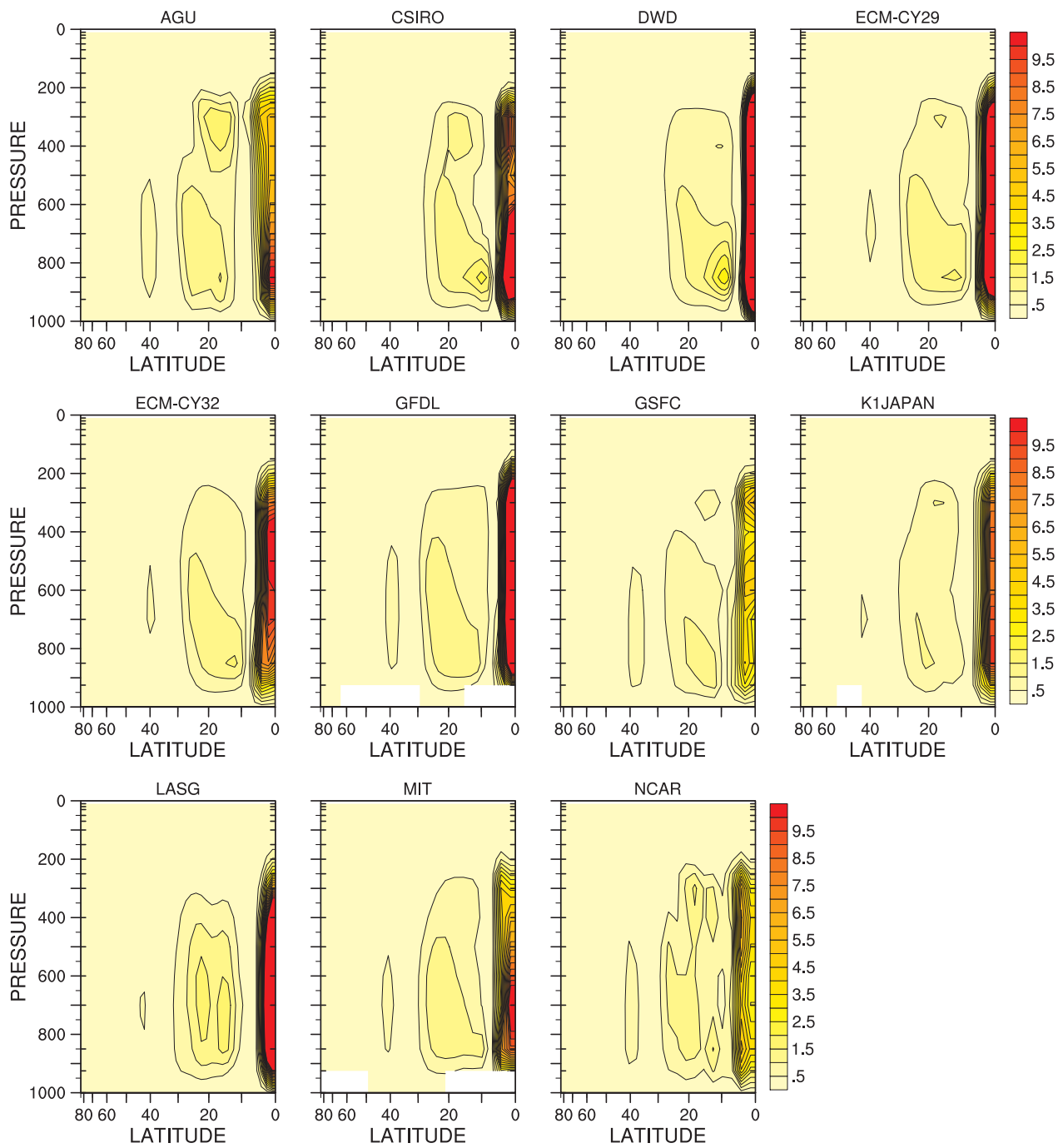
Figure 4.43: Individual model ω variance, stationary mean, sm_omom, $[\overline{\omega}]^2$, $\times 10^{-3}$ Pa^2 s^{-2}.
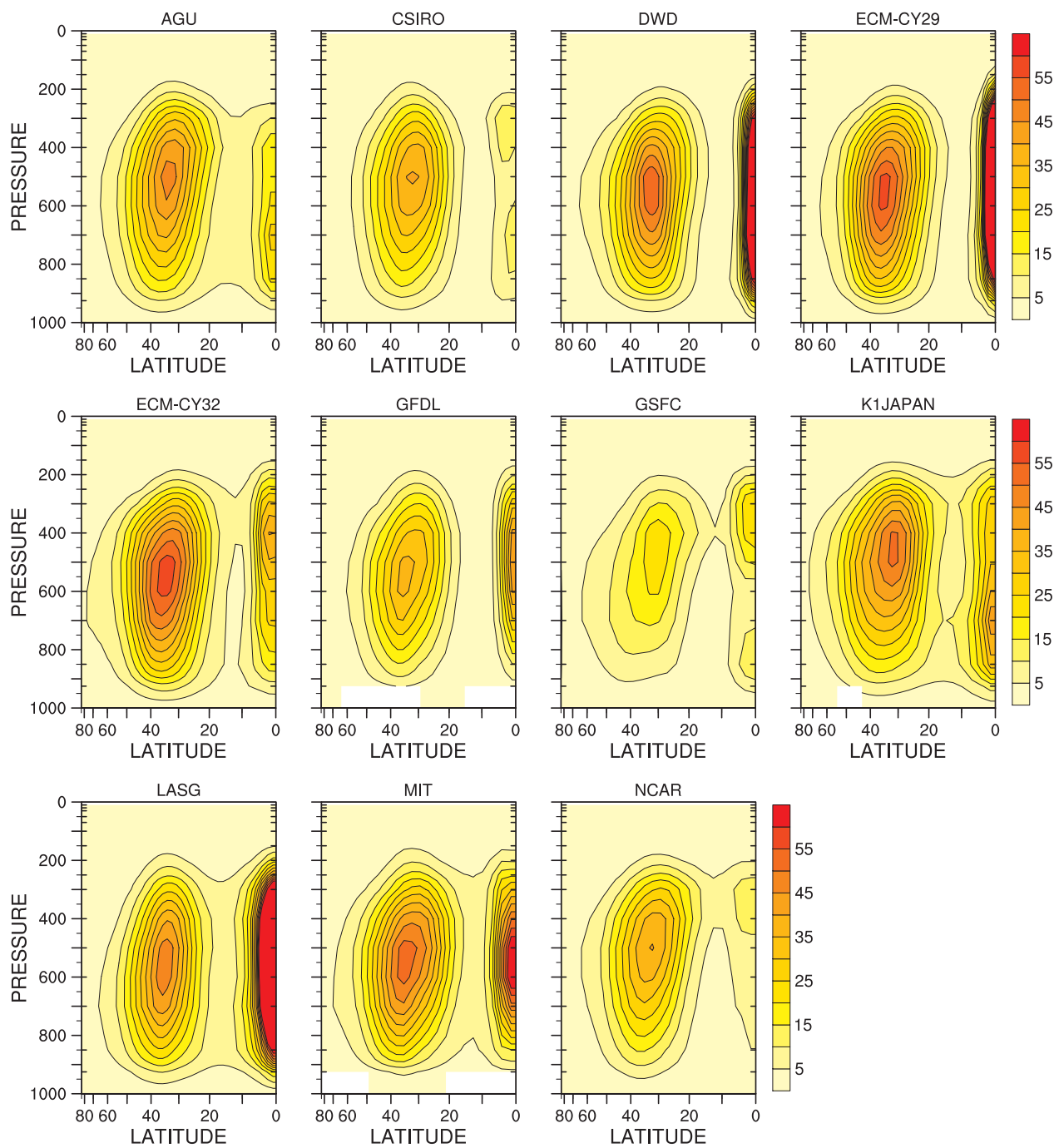
Figure 4.44: Individual model ω variance, transient eddy, te_omom, $\overline{\left[(\omega'^*)^2\right]}$, $\times 10^{-3}$ Pa^2 s^{-2}.
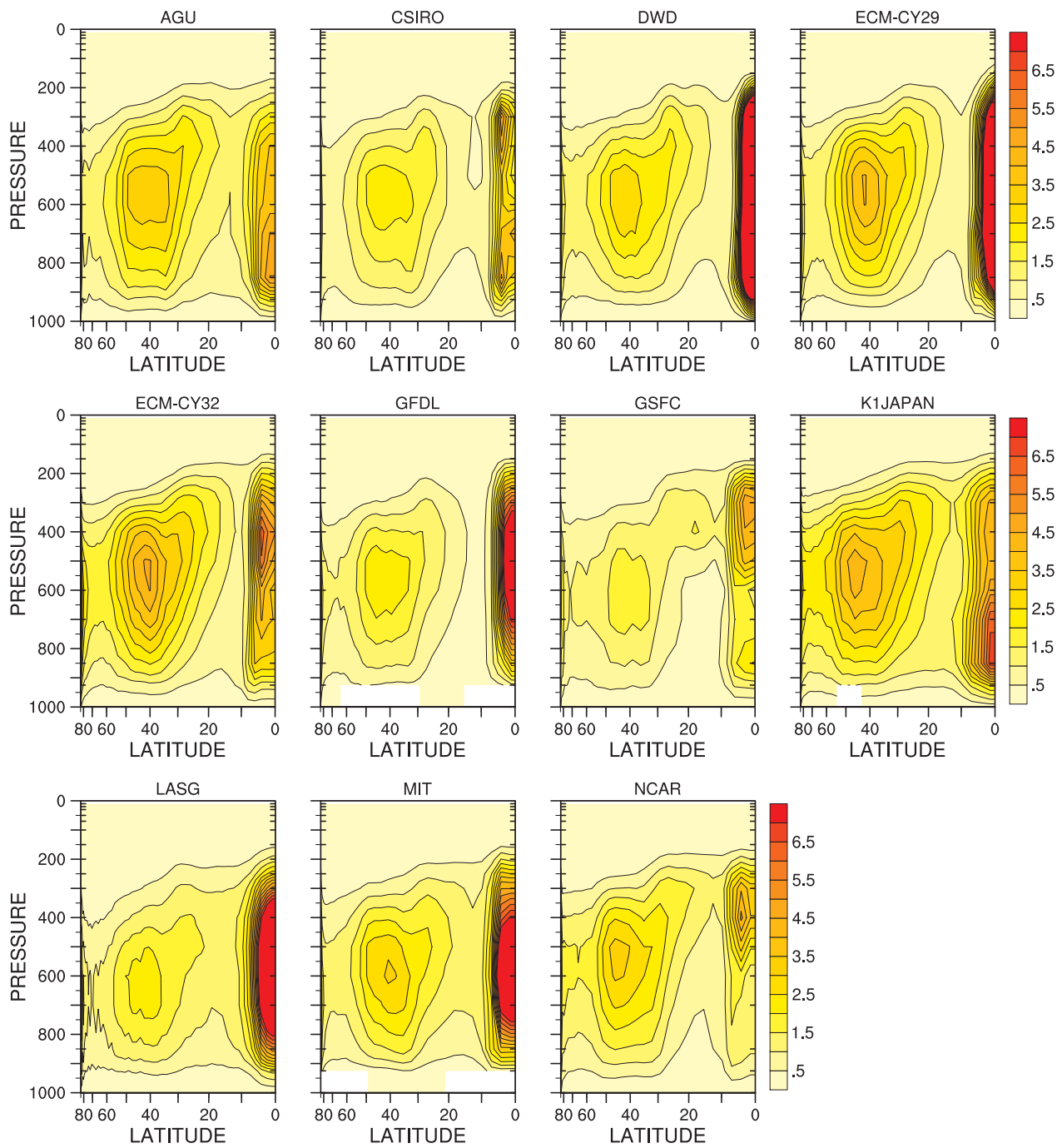
Figure 4.45: Individual model ω variance, transient mean, tm_omom, $\overline{[\omega]'^2}$, $\times 10^{-4}$ Pa^2 s^{-2}.
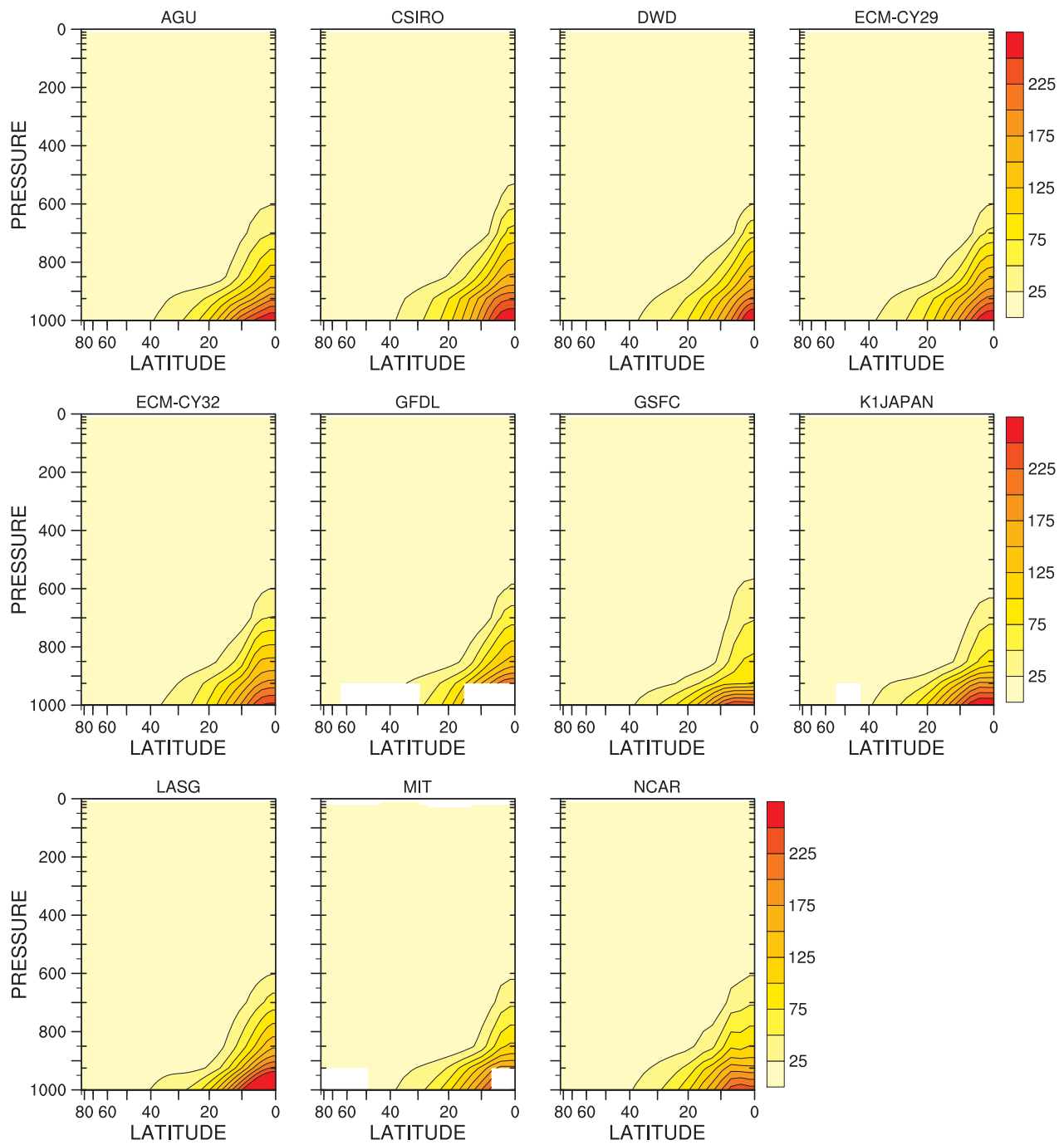
Figure 4.46: Individual model q variance, stationary mean, sm_qq, $[\overline{q}]^2$, $\mathrm{g}^2\ \mathrm{kg}^{-2}$.
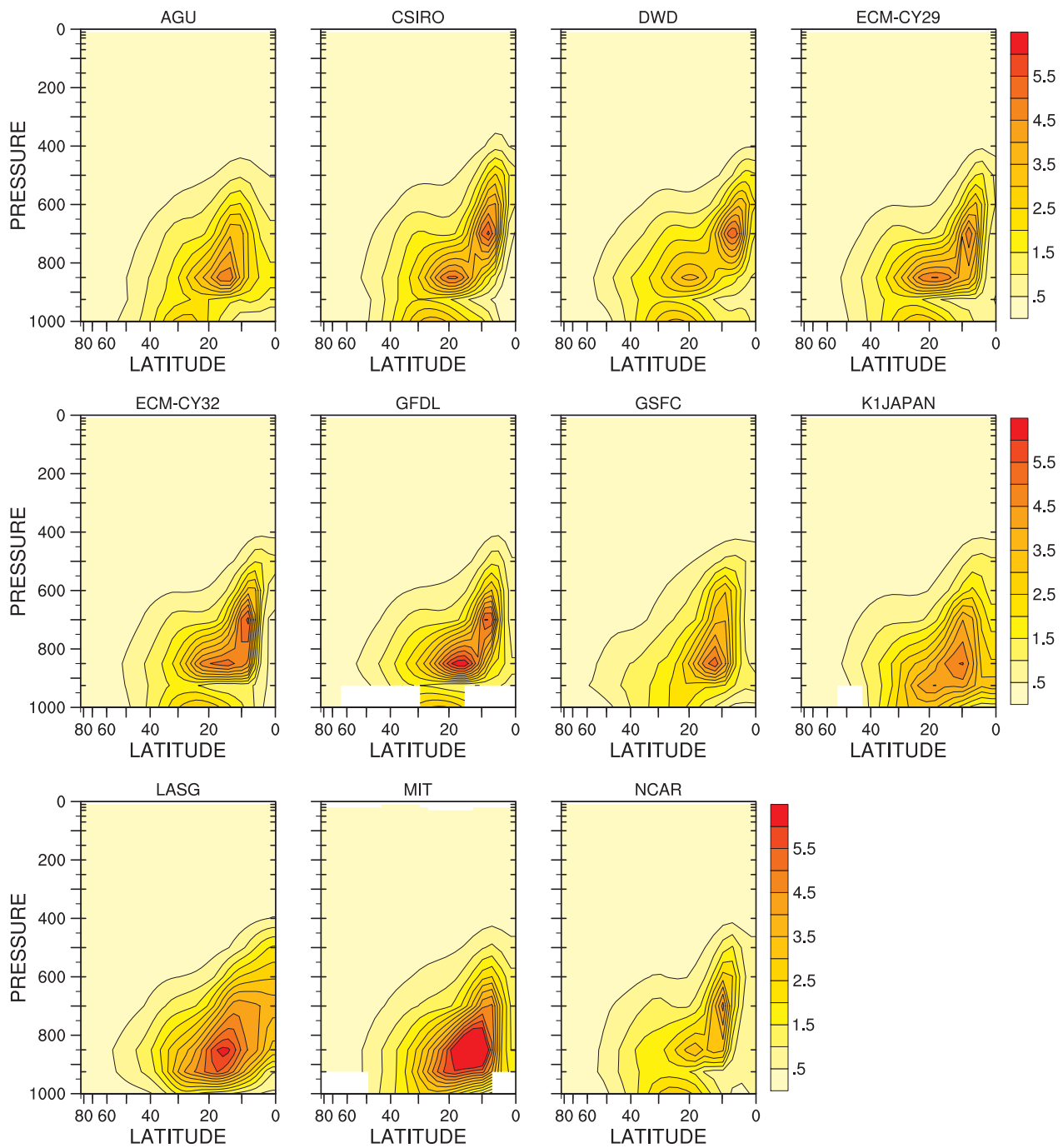
Figure 4.47: Individual model q variance, transient eddy, te_qq, $\overline{\left[(q'*)^2\right]}$, g^2 kg^{-2}.
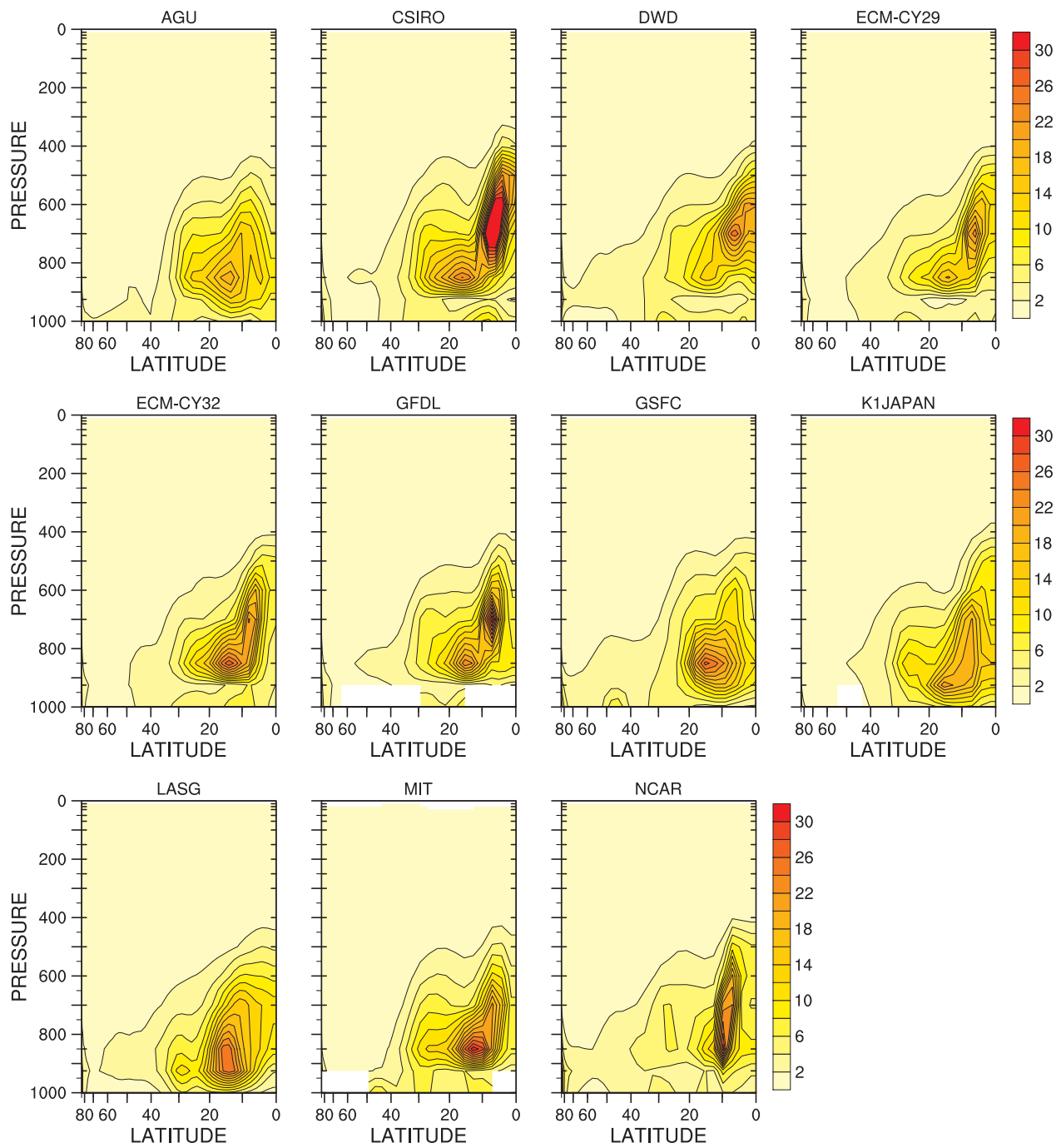
Figure 4.48: Individual model q variance, mean meridional, tm_qq, $\overline{[q]'^2}$, $\times 10^{-2} g^2$ kg^{-2}.
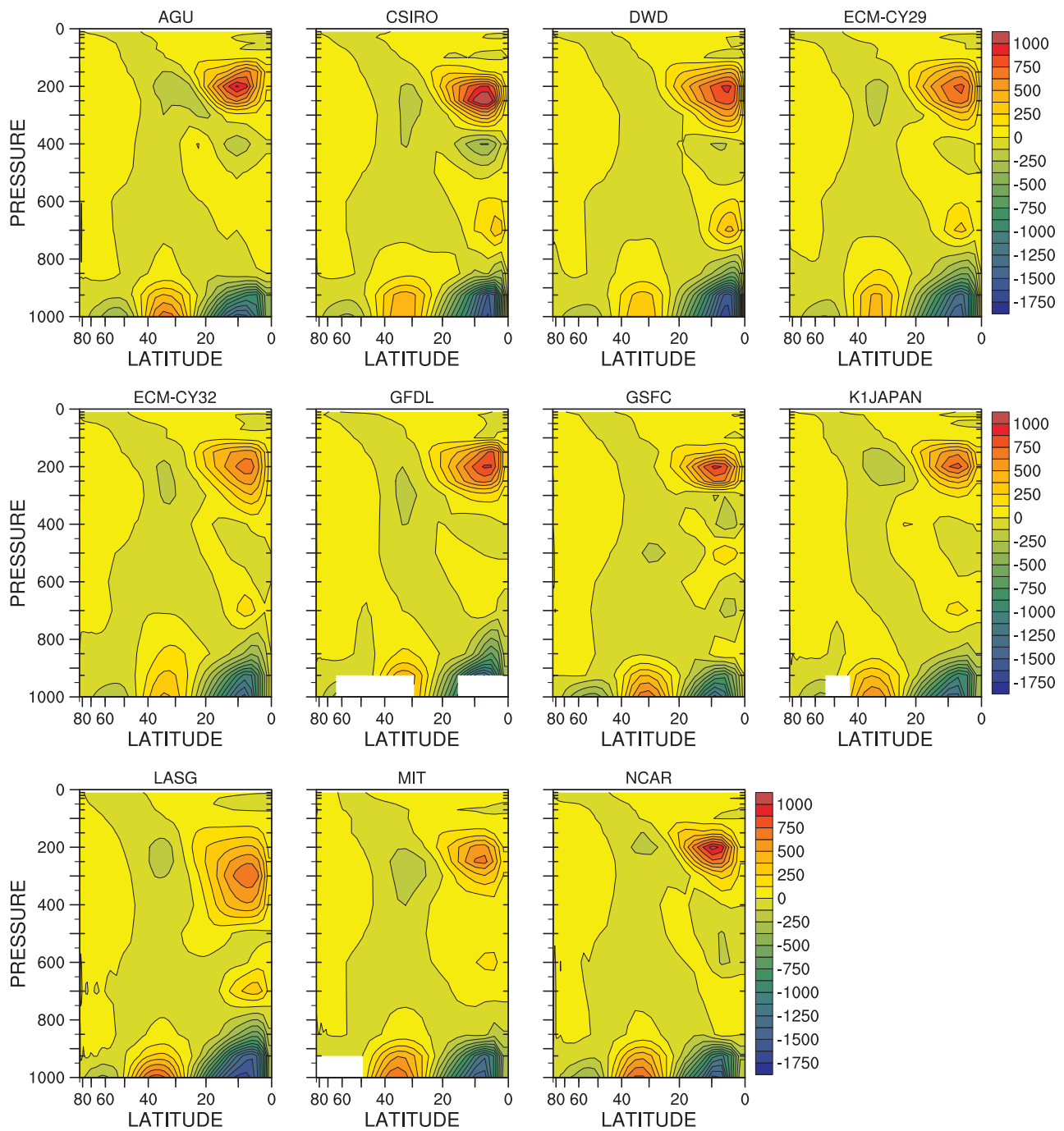
Figure 4.49: Individual model vT co-variance, stationary mean, sm_vt, $\left[\overline{v}\right]\left[\overline{T}\right]$, K m s^{-1}.
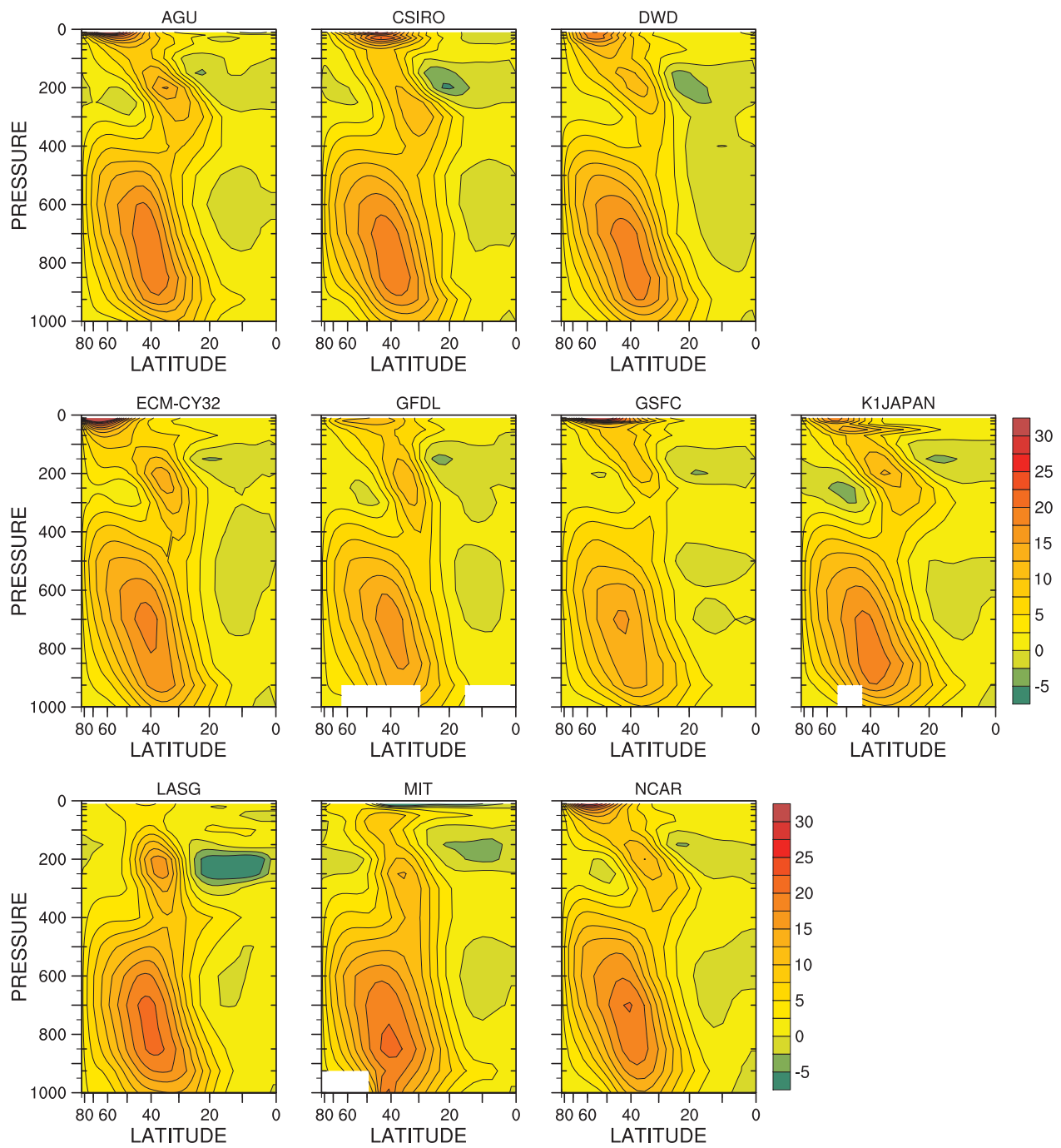
Figure 4.50: Individual model vT co-variance, transient eddy, te_vt, $\overline{[v'^* T'^*]}$, K m s^{-1}.

93
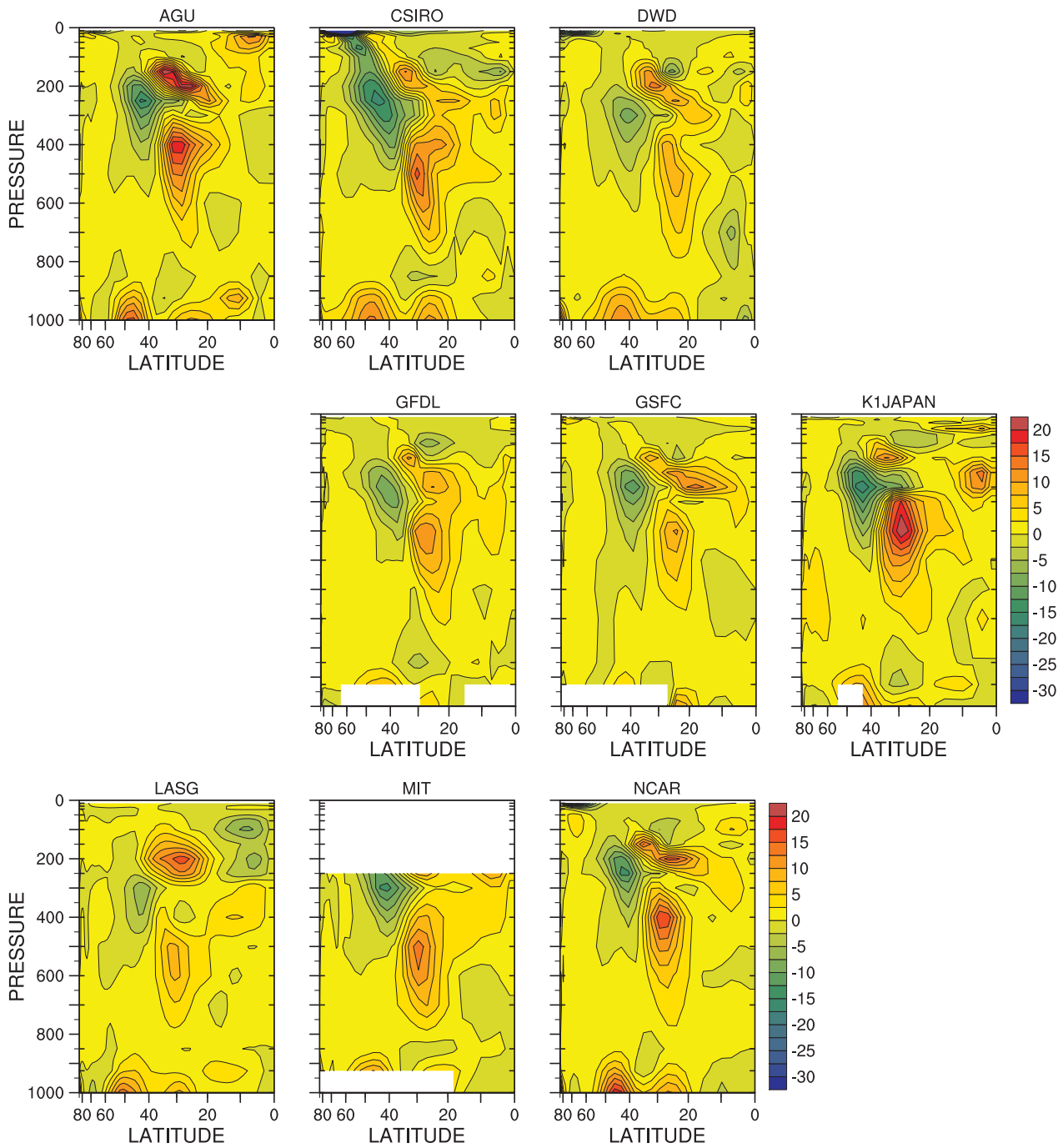
Figure 4.51: Individual model vT co-variance, transient mean, tm_vt, $\overline{[v]'\,[T]'}$, $\times 10^{-4}$ K m s^{-1}.
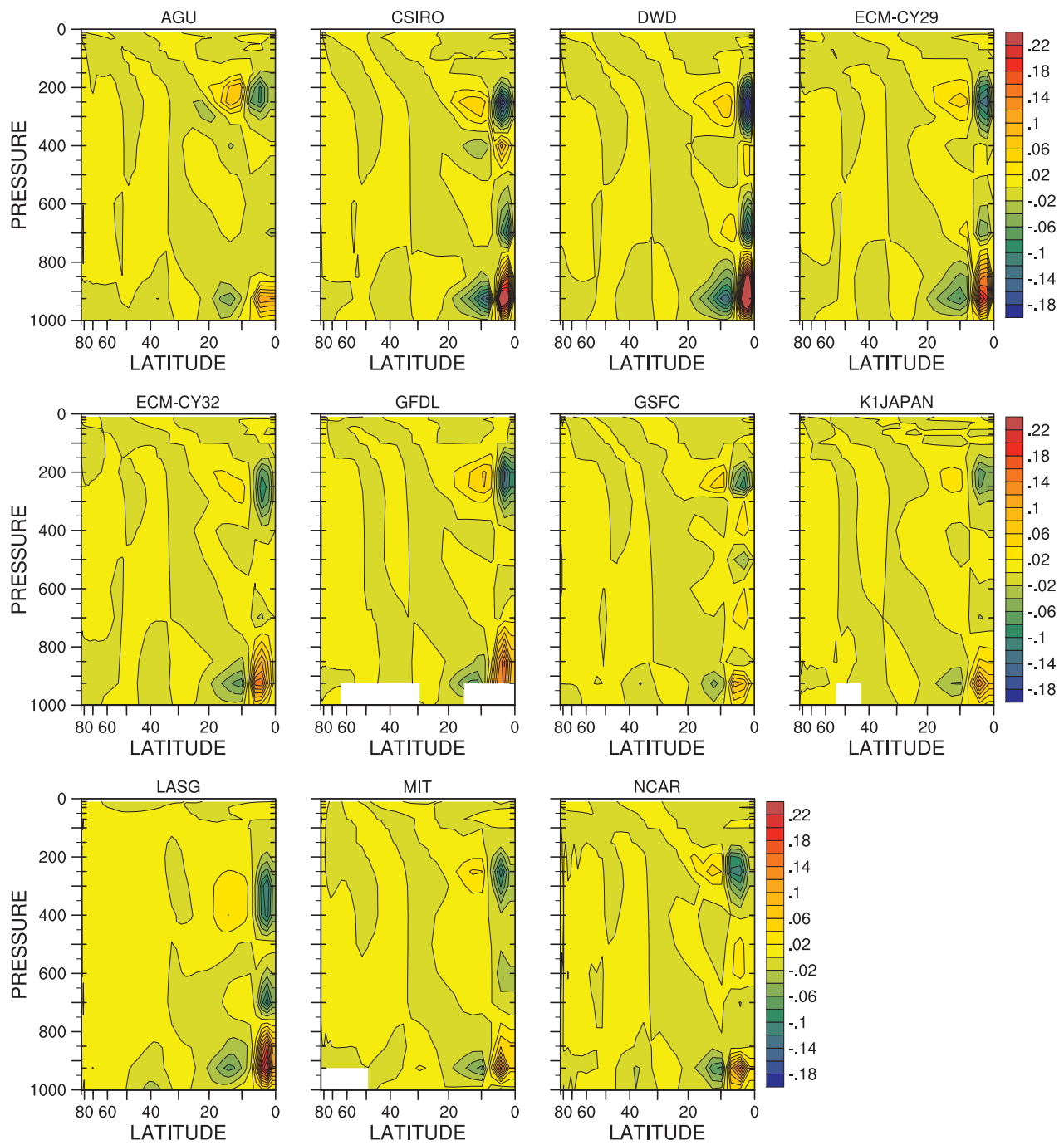
Figure 4.52: Individual model vω co-variance, stationary mean, sm_vom, $[\overline{v}]\,[\overline{\omega}]$, m Pa s^{-2}.
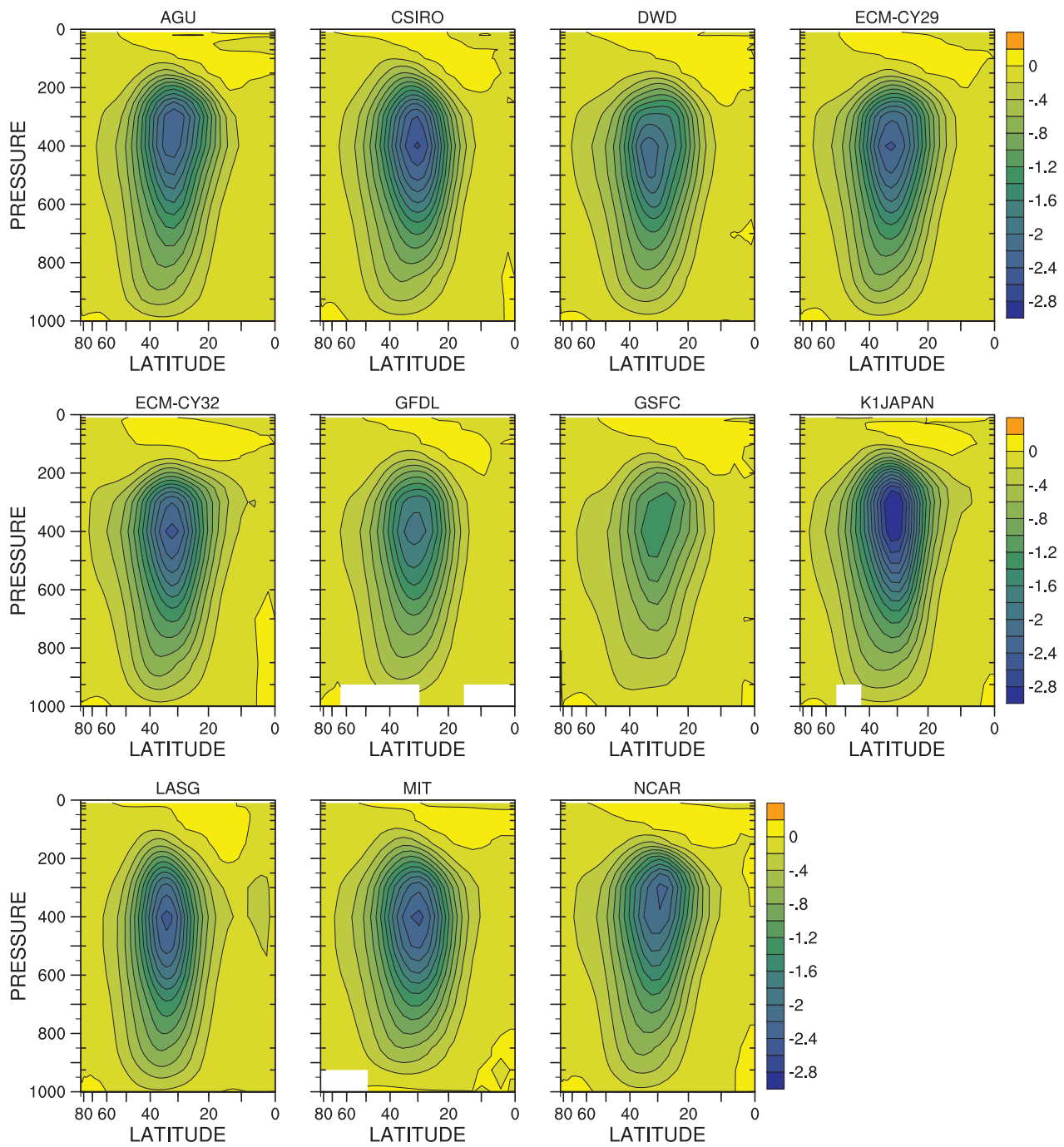
Figure 4.53: Individual model vω co-variance, transient eddy, te_vom, $\overline{[v'^*\omega'^*]}$, m Pa s^{-2}.
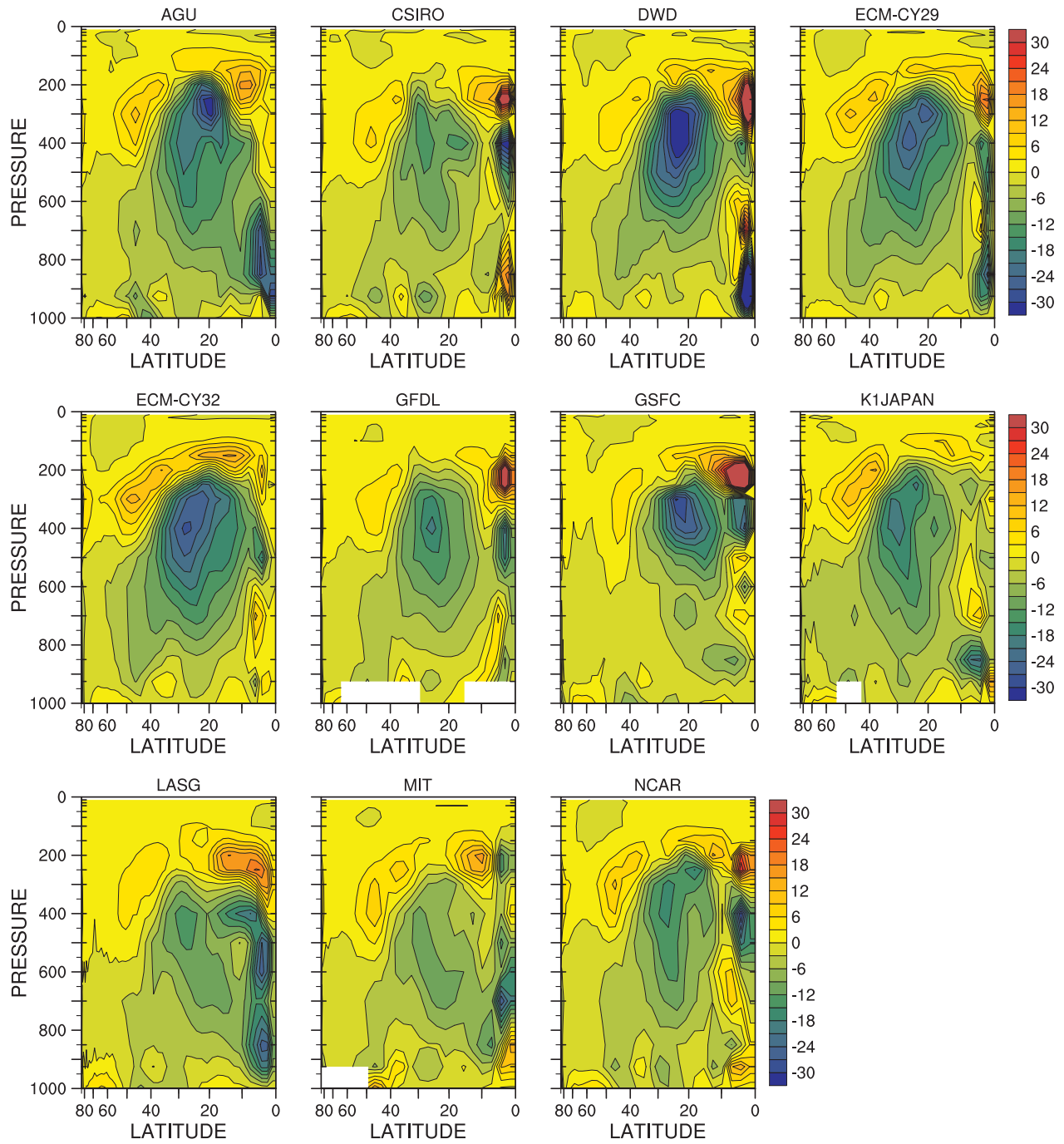
Figure 4.54: Individual model vω co-variance, transient mean, tm_vom, $\overline{[v]'[\omega]'}$, $\times 10^{-4}$ m Pa s^{-2}.
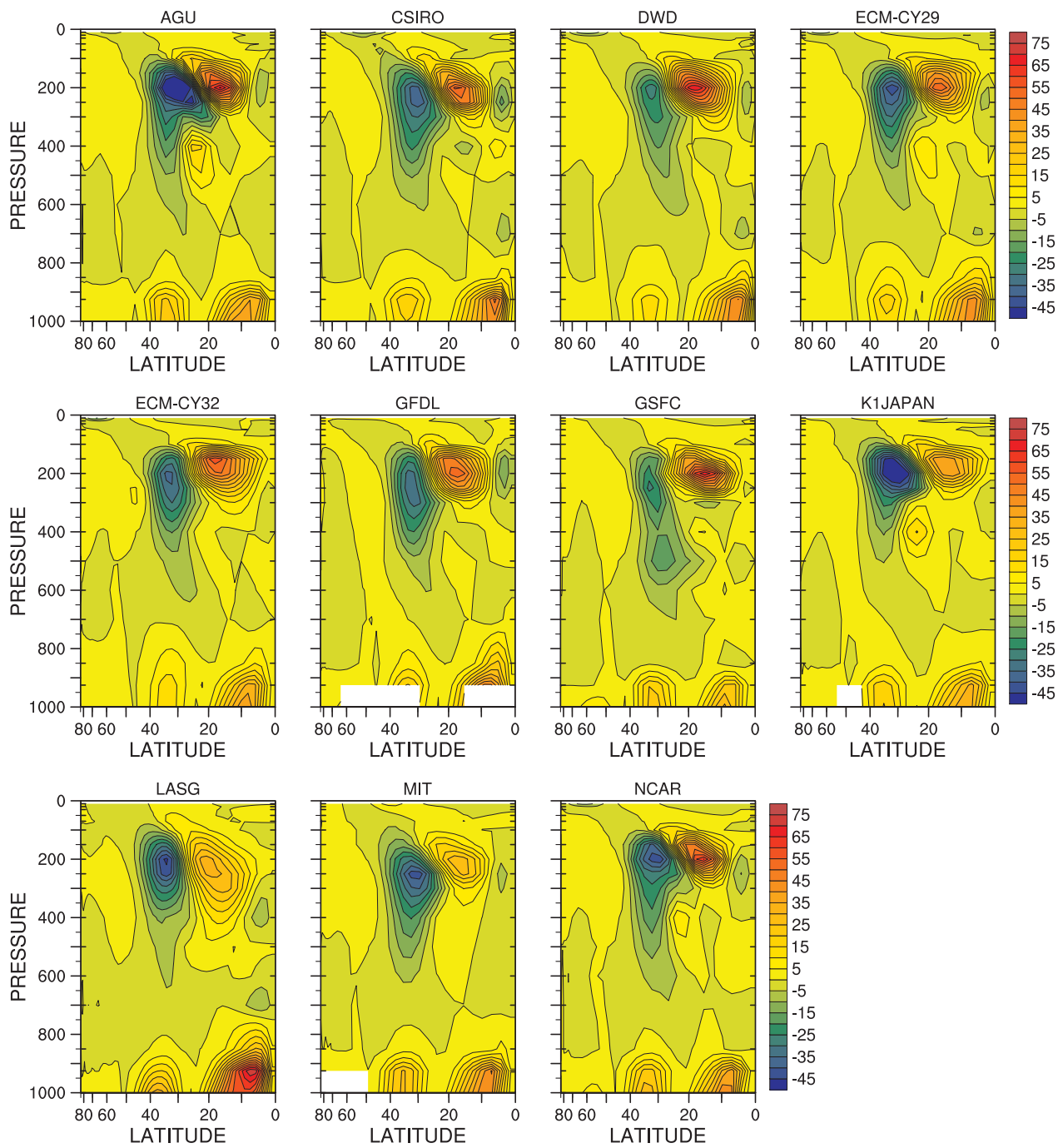
Figure 4.55: Individual model uv co-variance, stationary mean, sm_uv, $[\overline{u}]\,[\overline{v}]$, m^2 s^{-2}.
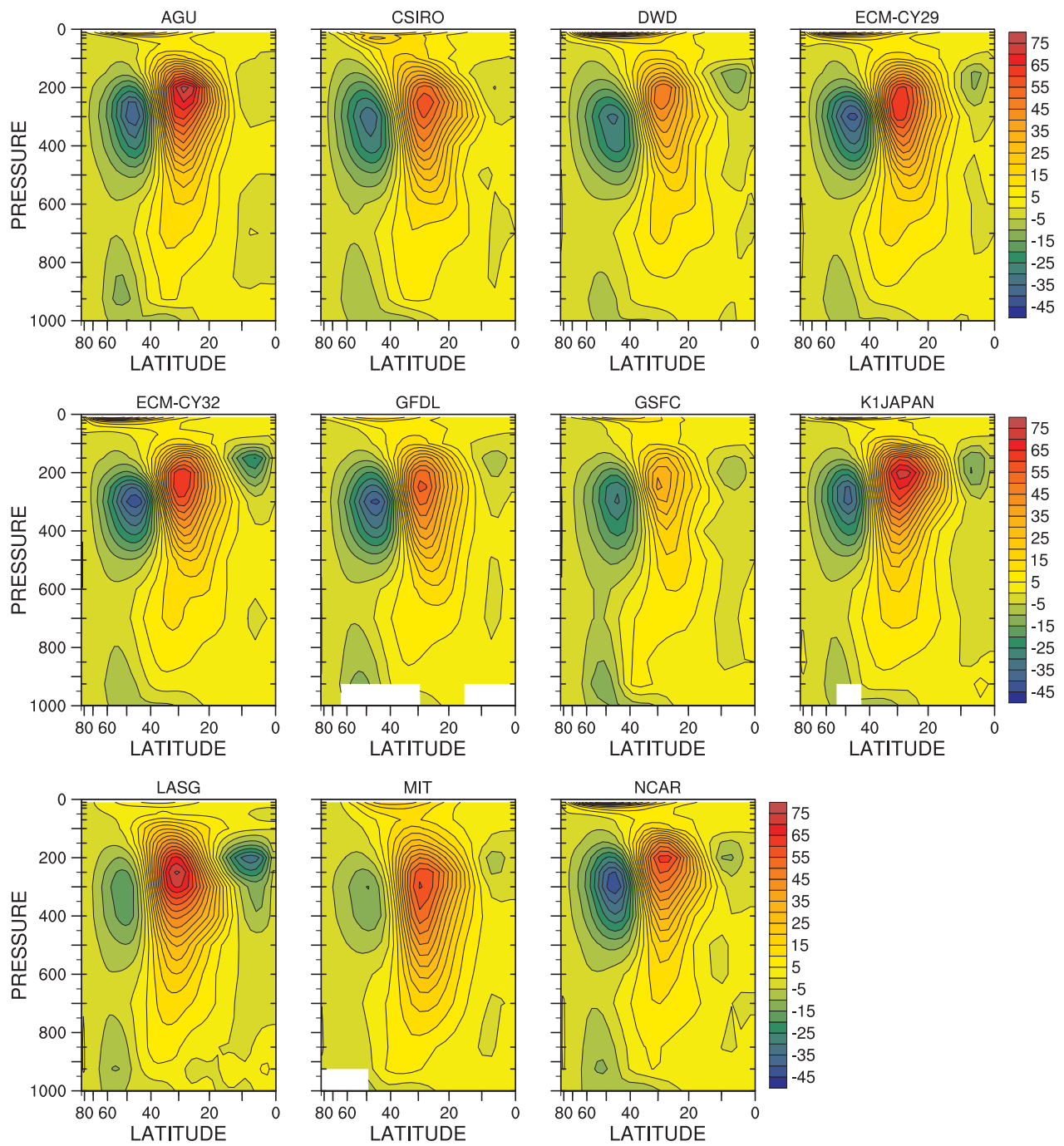
Figure 4.56: Individual model uv co-variance, transient eddy, te_uv, $\overline{[u'^* v'^*]}$, m^2 s^{-2}.
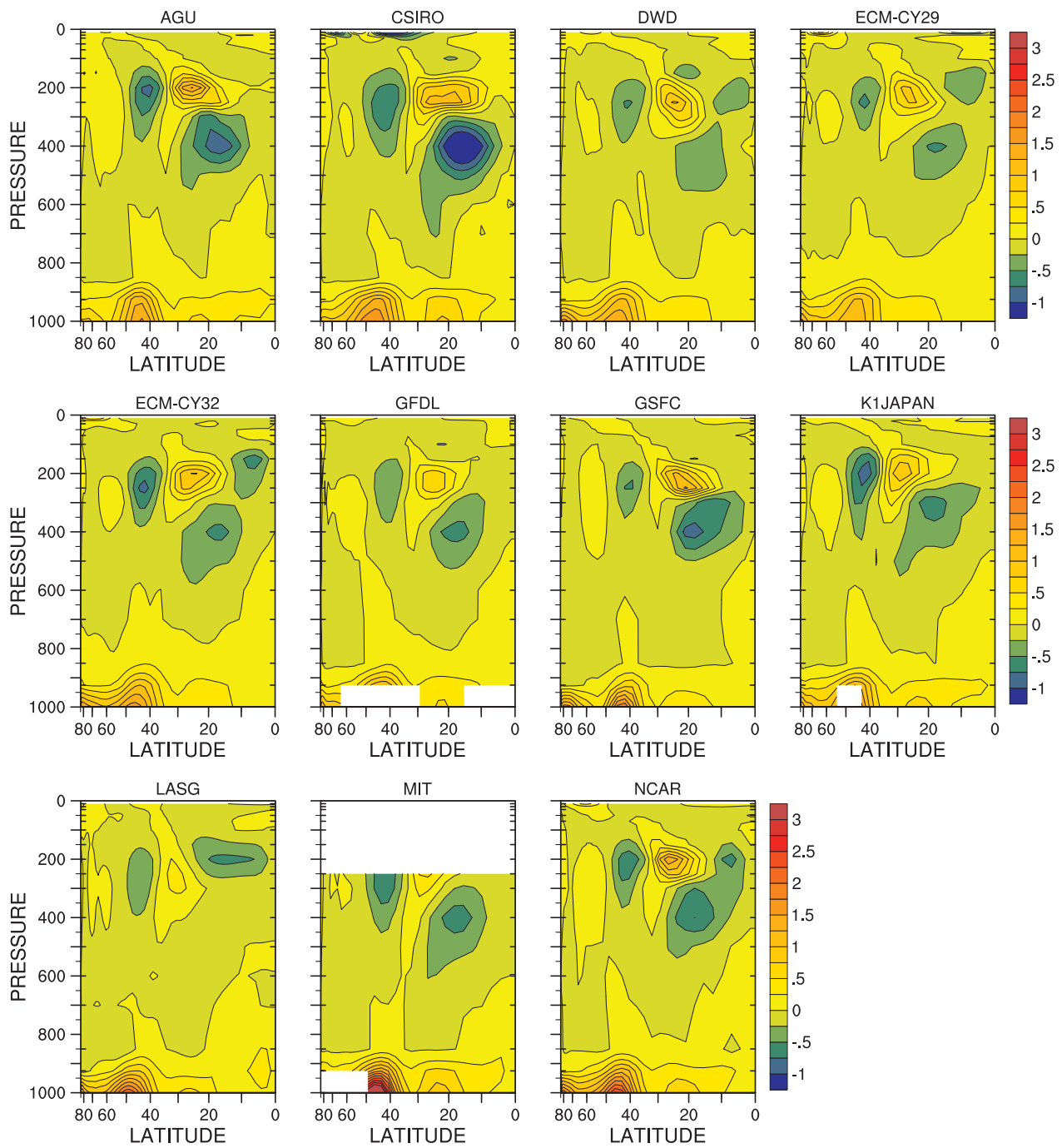
Figure 4.57: Individual model uv co-variance, transient mean, tm_uv, $\overline{[u]'[v]'}$, m^2 s^{-2}.
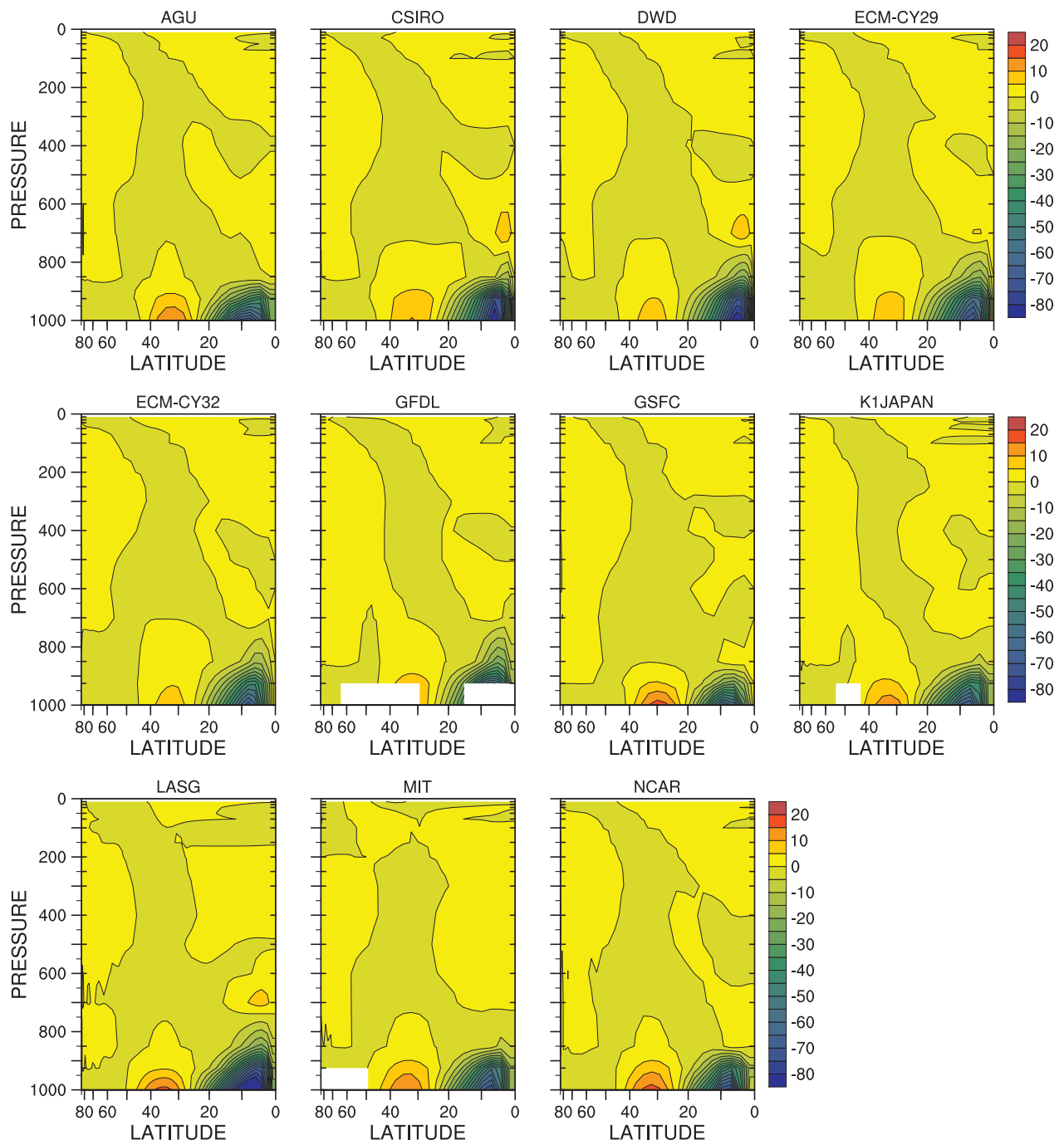
Figure 4.58: Individual model vq co-variance, stationary mean, sm_vq, $[\overline{v}]\,[\overline{q}]$, m s^{-1} g kg^{-1}.
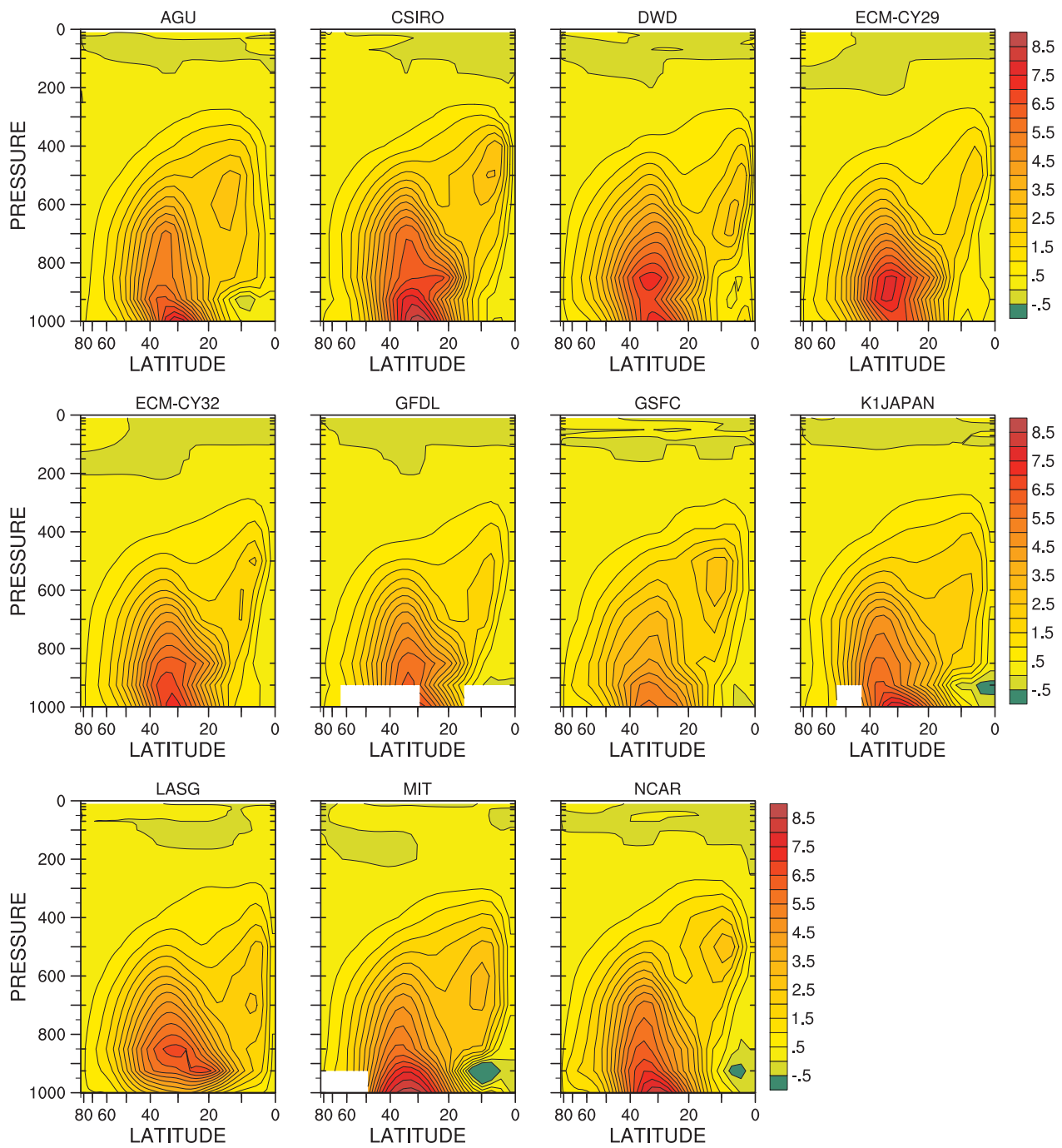
Figure 4.59: Individual model vq co-variances, transient eddy, te_vq, $\overline{[v'^* q'^*]}$, m s^{-1} g kg^{-1}.
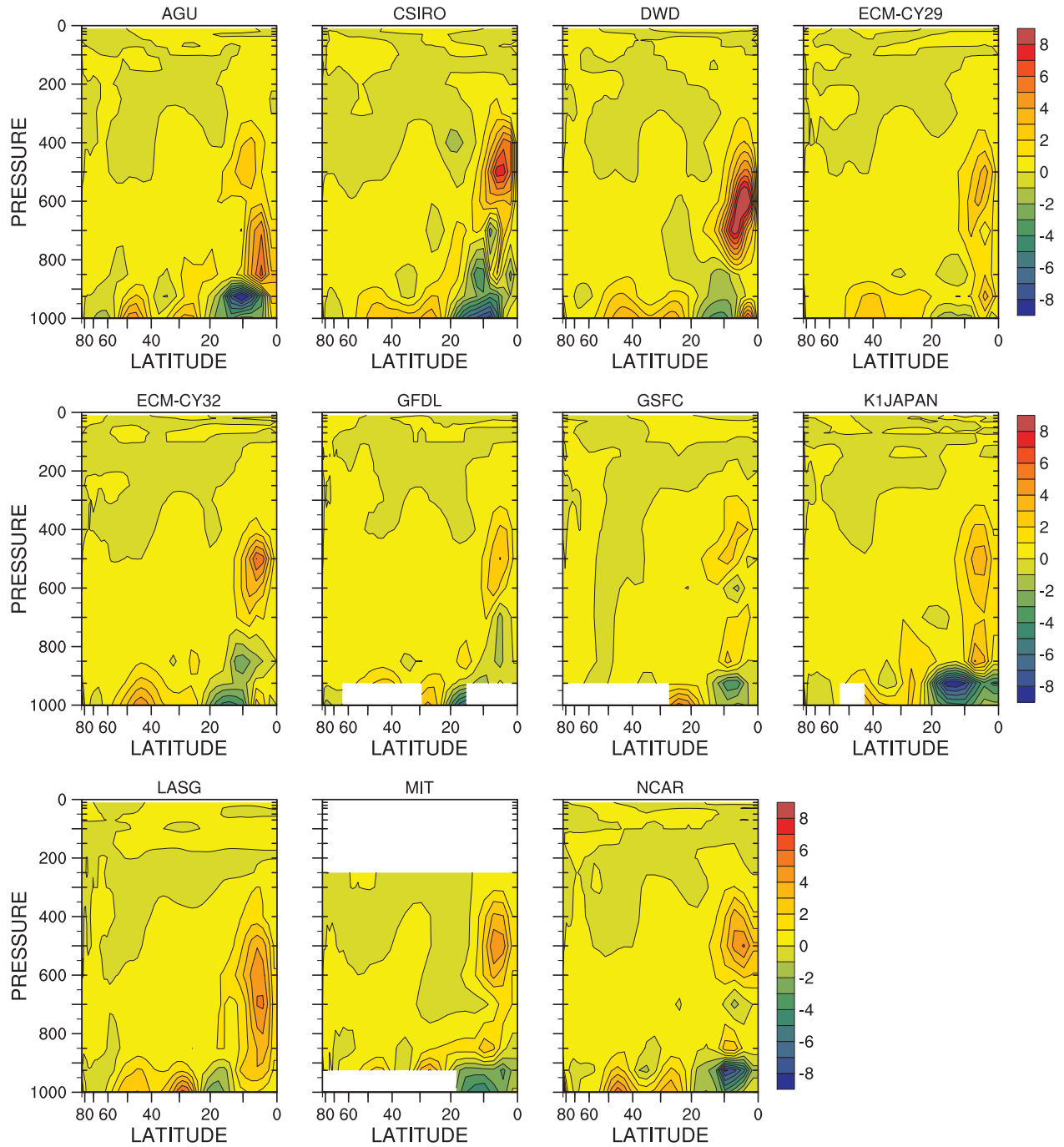
Figure 4.60: Individual model vq co-variance, transient mean, tm_vq, $\overline{[v]'[q]'}$, $\times 10^{-2}$ m s^{-1} g kg^{-1}.
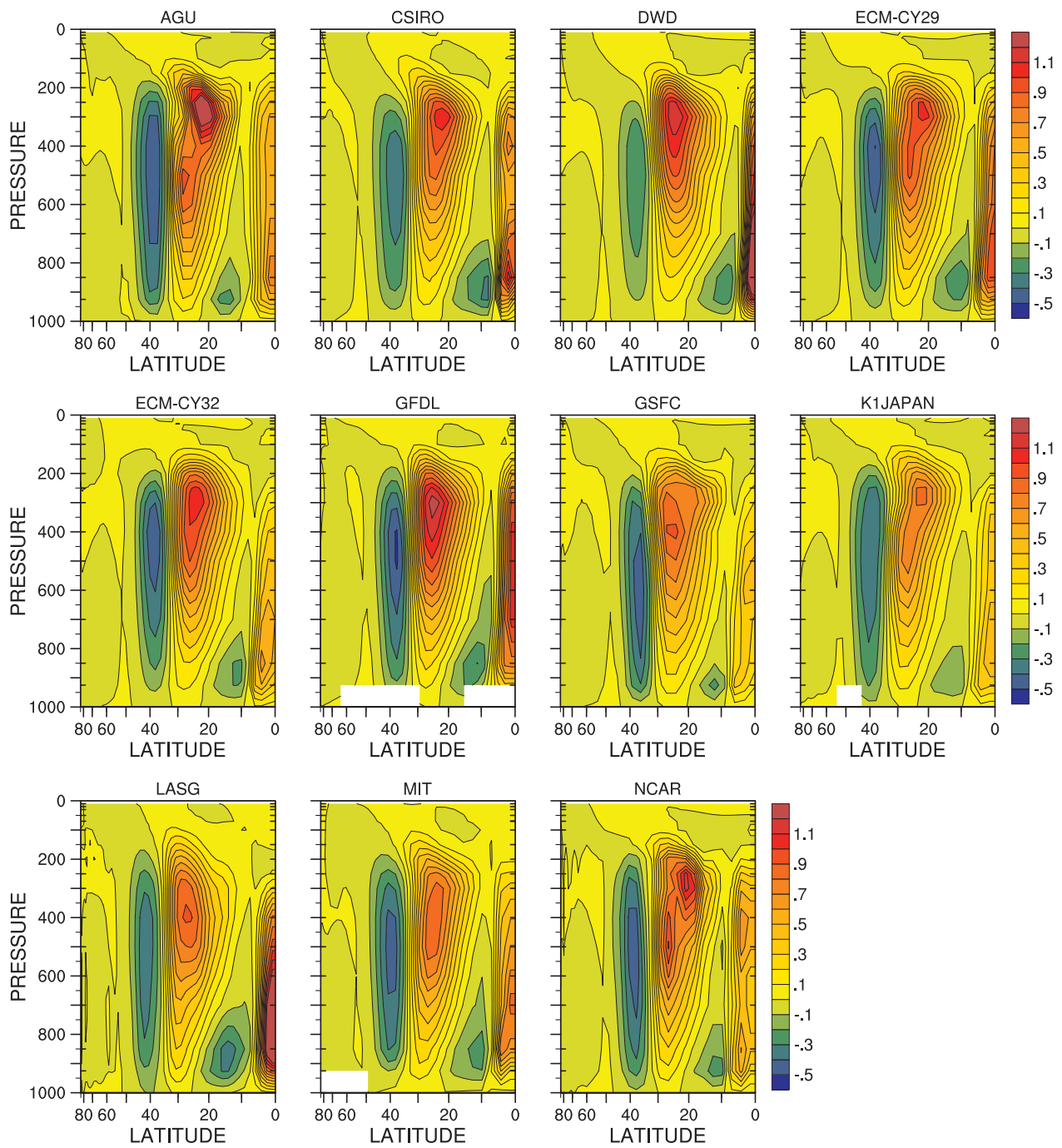
Figure 4.61: Individual model uω co-variance, stationary mean, sm_uom, $[\overline{u}]\,[\overline{\omega}]$, m Pa s^{-2}.

104
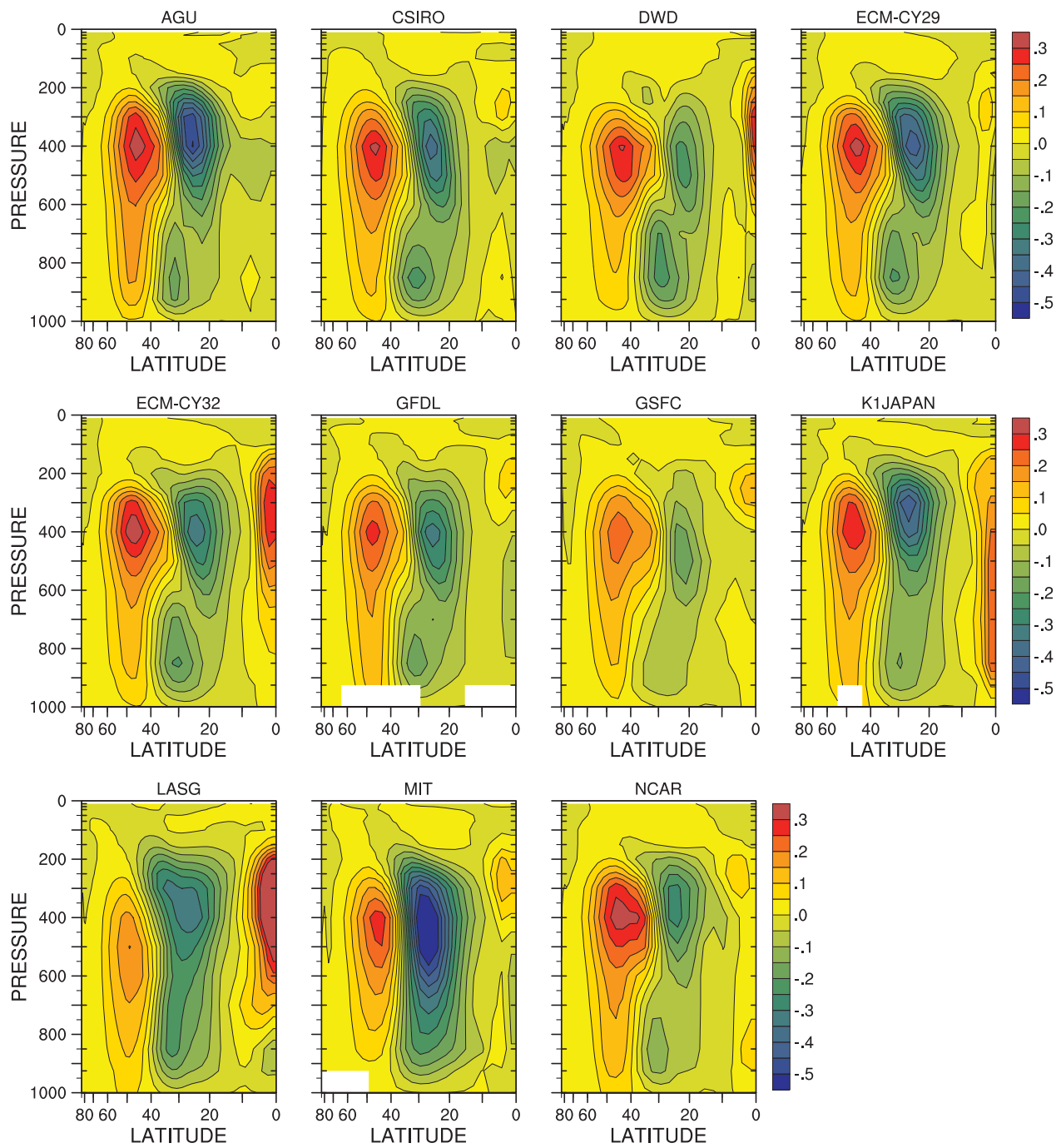
Figure 4.62: Individual model uω co-variance, transient eddy, te_uom, $\overline{[u'^*\omega'^*]}$, m Pa s^{-2}.

105
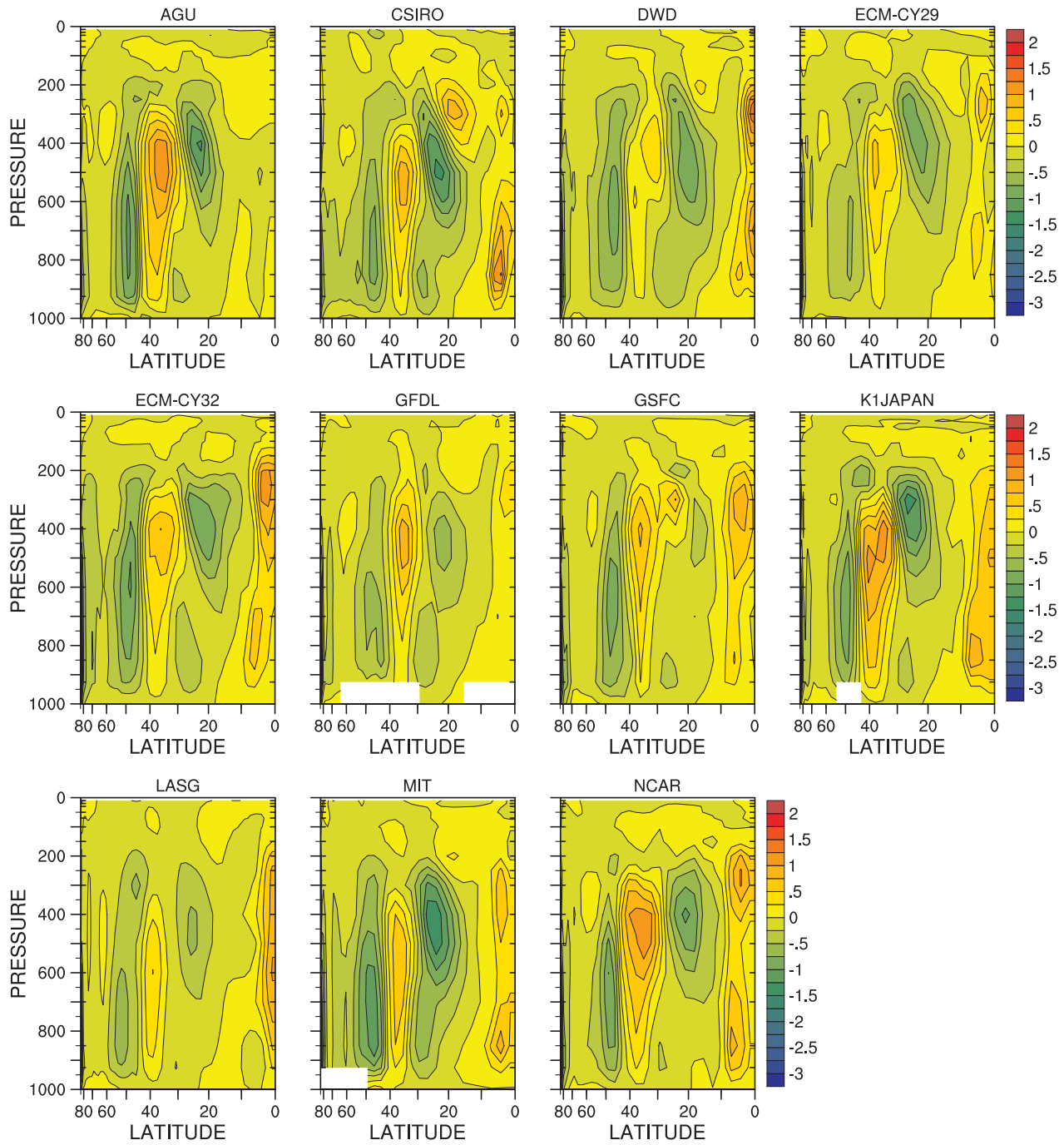
Figure 4.63: Individual model uω co-variance, transient mean, tm_uom, $\overline{[u]'[\omega]'}$, $\times 10^{-2}$ m Pa s^{-2}.
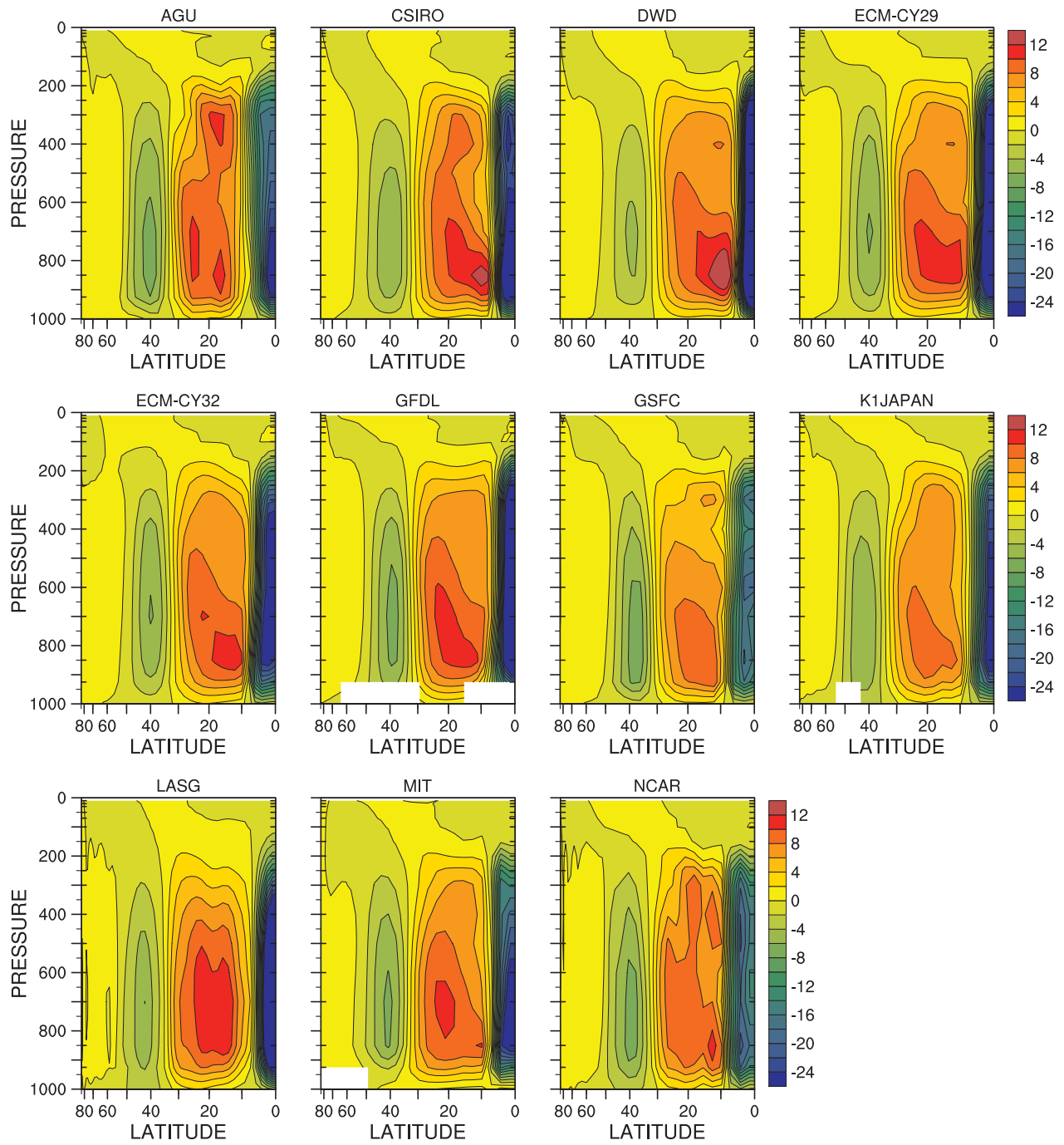
Figure 4.64: Individual model ωT co-variance, stationary mean, sm_omt, $\left[\overline{\omega}\right]\left[\overline{T}\right]$, K Pa s^{-1}.
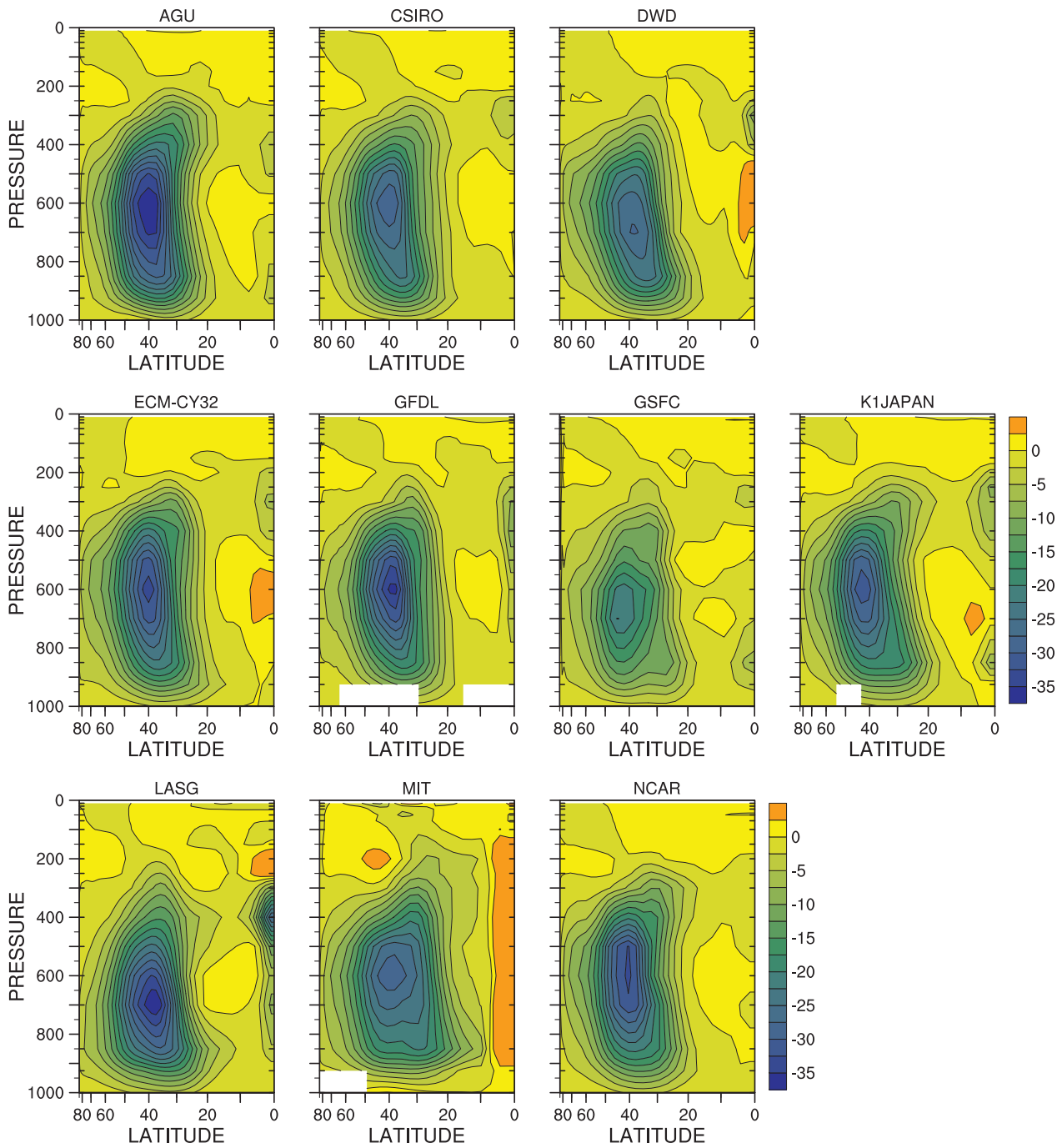
Figure 4.65: Individual model ωT co-variance, transient eddy, te_omt, $\overline{[\omega'^* T'^*]}$, $\times 10^{-2}$ K Pa s^{-1}.
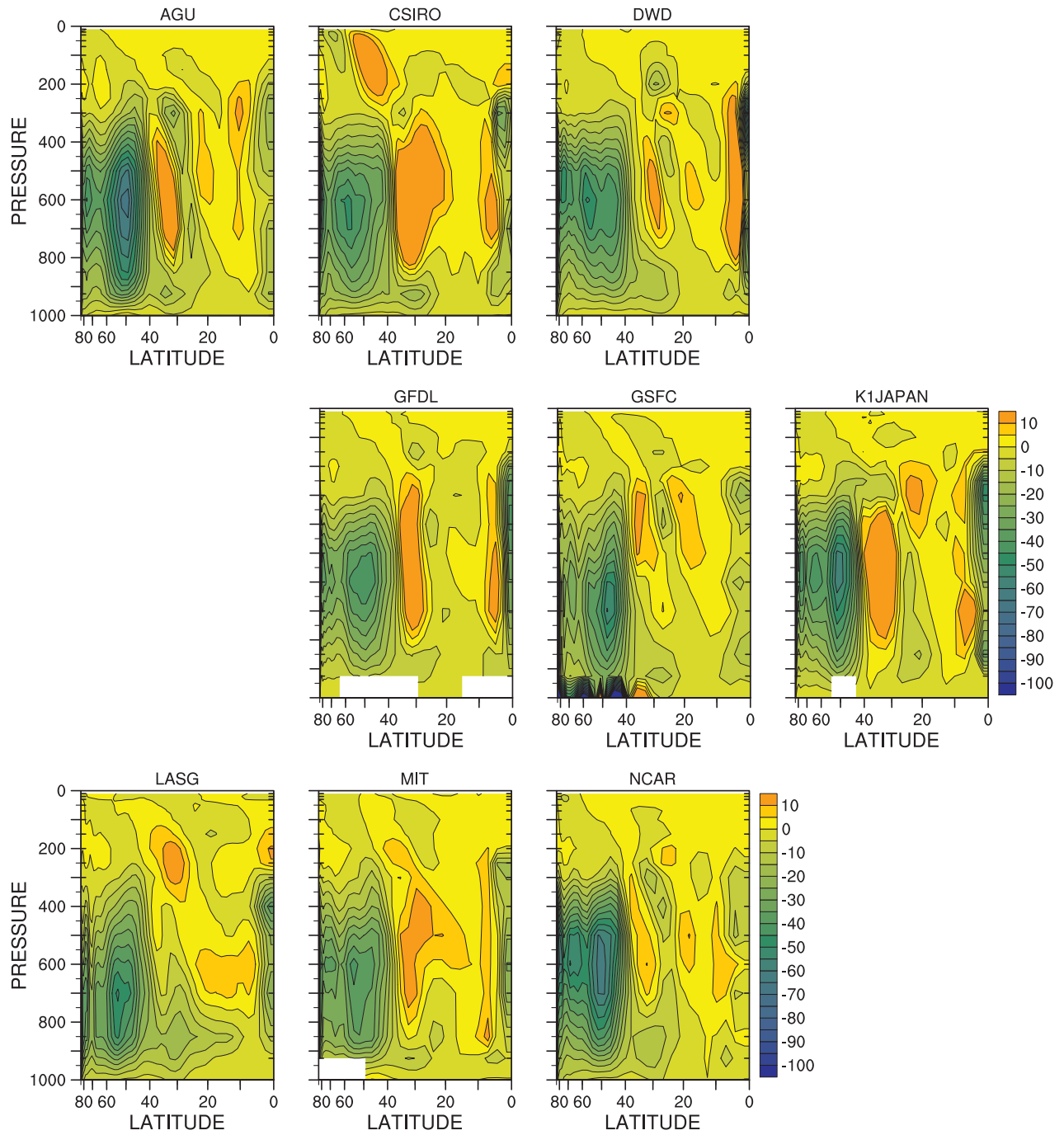
Figure 4.66: Individual model ωT co-variance, transient mean, tm_omt, $\overline{[\omega]'[T]'}$, $\times 10^{-4}$ K Pa s^{-1}.
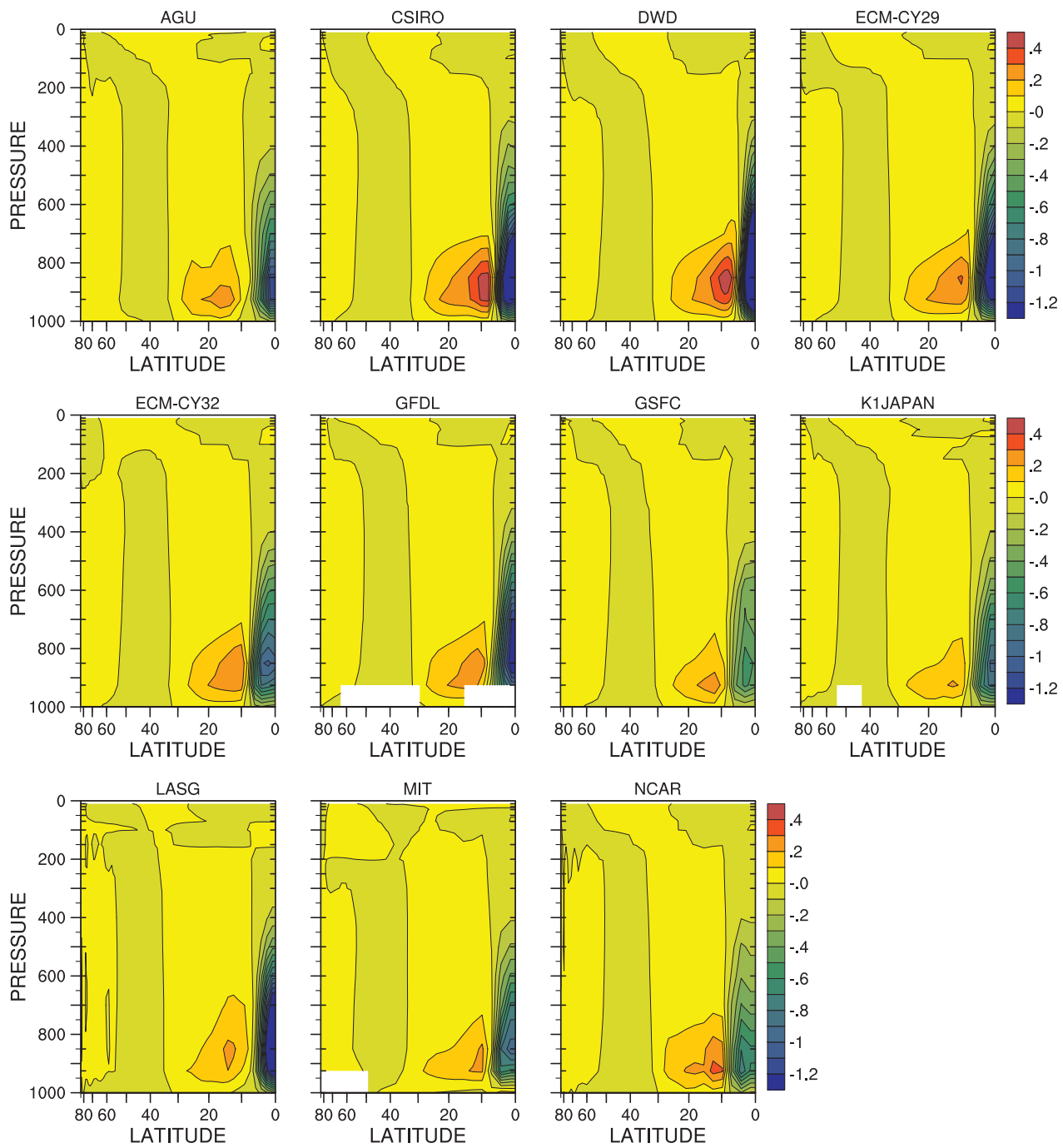
Figure 4.67: Individual model ωq co-variance, stationary mean, sm_omq, $[\overline{\omega}]\,[\overline{q}]$, g kg^{-1} Pa s^{-1}.
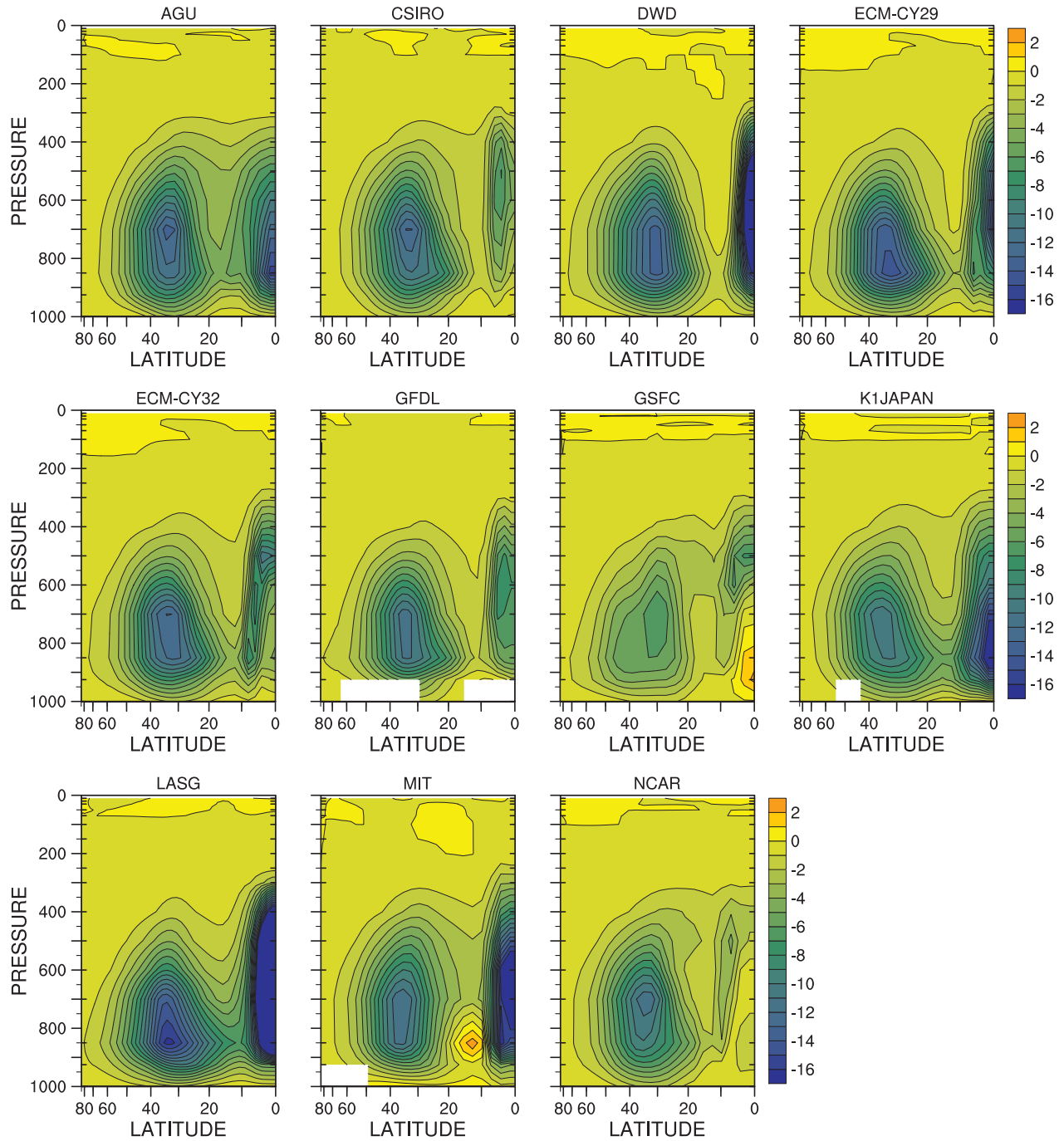
Figure 4.68: Individual model ωq co-variance, transient eddy, te_omq, $\overline{[\omega'^* q'^*]}$, $\times 10^{-2}$ g kg^{-1} Pa s^{-1}.
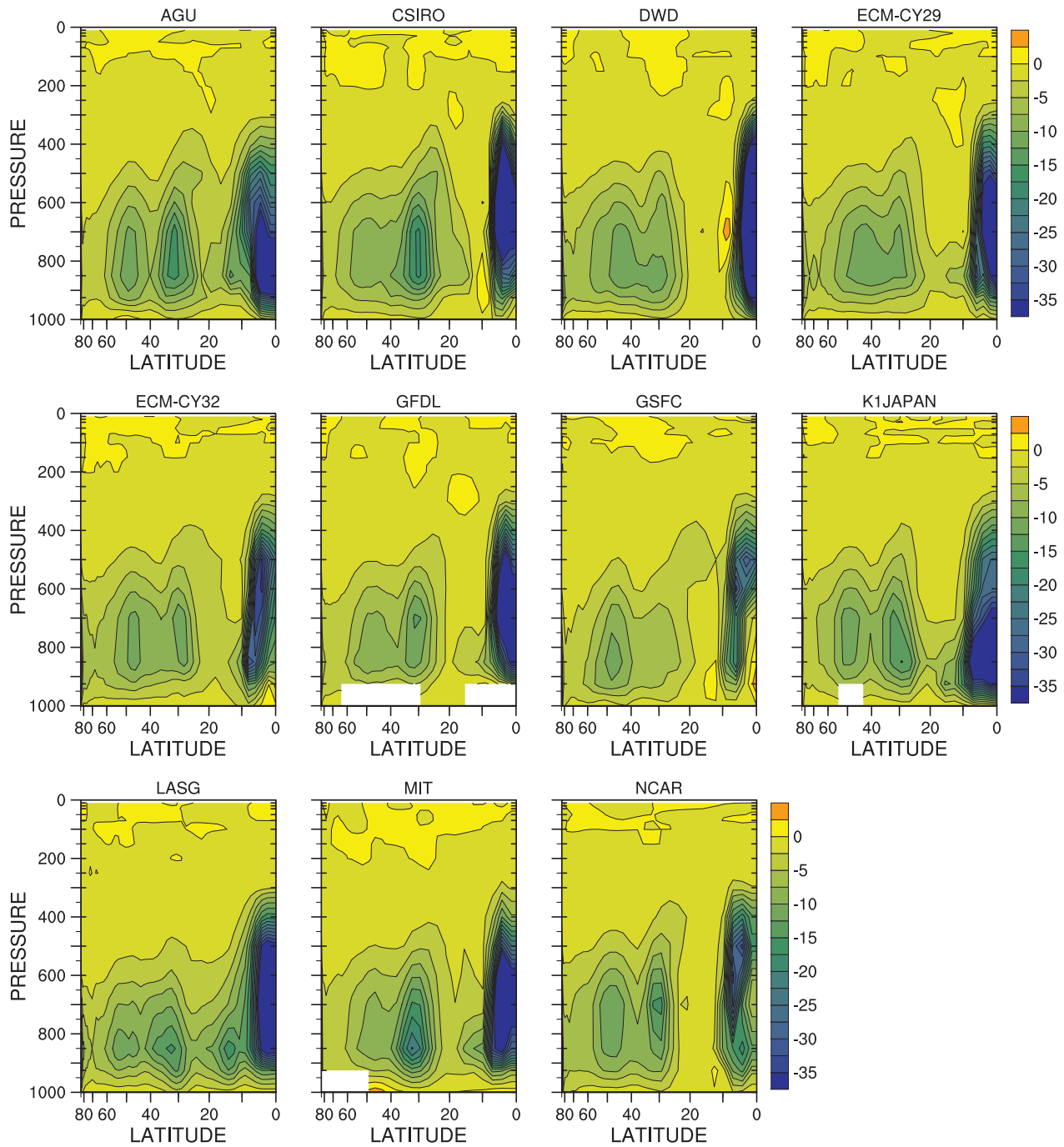
Figure 4.69: Individual model ωq co-variance, transient mean, tm_omq, $\overline{[\omega]'[q]'}$, $\times 10^{-4}$ g kg^{-1} Pa s^{-1}.
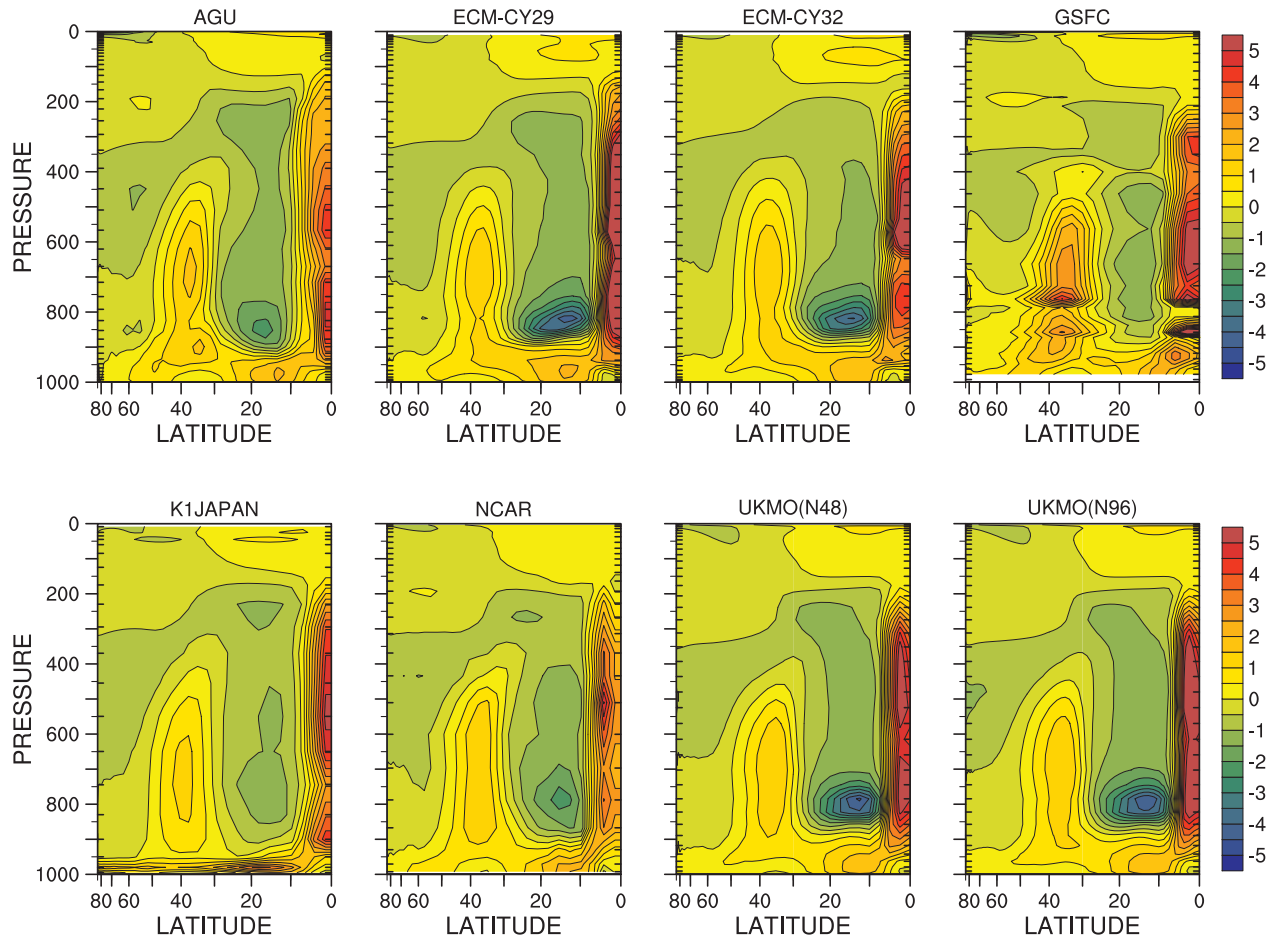
Figure 4.70: Zonal-time average total parameterized temperature tendency (t), K day^{-1}.
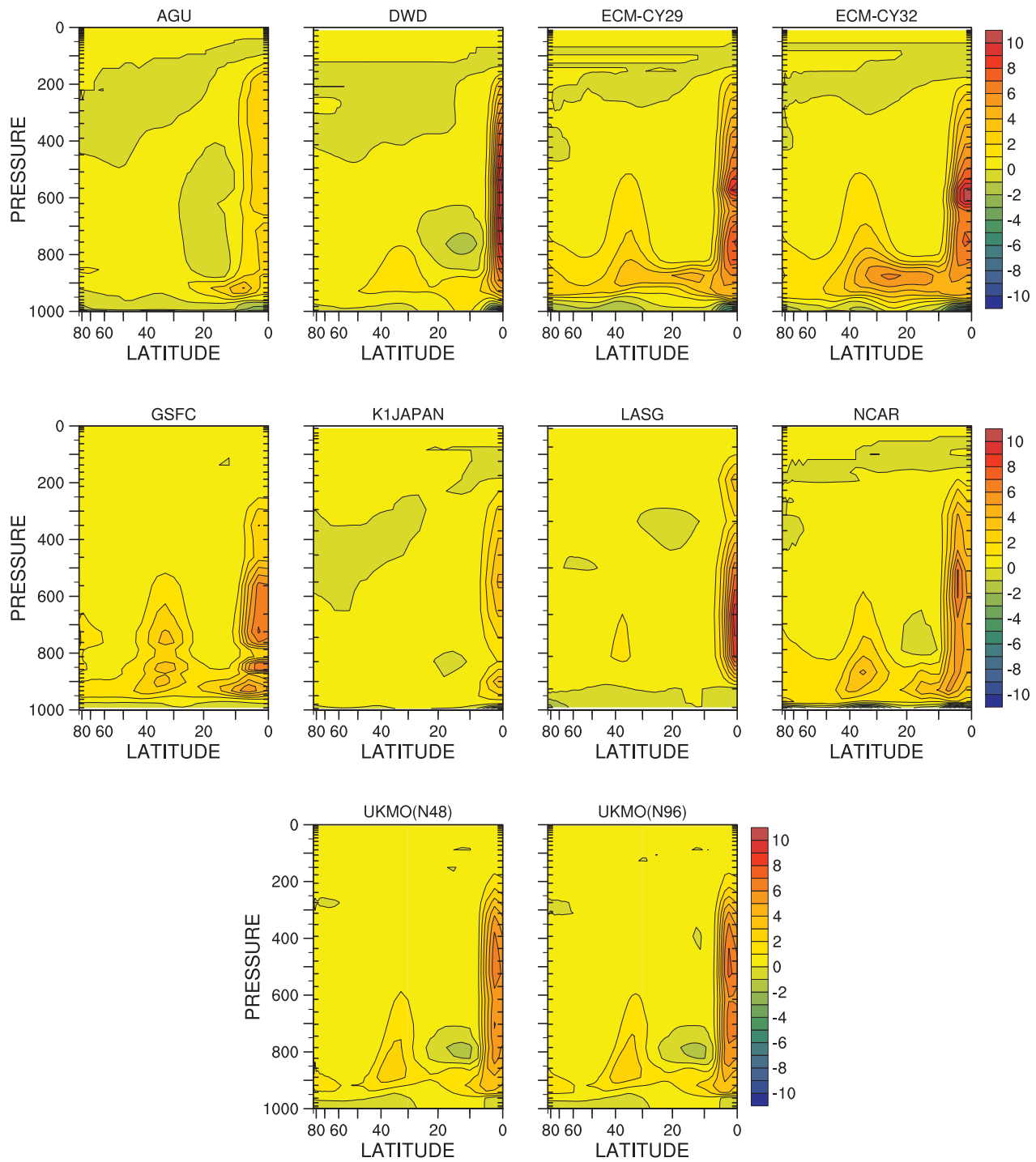
Figure 4.71: Zonal-time average parameterized convection temperature tendency (t_conv), K day^{-1}.
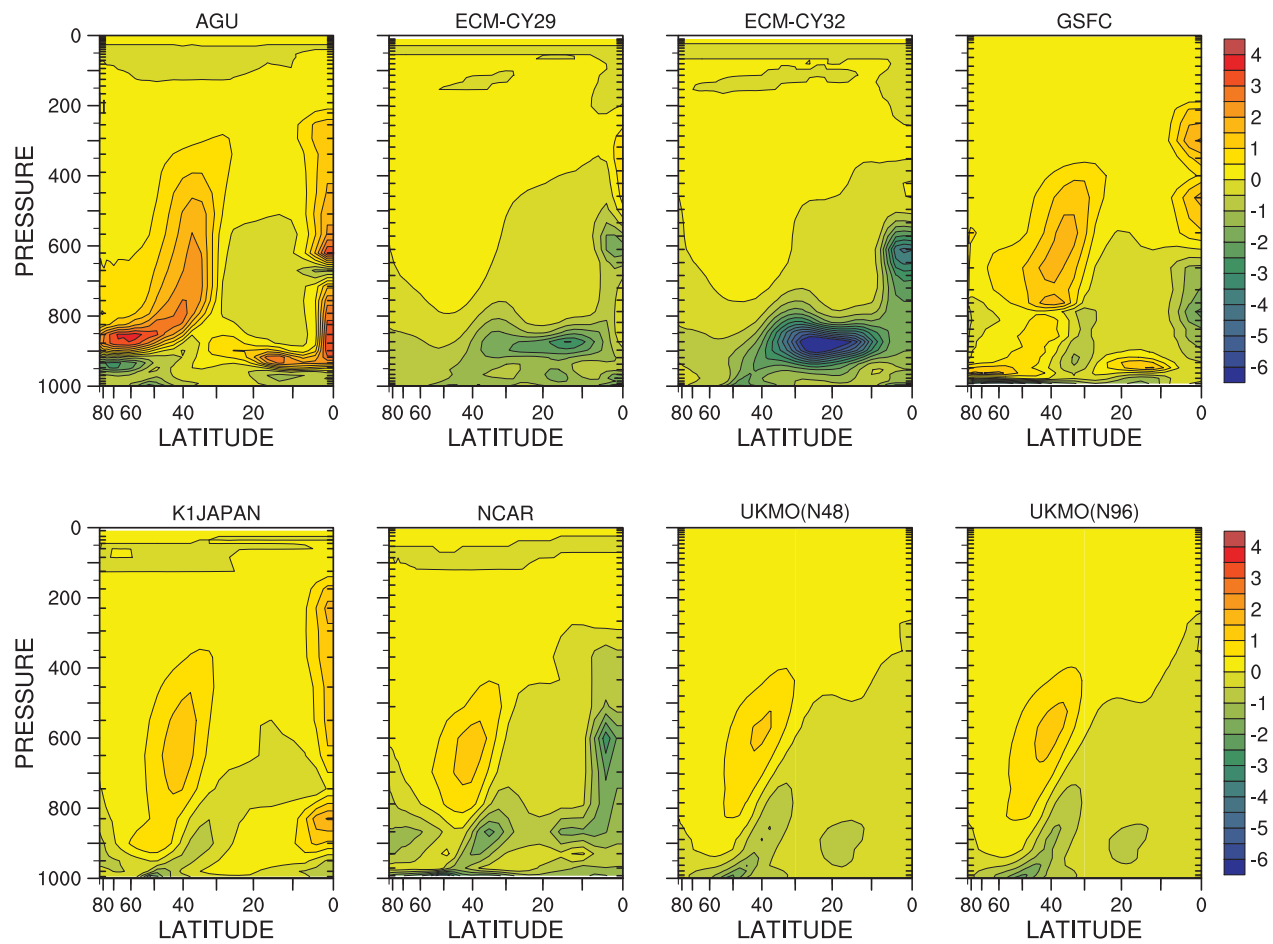
Figure 4.72: Zonal-time average parameterized cloud temperature tendency (t_cld), K day^{-1}.
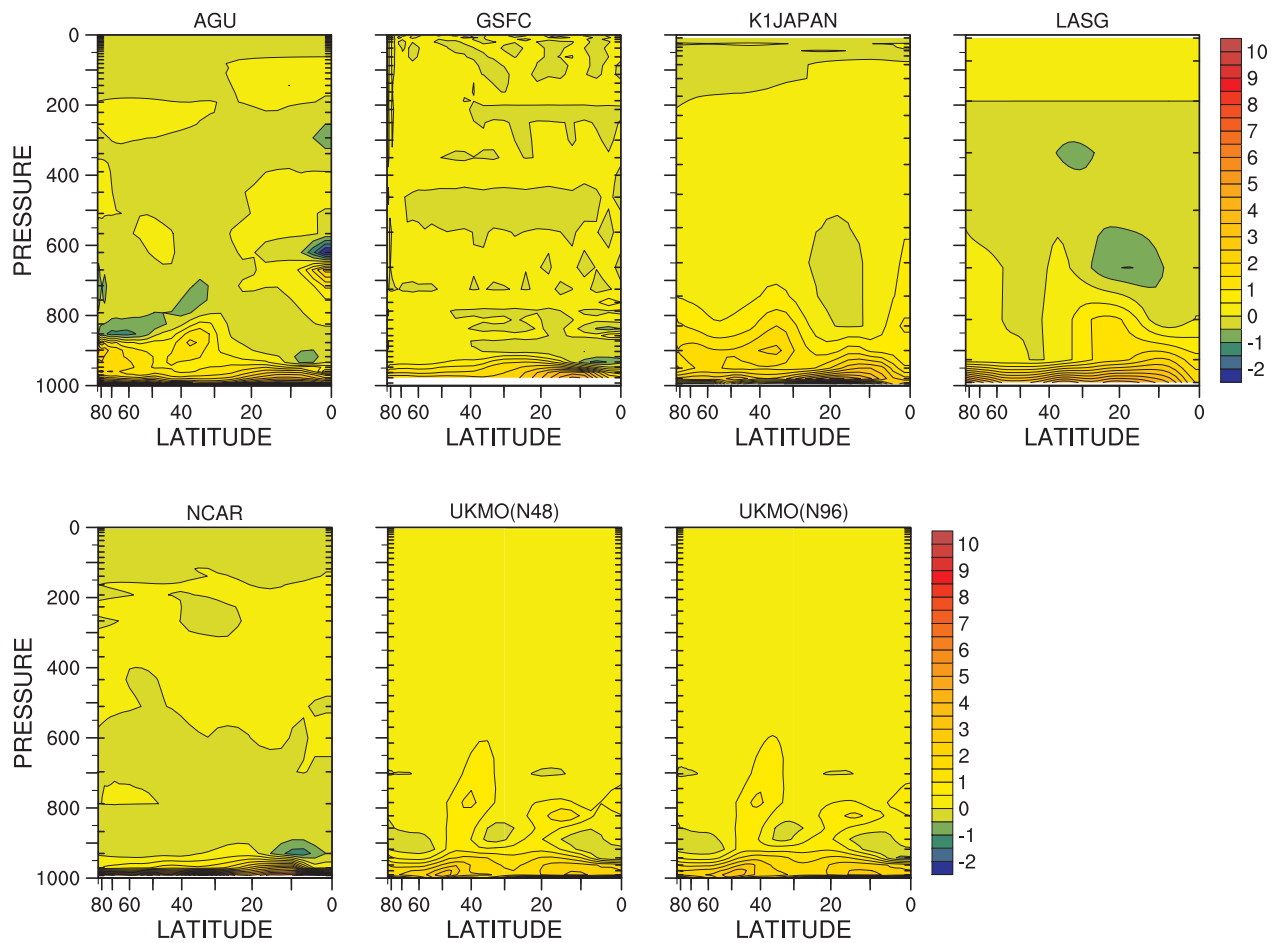
Figure 4.73: Zonal-time average parameterized turbulence temperature tendency (t_turb), K day^{-1}.
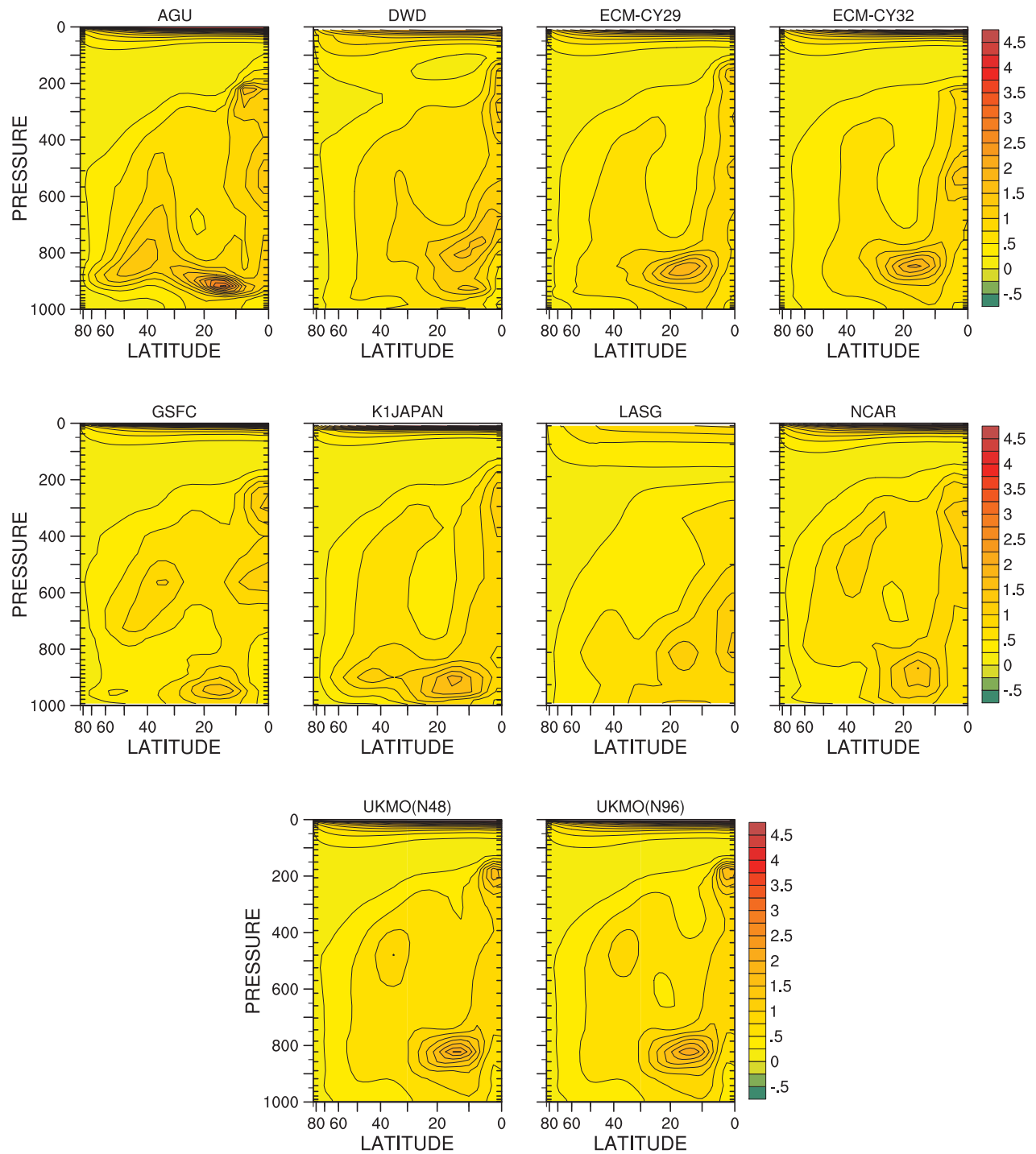
Figure 4.74: Zonal-time average shortwave radiation temperature tendency (t_sw), K day^{-1}.
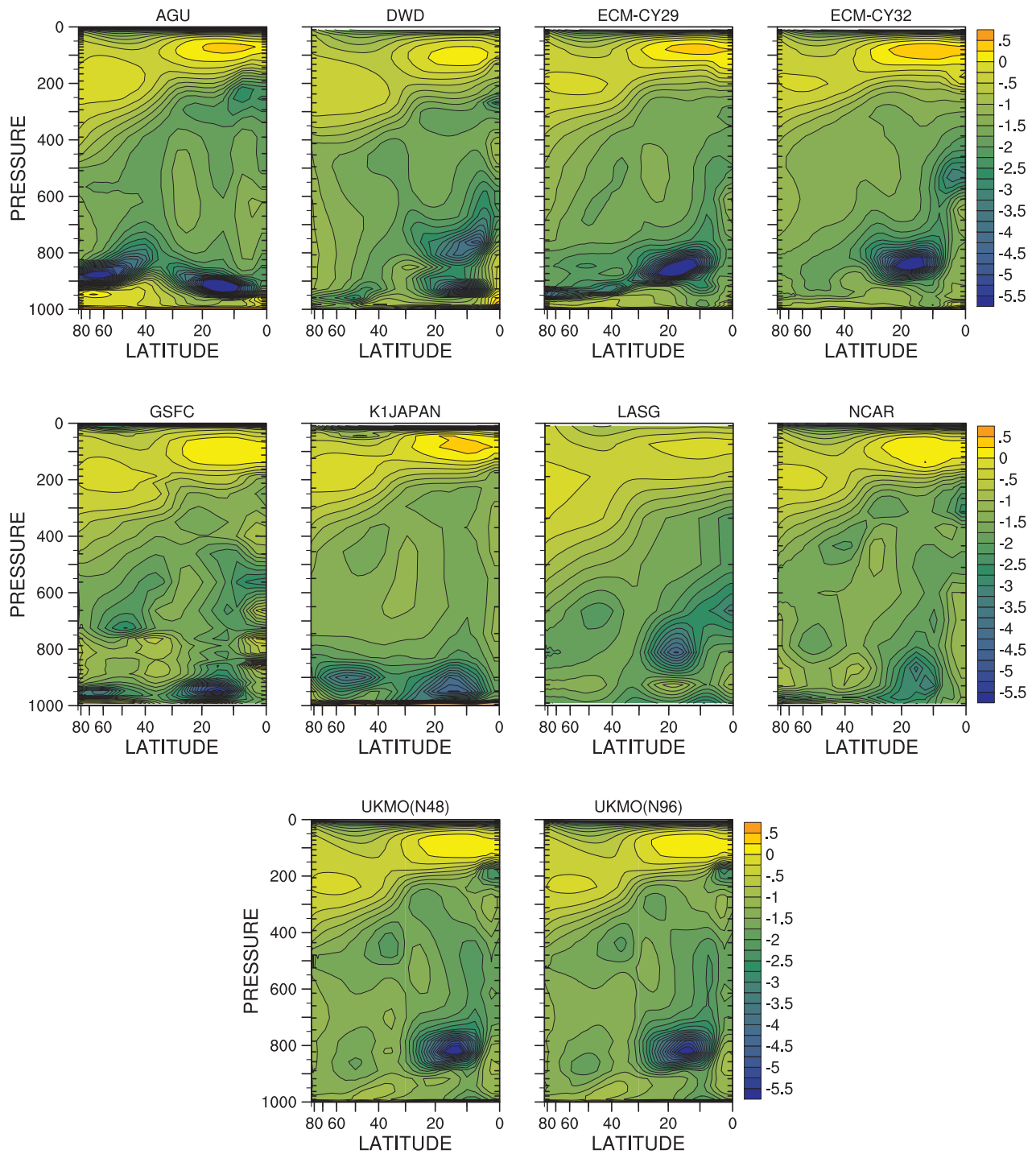
Figure 4.75: Zonal-time average longwave radiation temperature tendency (t_lw), K day^{-1}.
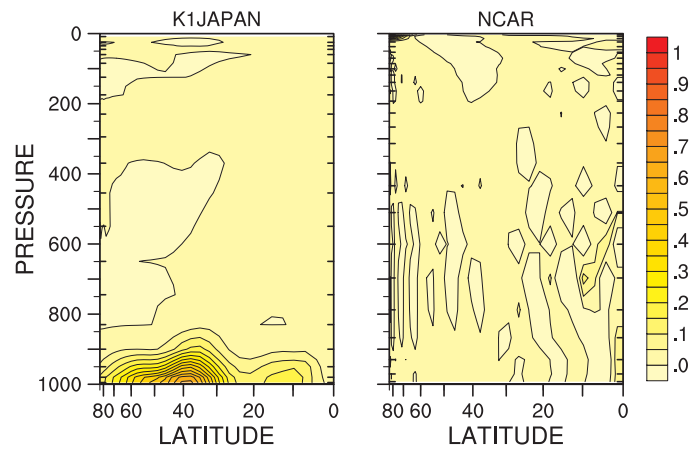
Figure 4.76: Zonal-time average dissipation temperature tendency (t_disp), K day^{-1}.
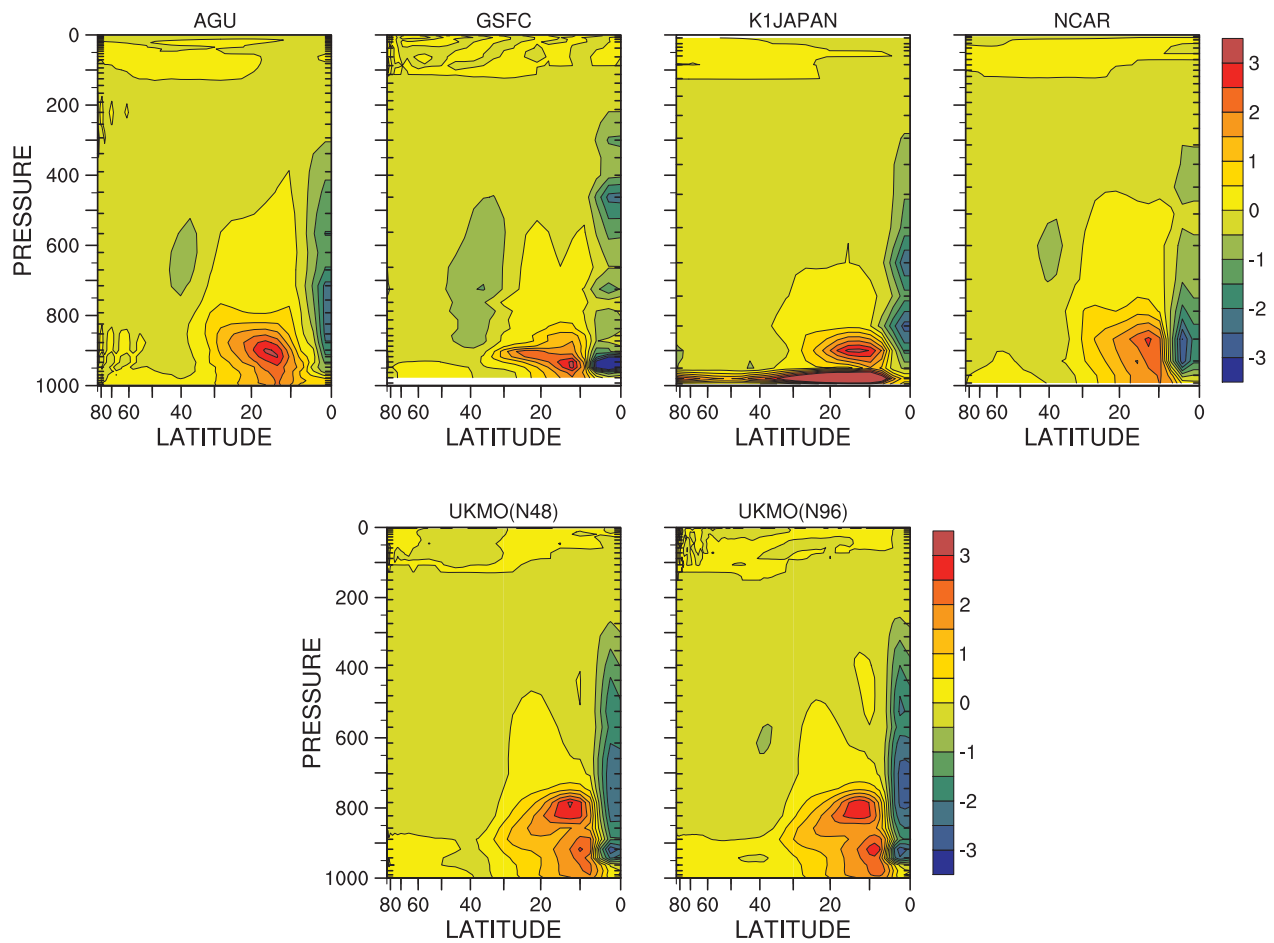
Figure 4.77: Zonal-time average total parameterized specific humidity tendency (q), g kg^{-1} day^{-1}.
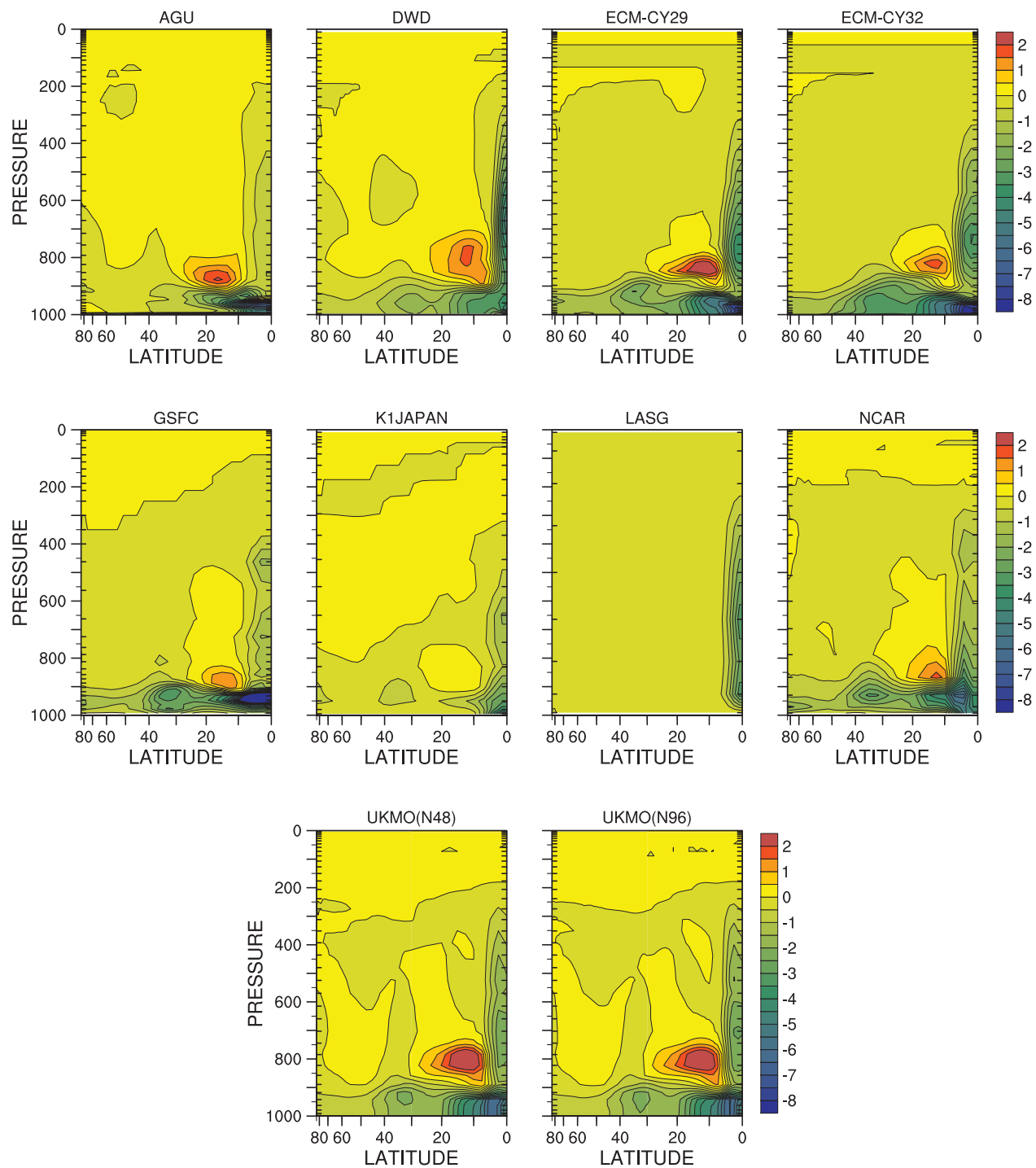
Figure 4.78: Zonal-time average parameterized convection specific humidity tendency (q_conv), g kg^{-1} day^{-1}.
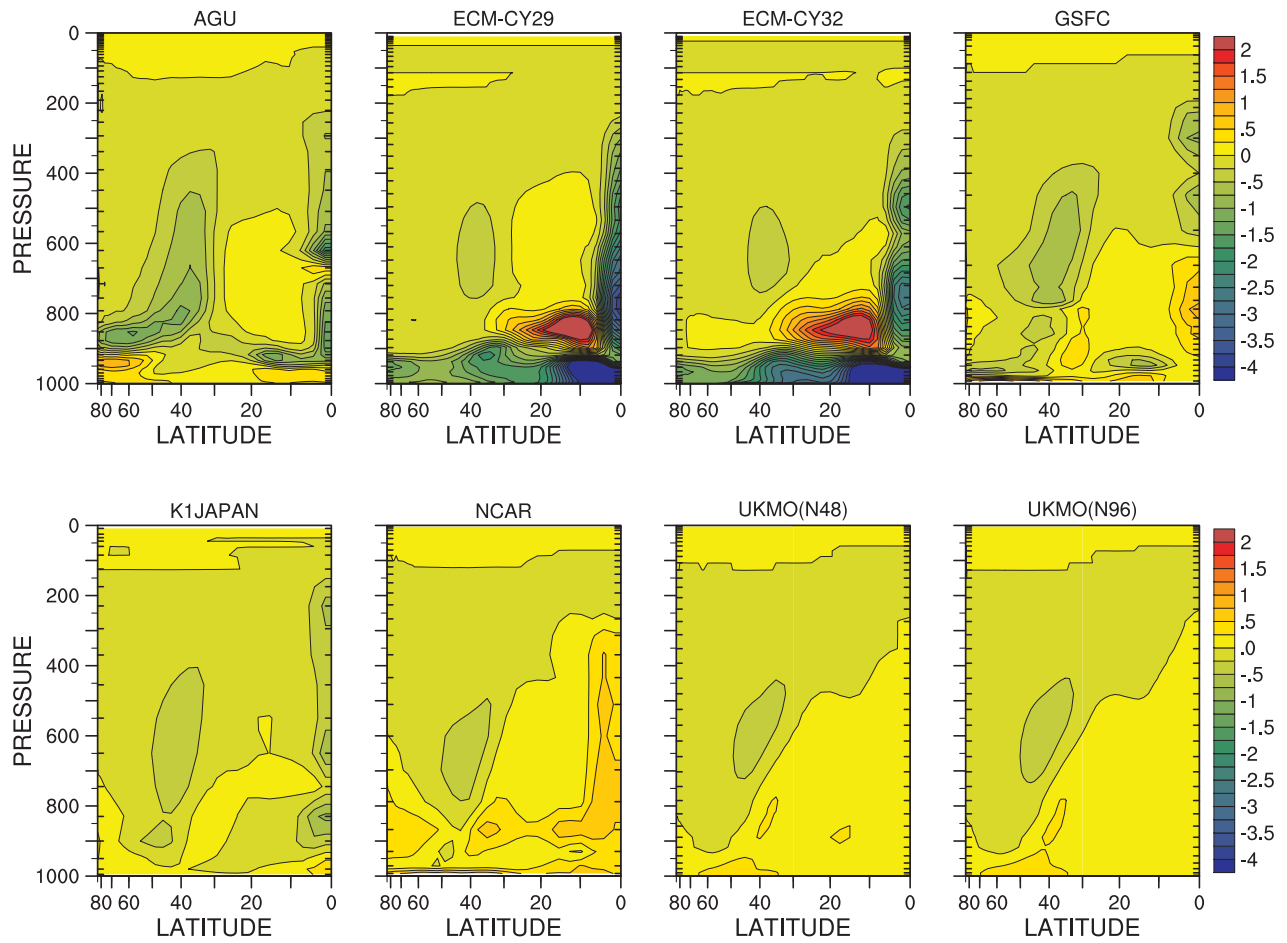
Figure 4.79: Zonal-time average parameterized cloud specific humidity tendency (q_cld), g kg^{-1} day^{-1}.
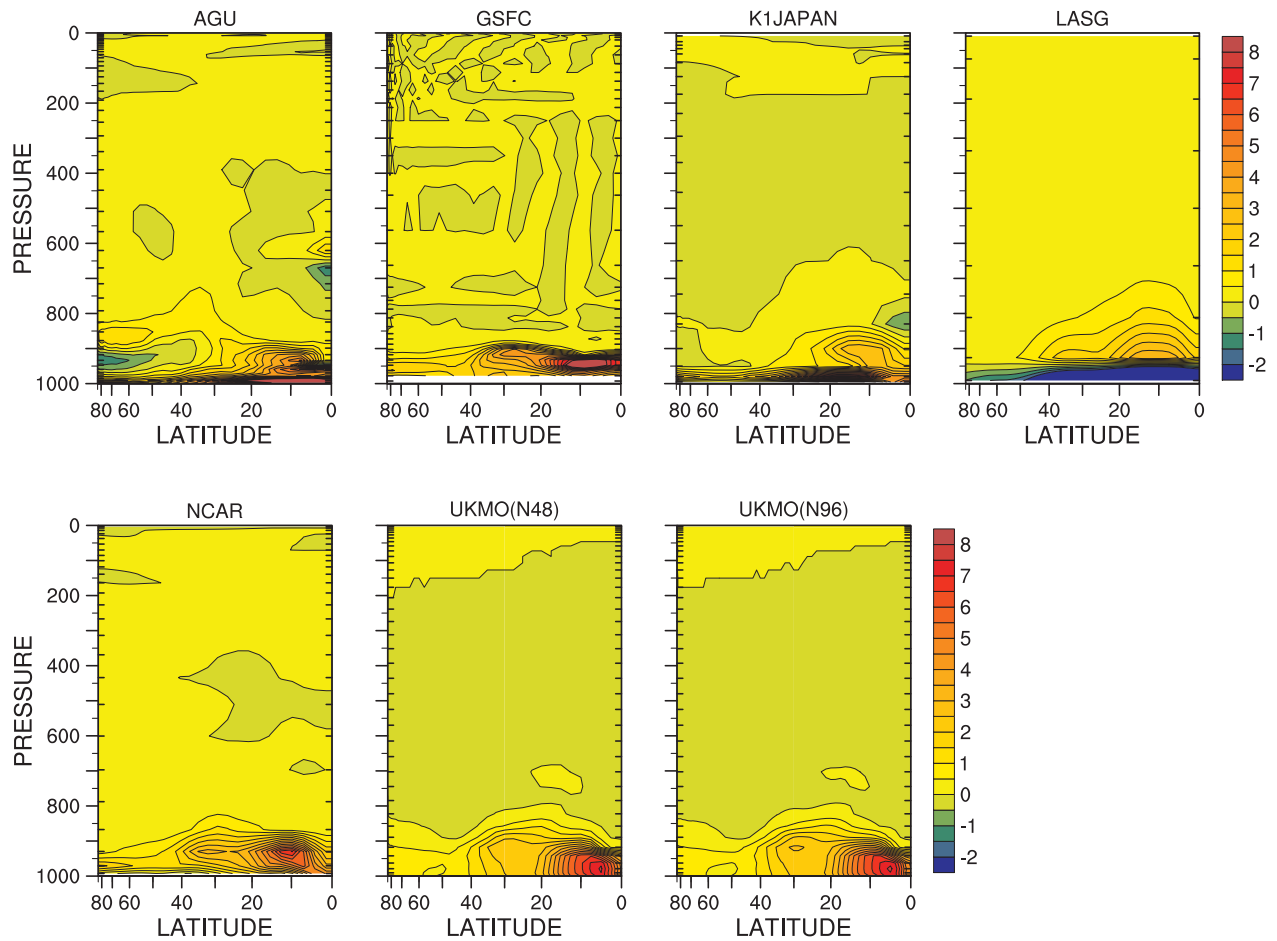
Figure 4.80: Zonal-time average parameterized turbulence specific humidity tendency (q_turb), g kg^{-1} day^{-1}.
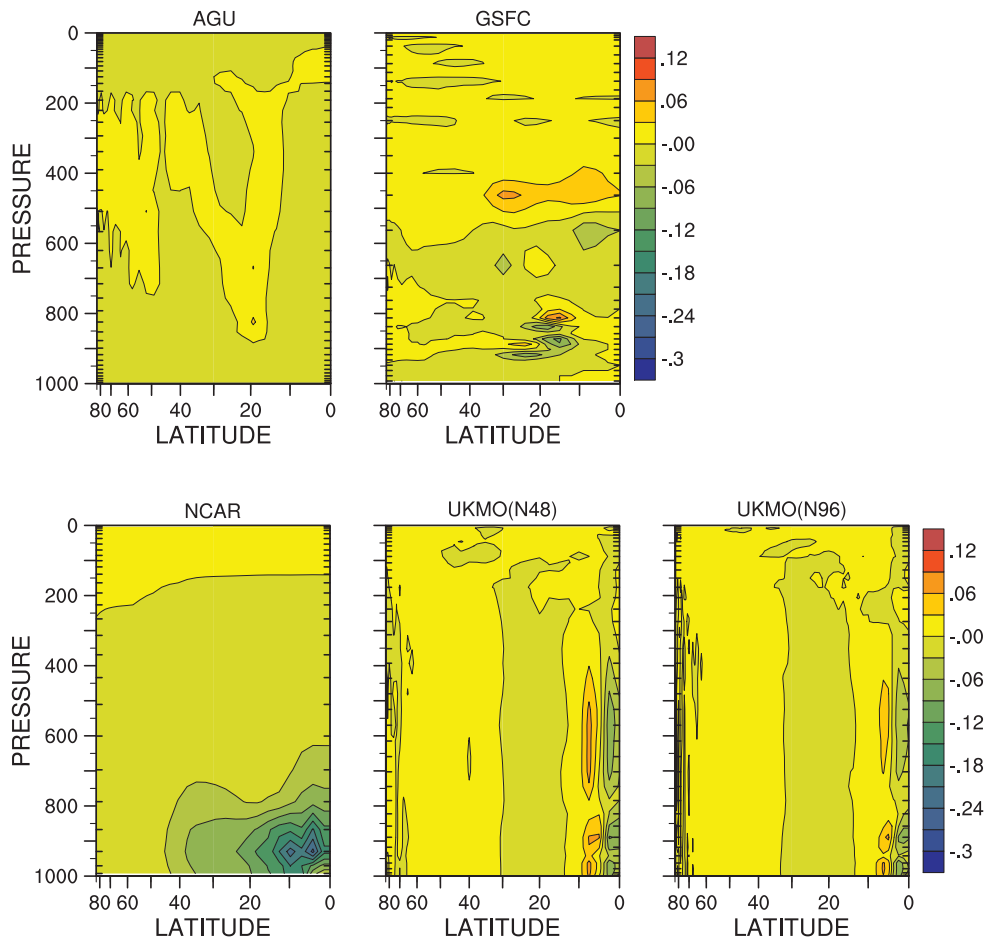
Figure 4.81: Zonal-time average negative specific humidity fixer tendency (q_negq), g kg^{-1} day^{-1}.
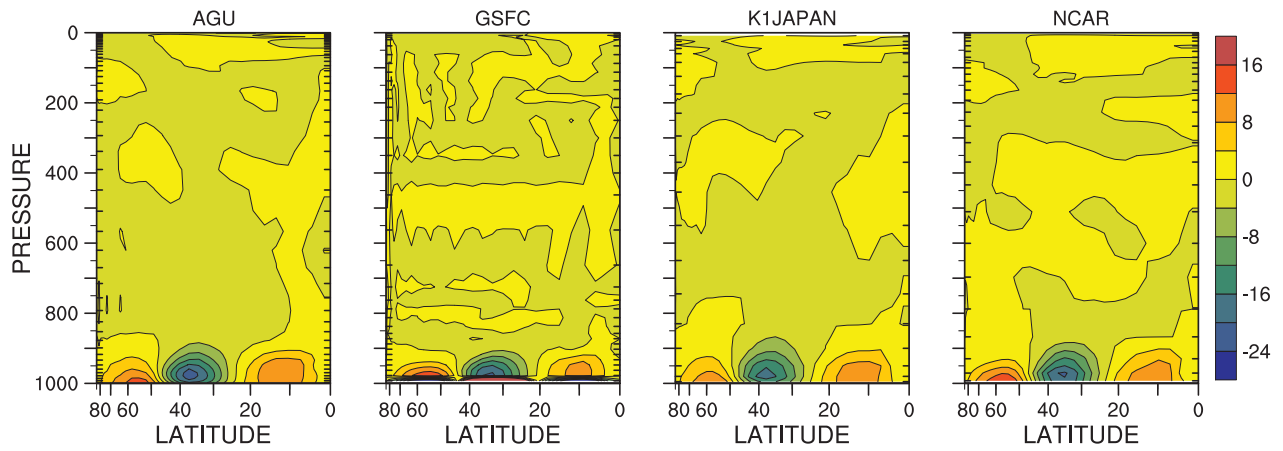
Figure 4.82: Zonal-time average total parameterized zonal wind tendency (u), m s^{-1} day^{-1}.
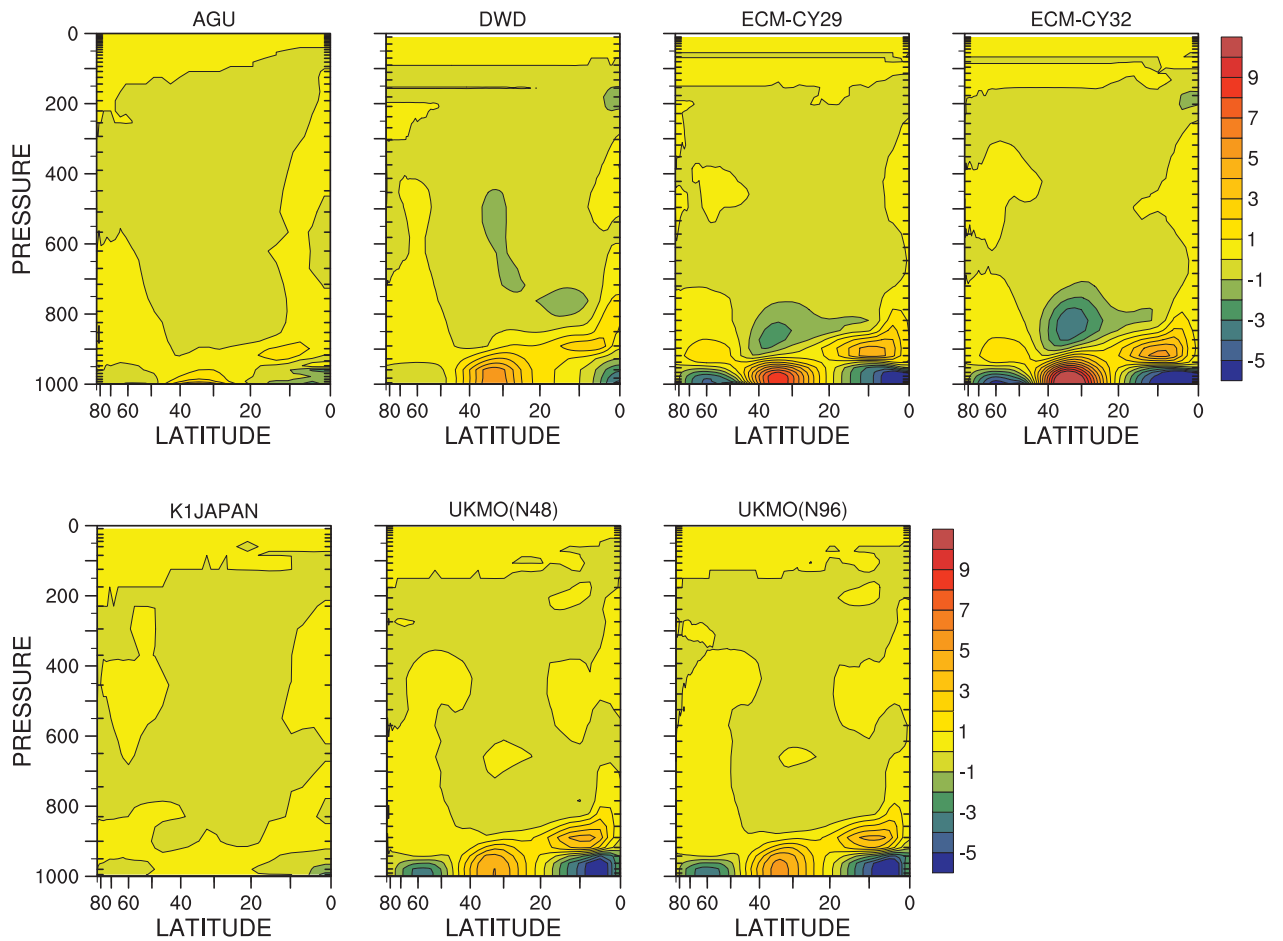
Figure 4.83: Zonal-time average parameterized convection zonal wind tendency (u_conv), m s^{-1} day^{-1}.
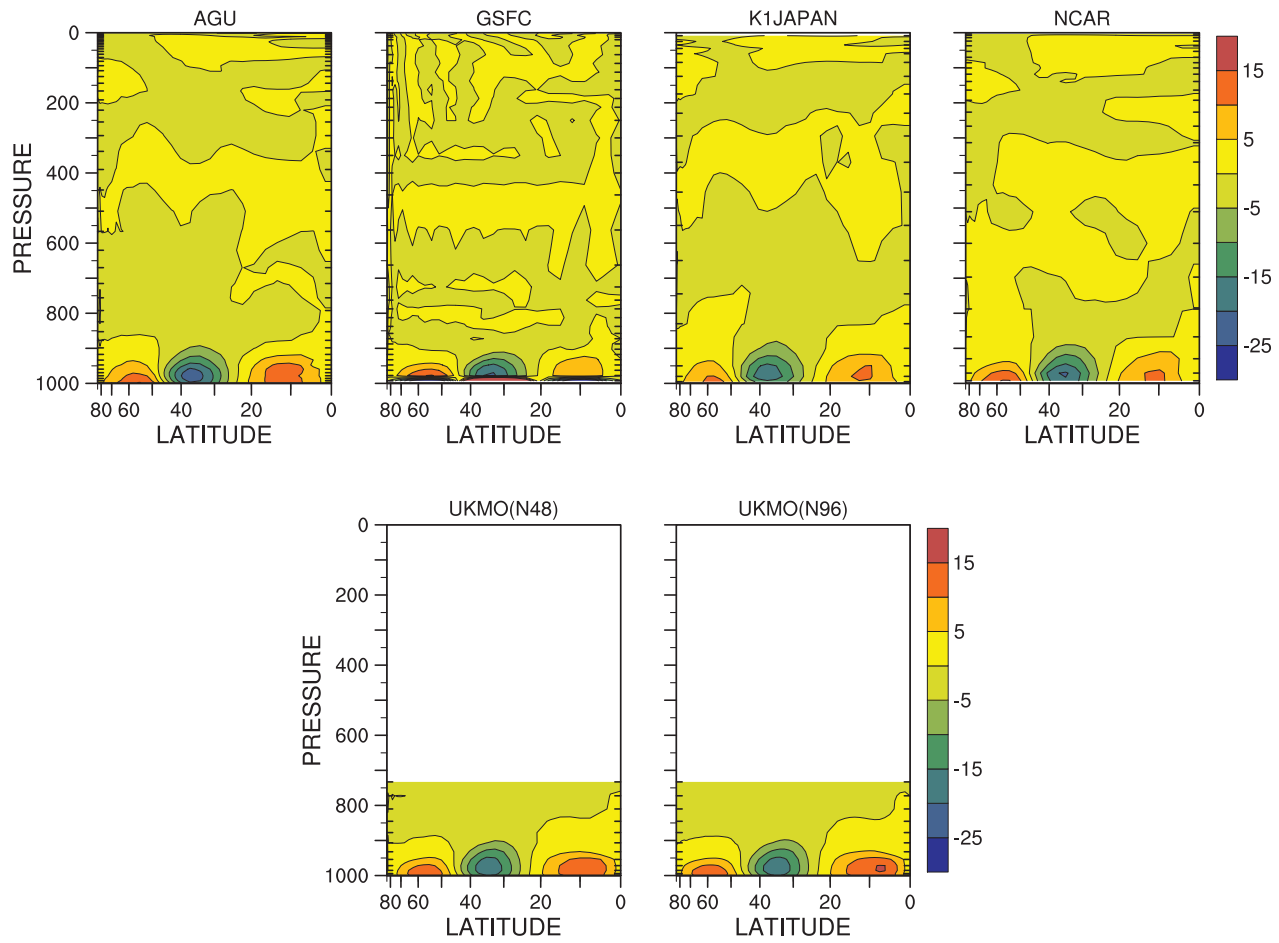
Figure 4.84: Zonal-time average parameterized turbulence zonal wind tendency (u_turb), m s^{-1} day^{-1}.
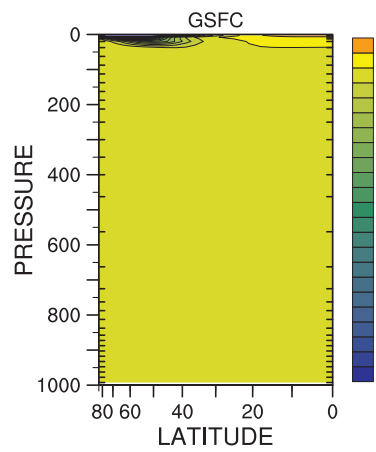
Figure 4.85: Zonal-time average gravity wave drag zonal wind tendency (u_gwd), m s^{-1} day^{-1}.
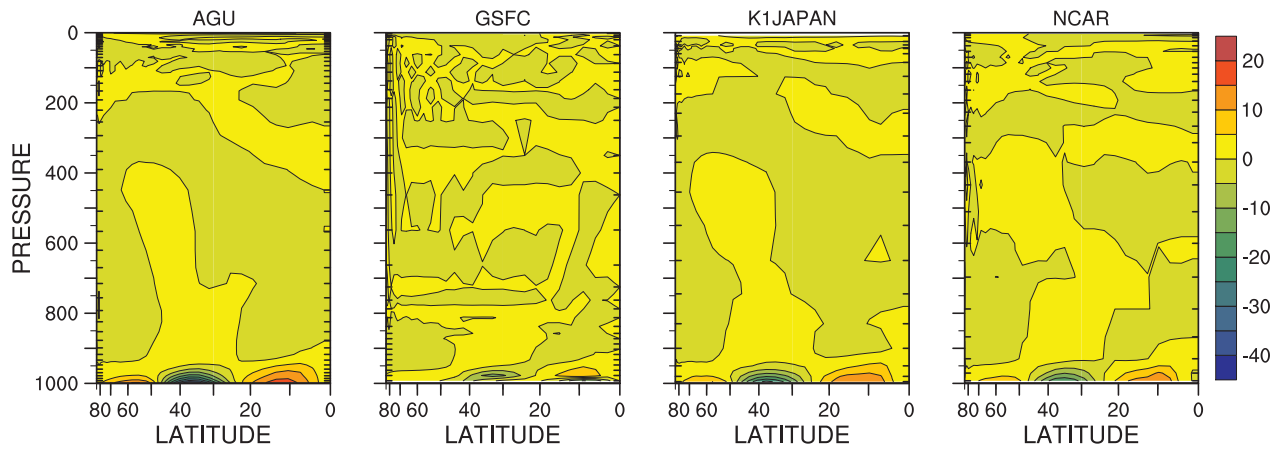
Figure 4.86: Zonal-time average total parameterized meridional wind tendency (v), m s^{-1} day^{-1}.
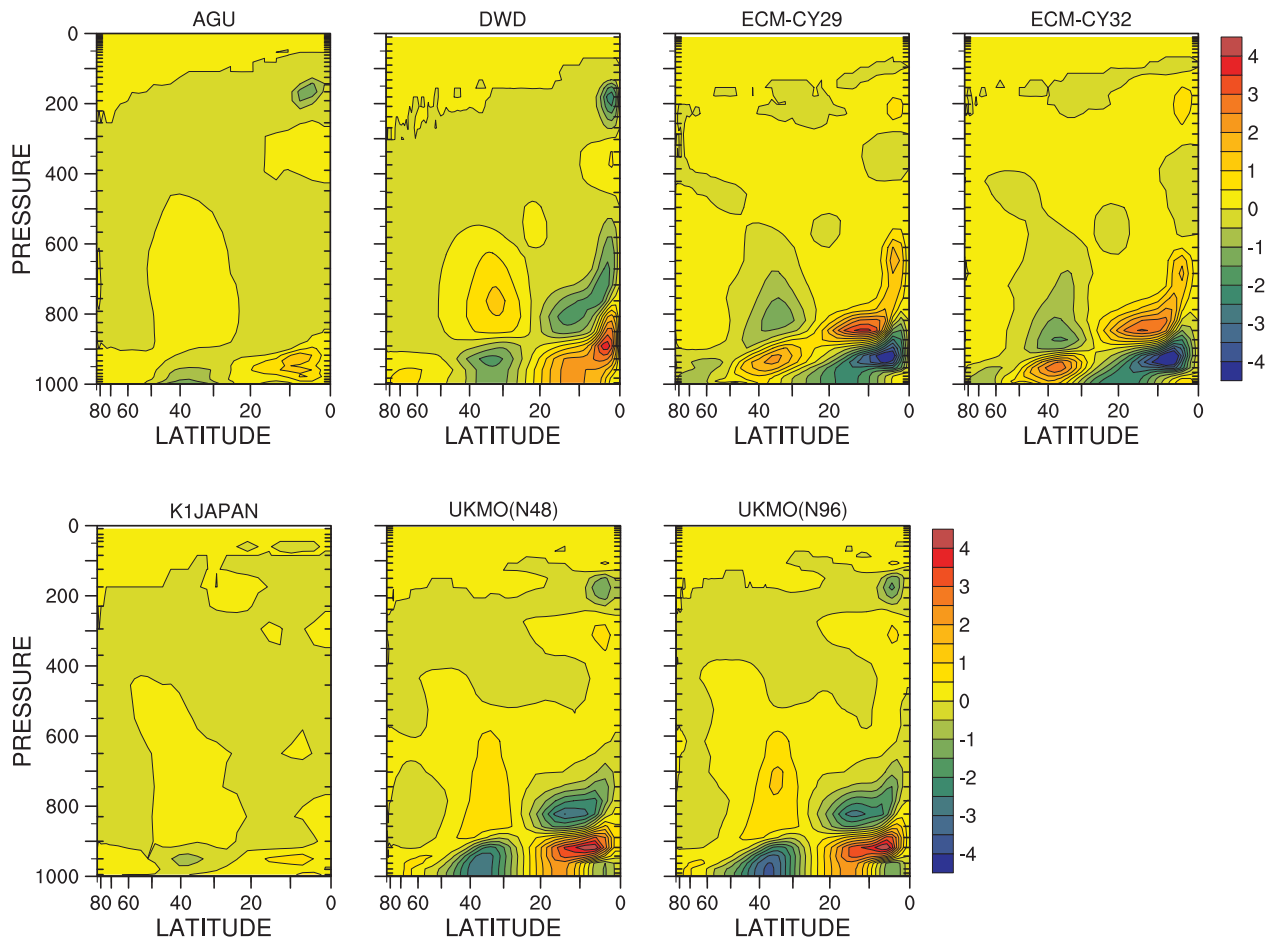
Figure 4.87: Zonal-time average parameterized convection meridional wind tendency (v_conv), m s^{-1} day^{-1}.
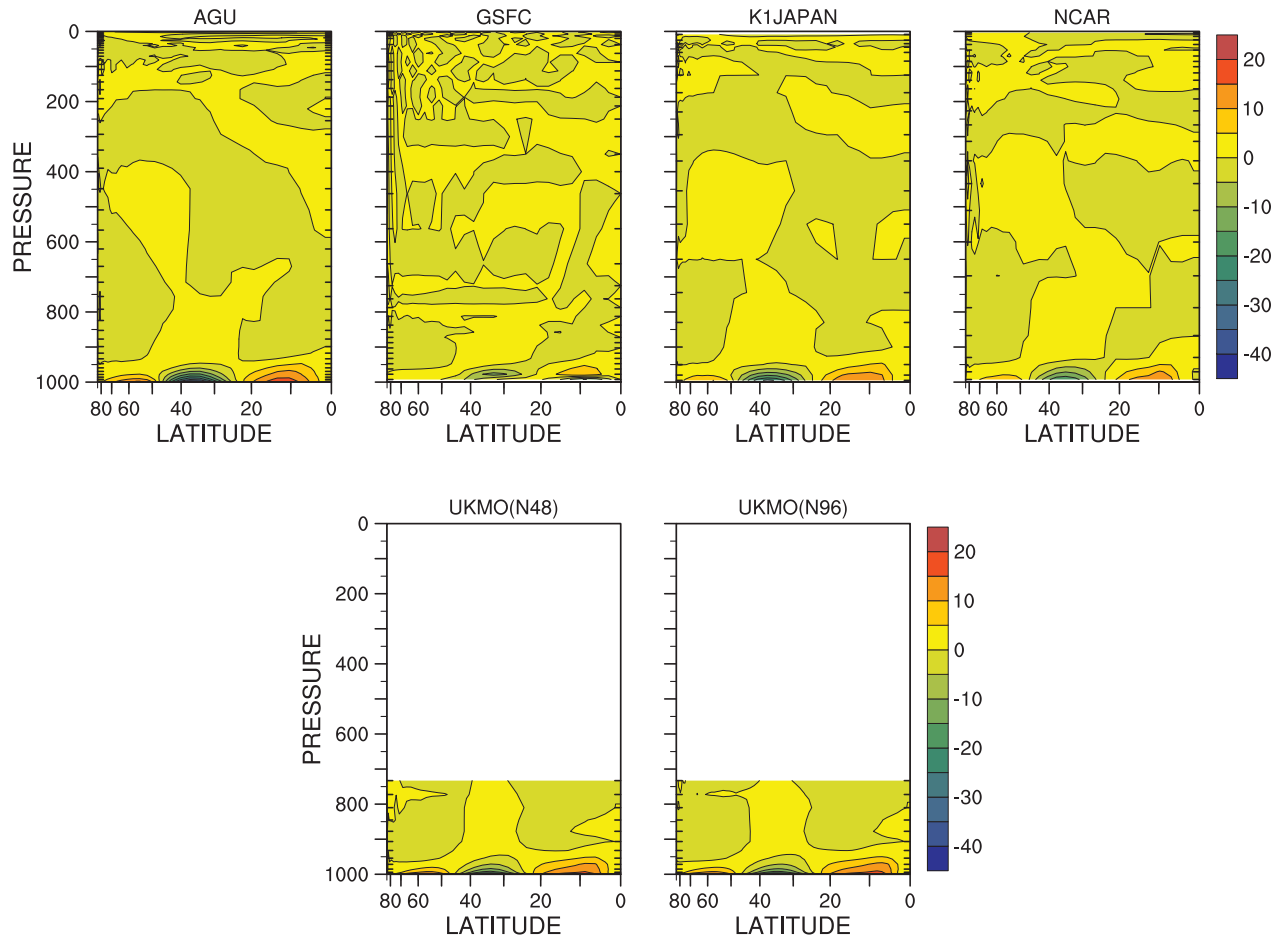
Figure 4.88: Zonal-time average turbulence parameterized meridional wind tendency (v_turb), m s^{-1} day^{-1}.
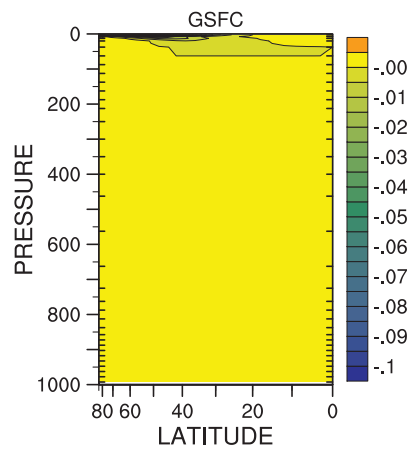
Figure 4.89: Zonal-time average gravity wave drag meridional wind tendency (v_gwd), m s^{-1} day^{-1}.
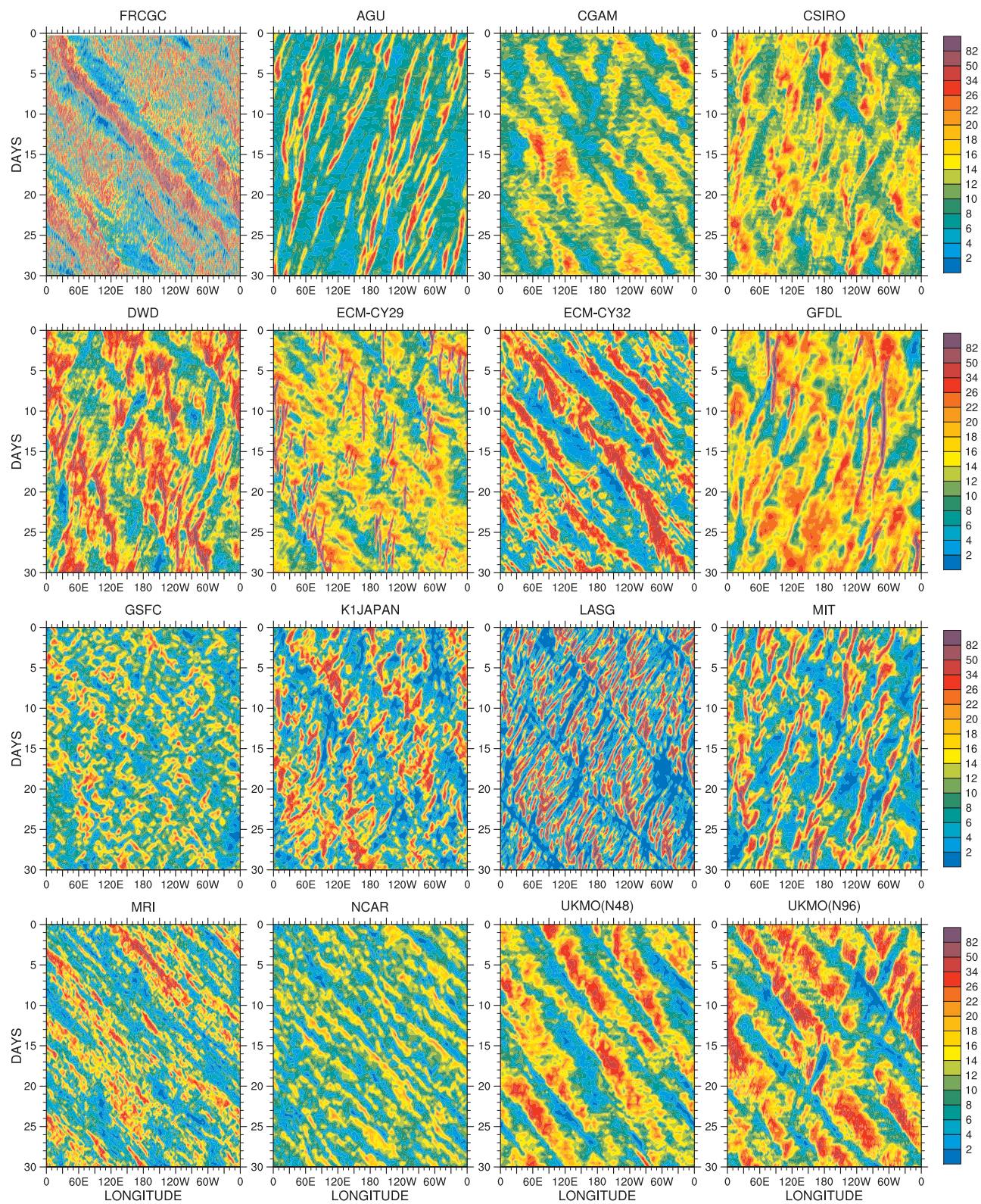
Figure 4.90: Hovmöller plots of equatorial precipitation (tppn) averaged from -5° to +5° latitude, mm day^{-1}.
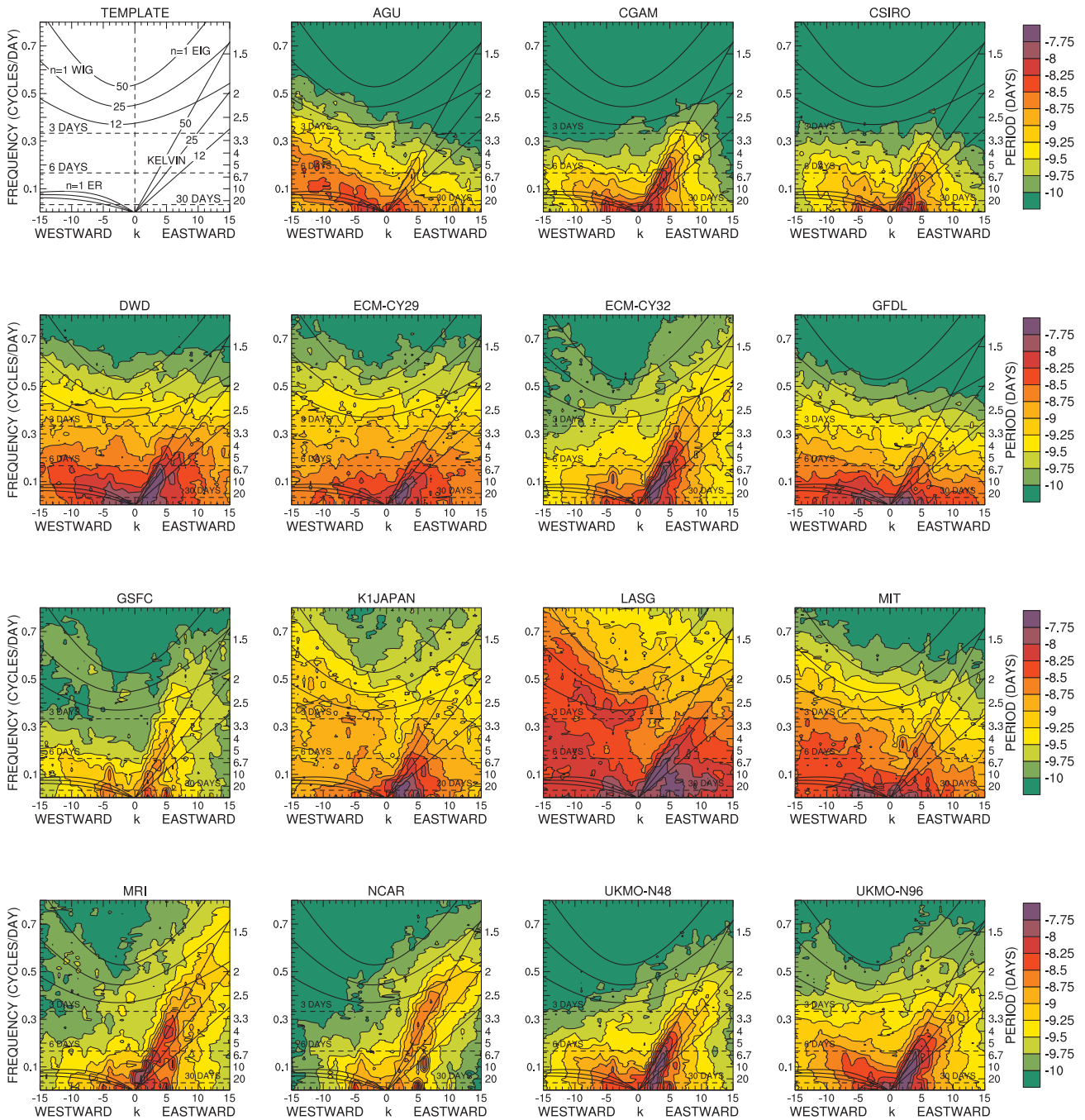
Figure 4.91: Wavenumber-frequency diagrams of log of power of symmetric modes of equatorial precipitation (tppn), 10°S to 10°N.
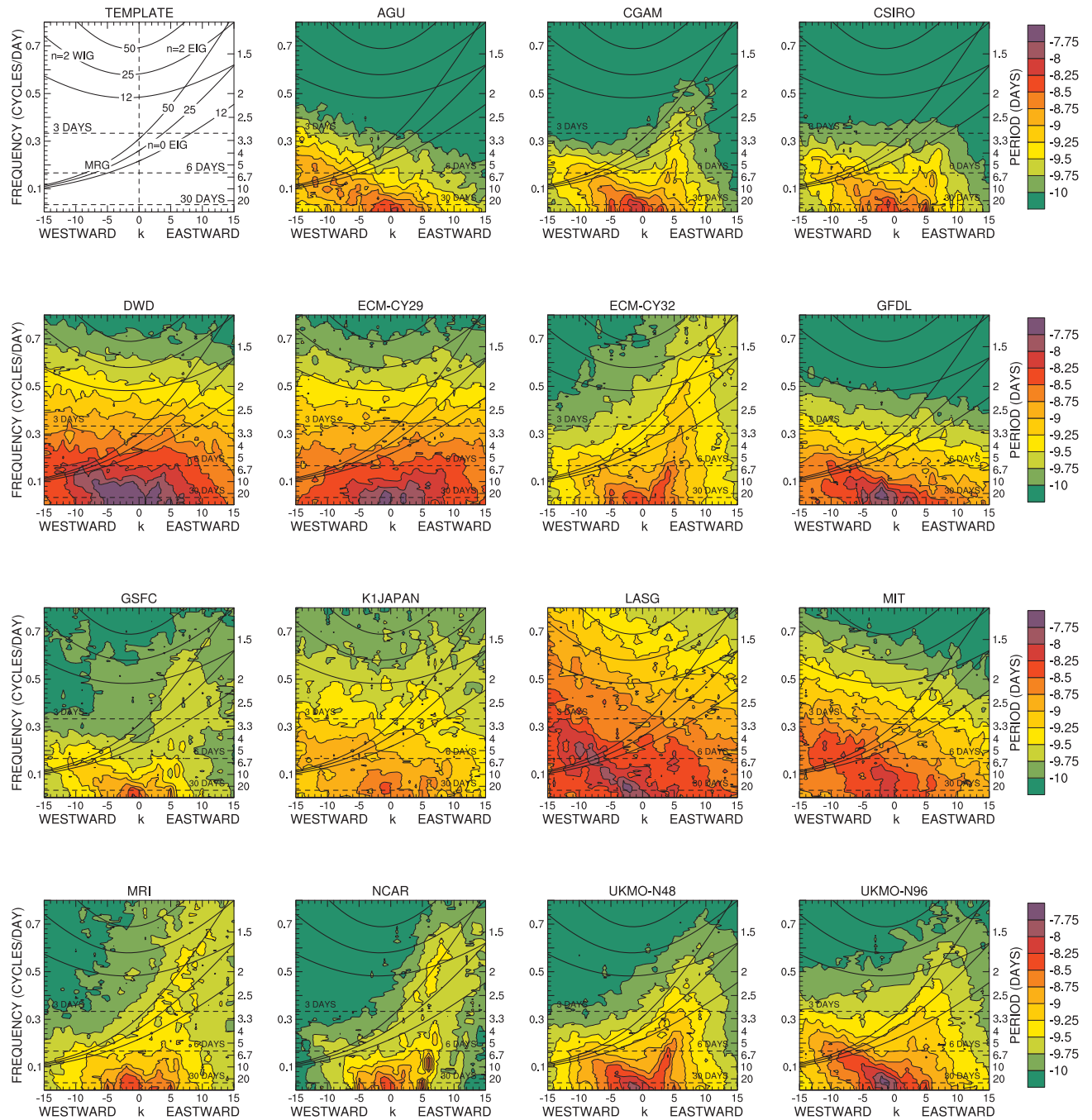
Figure 4.92: Wavenumber-frequency diagrams of log of power of anti-symmetric modes of equatorial precipitation (tppn), 10°S to 10°N.
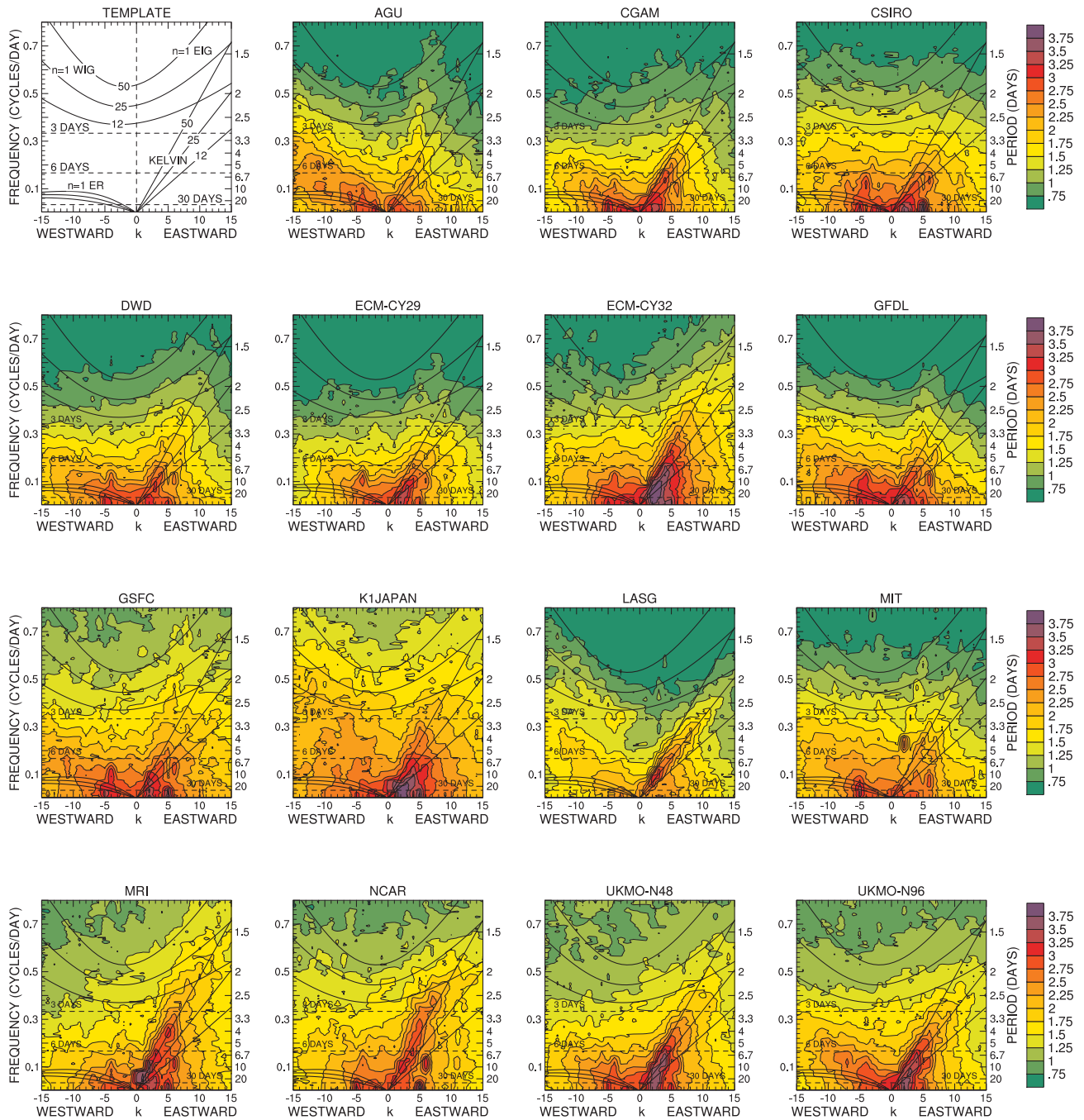
Figure 4.93: Wavenumber-frequency diagrams of log of power of symmetric modes of equatorial OLR (lw_toa), 10°S to 10°N.
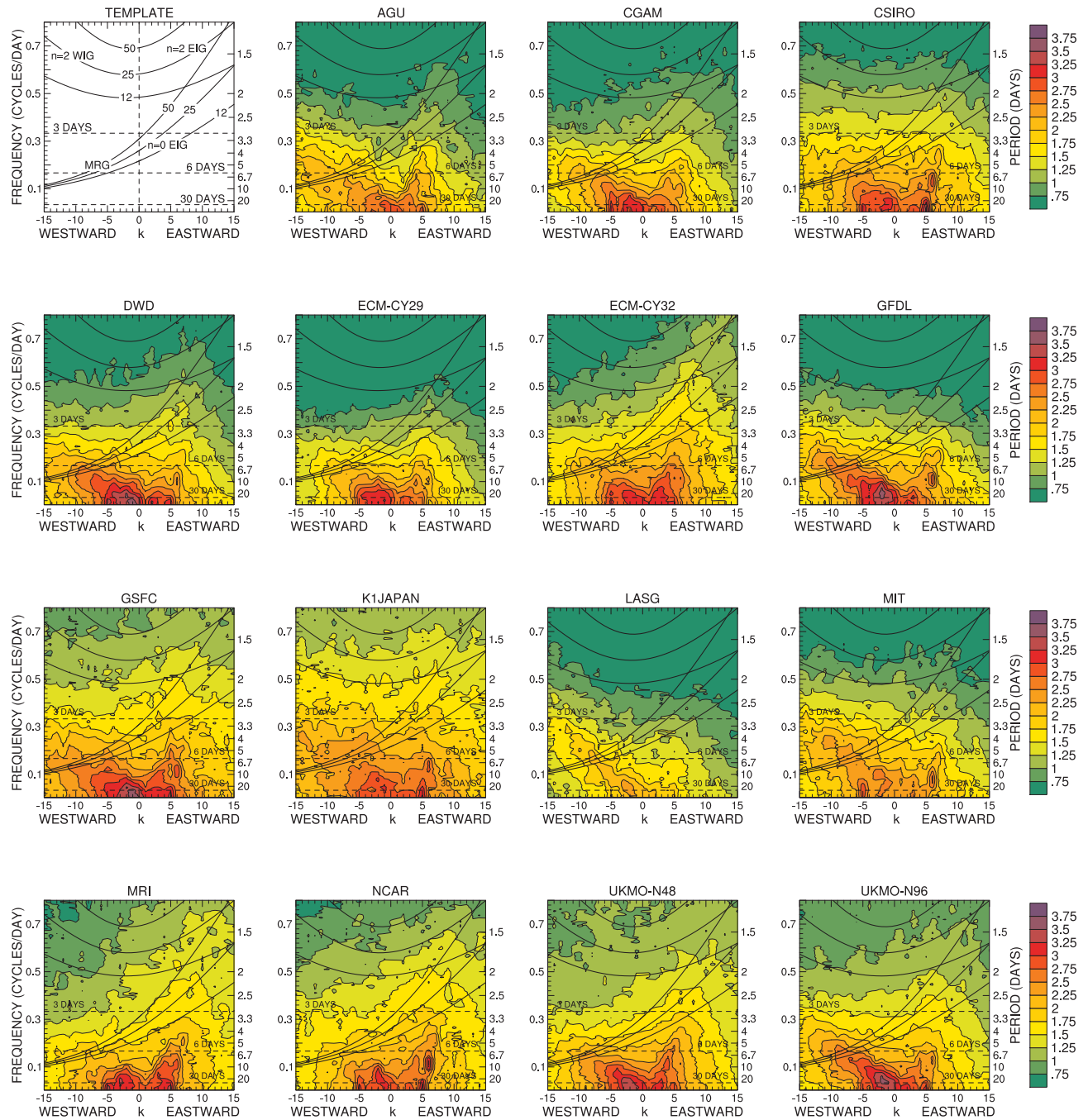
Figure 4.94: Wavenumber-frequency diagrams of log of power of anti-symmetric modes of equatorial OLR (lw_toa), 10°S to 10°N.
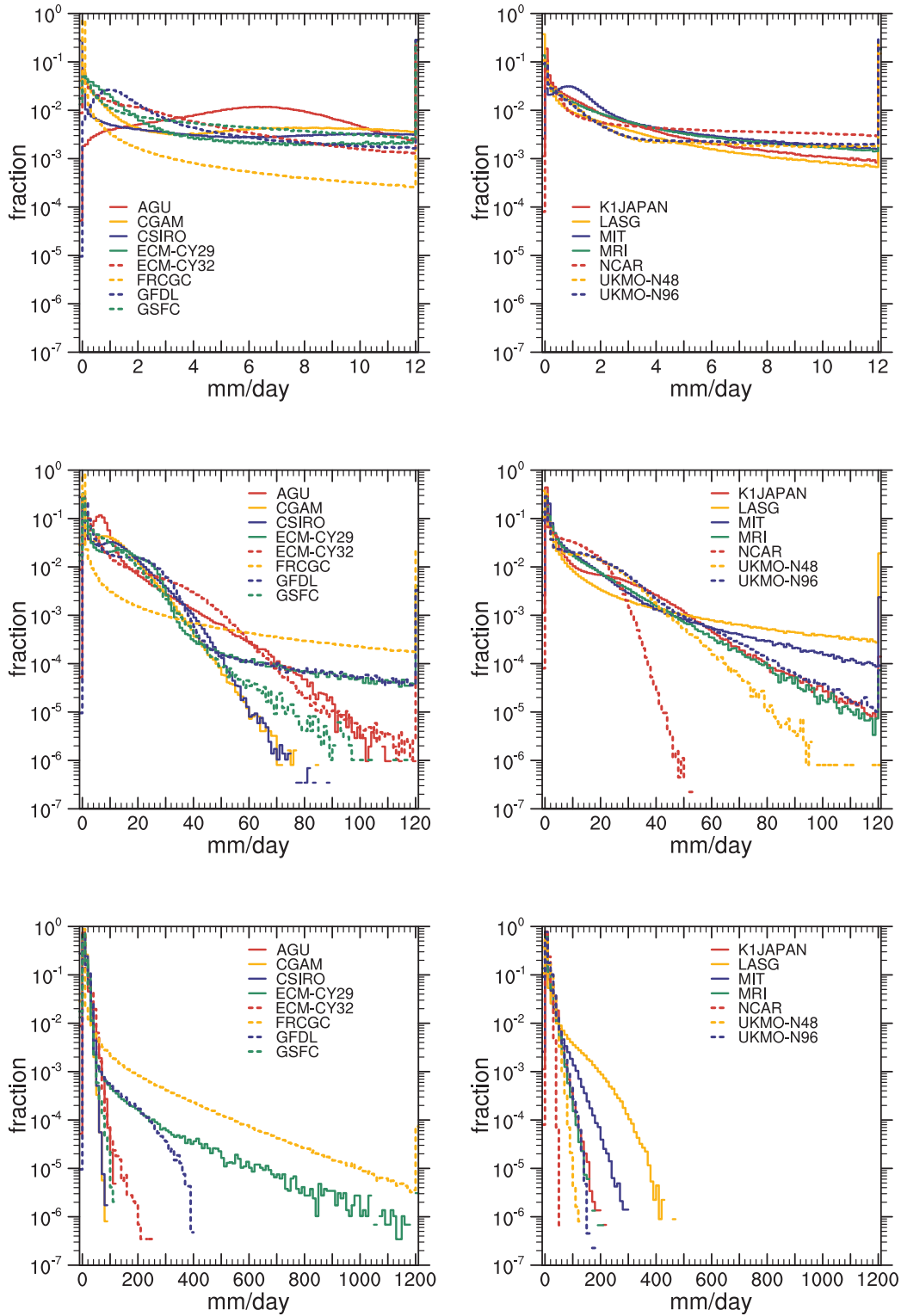
Figure 4.95: Fraction of time precipitation (tppn) from $-10°$ to $+10°$ latitude is in (top row) 0.1 mm day^{-1} bins ranging from 0 to 12 mm day^{-1}, (center row) 1 mm day^{-1} bins ranging from 0 to 120 mm day^{-1}, and (bottom row) 10 mm day^{-1} bins ranging from 0 to 1200 mm day^{-1}.
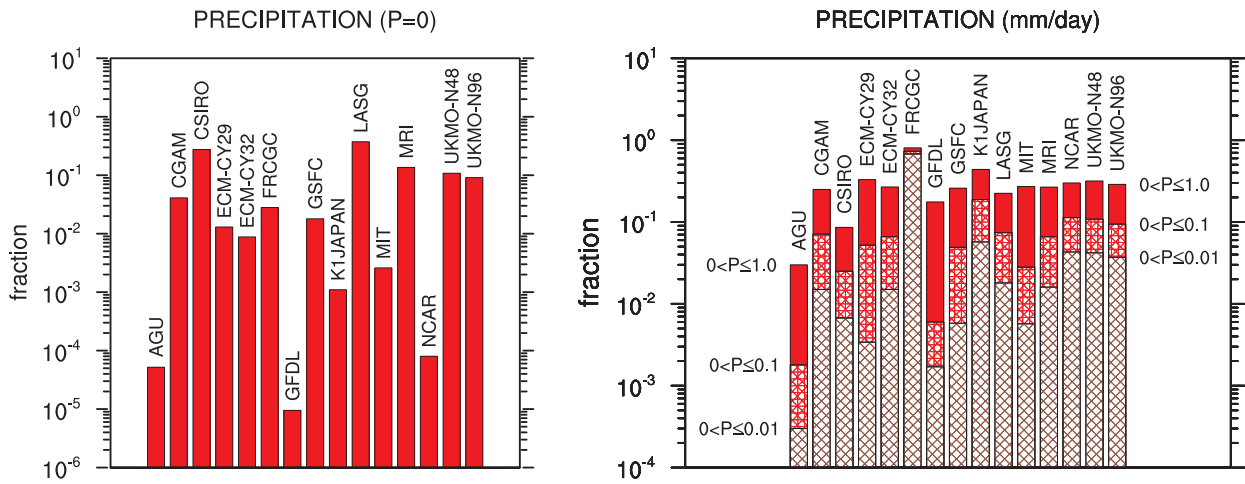
Figure 4.96: Fraction of time precipitation, p, is (left) equal to zero, and (right) in the ranges $0 < p \leq 0.01$, $0 < p \leq 0.1$ and $0 < p \leq 1.0$ mm day^{-1}.
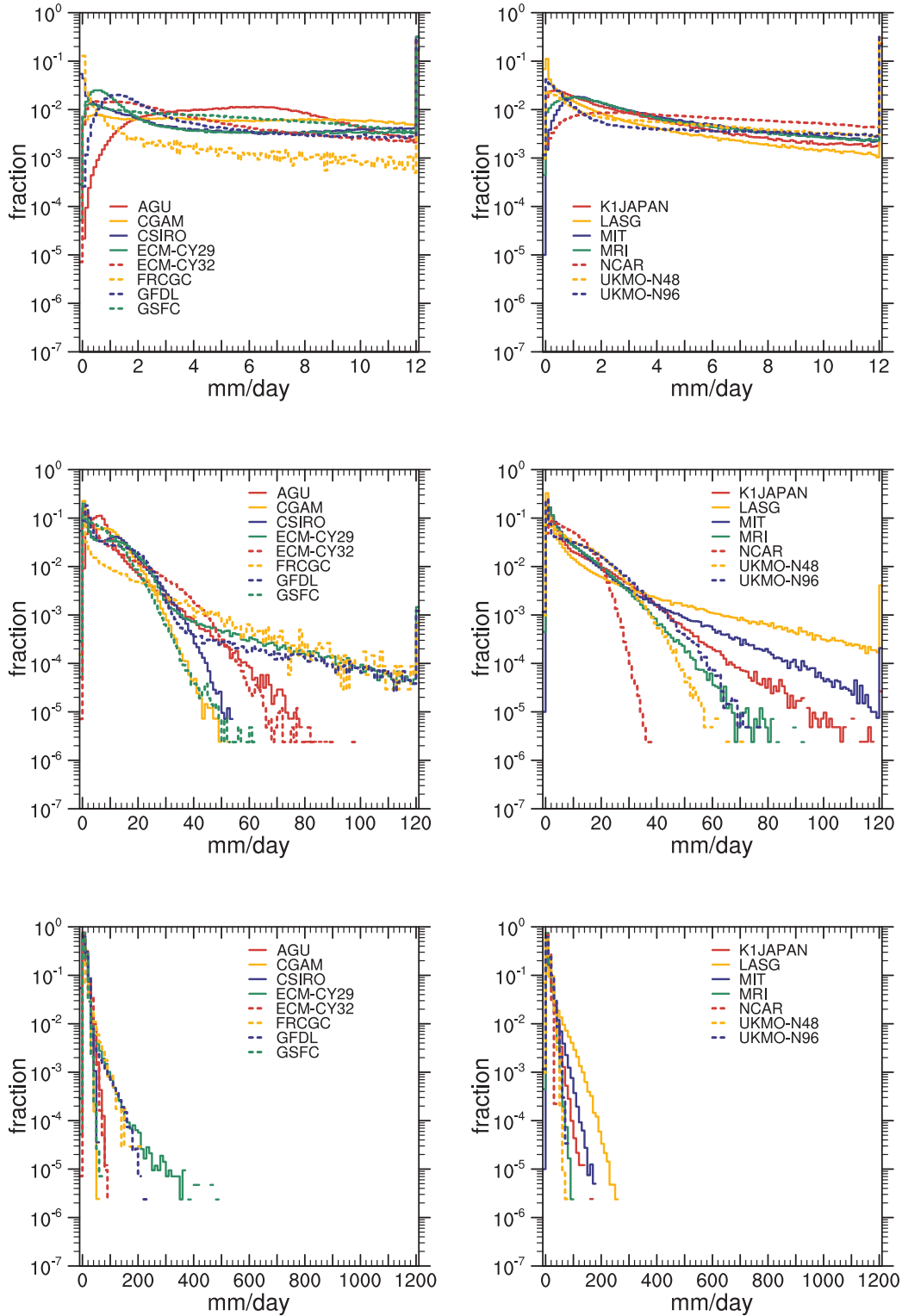
Figure 4.97: Fraction of time precipitation (tppn) from $-10°$ to $+10°$ latitude is in (top row) 0.1 mm day^{-1} bins ranging from 0 to 12 mm day^{-1}, (center row) 1 mm day^{-1} bins ranging from 0 to 120 mm day^{-1}, and (bottom row) 10 mm day^{-1} bins ranging from 0 to 1200 mm day^{-1}. Grid values have been conservatively averaged to a 5° latitude-longitude grid.
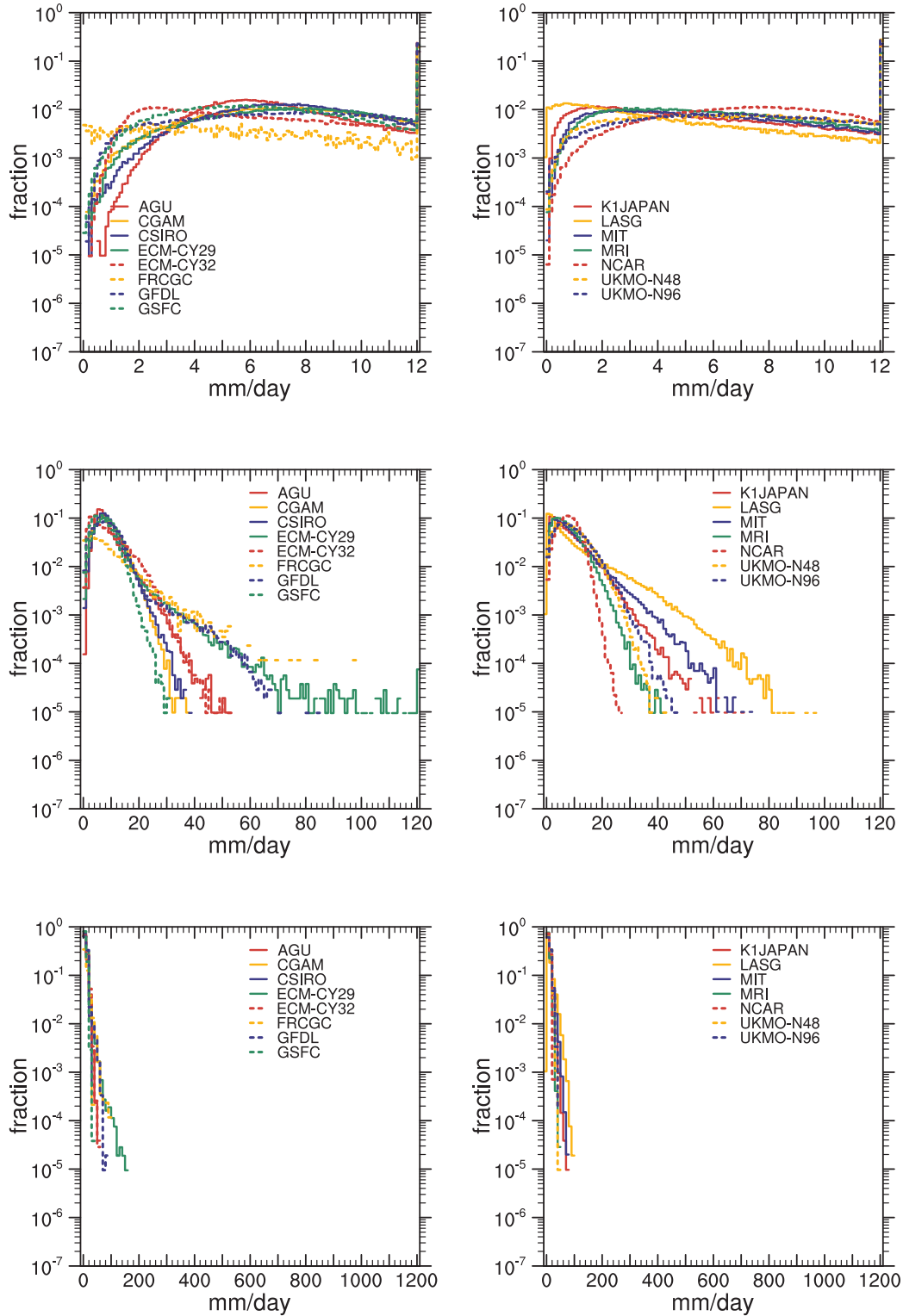
Figure 4.98: Fraction of time precipitation (tppn) from $-10°$ to $+10°$ latitude is in (top row) 0.1 mm day^{-1} bins ranging from 0 to 12 mm day^{-1}, (center row) 1 mm day^{-1} bins ranging from 0 to 120 mm day^{-1}, and (bottom row) 10 mm day^{-1} bins ranging from 0 to 1200 mm day^{-1}. Grid values have been conservatively averaged to a $10°$ latitude-longitude grid.
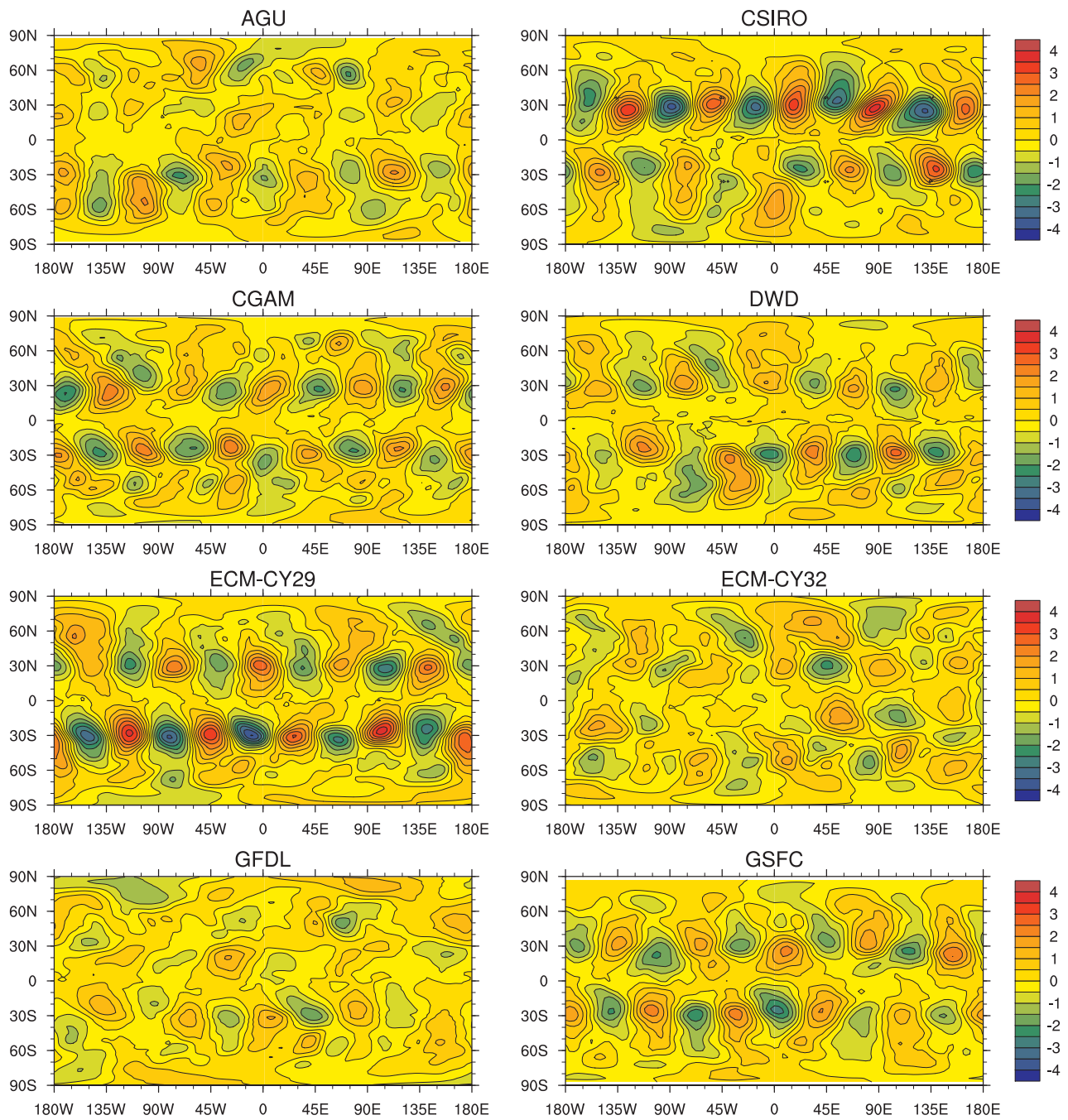
Figure 4.99: Time average 250 mb meridional velocity minus zonal average for individual models for the CONTROL (v250), m sec^{-1}
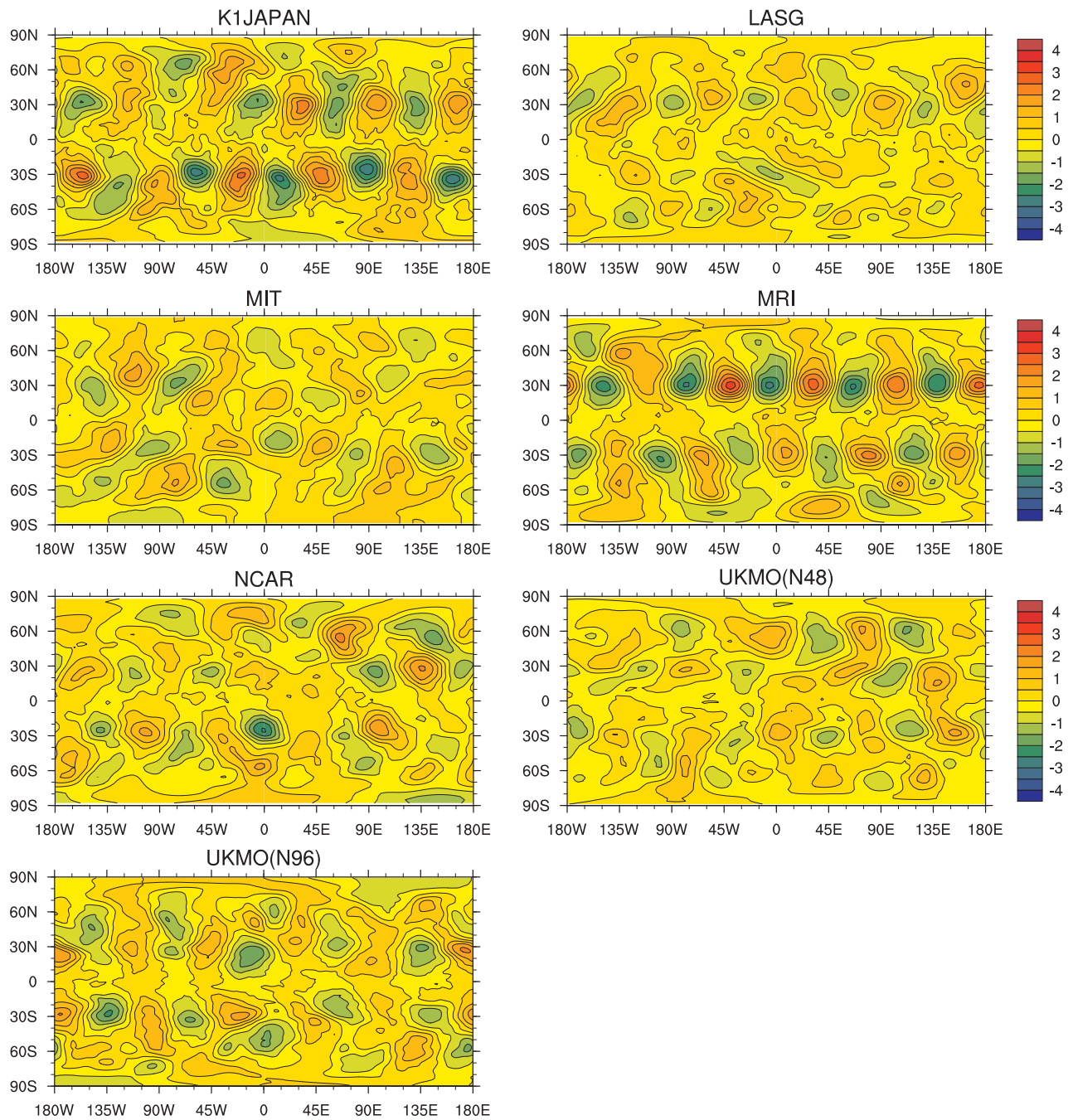
Figure 4.99 (continued): Time average meridional velocity at 250 mb minus zonal average for individual models for the CONTROL, m sec^{-1}
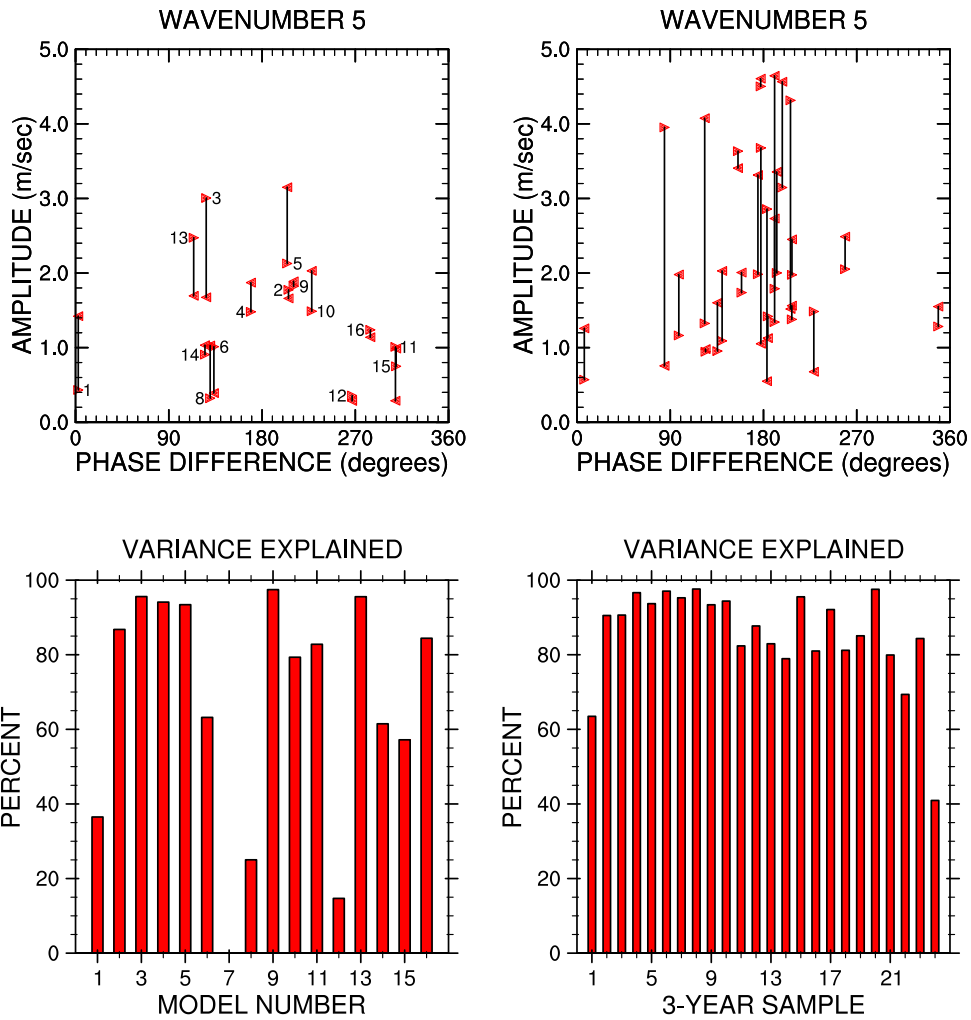
Figure 4.100: Top row: Amplitude of wavenumber-five of 3-year average meridional velocity at 30°N (right arrow head) and 30°S (left arrow head) at 250 hPa, versus harmonic phase difference between the hemispheres, for (left) 15 APE models omitting FRCGC and (right) 24 sequential 3-year averages from the NCAR model. Bottom row: percent variance explained by wavenumber 5 at 30°N. Model numbers are defined in Table 3.2.
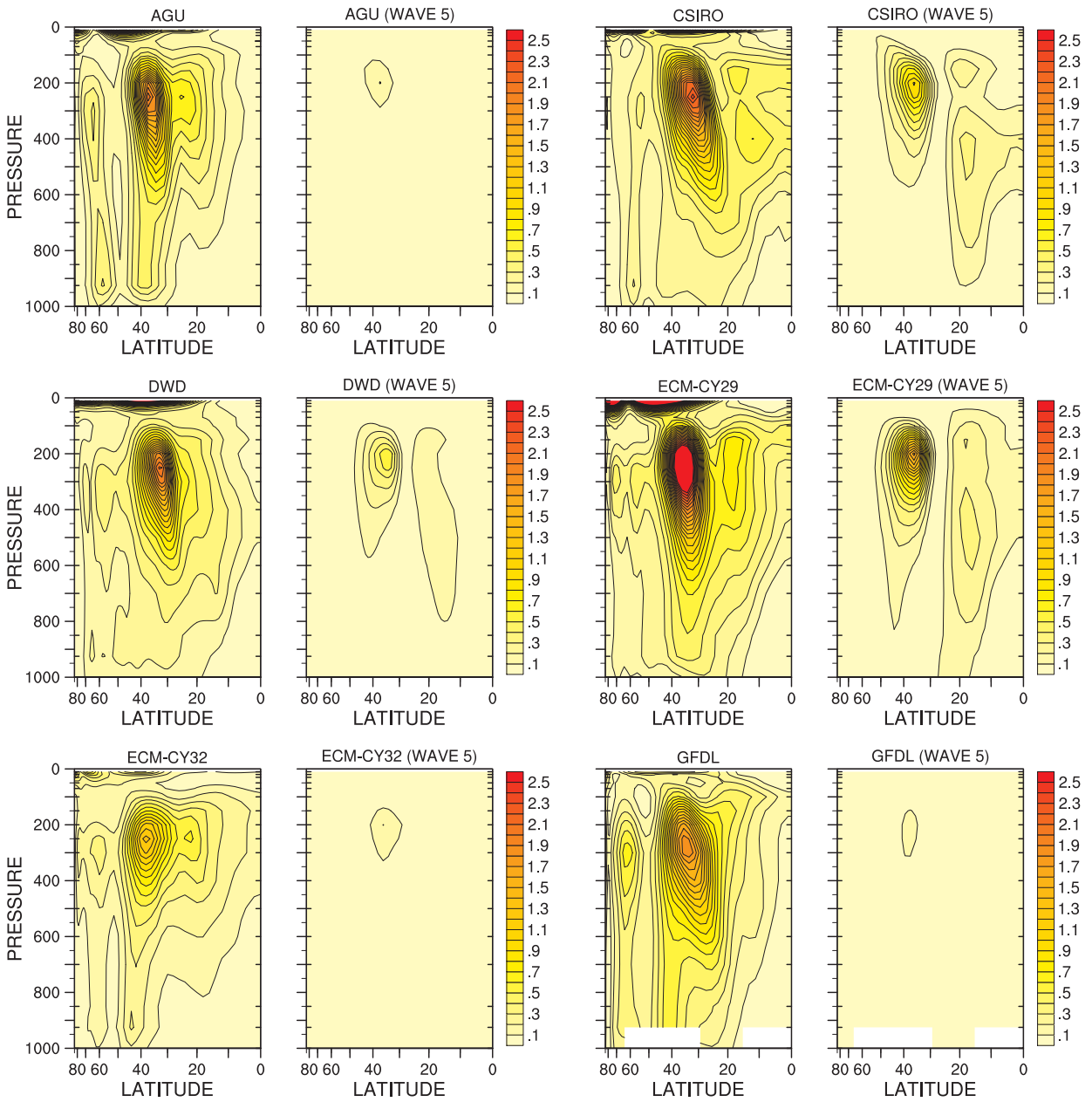
Figure 4.101: Individual model u variance, stationary eddy, total and wavenumber 5, se_uu, $\left[(\overline{u}^*)^2\right]$, m^2 s^{-2}.
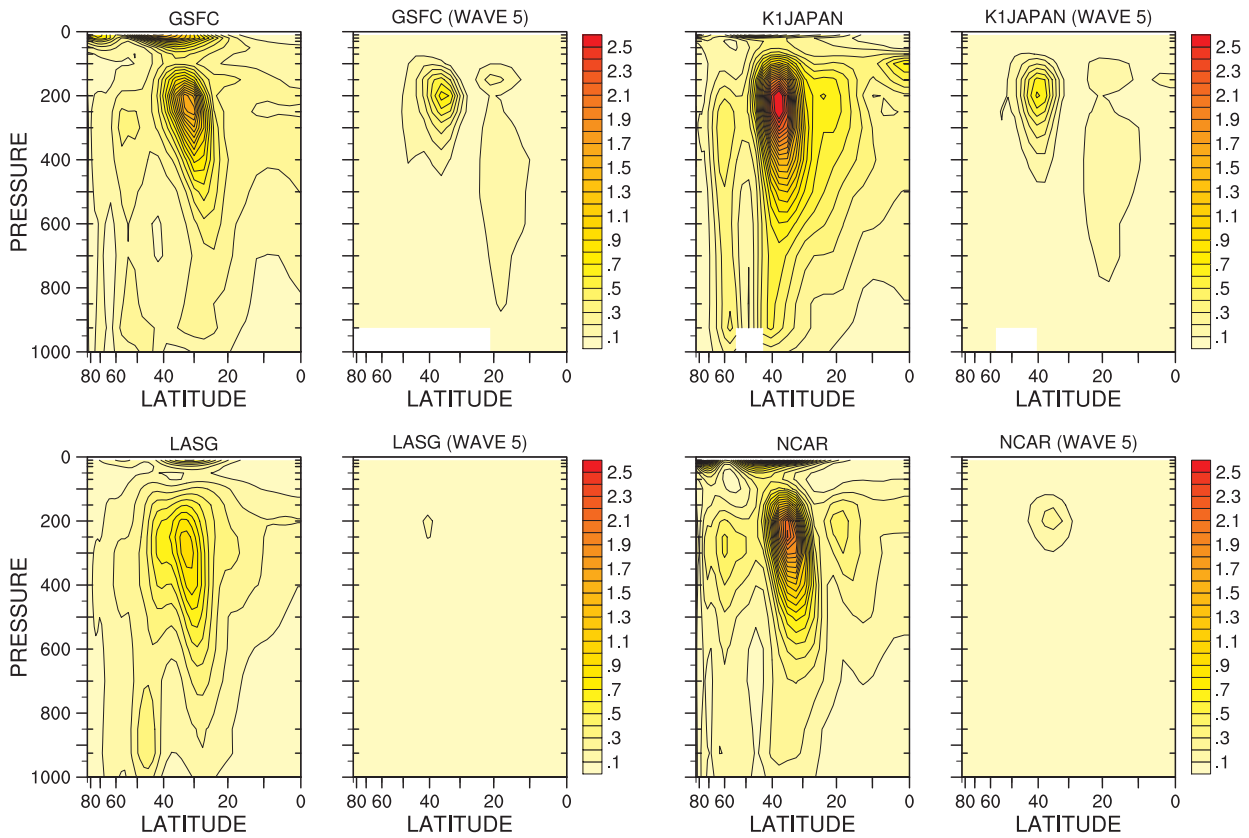
Figure 4.101 (continued): Individual model u variance, stationary eddy, total and wavenumber 5, se_uu, $\left[(\overline{u}^*)^2\right]$, $m^2\ s^{-2}$.
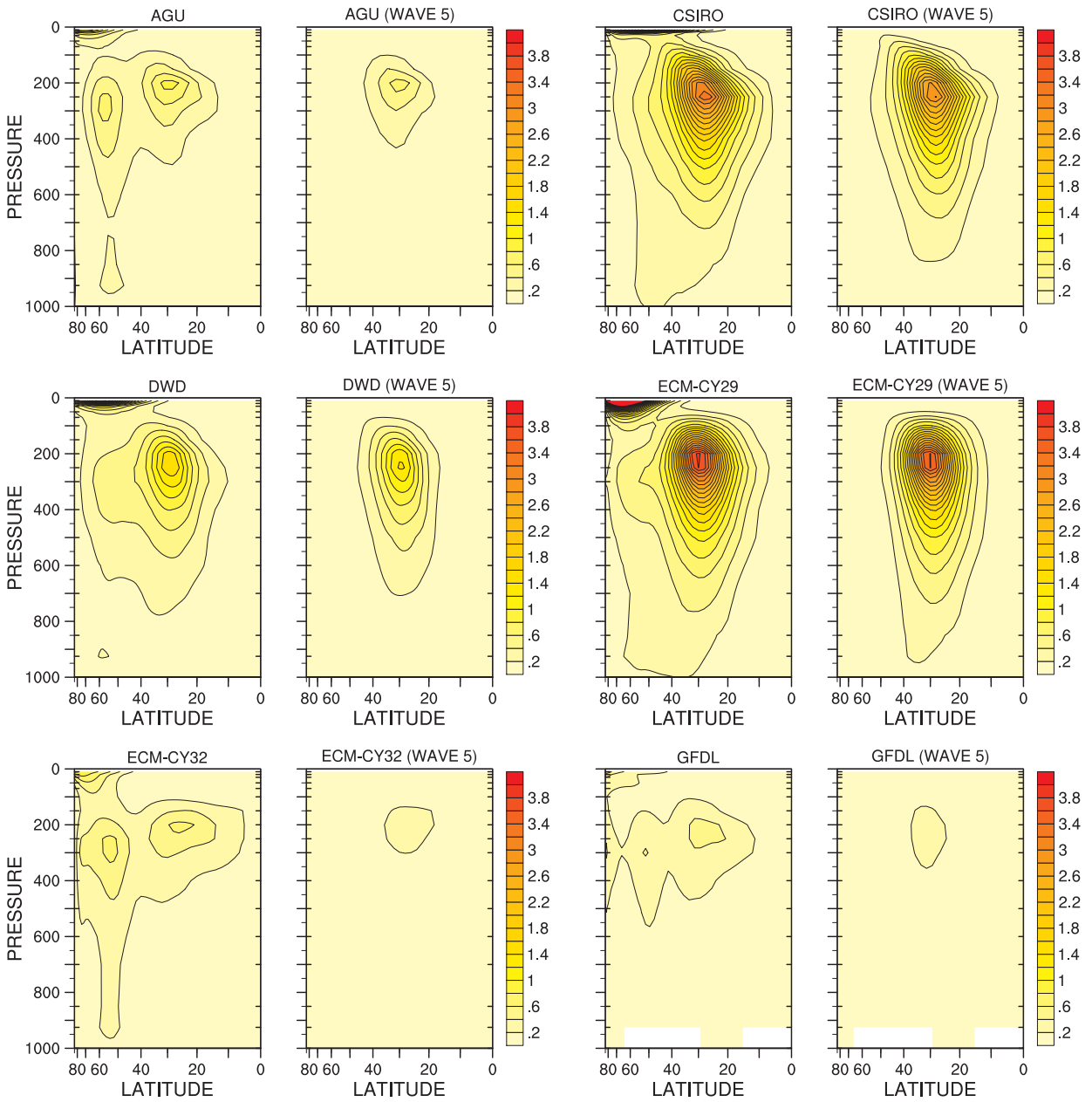
Figure 4.102: Individual model v variance, stationary eddy, total and wavenumber 5, se_vv, $\left[(\overline{v}^*)^2\right]$, m^2 s^{-2}.
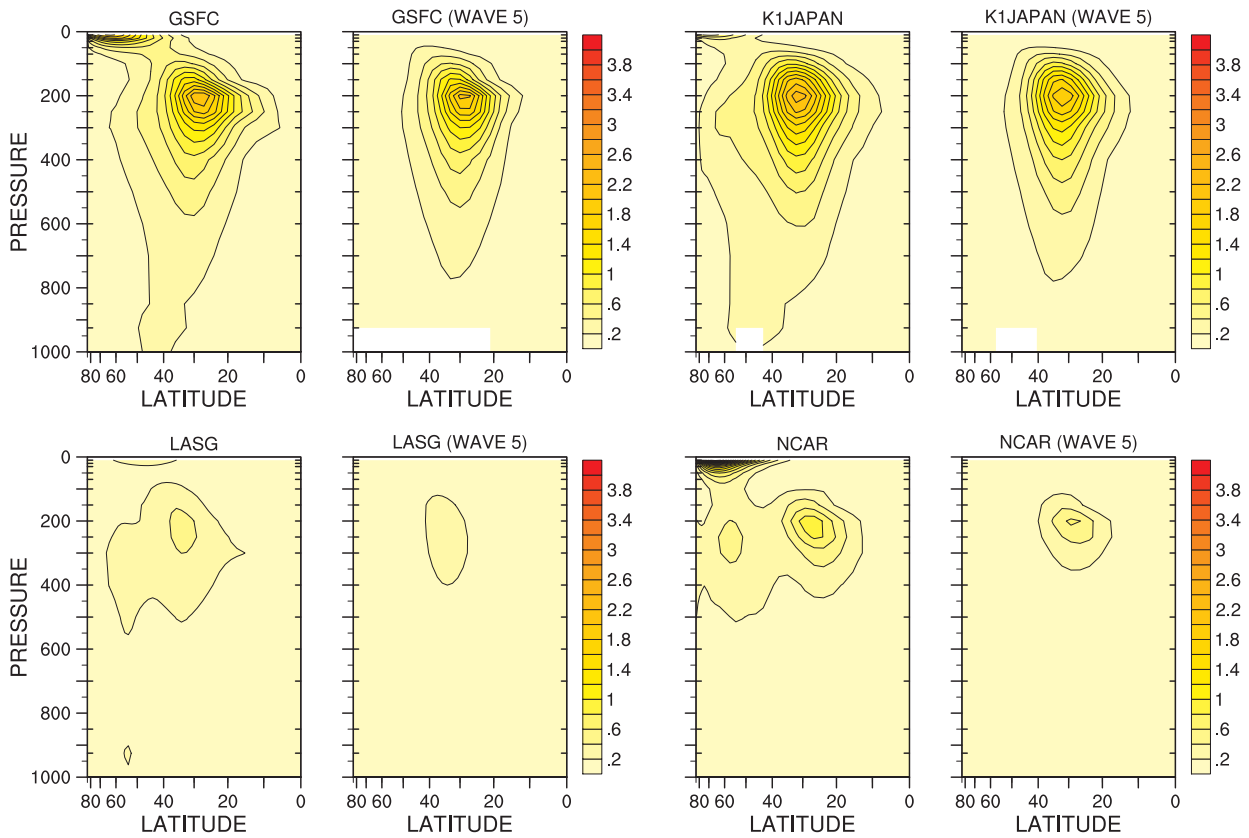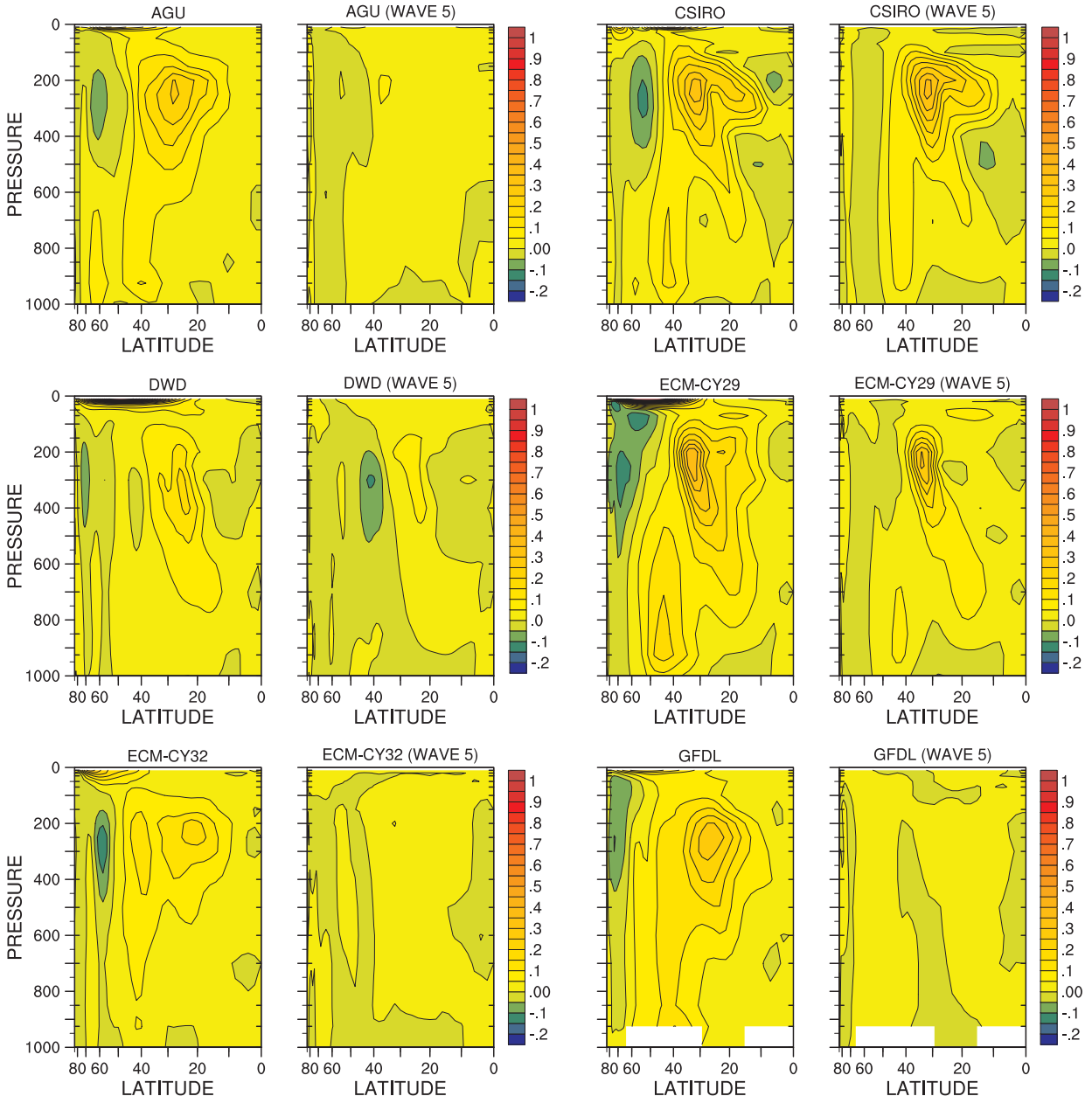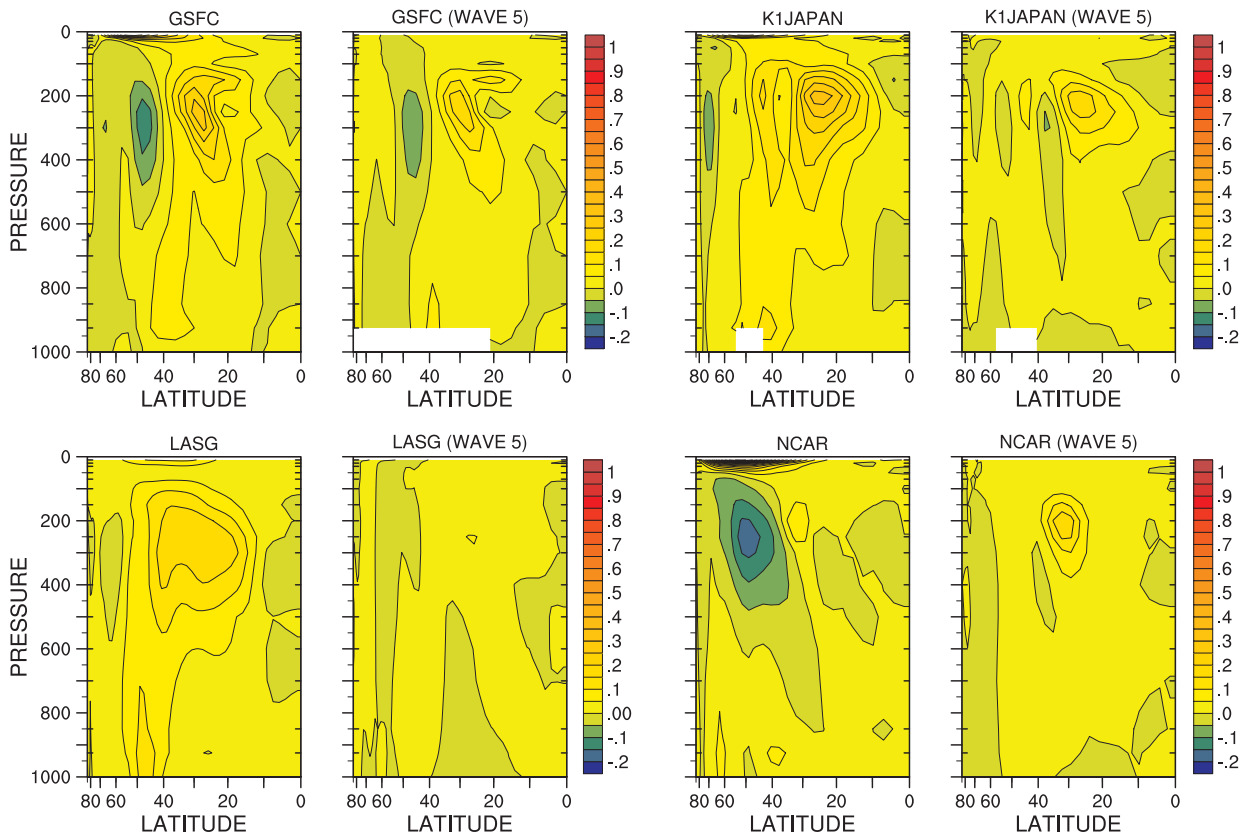
Figure 4.102 (continued): Individual model v variance, stationary eddy, total and wavenumber 5, se_vv, $\left[(\overline{v}^{\,*})^2\right]$, m^2 s^{-2}.

Figure 4.103: Individual model uv co-variance, stationary eddy, total and wavenumber 5, se_uv, $[\overline{u}^*\overline{v}^*]$, m^2 s^{-2}.

145

Figure 4.103 (continued): Individual model uv co-variance, stationary eddy, total and wavenumber 5, se_uv, $[\overline{u}^*\overline{v}^*]$, m^2 s^{-2}.
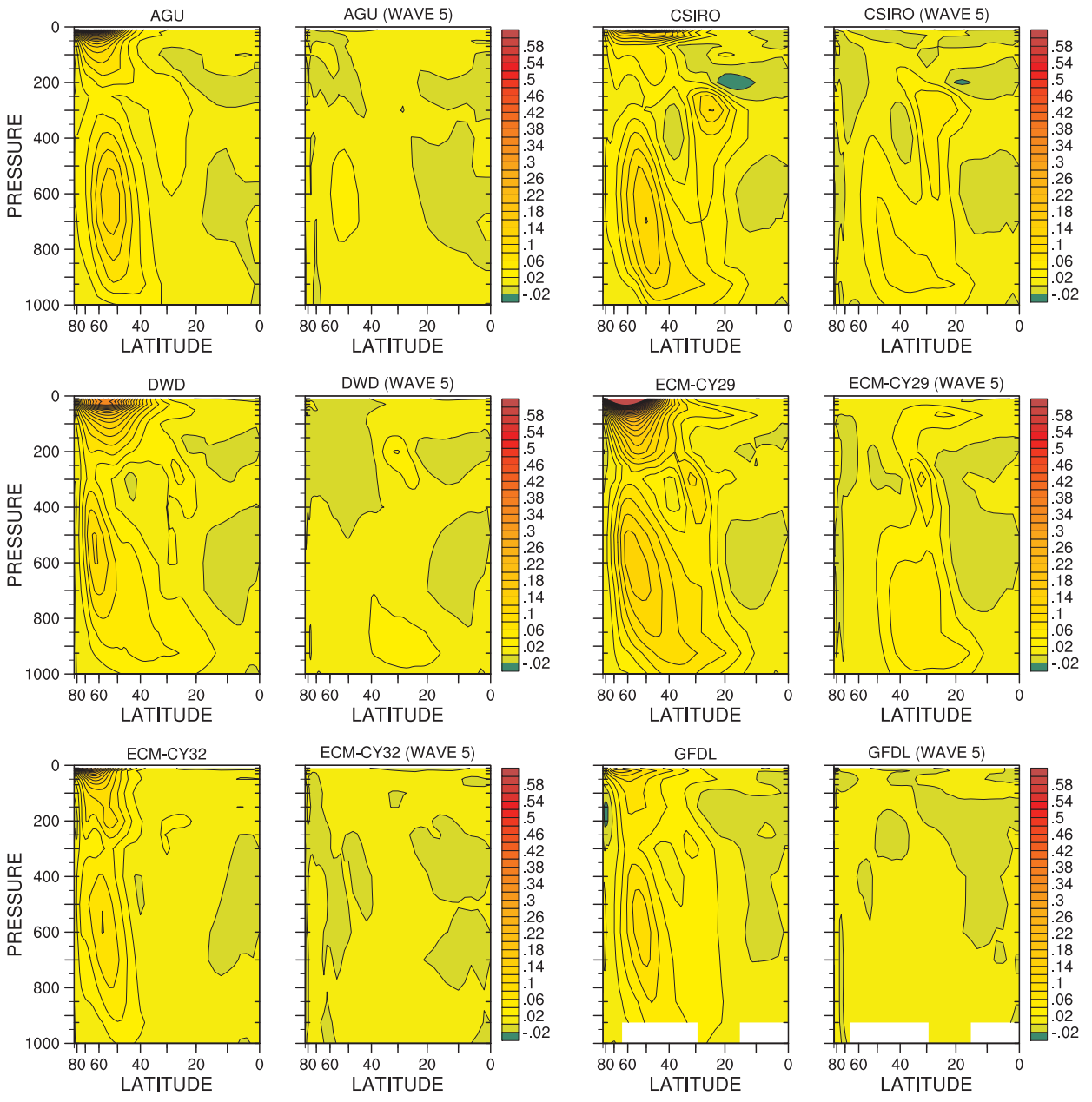
Figure 4.104: Individual model vt co-variance, stationary eddy, total and wavenumber 5, se_vt, $\left[\overline{v}^{*}\overline{T}^{*}\right]$, K m s^{-1}.
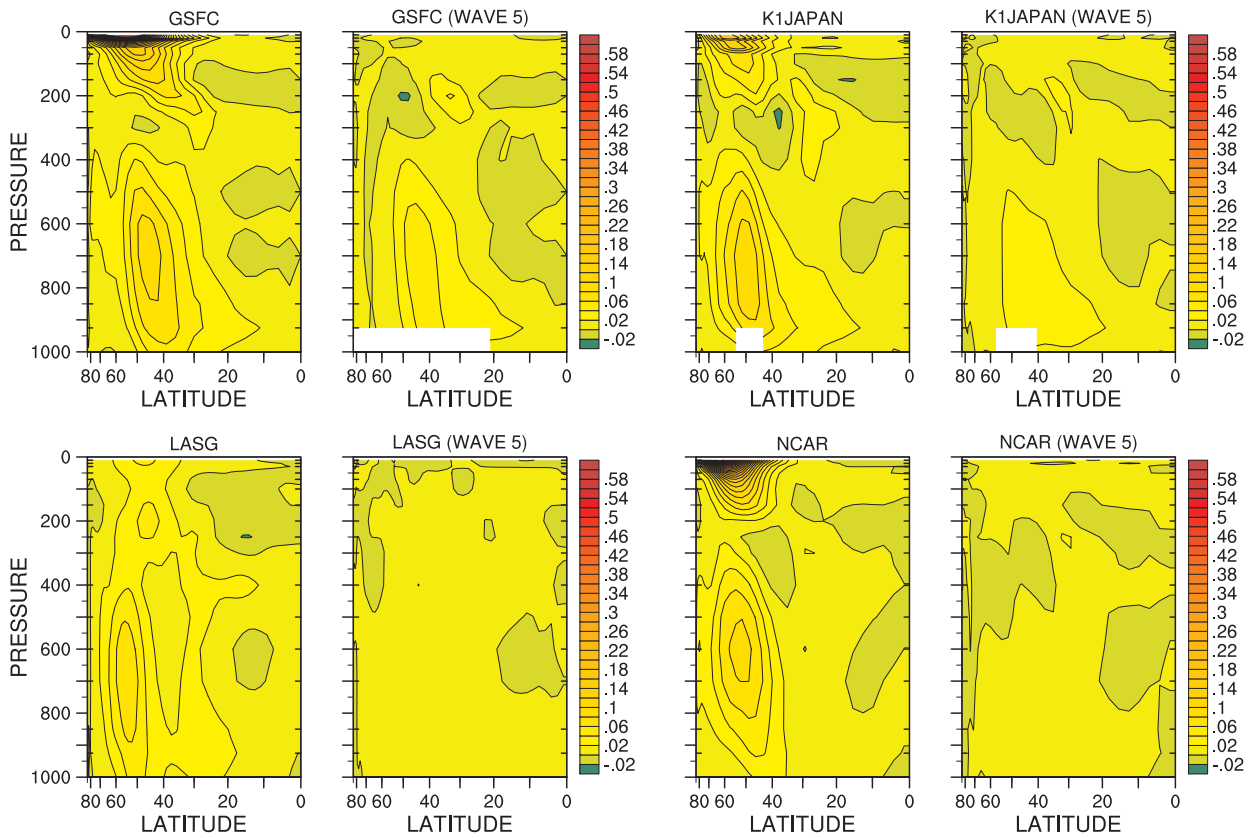
Figure 4.104 (continued): Individual model vt co-variance, stationary eddy, total and wavenumber 5, se_vt, $\left[\overline{v}^{*}\overline{T}^{*}\right]$, K m s^{-1}.
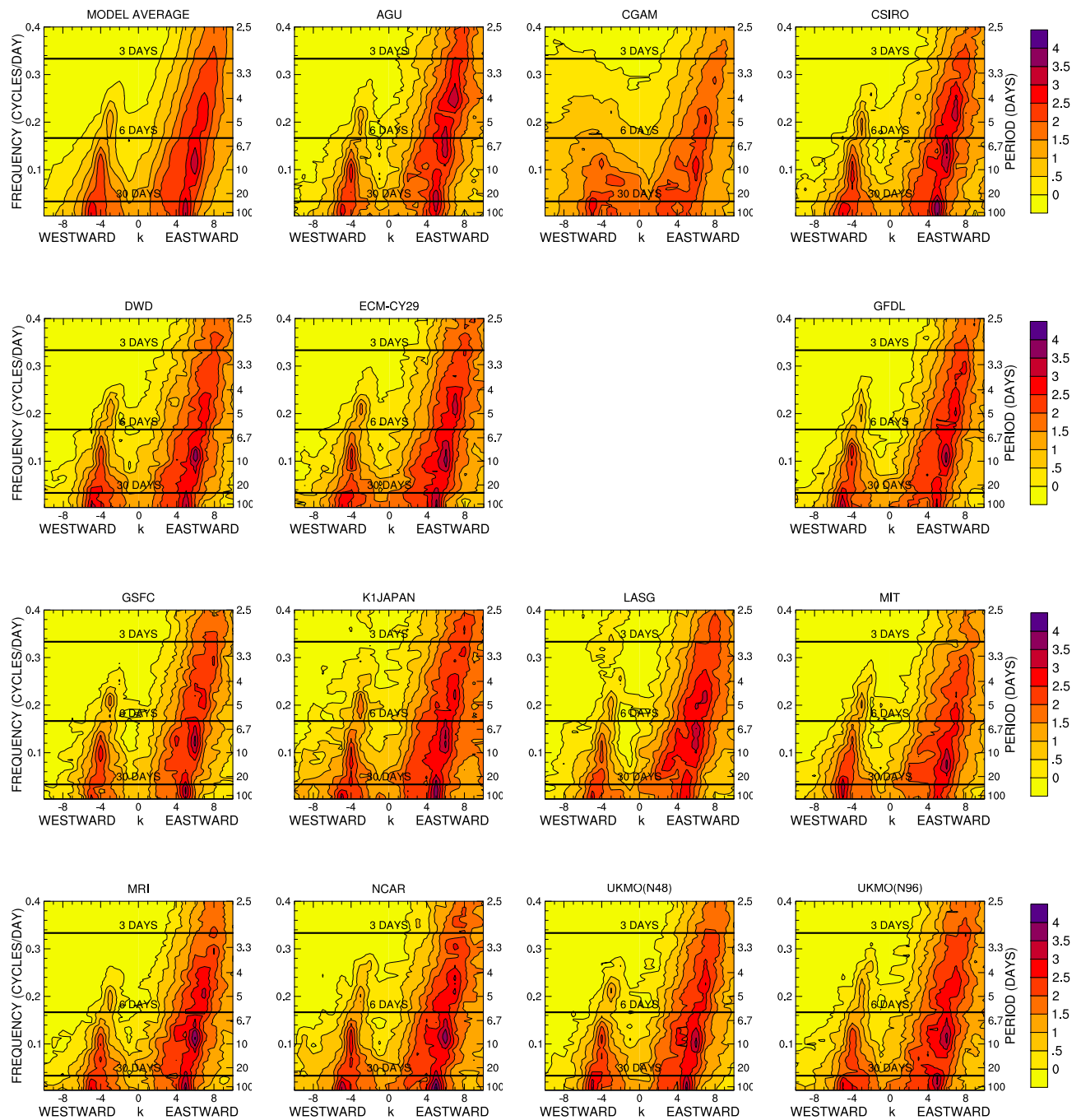
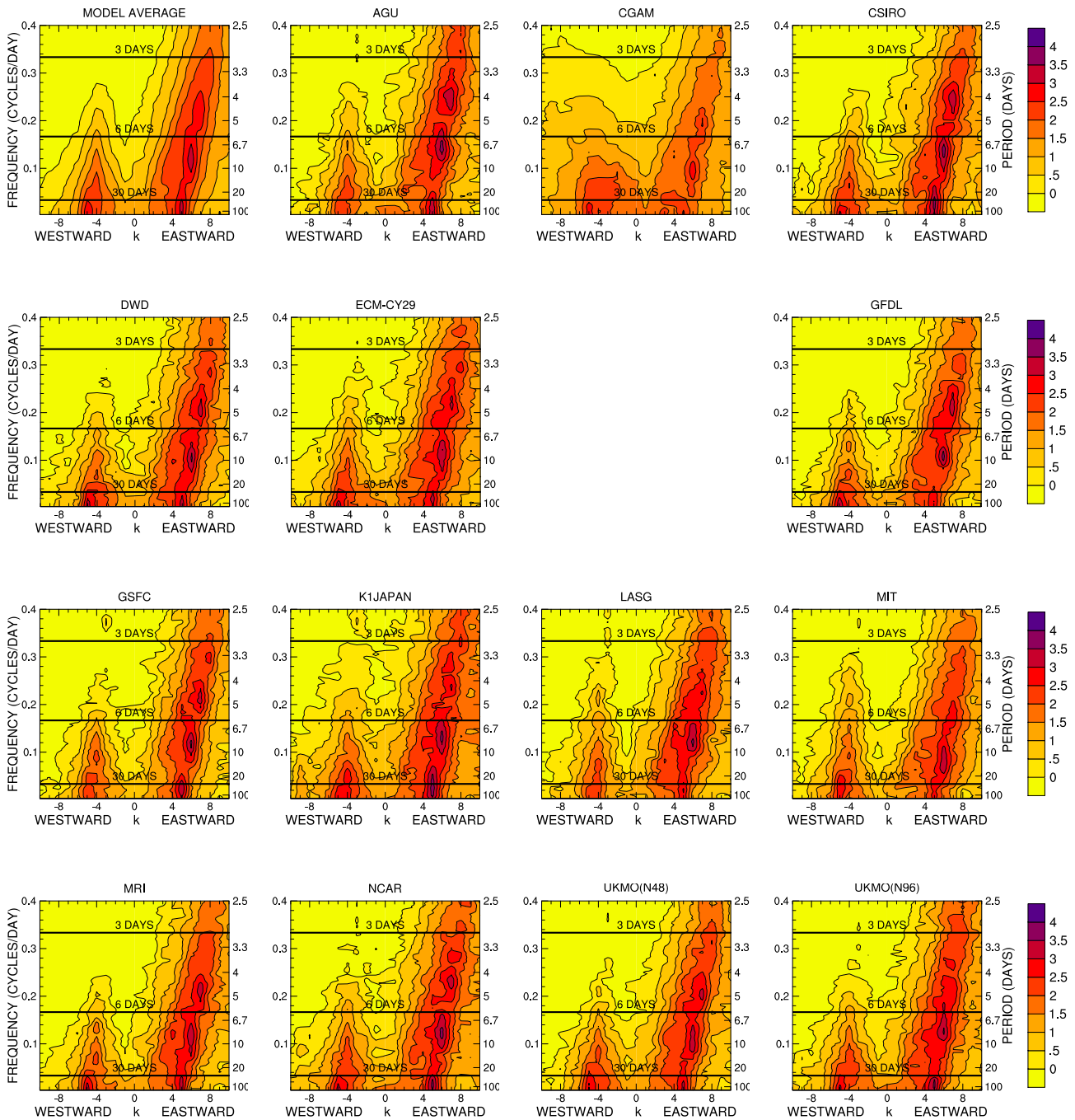Figure 4.105: Wavenumber-frequency diagrams of log of power of symmetric modes of 250 mb meridional wind (v250) at 30° latitude.

Figure 4.106: Wavenumber-frequency diagrams of log of power of anti-symmetric modes of 250 mb meridional wind (v250) at 30° latitude.
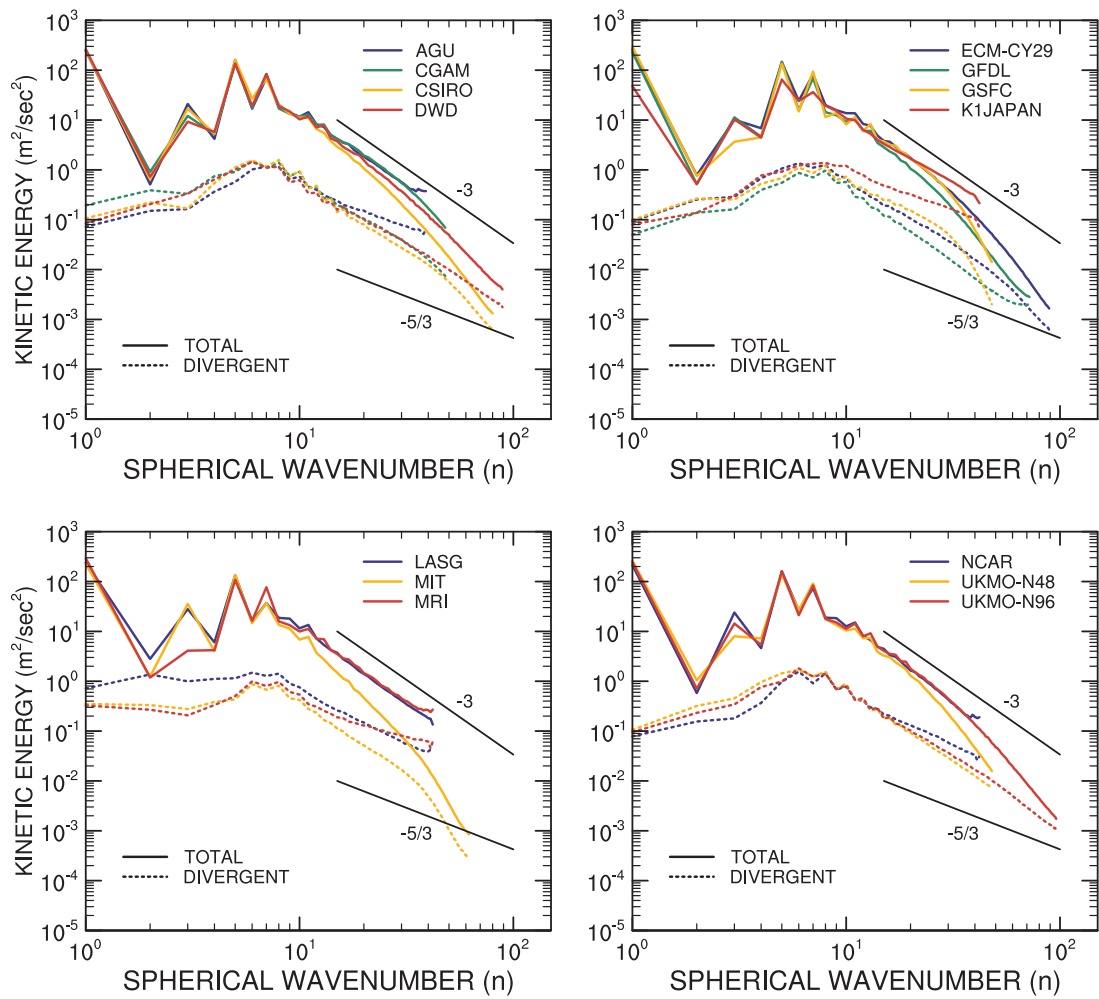
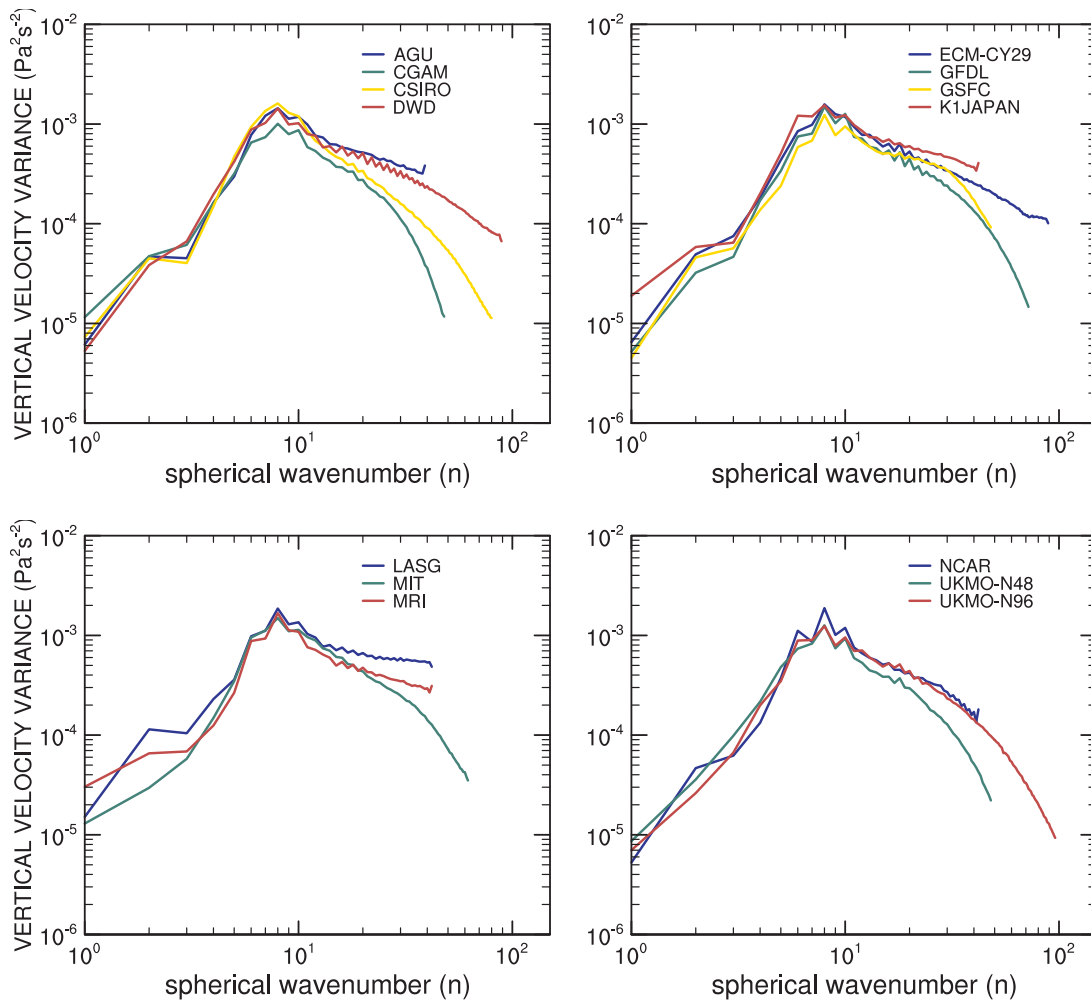Figure 4.107: Kinetic energy spectra at 250 mb, total and divergent component (m^2 s^{-2}).

Figure 4.108: Vertical velocity variance spectra at 500 mb (Pa² s⁻²).